



**HAL**  
open science

# Development of a process for the synthesis of magnetic metal nanoparticles using ionic liquids

Bishoy Morcos

► **To cite this version:**

Bishoy Morcos. Development of a process for the synthesis of magnetic metal nanoparticles using ionic liquids. Inorganic chemistry. Université de Lyon, 2017. English. NNT : 2017LYSE1168 . tel-01718291

**HAL Id: tel-01718291**

**<https://theses.hal.science/tel-01718291v1>**

Submitted on 27 Feb 2018

**HAL** is a multi-disciplinary open access archive for the deposit and dissemination of scientific research documents, whether they are published or not. The documents may come from teaching and research institutions in France or abroad, or from public or private research centers.

L'archive ouverte pluridisciplinaire **HAL**, est destinée au dépôt et à la diffusion de documents scientifiques de niveau recherche, publiés ou non, émanant des établissements d'enseignement et de recherche français ou étrangers, des laboratoires publics ou privés.



N°d'ordre NNT : xxx

## **THESE de DOCTORAT DE L'UNIVERSITE DE LYON**

opérée au sein de  
**l'Université Claude Bernard Lyon 1**

**Ecole Doctorale N° 206**  
**ECOLE DOCTORALE de CHIMIE**  
**Spécialité de doctorat : Chimie**

Soutenue publiquement le 26/09/2017, par :  
**Bishoy MORCOS**

---

# **Mise au point d'un procédé de synthèse de nanoparticules métalliques magnétiques utilisant des liquides ioniques**

---

Directeur de thèse : Timothy McKenna

Co-encadrant : Paul-Henri Haumesser

Devant le jury composé de :

Pr. Anja-Verena Mudring, Professeur, Stockholm University, Sweden	<b>Rapporteur</b>
Pr. Christophe Petit, Professeur, Université Pierre et Marie Curie, Paris	<b>Rapporteur</b>
Pr. Suzanne Giorgio, Professeur, Université Aix-Marseille, Marseille	<b>Examinatrice</b>
Pr. Dominique Luneau, Professeur, Université Claude Bernard Lyon1, Villeurbanne	<b>Examineur</b>
Dr. Catherine Santini, DREm. CNRS, CNRS-CPE Lyon, Villeurbanne	<b>Examinatrice</b>
Dr. Paul-Henri Haumesser, Ingénieur HDR, CEA Leti, Grenoble	<b>Co-directeur de thèse</b>



# UNIVERSITE CLAUDE BERNARD - LYON 1

## **Président de l'Université**

**M. le Professeur Frédéric FLEURY**

Président du Conseil Académique

M. le Professeur Hamda BEN HADID

Vice-président du Conseil d'Administration

M. le Professeur Didier REVEL

Vice-président du Conseil Formation et Vie Universitaire

M. le Professeur Philippe CHEVALIER

Vice-président de la Commission Recherche

M. Fabrice VALLÉE

Directrice Générale des Services

Mme Dominique MARCHAND

## ***COMPOSANTES SANTE***

Faculté de Médecine Lyon Est – Claude Bernard

Directeur : M. le Professeur G.RODE

Faculté de Médecine et de Maïeutique Lyon Sud-Charles  
Mérieux

Directeur : Mme la Professeure C. BURILLON

Faculté d'Odontologie

Directeur : M. le Professeur D. BOURGEOIS

Institut des Sciences Pharmaceutiques et Biologiques

Directeur : Mme la Professeure C. VINCIGUERRA

Institut des Sciences et Techniques de la Réadaptation

Directeur : M. X. PERROT

Département de formation et Centre de Recherche en Biologie  
Humaine

Directeur : Mme la Professeure A-M. SCHOTT

## ***COMPOSANTES ET DEPARTEMENTS DE SCIENCES ET TECHNOLOGIE***

Faculté des Sciences et Technologies

Directeur : M. F. DE MARCHI

Département Biologie

Directeur : M. le Professeur F. THEVENARD

Département Chimie Biochimie

Directeur : Mme C. FELIX

Département GEP

Directeur : M. Hassan HAMMOURI

Département Informatique

Directeur : M. le Professeur S. AKKOUCHE

Département Mathématiques

Directeur : M. le Professeur G. TOMANOV

Département Mécanique

Directeur : M. le Professeur H. BEN HADID

Département Physique

Directeur : M. le Professeur J-C PLENET

UFR Sciences et Techniques des Activités Physiques et  
Sportives

Directeur : M. Y.VANPOULLE

Observatoire des Sciences de l'Univers de Lyon

Directeur : M. B. GUIDERDONI

Polytech Lyon

Directeur : M. le Professeur E.PERRIN

Ecole Supérieure de Chimie Physique Electronique

Directeur : M. G. PIGNAULT

Institut Universitaire de Technologie de Lyon 1

Directeur : M. le Professeur C. VITON

Ecole Supérieure du Professorat et de l'Education

Directeur : M. le Professeur A. MOUGNIOTTE

Institut de Science Financière et d'Assurances

Directeur : M. N. LEBOISNE



*For my lovely wife Madona & my adorable princess Marly  
my parents Samy & Soheir and my sister Monica*



The work presented here was carried out as a part of the CEA-LETI, Grenoble/CPE (C2P2-LCOMS), Lyon collaboration platform between September 2015 and September 2017. Herein, I would like to thank CEA, Grenoble for funding my thesis contract. I would like to thank Dr. Timothy Mckenna for accepting to direct my thesis and for hosting me in C2P2-LCOMS during the whole part of my thesis and for giving access to all the laboratory facilities.

I would like to extend my heartfelt gratitude to Dr. Paul-Henri Haumesser, my supervisors, and to Dr. Catherine Santini, for all their support, encouragement, patience and assistance during these years, a support that exceeded the course of thesis work and writing to include caring about my future as well.

I would like to thank the rest of my thesis committee: Pr. Anja-Verena Mudring and Pr. Christophe Petit for accepting to be referees of my thesis manuscript and for their insightful comments and encouragement. I am also thankful to Pr. Suzanne Giorgio and Pr. Dominique Luneau for accepting to participate in my committee.

My sincere thanks also go to Dr. Robert Morel from INAC-CEA, Grenoble for his ultimate help in performing the SQUID measurements and for the valuable discussions. Dr. Pierre Lecante, CEMES, Toulouse, has been of great help as well for the WAXS measurements of Co-NPs and for the data treatment as well. My gratitude goes also to Dr. Mireille Maret for participating and helping in the ASAXS measurements that have been performed in the ESRF synchrotron and for her ultimate help in analyzing the data. I would like also to thank all the persons of the CT $\mu$  microscopy facility for help and training.

Thank you all, current and previous members of LCOMS, especially Walid, Cherif, Reine, Hassan, Ewelina, Guilina, Julia, Mark, Tapish, Nesrine, Matthieu, Iurii and Mathias for always being there, both for work and for making the work more enjoyable.

I would like to thank my parents and my family, for always being there and for encouraging me to pursue my dreams.

Last but the most important, I would like to express my sincere gratitude to my wife, Madona, for all her love and support and for the precious gift she gave me, our pretty little baby, Marly.





## Abbreviations and acronyms

### Units

h: hour                      min: minute                      g: gram                      MPa: Mega Pascal  
°C: degree Celsius

### Techniques

TEM: transmission electron microscopy  
HRTEM: high resolution TEM  
EDX: electron dispersive X-Ray analysis  
GC: gas chromatography  
MS: mass spectrometry  
HR-MS: high resolution mass spectrometry  
DRIFT: diffuse reflectance infrared Fourier transform  
ASAXS: anomalous small angle X-Ray scattering  
WAXS-RDF: wide angle X-ray scattering – Radial distribution function  
SQUID: superconducting quantum interference device

### Chemicals

IL: ionic liquid  
NPs: nanoparticles  
OM: organometallic precursor  
Im: imidazolium  
 $C_1C_nIm^+$ : 1-butyl-3-alkyl-imidazolium cation  
 $NTf_2^-$ : bis(trifluoromethanesulphonyl)imide anion

Co(COD)(COE): ( $\eta^4$ -1,5-cyclooctadiene)( $\eta^3$ -cyclooctadienyl) Cobalt (I)  
[Fe[mes]<sub>2</sub>]<sub>2</sub>: Tetramesityldiiron,  
Fe(mes\*)<sub>2</sub>: bis[2,4,6-tris(1,1-dimethylethyl)phenyl] Iron (II)  
{Fe<sup>II</sup>[N(SiMe<sub>3</sub>)<sub>2</sub>]<sub>2</sub>}<sub>2</sub>: bis(bis(trimethylsilylamido) Iron (II)  
Pd(dba)<sub>2</sub>: Bis(dibenzylideneacetone)palladium(0)  
Pt(dba)<sub>2</sub>: Bis(dibenzylideneacetone)platinum(0)  
(COD)Pt(Me)<sub>2</sub>: ( $\eta^4$ -1,5-cyclooctadiene) dimethylplatinum(II)  
Ru(2-methylallyl)<sub>2</sub>(COD)<sub>2</sub>: Bis( $\eta^3$ -2-methylallyl)( $\eta^4$ -1,5-cyclooctadiene)ruthenium(II)  
Ru(COD)(COT): ( $\eta^4$ -1,5-cyclooctadiene)( $\eta^6$ -1,3,5-cyclooctatriene)ruthenium(0)

Et<sub>3</sub>SiH: triethylsilane



## **Abstract: Development of a process for the synthesis of magnetic metal nanoparticles in ionic liquids**

Metallic nanoparticles (NPs) exhibit unique physical and chemical properties. However, their use is conditioned by the ability to control their size and structure. The decomposition of organometallic (OM) precursors under  $H_2$  is efficient to generate metallic NPs in organic solvents, but also in ionic liquids (ILs). We have shown that in the latter media, the size can be finely tuned without adding stabilizing agents. Moreover, the resulting “naked” metallic NPs are suitable for catalysis or further reaction with a second OM precursor to form bimetallic NPs.

In this work, we applied this knowledge to the synthesis of mono- and bimetallic NPs in imidazolium-based ILs  $C_1C_n\text{ImNTf}_2$ . Co-NPs with a diameter of *ca.* 4 nm were successfully synthesized by decomposition of  $[\text{Co}(\eta^3\text{-C}_8\text{H}_{13})(\eta^4\text{-C}_8\text{H}_{12})]$  under  $H_2$ . Structural analysis and magnetic characterizations demonstrated that these NPs are metallic and, as expected for this size, superparamagnetic. This approach was extended to the synthesis of bimetallic CoPt and CoRu-NPs. It turned out that the best strategy is probably to simultaneously decompose the Co and Pt (or Ru) precursors. This reaction provides monodisperse suspensions of NPs, a good indication that they are bimetallic. Further structural characterizations, in particular using anomalous SAXS, are also considered to elucidate their structure.

## **Résumé: Mise au point d'un procédé de synthèse de nanoparticules métalliques magnétiques utilisant des liquides ioniques**

Les nanoparticules (NPs) métalliques possèdent des propriétés physiques inhabituelles et suscitent un grand intérêt pour divers domaines d'application. En particulier, les NPs de métaux magnétiques offrent de nombreux avantages dans une grande variété d'applications technologiques, médicales et en catalyse. Généralement, ces applications nécessitent de fabriquer des NPs de taille et de composition contrôlées. Cette thèse vise à démontrer que de telles NPs peuvent être obtenues par décomposition de précurseurs organométalliques (OM) dans des solvants d'un genre particulier, les liquides ioniques (LIs). Ce sont des sels possédant un très bas point de fusion (inférieur à  $100^\circ\text{C}$ ) et qui possèdent des propriétés uniques, dont celle de stabiliser des nano-objets. Pour y parvenir, des précurseurs OM des métaux d'intérêt (Co et Fe) ont été identifiés. Des Co-NPs ont pu être synthétisées de manière contrôlée : Elles possèdent une structure cristalline  $\epsilon\text{-Co}$  et les propriétés superparamagnétiques attendues pour le  $\text{Co}^{(0)}$ . Dans le cas du Fe, une oxydation partielle des NPs n'a pu être évitée. La seconde partie du travail s'est donc concentrée sur l'obtention de NPs bimétalliques CoM, avec  $M=\text{Ru}$  ou  $\text{Pt}$ . Dans le cas de Ru, toutes les synthèses ont conduit à des NPs bimétalliques, tandis que seule une décomposition simultanée des deux précurseurs de Co et Pt a permis de former des CoPt-NPs. Ces NPs pourraient permettre de fabriquer des dispositifs de stockage de données plus performants ou des catalyseurs moins onéreux.



## Table of contents:

<b>Introduction</b>	<b>1</b>
<b>Chapter I-A. State of the art on the chemical synthesis and structural properties of Cobalt Nanoparticles (Co-NPs) in different solvents</b>	<b>7</b>
I-A. I. Basic properties and applications of Co-NPs	9
I-A. II. Synthesis of Co-NPs: physical versus chemical methods	10
I-A. III. Synthesis of Cobalt NPs in solution	11
I-A. IV. Synthesis of Cobalt NPs from organometallic precursors in organic solvent	12
I-A. V. Synthesis and characterization of Co-NPs from Co(COD)(COE), in organic solvents	13
i. Preparation and Characterization of Co(COD)(COE)	13
I-A. VI. Synthesis of Co-NPs from organometallic precursors in ionic liquids	16
I-A. VII. Crystal structures of metallic Co-NPs	18
I-A. VIII. Superparamagnetic nature of Co-NPs	23
I-A. IX. Conclusion and strategy	24
<b>Chapter I-B. Results: Synthesis and structural properties of Cobalt Nanoparticles (Co-NPs) in Ionic Liquids</b>	<b>25</b>
I-B. I. Thermal stability of Co(COD)(COE)	28
i. Thermo-gravimetric analysis (TGA) of solid Co(COD)(COE) under N <sub>2</sub>	28
ii. DRIFT analysis of solid Co(COD)(COE) under H <sub>2</sub>	29
iii. In situ GC-mass monitoring of the thermal stability under H <sub>2</sub> of Co(COD)(COE) in C <sub>1</sub> C <sub>4</sub> ImNTf <sub>2</sub> :	31
iv. In situ GC-mass monitoring of the thermal stability in C <sub>1</sub> C <sub>4</sub> ImNTf <sub>2</sub> : under Ar then H <sub>2</sub>	33
I-B. II. Influence of experimental parameters on the Co-NP size	35
i. Influence of reaction duration	35
ii. Influence of temperature	35
iii. Influence of the side alkyl chain length	36
I-B. III. Could R <sub>n</sub> SiH <sub>4-n</sub> be used as reducing agent of Co(COD)(COE) instead of H <sub>2</sub> ?	37
i. Triethylsilane (Et <sub>3</sub> SiH)	37
ii. Reaction with other silane compounds	39
I-B. IV. Physico-chemical properties of Co NPs	40
i. Structural analysis of Co-NPs	40
ii. Magnetic properties:	44
I-B. V. Conclusion	53
<b>Chapter II-A. State of the art on the chemical synthesis and structural control of cobalt based bimetallic nanoparticles</b>	<b>55</b>
II-A. I. General concepts of bimetallic nanostructures	57
i. Structure determining factors	58

<b>II-A. II.</b>	<b>Co-based nanoparticles of particular interests</b>	<b>60</b>
i.	Co-Pt NPs	60
ii.	Co-Ru NPs	63
<b>II-A. III.</b>	<b>Synthesis of bimetallic nanoparticles through the organometallic approach</b>	<b>64</b>
<b>II-A. IV.</b>	<b>Bimetallic nanoparticles in ionic liquids</b>	<b>67</b>
i.	CoPt NPs	67
ii.	RuCu NPs	69
<b>II-A. V.</b>	<b>Generalization to other bimetallic nanoparticles</b>	<b>75</b>
i.	Ruthenium-core based nanoparticles	76
ii.	Bimetallic Cu based nanoparticles	79
<b>Chapter II-B. Results: Synthesis and structural properties of bimetallic Co-based nanoparticles in ILs</b>		<b>85</b>
<b>II-B. I.</b>	<b>Surface chemistry of Co-NPs</b>	<b>87</b>
i.	Reaction with tetramethyltin	87
ii.	Catalytic hydrogenation of ethylene	88
<b>II-B. II.</b>	<b>Synthesis of Co-Ru bimetallic NPs</b>	<b>89</b>
i.	By successive decomposition of 2 metal precursors	89
ii.	One-pot synthesis approach for RuCo-NPs	92
iii.	Defining the structure of CoRu-NPs	93
<b>II-B. III.</b>	<b>Synthesis of CoPt bimetallic NPs:</b>	<b>97</b>
i.	By successive decomposition of 2 metal precursors	97
ii.	One-pot synthesis approach	100
iii.	Defining the structure of CoPt NPs	102
<b>II-B. IV.</b>	<b>CoPt-NPs as hydrogenation catalysts</b>	<b>103</b>
<b>II-B. V.</b>	<b>Conclusion</b>	<b>106</b>
<b>Chapter III. Iron Nanoparticles (Fe-NPs)</b>		<b>109</b>
<b>III. I.</b>	<b>Synthesis of Fe-NPs from organometallic precursors: State of the art</b>	<b>111</b>
i.	Synthesis of Fe-NPs in organic solvents	111
ii.	Synthesis of Fe-NPs in ionic liquids	113
<b>III. II.</b>	<b>Selection and synthesis of Fe organometallic precursors</b>	<b>115</b>
i.	Bis(1,3,5,7-Cyclooctatetraene) iron(0), Fe(COT) <sub>2</sub>	116
ii.	Bis(bis(trimethylsilylamido)Iron(II), {Fe <sup>II</sup> [N(SiMe <sub>3</sub> ) <sub>2</sub> ] <sub>2</sub> ] <sub>2</sub> (Collaboration Pr S. Daniele)	117
<b>III. III.</b>	<b>Synthesis of Fe-NPs from the Fe(COT)<sub>2</sub>: Results</b>	<b>118</b>
i.	Thermal decomposition of Fe(COT) <sub>2</sub> under H <sub>2</sub>	118
ii.	Reaction of Fe(COT) <sub>2</sub> solutions with H <sub>2</sub>	119
iii.	Characterization of Fe-NPs	120
<b>III. IV.</b>	<b>Synthesis of Fe-NPs from {Fe[N(SiMe<sub>3</sub>)<sub>2</sub>]<sub>2</sub>}: Results</b>	<b>123</b>
i.	Thermal decomposition of {Fe[N(SiMe <sub>3</sub> ) <sub>2</sub> ] <sub>2</sub> under H <sub>2</sub>	123
ii.	Reaction of {Fe[N(SiMe <sub>3</sub> ) <sub>2</sub> ] <sub>2</sub> solutions with H <sub>2</sub>	125
iii.	Characterization of Fe-NPs	127
<b>III. V.</b>	<b>Conclusion</b>	<b>129</b>

<b>Chapter IV. Experimental Part</b>	<b>131</b>
<b>IV.I. Synthesis of NPs</b>	<b>133</b>
i. Materials	133
ii. NMR spectroscopy	133
iii. GC analysis	133
iv. Synthesis of ionic liquids	133
v. Thermal analysis	134
vi. Synthesis of monometallic NPs	135
vii. Synthesis of bimetallic NPs	136
<b>IV.II. Determination of hydrides onto the surface of Co-NPs</b>	<b>137</b>
i. Reaction with SnMe <sub>4</sub>	137
ii. Hydrogenation of ethylene by Co-NPs in the IL	137
<b>IV.III. Catalytic hydrogenation of cyclohexadiene</b>	<b>138</b>
<b>IV.IV. High resolution transmission electron microscopy (HRTEM)</b>	<b>138</b>
<b>IV.V. Wide angle X-ray scattering (WAXS):</b>	<b>139</b>
<b>IV.VI. Anomalous Small Angle X-ray Scattering (ASAXS)</b>	<b>141</b>
<b>IV.VII. Magnetic measurement (SQUID)</b>	<b>142</b>
<b>Conclusion and outlook</b>	<b>145</b>
<b>I. Synthesis of monometallic NPs in ILs</b>	<b>147</b>
i. Synthesis of Co-NPs	147
ii. Synthesis of Fe-NPs	149
<b>II. Synthesis of bimetallic NPs in ILs</b>	<b>150</b>
i. Surface chemistry of Co-NPs	150
ii. Synthesis of CoRu-NPs	151
iii. Synthesis of CoPt-NPs	152
<b>Résumé substantiel en français</b>	<b>155</b>
<b>I. Introduction</b>	<b>157</b>
i. Intérêt et applications des nanoparticules (NPs) magnétiques	157
<b>II. Synthèse des NPs métalliques par voie chimique</b>	<b>158</b>
<b>III. Synthèse de NPs monométalliques dans les LIs</b>	<b>159</b>
i. Synthèse de Co-NPs	159
ii. Synthèse de Fe-NPs	162
<b>IV. Synthèse de NPs bimétalliques dans les LIs</b>	<b>163</b>
i. Chimie de surface des Co-NPs	163
ii. Synthèse de CoRu-NPs	164
iii. Synthèse de CoPt-NPs	166
<b>V. Conclusion</b>	<b>168</b>
<b>References</b>	<b>171</b>
<b>Appendix 1</b>	<b>191</b>



<b>Appendix 2</b>	<b>197</b>
<b>Appendix 3</b>	<b>201</b>
<b>Appendix 4</b>	<b>205</b>

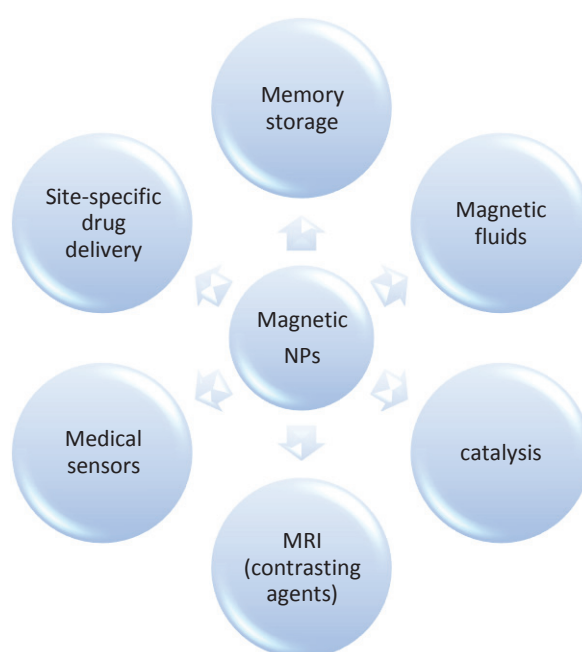
# Introduction

---



Mono-dispersed metallic nanoparticles (NPs) represent a very interesting area of research owing to their unusual magnetic, electrical, optical and thermal properties which originate from quantum effects associated with very high surface to volume ratio. For this reason, metallic NPs are of great interest for various fields of application. Generally, these applications require small (less than 10 nm) NPs with precise control of their size, composition and morphology in significant quantities.<sup>1</sup>

In particular, magnetic metal NPs offer many advantages in a variety of applications (Scheme 1).<sup>2</sup>



Scheme 1 : Different applications of magnetic NPs.

Magnetic NPs can be used in different technological applications such as data storage,<sup>3</sup> spintronics<sup>4</sup> or magnetic fluids (ferrofluids).<sup>5</sup> They can also be used in the medical field, particularly in diagnostic tools. For example, some magnetic NPs are very good contrasting agents for magnetic resonance imaging of cancer cells.<sup>6</sup> They can also treat certain forms of cancer by localized thermal destruction of the tumor as a result of excitation by an alternative magnetic field of appropriate frequency and amplitude.<sup>7</sup> Another possibility is to be used as a carrier for targeted drug delivery to the tumor.<sup>8</sup>

Moreover, some magnetic NPs such as Co-NPs are very promising in the field of catalysis.<sup>9</sup> For example, they can be used in the Fischer-Tropsch process to convert CO and

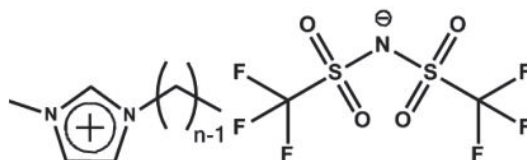
H<sub>2</sub> into liquid hydrocarbons.<sup>10</sup> In this particular example, Co-NPs showed increased selectivity compared to competing conventional catalysts. Another less direct use of magnetic NPs in catalysis is to use them as a chemically inert magnetic support for the catalyst itself. They then facilitate the recycling of the latter, since they make it possible to extract it easily from the reaction medium by application of an external magnetic field. For example, a Mn<sup>(III)</sup> complex supported on Co-NPs was successfully used to oxidize alcohols and sulfides, then to be recycled with a very good yield.<sup>11</sup>

For most of these applications, better performances are obtained when the magnetic metal (Co for example) is alloyed with a second metal. Indeed, this association with other metals such as Pt or Ru modifies the physical properties of the initial NPs in a positive way. For example, the ordered intermetallic compound CoPt is an excellent candidate for future high-density magnetic data storage devices. Indeed, this compound shows good chemical stability, high magnetocrystalline anisotropy and high coercivity, which gives it exceptionally “hard” magnetic properties.<sup>12, 13</sup> Other bimetallic CoPt NPs represent excellent fuel cell catalysts.<sup>14, 15, 16, 17, 18</sup> Similarly, Co-Ru NPs find applications as a catalyst for many reactions such as the Fischer-Tropsch CO hydrogenation reaction,<sup>19</sup> nitroarene reduction reactions<sup>20</sup> and as an electrocatalyst for oxygen reduction in fuel cells.<sup>21</sup> For all these examples, mixing Ru with Co significantly improved the catalyst performance.

In most of these applications, monodispersed NPs are needed with sizes ranging from a few to a few tens of nanometers. Chemical processes in solution are well suited to synthesize such metallic NPs from organometallic (OM) precursors or salt precursors.<sup>22, 23</sup> However, they usually require stabilizing agents such as ligands or polymers to control the size and prevent the aggregation of the NPs. In many applications, this surface contamination of the NPs is not desired.

In recent years, it has been demonstrated that this route of synthesis can be applied in some innovative solvents such as ionic liquids (ILs). In this case, monodisperse and stable NPs can be directly obtained, without adding a stabilizer.<sup>24</sup> ILs are salts that have a very low melting point (typically below 100°C) with very unique properties. They are nonvolatile, chemically and thermally stable and possess a high electrical conductivity.<sup>25</sup> Importantly, they can act as a self-stabilizing media for the synthesis of naked metallic NPs with enhanced size and structure control.

This synthetic route was developed in our Laboratory over the past years for the 1-butyl-3-alkyl-imidazolium bis(trifluoromethanesulphonyl)imide ( $C_1C_n\text{ImNTf}_2$ ) ILs family, Scheme 2.<sup>26</sup> It has yielded many metal NPs such as Cu, Ru, Pt, Mn, Ni, and even Ta. It has also demonstrated that bimetallic NPs with controlled structures could be accessible.<sup>27</sup>



Scheme 2: Structural formula of 1-butyl-3-alkyl-imidazolium bis(trifluoromethanesulphonyl)imide ( $C_1C_n\text{ImNTf}_2$ ) ILs.

The objective of this thesis is therefore to obtain, by this simple and relatively inexpensive method, mono- and bimetallic magnetic, Co and Fe based, NPs and to define their structural and magnetic properties.

The first chapter of this thesis deals with the synthesis, the structural and magnetic properties of Co-NPs suspensions in ILs. It includes also an all-liquid approach for the synthesis of Co-NPs in which the potentially dangerous  $H_2$  gas is replaced by a liquid reductant. The last part of the chapter is related to several attempts to achieve the synthesis of  $Fe^{(0)}$ -NPs in ILs through the decomposition of different Fe-OM precursors.

In the second chapter, Co-based bimetallic systems are targeted. Firstly, the presence of hydrides onto the surface of Co-NPs was investigated. Then, their role in controlling and facilitating the formation of the bimetallic NPs was studied. Based on this, the synthesis of different bimetallic systems, CoRu-NPs and CoPt-NPs, through different approaches (1 step, 2 steps synthetic approaches) was performed. Additionally, their structure was tentatively resolved by SAXS synchrotron measurements.

Finally, all the experimental procedures are detailed in the last (3<sup>rd</sup>) chapter of the thesis.



# **Chapter I-A.**

---

## **State of the art:**

### **Chemical synthesis and structural properties of Cobalt Nanoparticles (Co-NPs) in different solvents**





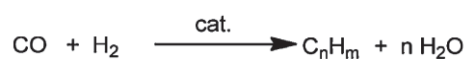
## I-A. I. Basic properties and applications of Co-NPs

Mono-dispersed metallic nanoparticles (NPs) represent a very interesting area of research owing to their special magnetic, electrical, optical and thermal properties which originate from the quantum effects as well as the very high surface to volume ratio of such small particles.<sup>28</sup> Metallic nanoparticles (NPs), in particular, have attracted much interest in a range of applications, which require small size NPs (below 10 nm) with precise control of size, composition and morphology in chemically significant quantities.<sup>28, 29, 30</sup> Cobalt nanoparticles (Co-NPs) represent one of the most interesting metallic nanoparticles due to their unique magnetic, catalytic and optical properties (Table 1).<sup>31</sup>

Table 1 : Main properties of metallic Cobalt

Atomic radius, non-bonded (Å)	2.00
Covalent radius (Å)	1.18
Boiling point	2927°C
Curie temperature	1115 °C
Density (g cm <sup>-3</sup> )	8.86
Melting point	1495°C
Electron affinity (kJ mol <sup>-1</sup> )	63.873
Electronegativity (Pauling scale)	1.88
1 <sup>st</sup> Ionisation energy (kJ mol <sup>-1</sup> )	760.402
Common oxidation states	3, 2, 0, -1
Isotopes	<sup>59</sup> Co
Specific heat capacity (J kg <sup>-1</sup> K <sup>-1</sup> )	421
Electrical resistivity	6 × 10 <sup>-8</sup> Ω m
Magnetic moment	1.6–1.7 μ <sub>B</sub> /atom
Crystal structure	hcp, fcc, ε-Co
Surface energy (bulk)	2.55 J.m <sup>-2</sup>

As catalysts, colloidal Co-NPs systems show a great potential because of the high ratio of atoms remaining at the surface, which are therefore available for acting in the chemical transformation of the substrates. For example, they may be used in the Fischer–Tropsch process to convert CO and H<sub>2</sub> into liquid hydrocarbons. Co-NPs showed enhanced selectivity compared to their conventional competitors.<sup>10</sup>



Another indirect use of Co-NPs in catalysis is as a magnetic support for the actual catalyst without interfering in the catalyzed reaction itself. In such a way, they facilitate the recovery of the catalyst from the reaction medium upon using an external magnetic field to collect the NPs. An example is the Schiff base of Mn(III) complex supported on magnetic Co-NPs that has proven a highly efficient retrievable heterogeneous catalyst in oxidation of alcohols and sulfides compounds.<sup>11</sup>

Co-NPs are also used in the medical field for the diagnosis and treatment of cancer.<sup>6, 7, 8, 32, 33</sup>

Due to their unique magnetic properties, Co-NPs are useful for data storage,<sup>2</sup> and magnetic fluids.<sup>34</sup> Indeed, some ferro-fluids are based on cobalt. They are liquids that become strongly magnetized in the presence of a magnetic field. They are composed of colloidal suspensions of very fine ( $\sim 10$  nm) magnetic nanoparticles and they can find applications in dynamic sealing devices, heat dissipation, dampers and many other technological applications.<sup>35</sup>

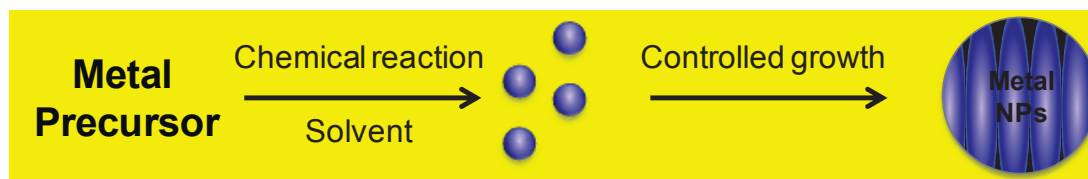
## **I-A. II. Synthesis of Co-NPs: physical versus chemical methods**

As reported for other metals, the metallic Co-NPs are generated through either physical or chemical methods. Physical methods include sputtering deposition, laser evaporation and then condensation in a gas flow, in a liquid or on a solid surface.<sup>36</sup> For example, Co-NPs with sizes ranging from 28 to 70 nm are successfully prepared by direct current arc plasma evaporation.<sup>37</sup> The NP size is increasing with the intensity of the current, the filling pressure, and the pressure ratio of hydrogen to argon ( $P_{H_2}/P_{Ar}$ ). Co-NPs were characterized by transmission electron microscopy (TEM), X-ray diffraction (XRD), X-ray fluorescence analysis (XRF) and selected area electron diffraction (SAED). They were spherical in shape with cubic crystal structure and presented a purity of 99.9% wt. However, the limitation of such techniques is the lack of size control for particles smaller than 100 nm.<sup>38</sup>

By contrast, the chemical routes, based on the reduction or decomposition of a suitable precursor of the desired metal, usually provide better size control for nanoparticles smaller than 10 nm. Several methods could be applied to decompose metal precursors like thermal decomposition, reduction ( $H_2$  gas, hydrazine, ...) ultrasonic activation, photolysis and hydrolysis reactions.<sup>39</sup> Several chemical processes for the synthesis of Co-NPs will be discussed in the following sections.

### I-A. III. Synthesis of Cobalt NPs in solution

Solution based methods represent an important category of the chemical methods of synthesis of NPs. In such approach, a suitable metal precursor is dissolved in a suitable solvent and then decomposed through a chemical reaction to produce first small nuclei of the metal (nucleation step) that grow up in a controlled way to result in metal NPs of controlled structure (growth step), Scheme 3.



Scheme 3 : Controlled precipitation reaction for the synthesis of metal NPs

To achieve small mono-dispersed NPs, it is important to have a very fast nucleation step that is followed by slow growth step. In addition, ligands or stabilizers must be used. Such compounds attach to the surface of the NPs to stabilize them and to prevent them from growing up to the bulk state.

One example for the synthesis of Co-NPs is the reduction of aqueous solutions of metal salts like  $\text{CoSO}_4$ <sup>40</sup> and  $\text{CoCl}_2$ <sup>41, 42</sup>. Indeed, the standard reduction potential of  $\text{Co}^{2+}/\text{Co}^0$ , -0.28 V (vs SHE), is much higher than that of water, -0.83 V, making it possible to reduce these salts in aqueous media. In addition, they are easy to handle, stable and commercially available at low cost. However, their anions could be strongly linked to the NP surface affording an oxidized Co shell.<sup>40, 41, 42</sup> An important limitation for the aqueous media based preparations is thus the oxidation of NPs surface after synthesis.

Another procedure developed by C. Petit, et al,<sup>43, 44</sup> is based on using pure Cobalt<sup>(II)</sup> 2,3-bis(2-ethylhexyl)-2-sulfosuccinate reverse micelles and reducing it using  $\text{NaBH}_4$  followed by the addition of lauric acid to the micellar solution and extracting the Co-NPs from the reverse micelles by ethanol. This method was very convenient and afforded Co-NPs around 8 nm with very good size distribution. Monolayer self-assembly of hcp cobalt nanocrystals was even achieved upon annealing the obtained Co-NPs.<sup>45</sup>

#### I-A. IV. Synthesis of Cobalt NPs from organometallic precursors in organic solvent

Due to the drawbacks in the aqueous solutions based methods, the need for new precursors soluble in non-aqueous solvents has emerged. In organic liquid phase, the synthesis of small Co NPs has been reported by chemical or thermal decomposition of Co organometallic precursors,<sup>46, 47, 48, 49, 50, 51, 52</sup> or Co carbonyl compounds.<sup>31, 53, 54, 55</sup> In all cases, the small nanoparticles were only kinetically stable and their agglomeration into the more thermodynamically stable bulk form must be prevented by the addition of an organic surfactant or polymer.<sup>47, 49, 50, 52</sup> As a result, the size and size distribution of NPs depended on the nature and the relative concentrations of the organic additives and the metallic precursor.<sup>56</sup>

Different Co precursors are commercially available. They can be classified following the Co valence. Among precursors containing Co<sup>(0)</sup>, Co<sub>2</sub>(CO)<sub>8</sub> is widely used to generate Co-NPs under thermal decomposition, using sonication or microwave irradiation methods.<sup>39, 57</sup> The main disadvantage of such carbonyl compounds is the possibility to leave some CO groups coordinated to the NP surface with risk of a dissociative adsorption leading to oxide species and carbon residue on the surface.<sup>58</sup>

Co<sup>(II)</sup> precursors are difficult to reduce and additives were always required to assist their reduction.<sup>59</sup> The bis(cyclopentadienyl) cobalt(II) in the presence of di-isobutyl aluminum hydride was spontaneously reduced but Co-Al bond were detected in the EXAFS spectrum.<sup>59</sup> The bis(cyclopentadienyl) cobalt(II) was reduced under H<sub>2</sub> above 150 °C, only in the presence of a platinum precursor to form bimetallic CoPt<sub>3</sub>-NPs.<sup>60</sup>

Another Co<sup>(II)</sup> precursor, Co[N(SiMe<sub>3</sub>)<sub>2</sub>]<sub>2</sub>, can be reduced under H<sub>2</sub> at 150°C to give Co-NPs.<sup>61</sup> However parasitic reactions involving the silylamide ligand could occur. Consequently, a variation of Co-NPs size from 4.6 nm to 13.7 nm or even to very large multipods was observed by changing the rate of ligand addition to Co[N(SiMe<sub>3</sub>)<sub>2</sub>]<sub>2</sub> solution (from slow to fast addition rates respectively), even if this step took place before applying H<sub>2</sub> and before starting the decomposition reaction itself.<sup>61</sup>

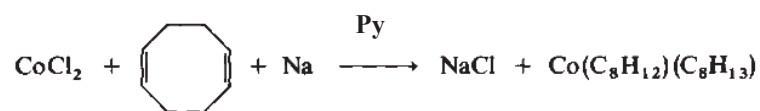
The Co<sup>(I)</sup> olefinic organometallic complex (η<sup>4</sup>-1,5-cyclooctadiene)(η<sup>3</sup>-cyclooctadienyl) Cobalt (I), Co(COD)(COE) was reduced by different reductants. In the presence of di-isobutyl aluminum hydride, Co-NPs with a size of 2.5±0.4 nm and a ε-Co structure were obtained.<sup>59</sup> Despite XANES measurements indicated that the NPs were not oxidized, EXAFS showed bonding to light elements, probably Al.<sup>59</sup> By contrast, when H<sub>2</sub> was used as a reducing agent

in mild conditions (20-150°C, 0.4 MPa H<sub>2</sub>), in the presence of different stabilizers, the same precursor afforded monodispersed metallic Co-NPs, with simultaneous formation of volatile hydrocarbons, mainly cyclooctane.<sup>46, 47, 48, 49, 50, 51, 52</sup> Subsequently, we focus our study on the use of Co(COD)(COE).

## I-A. V. Synthesis and characterization of Co-NPs from Co(COD)(COE) in organic solvents

### i. Preparation and Characterization of Co(COD)(COE)

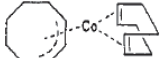
Co(COD)(COE) was formed through the reduction of CoCl<sub>2</sub> by sodium in the presence of pyridine and 1,5-cyclooctadiene.<sup>62, 63</sup> Obtained as black crystals, it exhibits a planar configuration,<sup>64</sup>



It is quite soluble in aromatics such as benzene or toluene as well in pentane or THF. It is air sensitive, stable at RT for short periods but stable for months under N<sub>2</sub> at – 35 °C. Upon warming at about 2 °C/min, the crystals collapse at 60-65°C, but the material does not become fluid even at 100 °C. This compound decomposes under vacuum (no H<sub>2</sub>) at 150-200 °C, and cyclooctene is found to be the main decomposition product together with some traces of cyclooctane.<sup>62</sup>

The characteristic data of Co(COD)(COE), <sup>1</sup>H NMR, <sup>13</sup>C NMR, and <sup>59</sup>Co NMR, published in the literature are shown in Figure 1 and Table 2.<sup>63, 65</sup>

Table 2 : 94.5 MHz <sup>59</sup>Co NMR shifts and line widths of [Co(η<sup>3</sup>-C<sub>8</sub>H<sub>13</sub>)(η<sup>4</sup>-C<sub>8</sub>H<sub>12</sub>)]<sup>63, 65</sup>

compd	no.	δ( <sup>59</sup> Co)	W <sub>1/2</sub> , Hz
	15 <sup>b</sup>	-275	3700

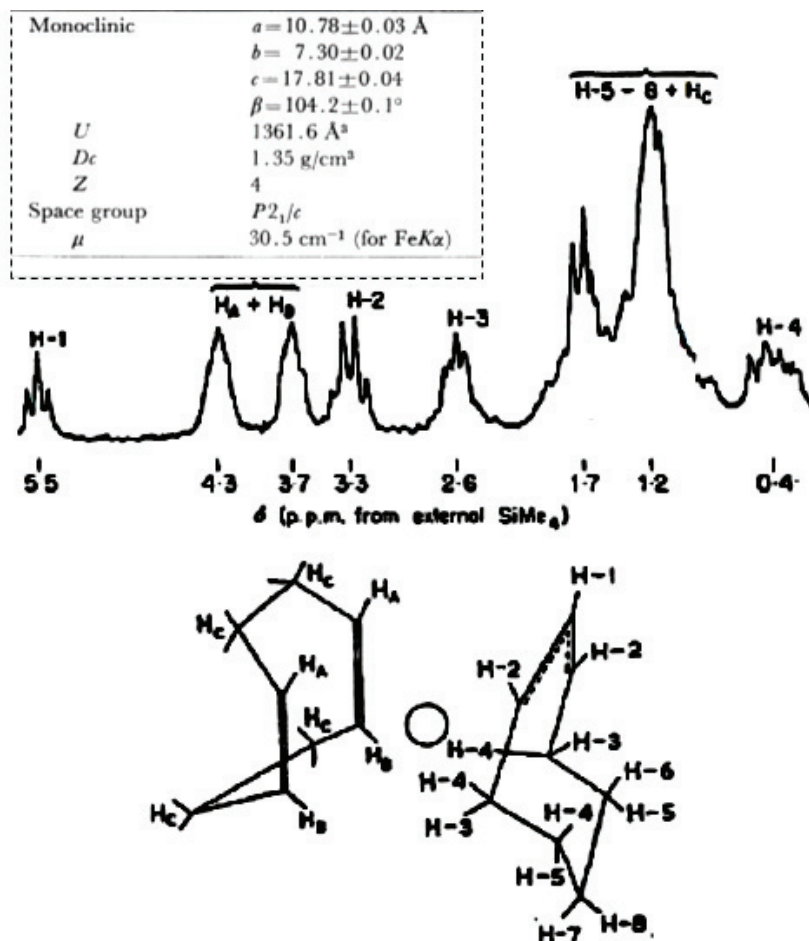


Figure 1 : NMR spectra and crystallographic structure of  $\text{Co}(\text{COD})(\text{COE})$ .<sup>63, 65</sup>

The reduction of  $\text{Co}(\text{COD})(\text{COE})$  by  $\text{H}_2$  was performed in THF in the presence of polyvinylpyrrolidone (PVP) as a stabilizer.<sup>49</sup> The size and structure of the resulting Co-NPs depended on the experimental conditions.

The Co-NP size increased i) from  $\leq 1$  to 1.6 nm upon increasing the temperature from  $0^\circ\text{C}$  to  $60^\circ\text{C}$  (Table 3, run 4-6) and, ii) with PVP concentration, (Table 2, run 8, 9).<sup>52</sup> Similar results were also reported in other media like an anisole/oleic acid solution and at higher temperature ( $150^\circ\text{C}$ , Table 3, run 1).<sup>48</sup> Moreover, changing the reaction time from 3 h to 48 h lead to the formation of Co nanorods (9 x 40 nm) instead of spherical NPs (3 nm) in the former case, (Table 3, run 2, 3).<sup>46</sup> The nature of the ligand was found to affect the NP size and shape.<sup>47</sup> Co nano-disks were obtained in the presence of a mixture of hexadecylamine and rhodamine B as ligands, while nano-rods and nano-wires were formed with long chain carboxylic acids as ligands (Table 3, run 2, 3).<sup>66</sup> For the Co-NP structure, in THF/PVP, (Table 3, run 4-6), Co-NPs (1-1.5 nm) presented a fcc-like structure,<sup>49</sup> while in THF/PPO (Table 3, run 11), the Co-NPs (5 nm) showed a hcp structure.<sup>47</sup> Surprisingly, a cubic phase was observed for Co-NPs (1.5-2 nm) generated in THF/ PVP medium (Table 3, run 8, 9).<sup>52</sup>

This cubic structure was first identified to be a bcc one. But finally, WAXS studies showed that a model including 30% of bcc particles and 70% of hcp ones yielded the best fit with the experimental results. More precisely, the Co-NPs showed a core-shell structure with a bcc structure closest to the center and a more relaxed organization of hcp structure at the surface.<sup>52</sup> Later on, this cubic structure of Co-NPs was interpreted by the same group as a metastable allotrope called  $\epsilon$ -Co.<sup>59</sup>

Table 3 : Size and shape of Co-NPs prepared through the H<sub>2</sub> decomposition of Co ( $\eta^3$ -C<sub>8</sub>H<sub>13</sub>) ( $\eta^4$ -C<sub>8</sub>H<sub>12</sub>) in different experimental conditions.

Run	P (MPa)	t (°C)	C	medium	duration	Magnetic moment emu.g <sup>-1</sup>	size / shape	JCPDS reference	ref
1	0.4	150		anisole/oleic acid		163	2.5(+/- 0.3)	hcp (04-007-2107)	48, 51
2					3 h	162	3 nm	hcp (04-007-2107)	
3	0.4	150		anisole/different ligands	48 h		9 x 40 nanorods	hcp (04-007-2107)	46
4		0					1	fcc (no reference)	49
5	0.4	20	10% wt (to PVP)	THF / PVP	10 h	184	1.5		
6		60					1.5		
7	0.4	R.T		THF/PVP/Pt precursor	15 h	1.35 – 1.95 ( in $\mu_B$ /Co, Increase with Pt ratio)	1.5 Co/Pt nanoalloys		50
8		60	10% wt (to PVP)	THF / PVP	10 h	184	1.5	Fits to theoretical model consisting of 30% bcc + 70% hcp	52
9			20% wt (to PVP)			173	2		
10		65	11% wt (to PVP)	THF / PVP		Not reported for the metallic NPs, dropped by a factor of 4 upon oxidation of NPs	1.6	Non-compact crystal structure	47, 67
11				THF / PPO			5	hcp (04-007-2107)	

In conclusion, Co-NPs can be generated in organic solvents from the reduction under H<sub>2</sub> of Co(COD)(COE) under mild conditions. Their size depends on the experimental conditions, mainly on the nature and quantity of the stabilizing additive. Indeed, the presence of a stabilizer is crucial. On the other hand, its interaction with the Co-NPs may reduce the



magnetic properties of the latter. To overcome this drawback, the use of ionic liquids (ILs) as solvent was proposed. Ionic liquids are salts that are liquid at (or near to) room temperature. They are virtually non-volatile, non-flammable and thermally stable solvents that possess high electrical conductivity.<sup>68</sup> Importantly, ILs have been shown to be smart media to generate mono-disperse metallic NPs with controlled size below 5 nm through a variety of processes (either chemical or physical) in the strict absence of stabilizing agents.<sup>24, 57, 69, 70</sup>

### **I-A. VI. Synthesis of Co-NPs from organometallic precursors in ionic liquids**

Co-NPs have been successfully prepared in ILs using either physical or chemical means by PVD,<sup>71</sup> by electrochemical reduction,<sup>72, 73</sup> or through thermal decomposition (by microwave or photolytic means).<sup>66, 67, 68, 69, 70</sup> Whatever the experimental conditions, Co-NPs prepared by thermal decomposition of  $\text{Co}_2(\text{CO})_8$  were metallic, as shown by XRD analysis under inert atmosphere.

Size and shape of CoNPs prepared from  $\text{Co}_2(\text{CO})_8$  in several ILs depend on the experimental conditions (Table 4). In most cases, the NP size was increasing with the precursor concentration, (Table 4, run 1-5).

The IL nature was found to impact the resulting NP size. Its physico-chemical properties (density, viscosity, conductivity and surface tension) influenced the nanoparticle nucleation and growth kinetics.<sup>74, 75, 76, 77, 78</sup> The nature of both the anion and the cation, related to their molecular volume, determine the high degrees of self-organization at the nanomolecular scale of IL through their hydrogen-bond network. This structural organization of ILs can act as an “entropic driver” for the spontaneous ordering of metallic NPs.<sup>79, 80, 81</sup>

In imidazolium based ionic liquids, the Co-NP size was equal to 10.8 nm, 7.2 nm and 4.1 nm when the anion was bis[(trifluoromethyl)sulfonyl]imide ( $\text{NTf}_2$ ), hexafluorophosphate ( $\text{PF}_6$ ), and tetrafluoroborate ( $\text{BF}_4$ ), respectively, (Table 4, run 3-5). Such effect of the nature of the anion on the NP size has previously been reported in the literature.<sup>82, 83</sup> For example, the size of chromium, molybdenum and tungsten NPs generated through the thermal decomposition of their corresponding metal carbonyl precursors was found to increase with the molecular volume of the anion (i.e. W-NP size is 1.5 nm in  $\text{C}_1\text{C}_4\text{ImBF}_4$  and 33 nm in  $\text{C}_1\text{C}_4\text{ImNTf}_2$ ).<sup>82</sup> Similarly, the size of Ag-NPs prepared through the  $\text{H}_2$  decomposition of  $\text{Ag}^{(1)}$

precursors in different  $C_1C_4Im$  based ILs was reported to increase linearly with the molar volume of the IL anion (2.8, 4.4, 8.7 and 26.1 nm for  $BF_4^-$ ,  $PF_6^-$ ,  $OTf^-$  and  $NTf_2^-$  anions respectively) (Figure 2).<sup>83</sup>

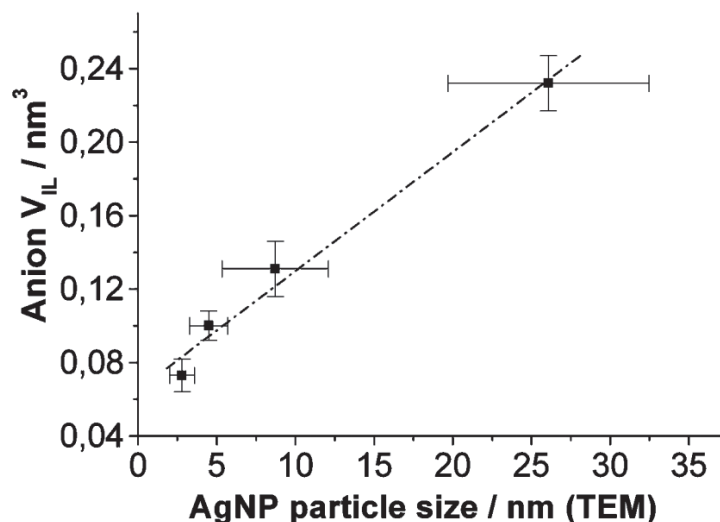


Figure 2 : Correlation between the observed AgNP size (from TEM) and the molecular volume IL anion ( $V_{IL}$  anion).<sup>83</sup>

According to Redel *et al.*,<sup>83</sup> M-NPs (core) would be stabilized in IL in a “core-shell system” by the formation of protective anionic and cationic layers (shells) around them. The thickness of these stabilizing shells around an Ag-NP was assumed to depend on the ions’ molecular volumes. According to the DLVO theory,<sup>84</sup> the first inner shell must be anionic. For this reason, the IL anion was expected to have the highest influence on the size and electrostatic stabilization of the Ag-NP.

Nevertheless, the molar volume of the cation impacted the Co-NP size in the same way *i.e.* for the same anion ( $NTf_2^-$ ) the Co-NP- size was reported to be 5.8 nm with methyltrioctylammonium cation  $[N_{1,8,8,8}]^+$  (molar volume =  $0.634 \text{ nm}^3$ ),<sup>85</sup> and 3.6 nm with pyrrolidinium  $[Py_{1,4}]^+$  cation (molar volume =  $0.213 \text{ nm}^3$ ),<sup>85</sup> (Table 4, run 1, 2).<sup>79</sup>

Another possible effect of the cation was related to the self-organization of the IL at the nano-scale. This was first discussed by Gutel *et al.*, for the synthesis of Ru-NPs from the decomposition of  $(\eta^4\text{-cyclo-octadiene})(\eta^6\text{-cyclo-octatriene})\text{ruthenium}(0)$ ,  $Ru(COD)(COT)$ , in various IL:  $[RC_1Im][NTf_2^-]$  ( $R = C_nH_{2n+1}$  with  $n = 2; 4; 6; 8; 10$ ).<sup>79</sup> For the ILs with  $n = 4; 6; 8$ , a linear correlation between the size of Ru-NPs generated *in situ* and the length of the alkyl chain was established.

It should be noted that this explanation was applicable at lower temperatures (0-25°C) where the IL is still retaining its internal structuring. It would not necessarily be the case at higher temperatures at which, such 3D organization is expected to have a weaker influence.

Table 4 : Size and shape of Co-NPs prepared from  $\text{Co}_2(\text{CO})_8$  in several ILs under different experimental conditions.

run	t ( °C)	C mol.L <sup>-1</sup>	medium	duration	Magnetic moment emu.g <sup>-1</sup>	Size (nm)	JCPDS reference	ref
1		0,0625	C <sub>1</sub> C <sub>8</sub> AmNTf <sub>2</sub>		82	5.8 ± 0.9	fcc (00-015-0806)	
		0.6			144	9.4 ± 1.1		
		1.2			---	9.8 ± 2.2		
		3			133	16.1 ± 3.3		
2		0,0625	C <sub>1</sub> C <sub>4</sub> PyrrNTf <sub>2</sub>		---	3.6 ± 0.7		
		0.6			---	17.1 ± 3.8		
		1.2			ramped to	---		
3	100°C for 30 min then heated to 200°C	0,0625 0.6	C <sub>1</sub> C <sub>4</sub> ImPF <sub>6</sub>	100°C, let for 30 min then ramp to	---	7.2 ± 1.2		53
					200°C, let for 30 min	---		
4		0,0625	C <sub>1</sub> C <sub>4</sub> ImNTf <sub>2</sub>		---	10.8 ± 3.2		
5		0,0625	C <sub>1</sub> C <sub>4</sub> ImBF <sub>4</sub>		---	4.1 ± 2.1		
6	150	0.1 M	C <sub>1</sub> C <sub>4</sub> ImNTf <sub>2</sub>	20–40 min	---	7.7 ± 1.2	---	54
			C <sub>1</sub> C <sub>1</sub> ImBF <sub>4</sub>			4.5 ± 0.6		
			C <sub>1</sub> C <sub>14</sub> ImNTf <sub>2</sub>					
7	150		C <sub>1</sub> C <sub>1</sub> ImNTf <sub>2</sub>	1 h	---	bimodal size (79 ± 17) and (11 ± 3)	ε-Co (04-017-5578)	31
8	Microwave irradiation		C <sub>1</sub> C <sub>4</sub> ImBF <sub>4</sub>	3 min		5.1 ± 0.9	---	55

### I-A. VII. Crystal structures of metallic Co-NPs

In organic solvents Co-NPs usually possess the stable hcp compact crystal structure (JCPDS ref. 04-007-2107) (Table 3, run 1, 2, 3, 11).<sup>47,36,39</sup> The hcp structure was confirmed by both HRTEM and WAXS-RDF techniques (Figure 3, Figure 4). As shown in Figure 4, the

hcp model fitted well with radial distribution function (RDF) obtained from Co-NPs with the peak at 0.35 nm referring to a compact Co structure.

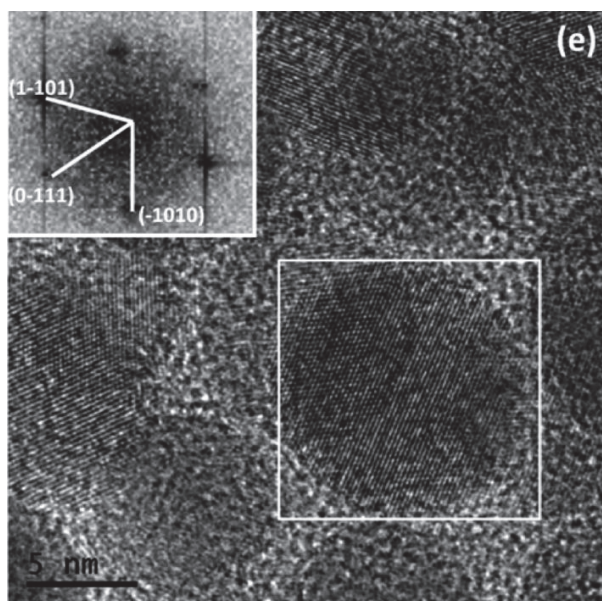


Figure 3 : HRTEM image of metallic Co-NPs ( Table 3 run 1), reproduced. The fast Fourier transform image in the top-left corner shows hcp pattern.

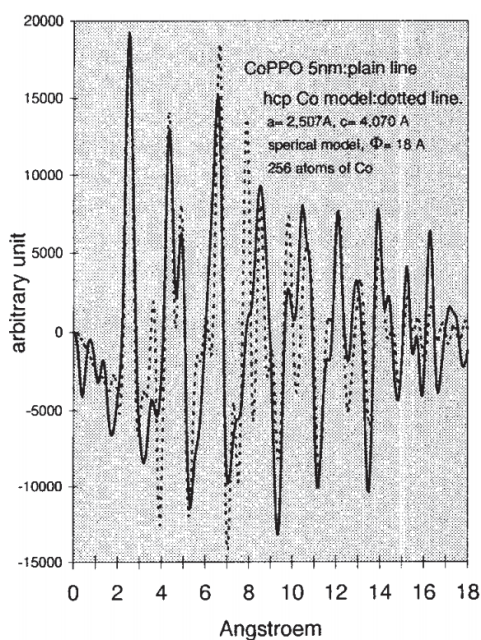


Figure 4 : RDF of 5.0 nm Co-NPs (Table 3, run 11) as reproduced from reference <sup>67</sup>.

Even if fcc (JCPDS ref. 00-015-0806) Co-NPs were not so common for low temperature synthesis (<400°C), there were some few cases in which this crystal structure was reported in organic solvent and in ILs (Table 3, runs 4-6, Table 4, run 1). However, it should be mentioned that the fcc structure in these studies was based only on HRTEM observations

(Figure 5) and XRD spectra showing only one sharp peak at  $44.27^\circ$  which is not enough to ascertain the structure.

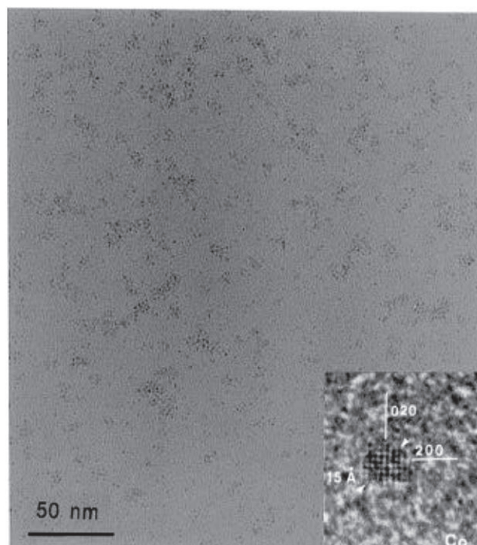


Figure 5 : TEM, HRTEM images of Co-NPs (1.5 nm) with a fcc structure (Table 3, run 4-6).<sup>49</sup>

Another crystal structure of Co-NPs that is well represented in the literature is the  $\epsilon$ -Co structure (Figure 6, JCPDS ref. 04-017-5578).<sup>86</sup> It is a non-compact, meta-stable cubic crystal structure that can be transformed upon annealing into the more stable hcp and fcc structures.  $\epsilon$ -Co was proposed as the structure of Co-NPs generated either in organic solvents (Table 3, run10) or in ILs (Table 4, run 7).<sup>31, 47, 52, 67, 86, 87</sup> This  $\epsilon$ -Co structure was fully characterized by HRTEM, XRD and WAXS techniques. From WAXS, it was interpreted as a mixture of bcc and hcp Co (Figure 7 and Figure 8)<sup>52</sup>. However, this description did not fully account for the experimental results. In particular, the experimental RDF lacked the peak at 3.5 nm characteristic of compact structures (Figure 8).<sup>52</sup>

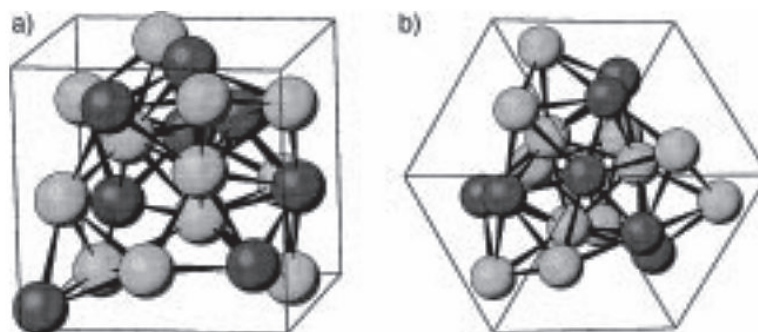


Figure 6 : The unit cell of  $\epsilon$ -cobalt: a) unit cell cube filled with eight atoms of Type I (dark) and twelve atoms of Type II (light); b) 111-projection of the same cube showing threefold symmetry along its main diagonal.

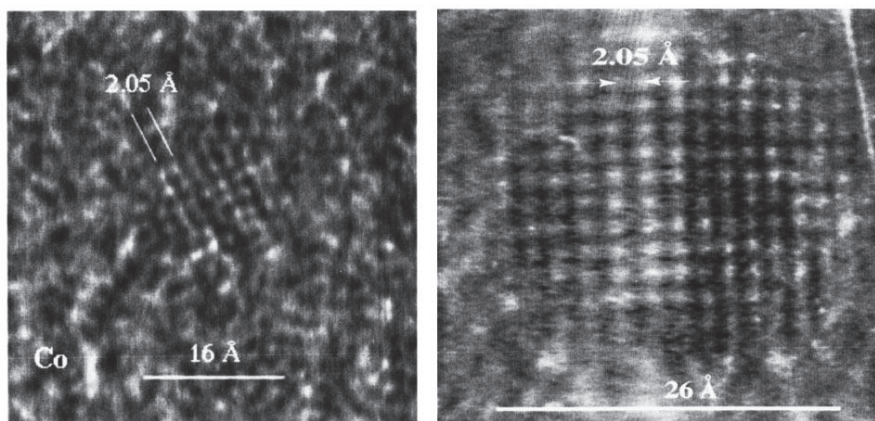


Figure 7 :HRTEM images for 1.6nm and 2.6nm Co-NPs (Table 3 run 8-9).<sup>52</sup>

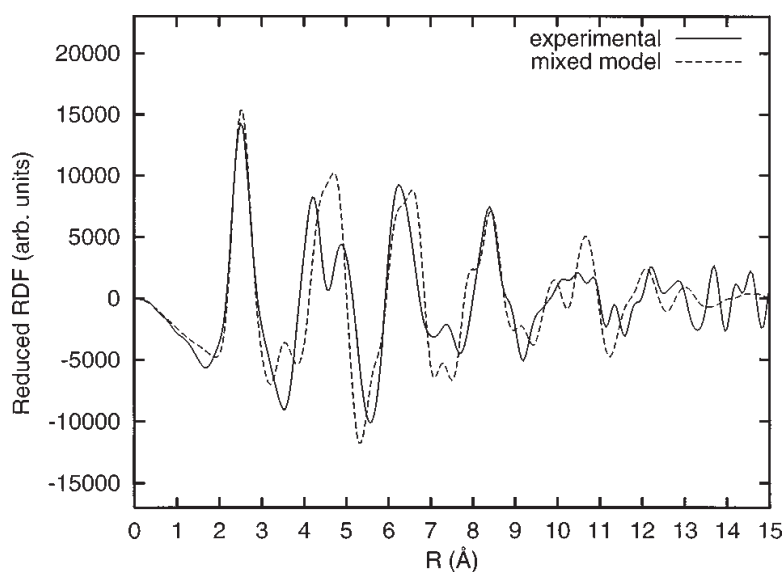


Figure 8 : Experimental (solid line) and simulated (dashed line) reduced RDF for Co-NPs (Table 3 run 8-9).<sup>52</sup>

The XRD diagram of Co-NPs prepared in  $C_1C_1ImNTf_2$  (Table 4, run 7 and Figure 9) indicates that these Co-NPs did not present a hcp or fcc structure. The observed reflections at  $2\theta = 44.578, 47.128, \text{ and } 49.558^\circ$ , are related to the indexed planes of metallic  $\epsilon$ -Co crystals: (2 2 1), (3 1 0), and (3 1 1), respectively.<sup>31, 86</sup> Note that the XRD diagrams confirm that the metastable  $\epsilon$ -phase could be transformed to hcp phase then to fcc phase upon successive annealing at 300 then at 500°C. CoO peaks were also detected resulting from the probable thermal degradation of the IL at 500°C.<sup>31</sup>

Finally, another original polytetrahedral structure for Co-NPs was proposed by Dassenoy, et al.<sup>87</sup> This model also fitted well with the experimental results (Figure 10).

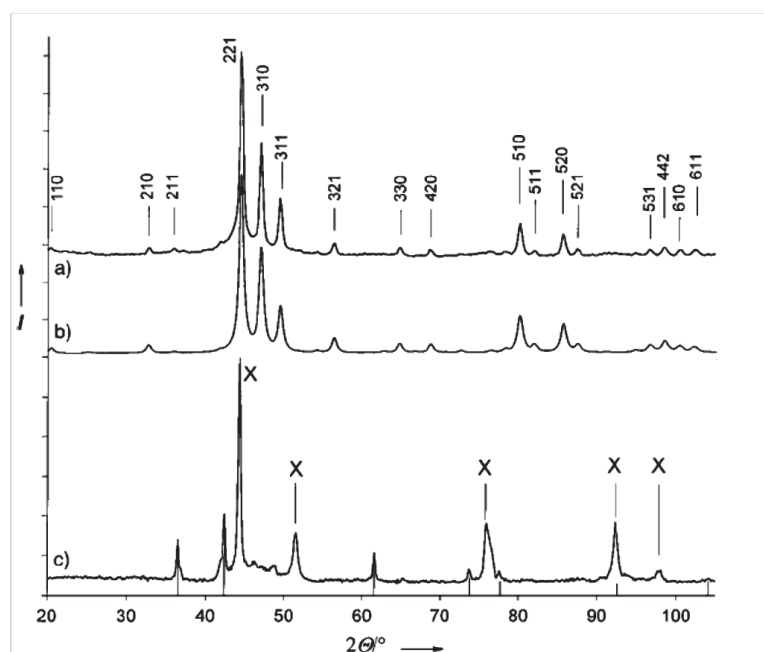


Figure 9 : XRD pattern of Co-NPs in IL with a  $\epsilon$ -Co structure (Table 4 run 7): a) experimental; b) calculated; c) the sample shown in a) after being heated to 500 °C, peaks corresponding to fcc are denoted by X, peaks corresponding to CoO are marked with a stick spectrum.<sup>31</sup>

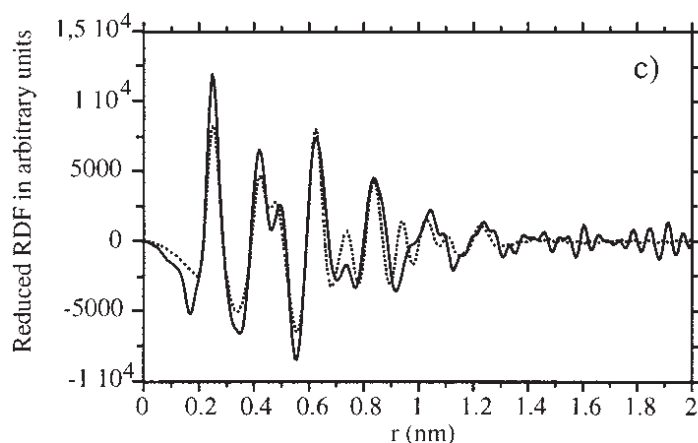


Figure 10 : Experimental (solid line) and simulated polytetrahedral model (dashed line) reduced RDF for Co-NPs (Table 3 run 8-9).<sup>87</sup>

## I-A. VIII. Superparamagnetic nature of Co-NPs

Generally speaking, all small metallic Co-NPs prepared in organic solvents (Table 3, run 1-11) showed a superparamagnetic behavior at room temperature with a blocking temperature ( $T_B$ ) values ranging from 9 to 20 K (see appendix 1). The only exceptions were Co nanorods (Table 3, run 3) showing a typical ferromagnetic behavior at room temperature. This result highlights the importance of the shape anisotropy in such systems with higher aspect ratio leading to higher shape anisotropy and hence, to much higher blocking temperatures above room temperature.

Partial oxidation induced a sharp drop of the magnetic moment values (Table 3, runs 10, 11). For example, the core@shell structured, Co@CoO NPs showed lower magnetic moment of 18-40  $\text{A.m}^2.\text{kg}^{-1}$  as compared to the bulk Co value, 160  $\text{A.m}^2.\text{kg}^{-1}$ . Results from the smaller Co-NPs (Table 3, runs 8,9) showed some enhancement in the magnetic moments explained by the enhancement of the magnetic moment per atom in the two or three surface atomic layers in nanoscale particles.<sup>88</sup> Another important finding from these results is the demonstration of the strong effects of chemical binding on the magnetic properties of surface atoms. For instance, exposing the Co-NPs to carbon monoxide environment caused a huge drop in their magnetization ( $M_s = 55 \pm 5 \text{ A.m}^2.\text{kg}^{-1}$ ), (Table 3, run 7) because CO molecules strongly coordinate with the metal.

Similar to Co-NPs prepared in organic solvents, Co-NPs prepared from the decomposition of  $\text{Co}_2(\text{CO})_8$  in IL showed a superparamagnetic behavior at room temperature (Table 4, run1-7) with very low  $T_B$  of 7 K.<sup>31</sup> The only exception (Table 4, run 7) was observed with a bi-distribution of large Co nanocubes of size  $79 \pm 17 \text{ nm}$ , that were ferromagnetic at room temperature with high  $T_B$  values, together with small nano-sphere NPs,  $11 \pm 3 \text{ nm}$  in size, that showed superparamagnetic behavior and  $T_B$  values of 7 K. For Co-NPs (Table 4, run 1), the magnetic moment showed some dependence on the Co-NP size changing from 81  $\text{A.m}^2.\text{kg}^{-1}$  to 142  $\text{A.m}^2.\text{kg}^{-1}$  and to 132  $\text{A.m}^2.\text{kg}^{-1}$  by increasing the Co-NP diameter from 6 to 9 nm and then to 16 nm respectively. These values compare well with those of NPs generated in organic solvent in the presence of a ligand (Table 3). Consequently, the fact that these values were relatively lower than that of bulk Co (160  $\text{A.m}^2.\text{kg}^{-1}$ ) could be related to the presence of CO ligands coordinated to the Co-NP surface.<sup>50</sup>



## I-A. IX. Conclusion and strategy

In conclusion, in IL media, besides the preparation of Co-NPs from carbonyl by thermal decomposition, the H<sub>2</sub> reduction of any organometallic precursor under mild conditions is scarcely reported, even if this chemical route is widely developed in organic solvents. In fact, the only example was reported by Dupont et al when they used a Co<sup>(II)</sup> OM precursor, bis(cyclopentadienyl)cobalt(II), to prepare Co-based NPs. This precursor was not easy to decompose, except in the presence of [tris(dibenzylideneacetone) bisplatinum(0)], to afford CoPt<sub>3</sub>@Pt nano-alloys.<sup>60</sup> In that particular case, the initially formed Pt seeds were needed to catalyze the reduction of the Co precursor.

In our Laboratory, we developed in IL media a general and versatile route to access to size controlled NPs from the reaction of organometallic precursor under H<sub>2</sub> atmosphere (Figure 11).<sup>26, 89, 90, 91</sup> From this bibliography analysis, we choose Co(COD) (COE) as Co-OM precursor to generate, under mild conditions, metallic NPs under H<sub>2</sub> in different ionic liquids, following the general procedure depicted in Figure 11.

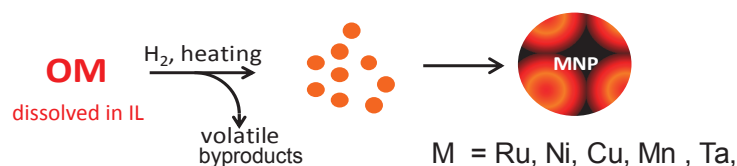


Figure 11 : Mechanism of metal NPs formation through the H<sub>2</sub> decomposition of organometallic precursors dissolved in IL.

# **Chapter I-B.**

---

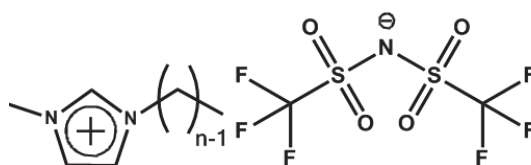
## **Results:**

### **Synthesis and structural properties of Cobalt Nanoparticles (Co-NPs) in Ionic Liquids**



Unlike traditional solvents, ionic liquids (ILs) can be used to generate metallic NPs by several physical and chemical routes and stabilize them in the absence of further additives.<sup>24</sup>

IL formed by the association of the n-alkylimidazolium cation, [C<sub>1</sub>C<sub>n</sub>Im] (n=length of the alkyl side chain), with the bis(trifluoromethylsulfonyl) imide anion [NTf<sub>2</sub>] (Scheme 4), are the most commonly used to generate mono-disperse metallic NPs below 5 nm through a variety of processes (either chemical or physical) in the strict absence of stabilizing agents.<sup>24</sup> They are easily synthesized in a high purity, preventing NP contamination by the residual halide, water, or other starting material (see the experimental chapter).



Scheme 4: Methylalkylimidazolium cation [C<sub>1</sub>C<sub>n</sub>Im] and bis(trifluoromethylsulfonyl) imide anion (TFSI = NTf<sub>2</sub> = TFSA)

Fortunately, these IL can dissolve various precursors. Inspired by Chaudret's work in organic solvents,<sup>56</sup> the generation of NPs in ILs can be carried out by the decomposition under dihydrogen of organometallic (OM) precursors whose ligands do not interfere with the formation of NPs. A very good example is the formation of Ru-NPs by decomposing Ru(COD)(COT), with elimination of cyclooctane (COA).<sup>26, 79, 90, 92, 93</sup>

For this PhD work, we choose Co(COD) (COE) as a Co<sup>(I)</sup> organometallic precursor to be reduced in to metallic NPs under H<sub>2</sub> in different ILs based on imidazolium.

Firstly, the thermal stability of Co(COD) (COE) was investigated both for the precursor alone and for solutions in C<sub>1</sub>C<sub>4</sub>ImNTf<sub>2</sub>, under nitrogen and under hydrogen atmosphere. The byproducts were quantitatively analyzed in order to get information on the mechanism and the kinetics of the reactions.

The experimental conditions of the decomposition reaction were optimized in order to get reproducible small and monodispersed metallic Co-NPs. Several parameters were considered like temperature, pressure, concentration, reaction duration and the nature of the imidazolium based IL (chain length of the cation). Then, the impact of the experimental conditions on the Co-NP structure and magnetic properties was studied through several techniques (HRTEM, WAXS-PDF and SQUID).

## I-B. I. Thermal stability of Co(COD)(COE)

### i. Thermo-gravimetric analysis (TGA) of solid Co(COD)(COE) under N<sub>2</sub>

In the literature, Co(COD)(COE) was reported as a very sensitive compound that should be kept at very low temperature under inert atmosphere. This observation raised some doubts about the possibility to handle such compound during our experiments without being partially decomposed (before applying H<sub>2</sub>). For that reason, TGA was used to investigate the thermal stability and the decomposition temperature ( $T_d$ ) of Co(COD)(COE) under N<sub>2</sub>.

Regarding how to define  $T_d$ , several definitions are reported in the literature affording different values: start temperature, onset temperature, x% mass loss temperature, and peak temperature. **The start temperature** ( $T_{start}$ ) is the temperature at which the sample starts to lose some mass,<sup>94</sup> and was defined as the temperature at which the first derivative of the weight loss vs. time curve is  $|dm/dT| > 10^{-4} \text{ \%}\cdot\text{s}^{-1}$ . The associated uncertainty was 5 °C. **The x% mass loss temperature** is the temperature at which x% of the mass, (*e.g.*, x=1), are lost.<sup>95</sup> **The peak temperature** ( $T_{peak}$ ) is the temperature at which the derivative of the mass versus the temperature is the highest.<sup>95</sup> This analysis gives results even up to 80 °C higher than onset temperatures. **The onset temperature** ( $T_{onset}$ ) is generally defined by the tangent method, but also by the 5% mass loss temperature.<sup>95</sup> For the first case, it is determined either by software or manually by the intersection of two lines. The first one is a straight baseline along the temperature axis (in the low-temperature region with no weight-loss or after the drying step), and the second is the tangent of the weight versus temperature curve as decomposition occurs (in the high-temperature decomposition region, see Figure 12).<sup>96</sup>

In the literature authors are now well aware of the disparity between these different definitions when presenting TGA results and it is admitted that the thermal degradation occurs well before the onset temperature based on tangents methods.

Back to our results, Figure 12 shows the variation of the Co(COD)(COE) mass as a function of temperature (black curve). The red curve represents its 1<sup>st</sup> derivative. From the black curve, the extrapolated  $T_{onset}$  is found to be 132°C and the maximum decomposition rate is obtained from the large peak minimum in the red curve at 160°C ( $T_{peak}$ ). These temperatures are reproducible experimental values specified and used by ASTM and ISO but that does not necessarily mean that there is no decomposition below those temperatures. In order to be sure,  $T_{onset}$ , recalculated using the 1<sup>st</sup> derivative curve indicates a  $T_{start}$  equal to 60°C (red curve). This means that the spontaneous decomposition of Co(COD)(COE) under N<sub>2</sub> atmosphere starts taking a considerable rate at temperatures above 60°C which leave us a

wide window near room temperature to handle it (to weigh and dissolve in IL) before being decomposed.

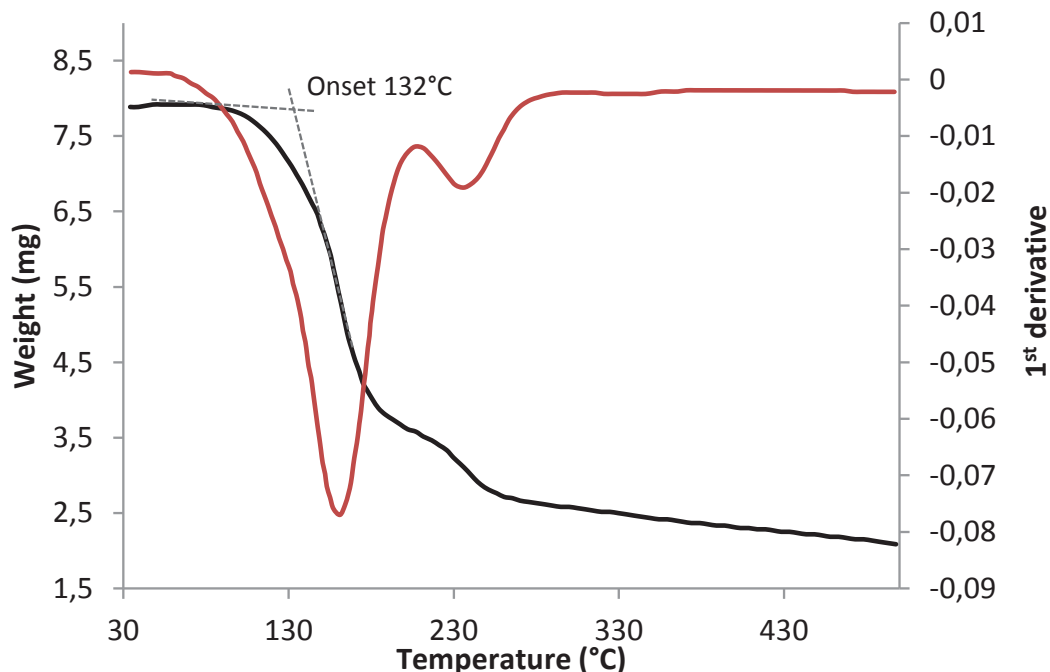


Figure 12 : Comparison of the  $T_d$  values of  $\text{Co}(\text{COD})(\text{COE})$  ( $5^\circ\text{C}\cdot\text{min}^{-1}$ ,  $\text{N}_2$  atmosphere) according to the definitions  $T_o$ ,  $T_{\text{start}}$  and  $T_{\text{peak}}$ ; black line represents the sample mass and red line represents the first derivative.

## ii. DRIFT analysis of solid $\text{Co}(\text{COD})(\text{COE})$ under $\text{H}_2$

The thermal decomposition of pure  $\text{Co}(\text{COD})(\text{COE})$  under 0.4 MPa of  $\text{H}_2$  was monitored using online IR and online GC-mass analysis during 5 h at  $20^\circ\text{C}$ .

The evolution of the IR spectra with time is shown in Figure 13. The spectrum at zero time was recorded for the sample under inert (Argon) atmosphere (just before applying  $\text{H}_2$ ). It shows the C-H bending peaks (around  $900\text{ cm}^{-1}$ ) and C=C stretching peaks (around  $1500\text{ cm}^{-1}$ ) characteristic to cyclooctadiene and cyclooctadienyl ligands coordinating to the  $\text{Co}^{(\text{I})}$  atom. Upon applying  $\text{H}_2$ , all these peaks gradually disappeared together with the domination of the characteristic peaks of cyclooctane ( $2900$ ,  $2680\text{ cm}^{-1}$  for alkane C-H stretching and  $1480$ ,  $1450\text{ cm}^{-1}$  for alkane C-H bending). This was a direct indication of the decomposition of the  $\text{Co}^{(\text{I})}$  precursor upon exposure to  $\text{H}_2$ , even at room temperature, together with the hydrogenation of the unsaturated ligands into saturated cyclooctane. The fact that the unsaturated ligand peaks almost disappeared after 30 minutes of exposure to  $\text{H}_2$  indicated that the decomposition reaction was completed within this short time.

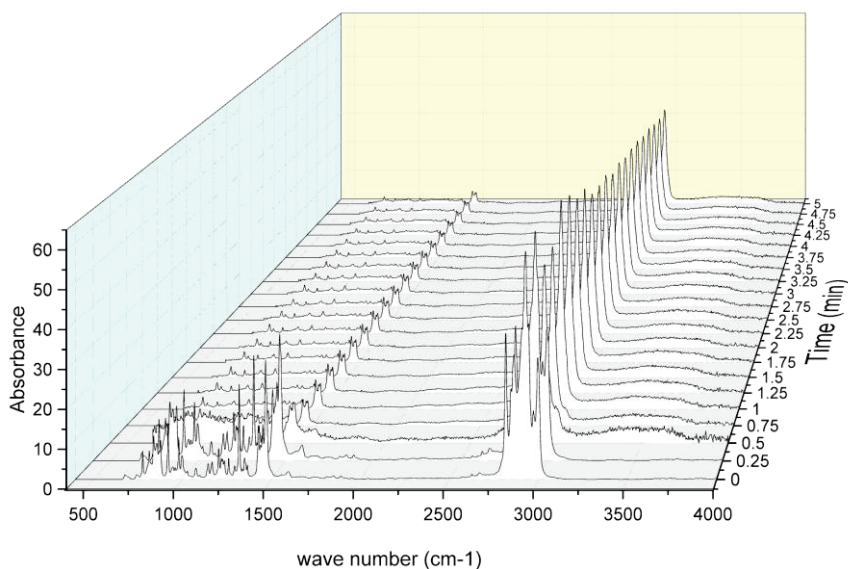


Figure 13 : Evolution of the IR spectra of solid Co(COD)(COE) with time upon exposure to 0.4 MPa of H<sub>2</sub> at 20°C.

Simultaneously, the evolved gaseous by-products were monitored by GC-mass spectroscopy. As expected, cyclooctane (C<sub>8</sub>H<sub>16</sub>) was the main component in the evolved gas phase together with trace amounts of other gaseous byproducts which were cyclooctene and pentalene (Figure 14, left).

The kinetics of the reduction reaction were approximately determined through integration of the peaks corresponding to cyclooctane. This integration signal is plotted as a function of the reaction duration in Figure 14, right. Co(COD)(COE) was fully decomposed after 5.5 hours at 20°C. This was in apparent contradiction with the IR results indicating a full decomposition after ~30 min. This was probably related to the low vaporization rate of cyclooctane at 20°C (cyclooctane b.p. 149°C). Hence, the reaction was certainly much faster (as observed by the IR spectra) but the vaporization of the resulting cyclooctane into the gas phase is not fast enough to reflect the real reaction kinetics.

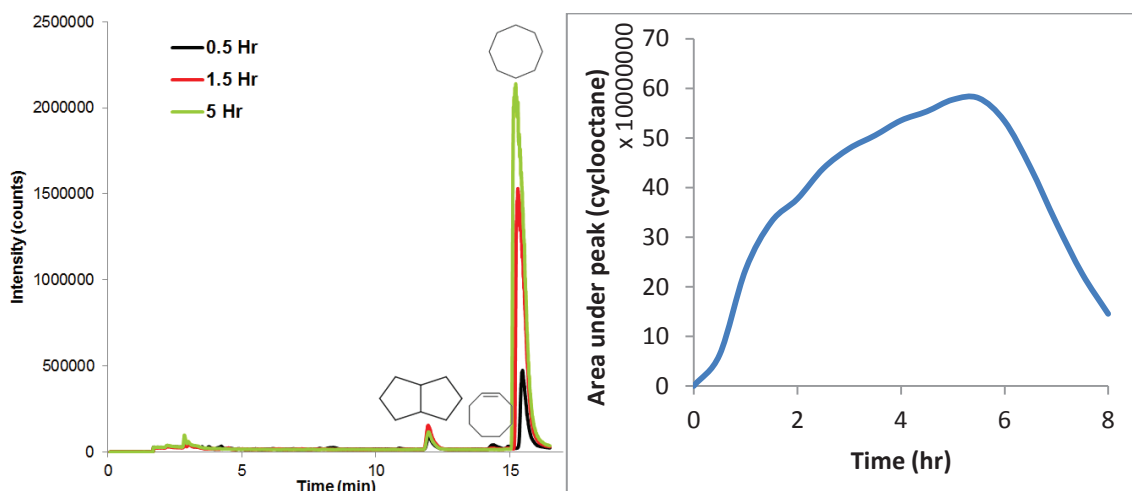


Figure 14 : (left) Chromatogram of the gas phase during the decomposition of solid  $\text{Co}(\text{COD})(\text{COE})$  under 0.4 MPa of  $\text{H}_2$ ,  $20^\circ\text{C}$  at different time intervals; (right) evolution of cyclooctane peak area with time.

As a conclusion,  $\text{Co}(\text{COD})(\text{COE})$  was decomposing fast under  $\text{H}_2$  even at  $20^\circ\text{C}$  with the formation of cyclooctane as the main decomposition product. The fact that the unsaturated ligands could be hydrogenated in cyclooctane at  $20^\circ\text{C}$  suggested that  $\text{Co}^{(0)}$  species known as a hydrogenation catalyst were generated in these experimental conditions.

### iii. In situ GC-mass monitoring of the thermal stability under $\text{H}_2$ of $\text{Co}(\text{COD})(\text{COE})$ in $\text{C}_1\text{C}_4\text{ImNTf}_2$ :

In order to get an idea about the kinetics of formation of Co-NPs in ILs an online GC-mass tool was used to follow the gaseous decomposition products through the progress of the reaction. In this experiment, a solution of  $5 \times 10^{-2} \text{ mol.L}^{-1}$  of  $\text{Co}(\text{COD})(\text{COE})$  in  $\text{C}_1\text{C}_4\text{ImNTf}_2$  was injected into a clean autoclave under argon purging. The autoclave was heated up to  $100^\circ\text{C}$  then 0.4 MPa of  $\text{H}_2$  were applied. As for the solid, GC-mass spectra of the gas phase showed cyclooctane as the main decomposition product together with traces of cyclooctene and pentalene (Figure 15).

In order to get some information about the kinetics of the reaction, the integrated peak intensities of these gaseous products were correlated with standard calibration curves in order to get information about the progress of the reaction. That was then represented as %decomposition (Figure 16, red curve) which corresponds to the actual cyclooctane peak area/theoretical peak area assuming full decomposition multiplied by 100.  $\text{Co}(\text{COD})(\text{COE})$  was found to be fully decomposed after 8 hours (Figure 16). As previously mentioned, this duration may not indicate the real decomposition time because it is hard to vaporize cyclooctane out of the IL.



The fact that the unsaturated ligands are hydrogenated to form cyclooctane, taking into account that this reaction can be catalyzed only by metallic Co and not by  $\text{Co}^{(I)}$ , confirms the formation of metallic Co structures as a result of the decomposition of  $\text{Co}(\text{COD})(\text{COE})$ .

The formation of traces of pentalene can be explained in terms of a series of isomerization reactions according to the mechanism depicted in Figure 17. The fact that the pentalene concentration is very small compared to cyclooctane proves the very slow kinetics of this side reaction as compared to  $\text{H}_2$  reduction of cyclooctadiene. For this reason, it should not be very significant.

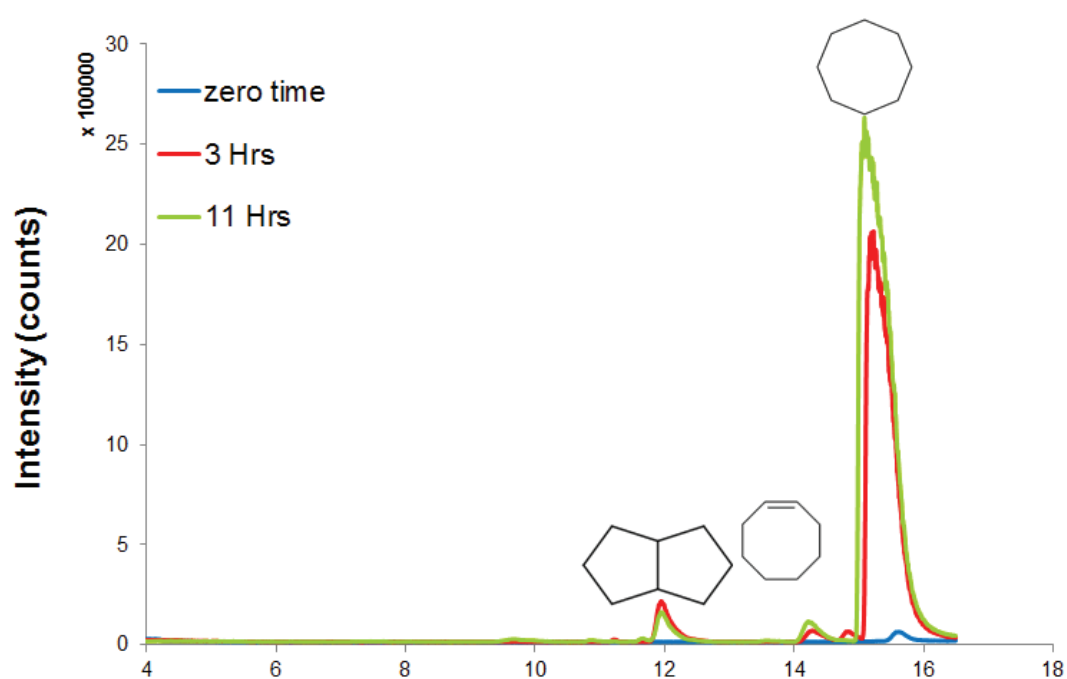


Figure 15 : Evolution with time of the chromatogram of the gas phase during the reaction of  $\text{Co}(\text{COD})(\text{COE})$  [ $5 \times 10^{-2} \text{ mol.L}^{-1}$ ] in  $\text{C}_1\text{C}_4\text{ImNTf}_2$ , with  $\text{H}_2$  (0.4 MPa) at  $100^\circ\text{C}$ .

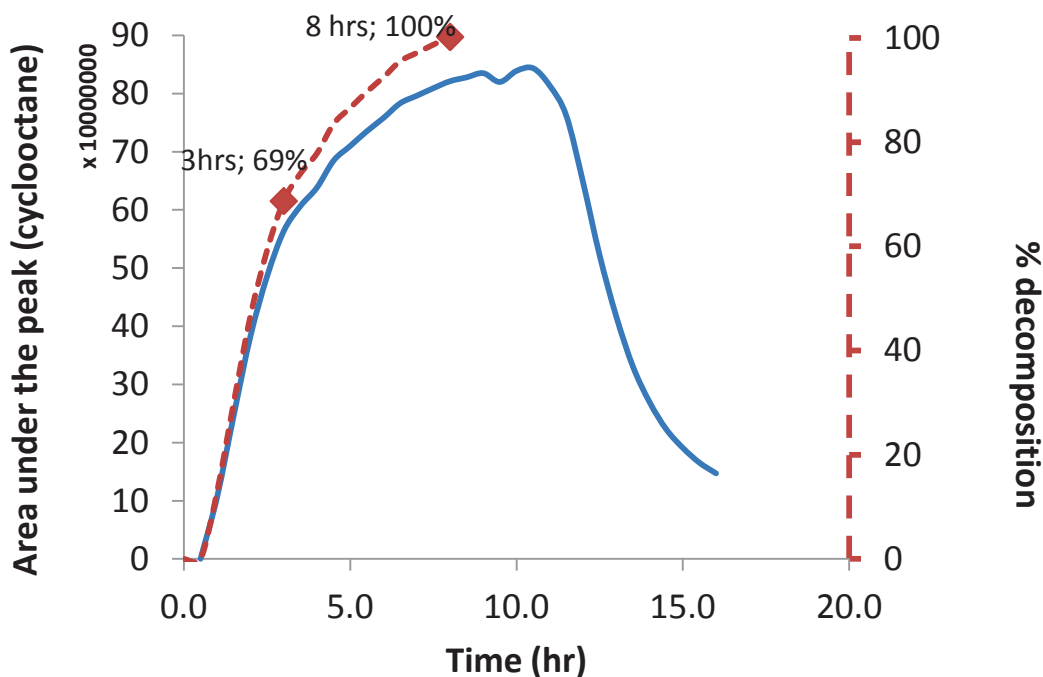


Figure 16 : Evolution of cyclooctane peak area with time (full line); % of Co(COD)(COE) decomposition (dashed line).

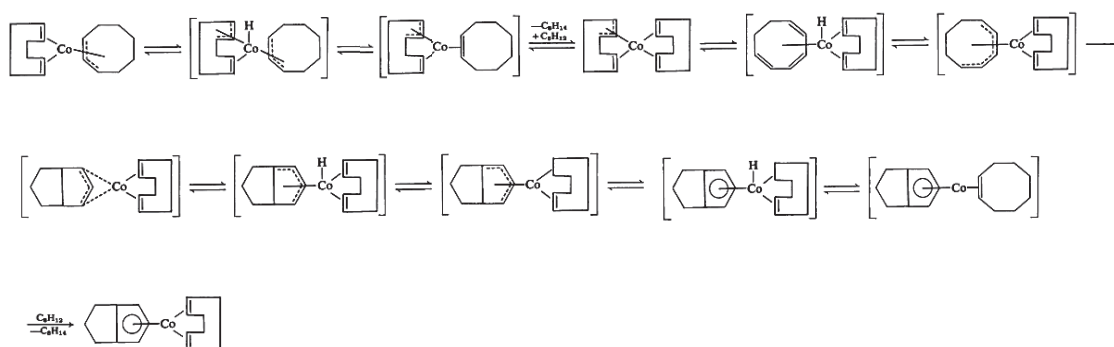


Figure 17 : Proposed mechanism for the possible isomerization reactions catalyzed by Co(COD)(COE) in the presence of hydrogen.<sup>97</sup>

#### iv. In situ GC-mass monitoring of the thermal stability in $C_1C_4ImNTf_2$ : under Ar then $H_2$

In order to further confirm our conclusions, another experiment setup was considered. In this experiment, a solution of Co(COD)(COE) in  $C_1C_4ImNTf_2$  was first heated up to 150 °C for 20 minutes under Ar. In this step, only the products resulting from a simple thermal decomposition of the precursor under inert atmosphere would be detected. In a second step, 0.4 MPa of  $H_2$  were applied for 2 h. The purpose of this step was to study the reduction and

hydrogenation reactions taking place upon applying H<sub>2</sub> gas. Online GC-mass analysis of the evolved gas phase was performed for both steps (Figure 18).

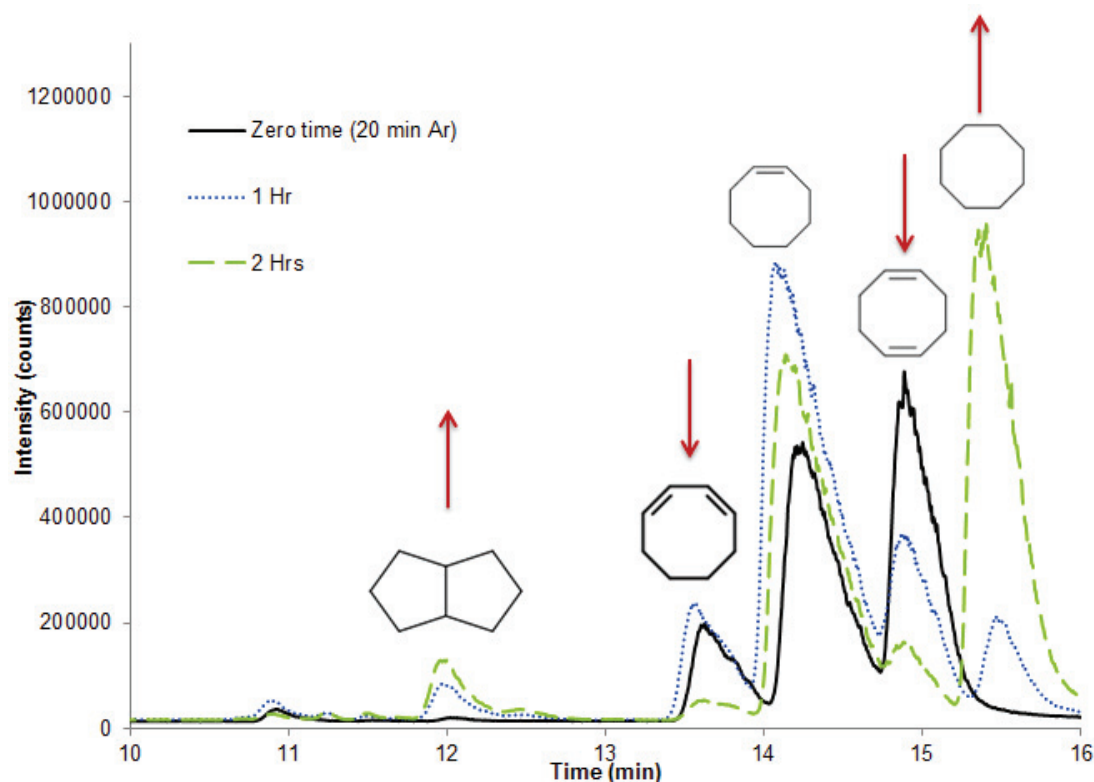


Figure 18 : Evolution of the chromatograms of the evolved gas phase during the decomposition at 150°C of the solution of Co(COD)(COE) [  $5 \times 10^{-2} \text{ mol.L}^{-1}$  ] in  $\text{C}_1\text{C}_4\text{ImNTf}_2$  for 20 min under Ar (0.2 MPa), then 60 and 120 min under 0.4 MPa of H<sub>2</sub>.

Before applying H<sub>2</sub>, after 20 min under Ar (0.2 MPa) at 150 °C, only cyclooctene, 1,3-cyclooctadiene and 1,5-cyclooctadiene were detected. The presence of cyclooctene suggested a partial hydrogenation of cyclooctadiene even in absence of H<sub>2</sub>. Such a reaction in the presence of Co(COD)(COE) was reported in the literature (Figure 17).<sup>97,98</sup>

Upon applying H<sub>2</sub>, the 3 peaks of cyclooctene, 1,3-cyclooctadiene and 1,5-cyclooctadiene started to decrease together with the appearance of two new peaks corresponding to cyclooctane and pentalene. The formation of the latter compounds was a good indication of the presence of metallic Co-NPs.

In conclusion, results from the two previous experiments in IL indicate that Co(COD)(COE) could be quite easily decomposed into metallic Co under H<sub>2</sub> atmosphere at 100-150°C.

## I-B. II. Influence of experimental parameters on the Co-NP size

Taking into account these data, the reduction of Co(COD)(COE) into Co-NPs was tentatively conducted in imidazolium based ILs, namely  $C_1C_n\text{ImNTf}_2$  with  $n = 4, 8, 12, 14$  under  $H_2$ . The influence of different experimental parameters *e.g.* reaction temperature, reaction duration, pressure of  $H_2$ , and alkyl chain length of IL cation on the NP morphology was examined.

### i. Influence of reaction duration

Based on our understanding of the results of the previous thermal decomposition studies, the decomposition of Co(COD)(COE) in  $C_1C_4\text{ImNTf}_2$ , at  $100^\circ\text{C}$  under 0.4 MPa of  $H_2$  was carried out during 0.5, 4 and 24 h to fine tune the reaction duration. The main observation is that the size of obtained Co-NPs was always the same whatever the reaction duration ( $4.1\pm 0.4$ ,  $4.1\pm 0.5$ ,  $4.1\pm 0.4$  nm for 0.5, 4 and 24 h respectively) indicating that Co-NPs (like Ru-NPs) were stable in IL under  $H_2$ .<sup>112, 90</sup> In line with the *in-situ* IR study of the decomposition of Co(COD)(COE) under  $H_2$ , it seems that the decomposition of this compound under  $H_2$  is quite fast. It seems to be almost complete even for very short reaction duration (30 min).

### ii. Influence of temperature

The solution of Co(COD)(COE), ( $5\times 10^{-2}$  mol.L<sup>-1</sup>) in  $C_1C_4\text{ImNTf}_2$  was heated at 65, 100 and  $150^\circ\text{C}$  under 0.2 MPa of  $H_2$  then the pressure was adjusted to 0.4 MPa after thermal equilibrium was reached and kept for 4 h. As reported for Ru-NPs in  $C_1C_4\text{ImNTf}_2$ ,<sup>92, 93</sup> the NPs size increased with the reaction temperature from  $3.6\pm 0.7$  nm at  $65^\circ\text{C}$ ,  $4.1\pm 0.5$  nm at  $100^\circ\text{C}$  and  $7.0\pm 0.8$  nm at  $150^\circ\text{C}$  (Figure 19). A similar effect was observed with Co(COD)(COE) in organic solvents. The Co-NP size increased from 1.0 nm to 1.5 nm upon increasing the reaction temperature from 0 to  $20^\circ\text{C}$ .<sup>49</sup> Increasing the temperature induces a higher rate of nucleation leading to smaller NPs but it also enhance the rate of NP growth.<sup>99</sup> In our case, it thus seems that the second effect dominates.

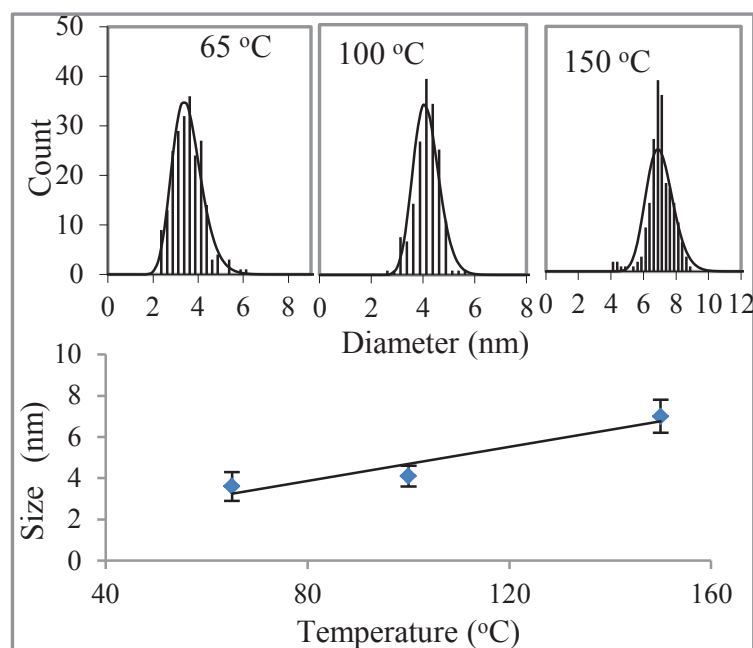


Figure 19 : Evolution of Co-NP size with reaction temperature; Co-NP formed during the reaction of Co(COD)(COE) under 0.4 M Pa of H<sub>2</sub> for 4 hours.

### iii. Influence of the side alkyl chain length

The Co-NP synthesis was performed in different ILs C<sub>1</sub>C<sub>n</sub>ImNTf<sub>2</sub> where n = 4; 8; 12; 14, 4 hours at 100°C under 0.4 MPa of H<sub>2</sub>. Contrarily to the Ru-NPs but similarly to Ni-NPs generated in similar conditions,<sup>100</sup> the Co-NPs mean size does not significantly change with the IL chain length (Table 5).

Table 5 : Size evolution of M- NPs (M = Co, Ru and Ni) generated from Co(COD)(COE), Ni(COD)<sub>2</sub> and Ru(COD)COT, respectively, at 100°C (75°C in case of Ni-NPs) under 0.4 MPa of H<sub>2</sub>, 4 h, in C<sub>1</sub>C<sub>n</sub>ImNTf<sub>2</sub> where n = 4; 8; 12; 14 within 4 h (30 min in case of Ni-NPs).

Alkyl chain length (n)	4	8	12	14
Mean size(nm) Co-NP	4.1±0.3	4.0 ± 0.3	4.4 ± 0.3	3.2 ± 0.2
Mean size(nm) Ru-NP <sup>90</sup>	3.8 ± 0.9	1.8 ± 0.5	1.7 ± 0.5	1.8 ± 0.3
Mean size(nm) Ni-NP <sup>89</sup>	5.9 ± 1.4	5.6 ± 1.3	---	5.1 ± 0.9

Note that Co-NPs generated in IL with n > 10, Figure 20, were well separated showing larger inter-particle distance. This separating distance could be resolved in the TEM in the case of n=14. It was measured at 1.7±0.3 nm. This is most probably due to the fact that NPs were surrounded by a layer of IL which kept them apart. Indeed the observed spacing distance is comparable to what is observed for Au-NPs prepared in C<sub>1</sub>C<sub>10</sub> imidazolium imide (1.33 nm)<sup>101</sup> and for Ni-NPs in long chain imidazolium ILs.<sup>89</sup>

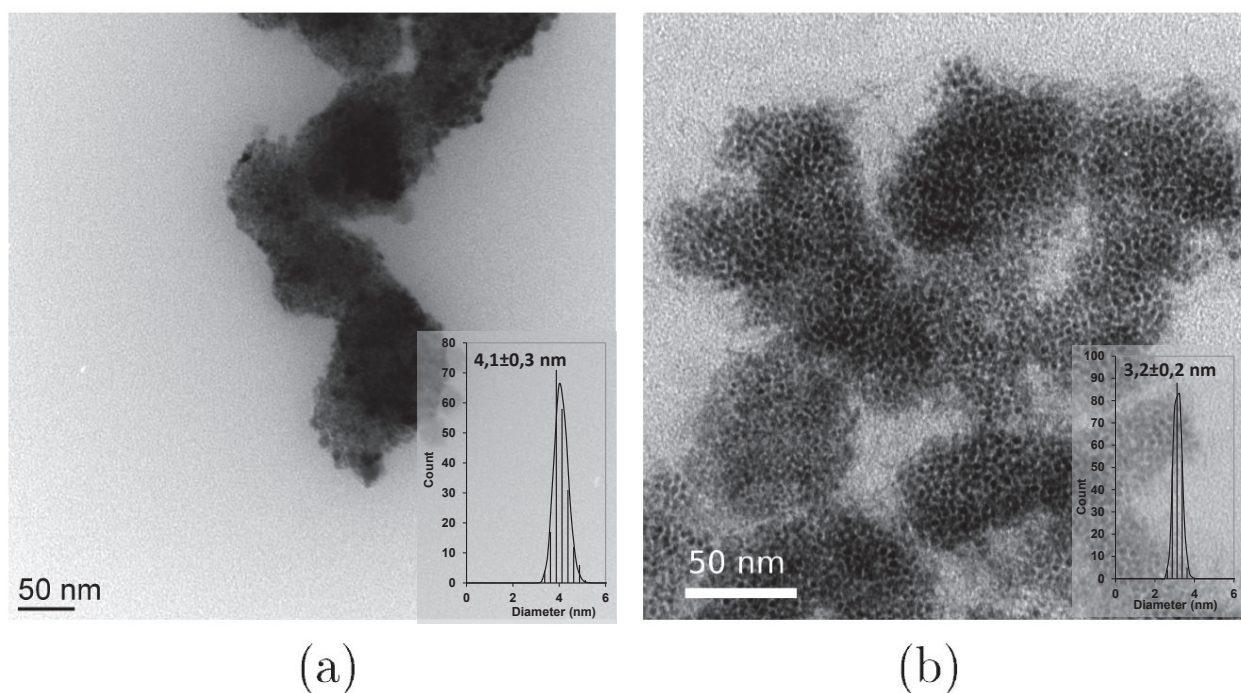


Figure 20 : TEM images for Co-NPs generated at 100°C, 0.4 M Pa of H<sub>2</sub> in (a) C<sub>1</sub>C<sub>4</sub>ImNTf<sub>2</sub>, (b) C<sub>1</sub>C<sub>14</sub>ImNTf<sub>2</sub>.

### I-B. III. Could R<sub>n</sub>SiH<sub>4-n</sub> be used as reducing agent of Co(COD)(COE) instead of H<sub>2</sub>?

Recently, in our group, it was evidenced that the surface silane could reduce OM precursors.<sup>102</sup> To our knowledge, only one example was reported in the literature for the NP preparation using alkylsilane as reducing agent. In that particular example, Pt-NPs were prepared by the reduction of (COD)PtX<sub>2</sub> (X = Me, OSi(OtBu)<sub>3</sub>) and Pt(dba)<sub>2</sub> using octylsilane, acting as both the reducing agent and the stabilizer.<sup>103</sup>

As it will be advantageous in terms of replacing the dangerous H<sub>2</sub> gas with an easy to handle liquid compound, alkylsilane could be an option. Due to its low boiling point, it could also be easily recovered after the reaction. This approach was further investigated for Co(COD)(COE) to generate magnetic Co-NPs which is the main goal of this work. In particular, the possible formation of undesired Co silicides in this reaction was examined.

#### i. Triethylsilane (Et<sub>3</sub>SiH)

In a Schlenk tube, an equimolar amount of Et<sub>3</sub>SiH was added via a syringe to a 2 mL solution of Co(COD)(COE) (concentration 5x10<sup>-2</sup> mol.L<sup>-1</sup>) in C<sub>1</sub>C<sub>4</sub>ImNTf<sub>2</sub> under argon at 20°C. The mixture was then stirred and kept at 50 °C for 2 h or for 4h under static argon conditions.

The color of the reaction medium changed from dark brown to black indicating the occurrence of a reaction and the possible formation of NPs. For both experiments, the GC chromatograms of the volatile compounds condensed after the reaction exhibit peaks corresponding to unreacted  $\text{Et}_3\text{SiH}$  and several peaks identified as cyclooctadiene, cyclooctene and pentalene, resulting from partial hydrogenation of  $\text{Co}(\text{COD})(\text{COE})$  ligands. The relative quantity of these compounds was dependent on the reaction duration, Figure 21.

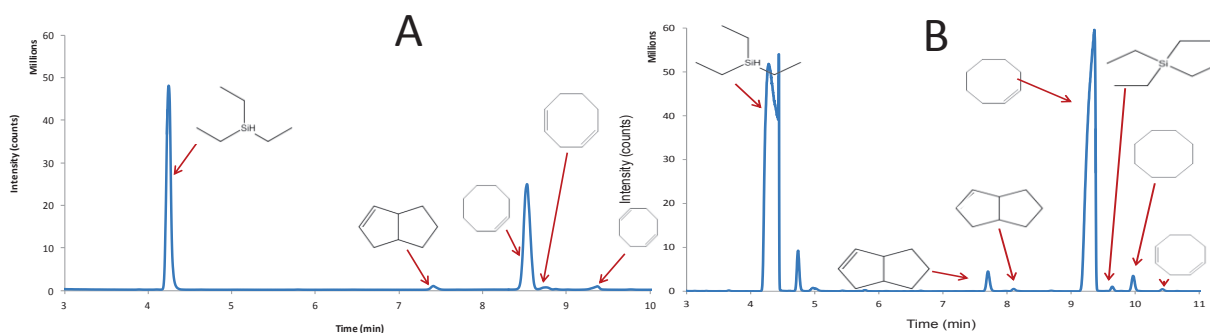


Figure 21 : GC spectra of condensed volatile compounds after the reaction of  $\text{Et}_3\text{SiH}$  and  $\text{Co}(\text{COD})(\text{COE})$  in  $\text{C}_1\text{C}_4\text{ImNTf}_2$  at  $50^\circ\text{C}$  under Ar, A) during 2 h, and B) during 4 h.

TEM observations confirmed the presence of NPs whose size decreased with reaction duration, from  $5.5 \pm 0.4$  nm after 2h to  $4.5 \pm 0.3$  nm after 4h (Figure 22). Such an unexpected trend is usually associated with an incomplete reaction for shorter durations. In fact, the reaction goes on after cooling down the medium, under conditions where the growth of existing NPs dominates the nucleation of new clusters. In this case, there is no accurate size control of NPs.<sup>27, 104</sup>

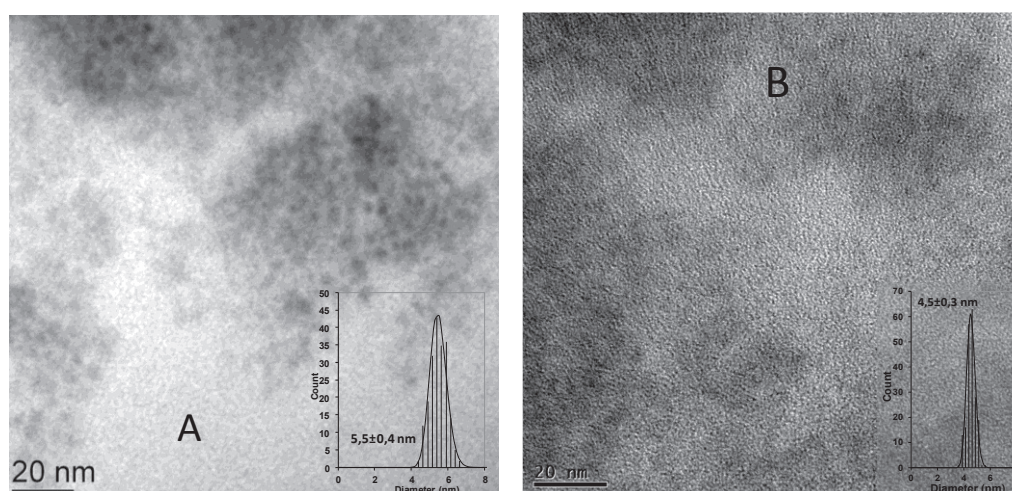


Figure 22 : TEM image of NPs generated by the reaction of  $\text{Co}(\text{COD})(\text{COE})$  with  $\text{Et}_3\text{SiH}$  at  $50^\circ\text{C}$  under argon, A) during 2 h, and B) during 4 h.

Indeed, GC measurements confirmed that the quantity of evolved hydrocarbons resulting from the reduction of Co(COD)(COE) by Et<sub>3</sub>SiH increased with the time. This is a clear evidence that the reaction was not complete within the 2h duration.

To verify the chemical composition of the NPs (Co or silicide), the latter were extracted from the IL by centrifugation and washing with CH<sub>2</sub>Cl<sub>2</sub>. An elemental analysis of the solid showed that there was only a little contamination of the obtained NPs with Si (1.8% mass). This small contamination (3.6%at) could be due to the residual Et<sub>3</sub>SiH that was not properly washed prior to the elemental analysis. Finally, this result clearly demonstrates that the NPs generated during this reaction are Co-NPs.

## ii. Reaction with other silane compounds

The reactivity of different silane compounds C<sub>8</sub>H<sub>17</sub>SiH<sub>3</sub>, (t-Bu)<sub>2</sub>SiH<sub>2</sub>, Et<sub>2</sub>SiH<sub>2</sub> with Co(COD)(COE) under similar conditions was also investigated (Ar atmosphere, 2 h, 50°C). In all cases, the reaction afforded Co-NPs with nearly equal sizes ranging between 5.5 nm to 6.1 nm (Figure 23).

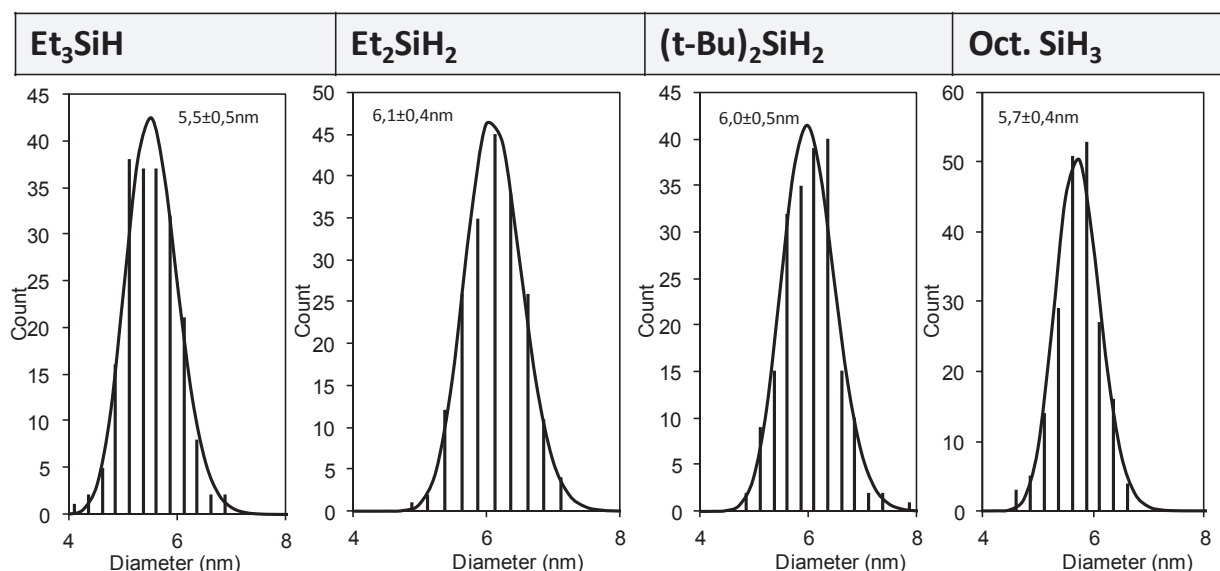


Figure 23 : Size distribution of Co-NPs generated by reaction of Co(COD)(COE) with different R<sub>x</sub>SiH<sub>4-x</sub> compounds under argon, during 2 h at 50°C.

Since the Si-H group should be the one involved in the decomposition reaction, it might not be accurate to fix the R<sub>x</sub>SiH<sub>4-x</sub> concentration. For example, using 0.05 mol.L<sup>-1</sup> of OctSiH<sub>3</sub> gives 0.15 mol.L<sup>-1</sup> of Si-H content which is 3 times higher than the Si-H concentration



resulting from using  $0.05 \text{ mol.L}^{-1} \text{ Et}_3\text{SiH}$ . However, besides a narrower size distribution with  $\text{OctSiH}_3$ , both afforded similar Co-NP size.

Therefore, a second set of experiments was repeated at  $50 \text{ }^\circ\text{C}$  for 4 h with an equimolar ratio of Si-H/  $\text{Co(COD)(COE)}$  (*i.e.* a Si-H concentration of  $0.05 \text{ mol.L}^{-1}$ ) for  $\text{Et}_3\text{SiH}$  and  $\text{OctSiH}_3$ . Upon collecting and analyzing the volatile byproducts (mainly unsaturated cyclooctane derivatives), the amount of evolved byproducts was 1.7 times higher for  $\text{OctSiH}_3$  as compared to  $\text{Et}_3\text{SiH}$ , indicating higher decomposition rates. In the same time, smaller NPs were formed with  $\text{OctSiH}_3$  ( $3.8 \pm 0.3 \text{ nm}$ ) as compared to  $\text{Et}_3\text{SiH}$ , ( $4.5 \pm 0.3 \text{ nm}$ ), indicating faster nucleation step in case of the former reagent.

## **I-B. IV. Physico-chemical properties of Co NPs**

### **i. Structural analysis of Co-NPs**

The as-prepared Co-NPs exhibited a well-defined crystalline structure under high-resolution TEM (HRTEM) as shown in Figure 24. As a result, fast-Fourier transform (FFT) analysis of the pictures yielded a pattern of clearly defined spots in the reciprocal space. This pattern was compared to the known crystalline structures of metallic Co (non-metallic structures were discarded, as magnetic measurements unambiguously demonstrate that our CoNPs are metallic).

In all cases, spots corresponding to an interplanar distance of about  $3.5 \text{ \AA}$  were observed. It could correspond to the (001) distance in the hexagonal close-packed (hcp) structure, the stable allotrope of Co, or to the (100) distance in the fcc structure. Nevertheless, the other spots could not be indexed using neither of these structures. Finally, this distance could correspond to the (111) planes of a metastable cubic structure of Co usually referred to as  $\epsilon\text{-Co}$ .<sup>86</sup> Indeed, it is shown in Figure 24b that the pattern in the FFT image can be completely indexed using this phase. The same was observed for all other NPs analyzed by HRTEM.

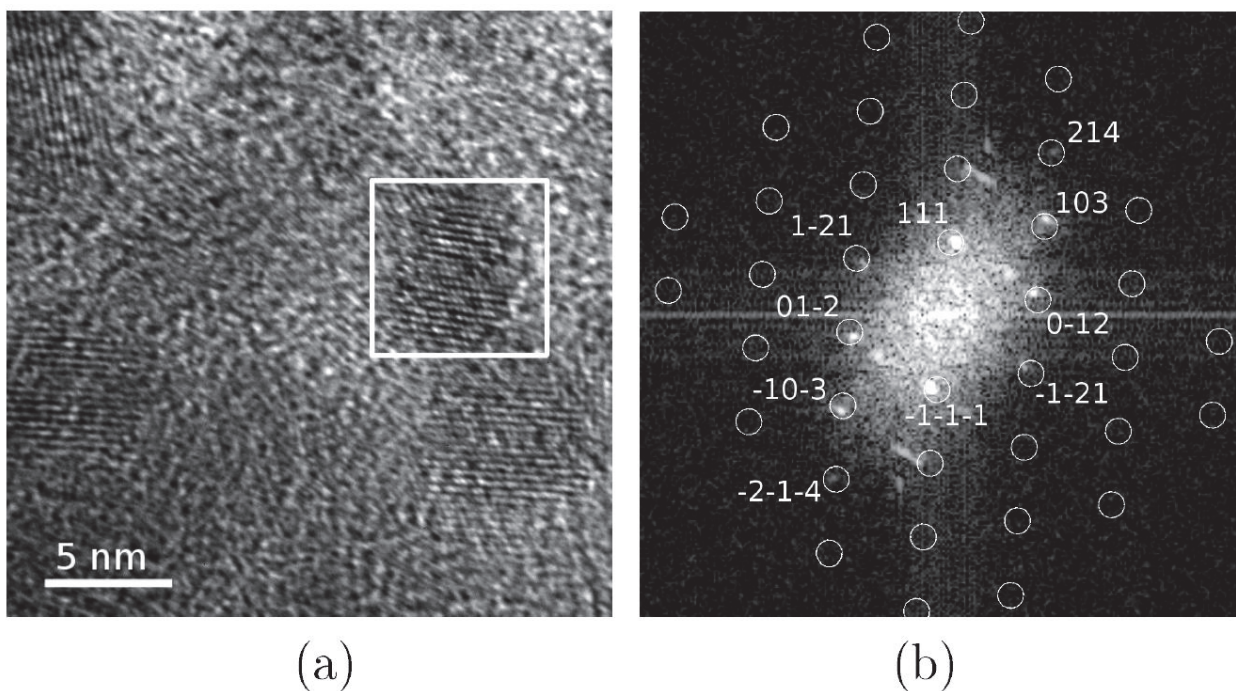


Figure 24 : (a) Exemplary HRTEM image of CoNPs generated by the decomposition of Co(COD)(COE) in  $C_1C_4ImNTf_2$  under 0.4MPa of  $H_2$  for 4 h and (b) FFT of the particle in the white square indexed by a cubic structure along the (-321) zone axis with a lattice parameter of 6.1Å corresponding to  $\epsilon$ -Co.

To confirm this, a more comprehensive study was undertaken using wide angle X-ray scattering (WAXS). These measurements were conducted on a sample suspension in  $C_1C_4ImNTf_2$  placed in a sealed quartz capillary using a Mo- $K_\alpha$  source at 0.71069 Å (see experimental chapter).

Prior to the WAXS measurements, the X-ray fluorescence was first measured at  $2\theta=110^\circ$  for 10 minutes between 15 and 18keV. The recorded signal showed both inelastic scattering (the 2 fine peaks just below 18keV) and elastic scattering (Figure 25). The high proportion of the inelastic scattering is typical of a sample rich in light elements (IL). The small peaks between 6.5 and 8keV correspond to the Co  $K_\alpha$  (left) and  $K_\beta$  (right) fluorescence. Finally, the capillary was placed at a position in which the fluorescence signal was maximum (corresponding to a local maximal concentration of Co).

The WAXS response of the suspension is plotted in Figure 26, along with the response of blank IL sample.

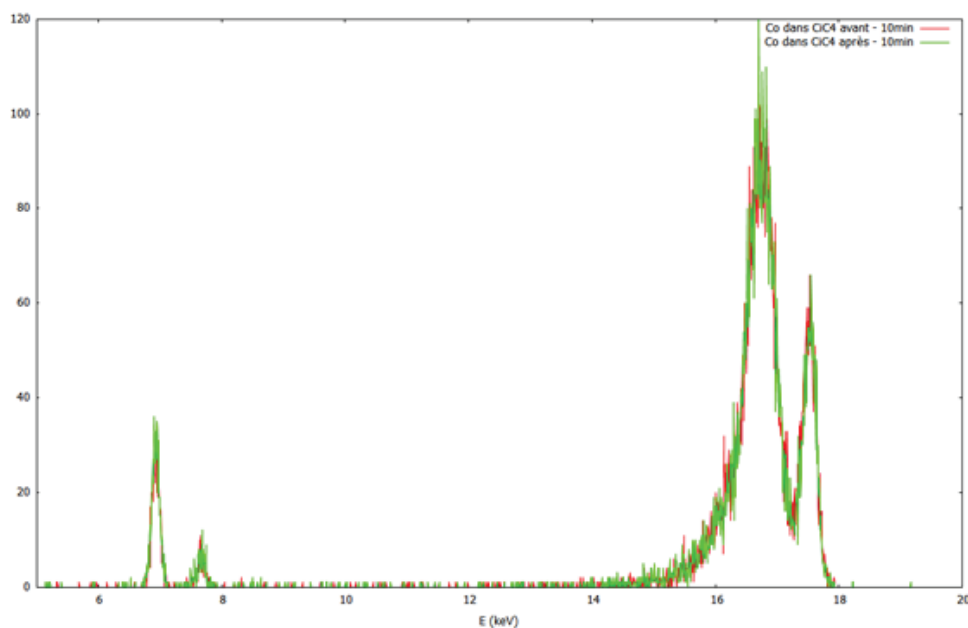


Figure 25 : X ray fluorescence spectra of a suspension of Co-NPs in  $C_1C_4ImNTf_2$  measured at  $2\theta=110^\circ$  for 10 minutes between 15 and 18keV.

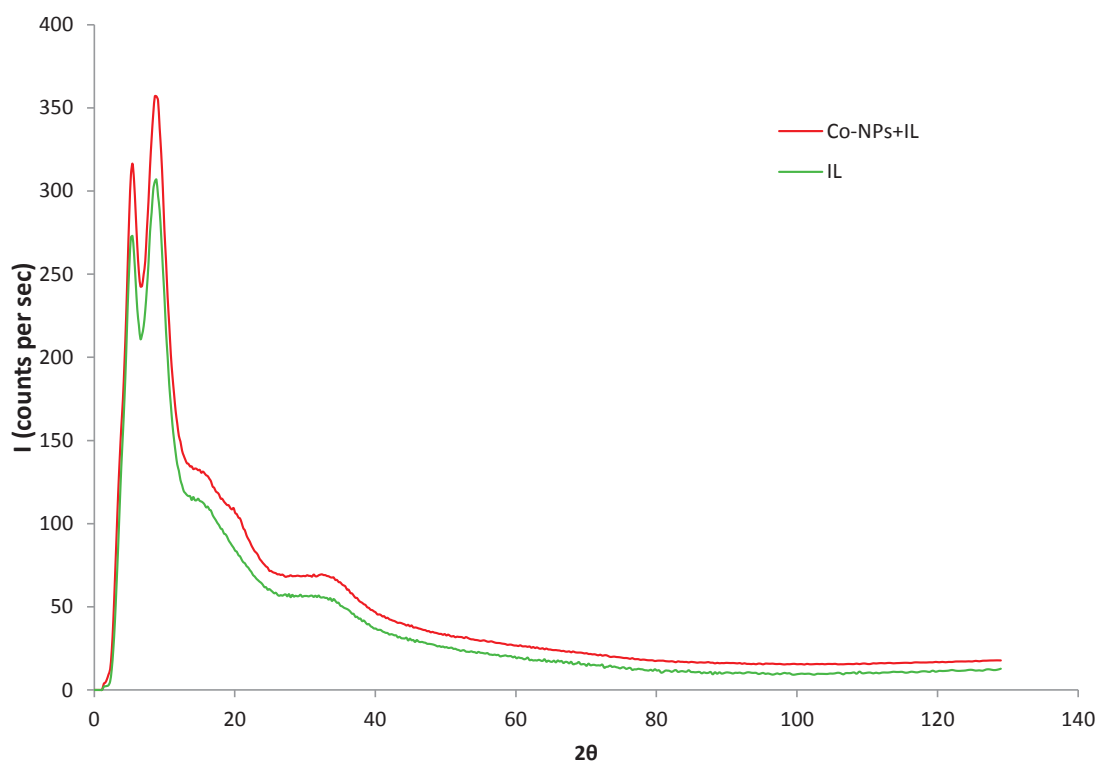


Figure 26 : WAXS curves of Co-NPs as-prepared, suspended in  $C_1C_4ImNTf_2$  (red line) and of pure  $C_1C_4ImNTf_2$  (green line).

After subtracting the IL signal, it was possible to get the response of the Co-NPs (Figure 27a). As expected, as-prepared Co-NPs did not produce well defined diffraction peaks. Rather the diffusion curve compares well with the signal reported for Co-NPs with the  $\epsilon$ -Co structure.<sup>105</sup> The deduced radial distribution function (RDF) is also in good agreement with

this structure, with a first metal-metal distance close to 0.255 nm (Figure 27b). A noticeable feature is the absence of a metal-metal distance near 0.35nm (grey area in Figure 27b), which is the signature for a non-close packed structure. All these results thus confirm that our Co-NPs adopt the  $\epsilon$ -Co phase. Finally, it should be noted that the coherence length is well below 2 nm, which is significantly smaller than the size estimated by TEM.

Interestingly enough, a drastic modification of the WAXS response was observed for Co-NPs in  $C_1C_4ImNTf_2$  after a 2 -day decantation over a magnet, as shown in Figure 27a. Better defined peaks appeared at positions corresponding to the diffraction angles of hcp Co (red dots in Figure 27a).

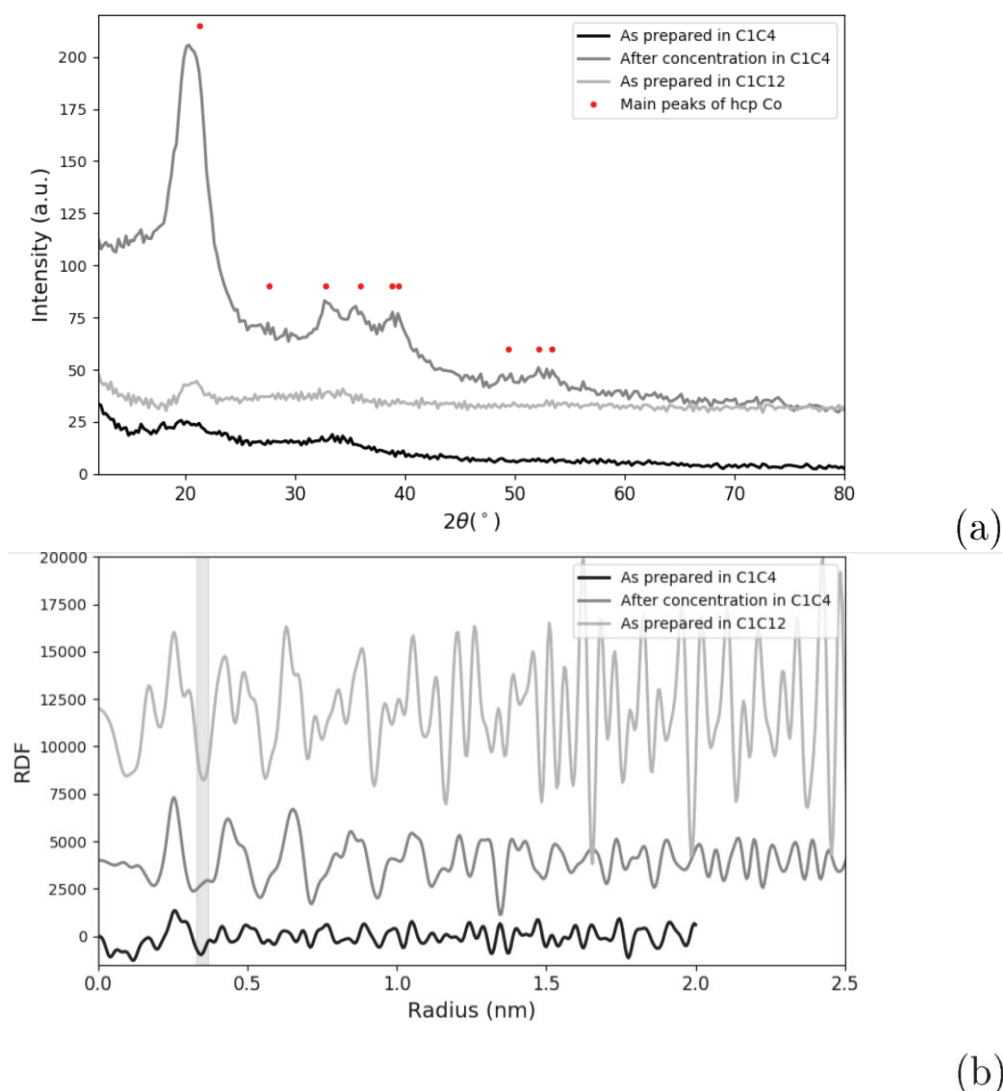


Figure 27 : (a) Scattering curves and (b) corresponding radial distribution functions (RDF) of Co-NPs as-prepared in  $C_1C_4ImNTf_2$  and in  $C_1C_{12}ImNTf_2$ , and after decantation over a magnet in  $C_1C_4ImNTf_2$ .

The RDF is also in good agreement with this structure, with the development of a metal-metal distance near 0.35 nm (Figure 27b).<sup>105</sup> Hence, it seems that the metastable  $\epsilon$ -Co-NPs have evolved during the decantation process into stable hcp Co-NPs. In the same time, the coherence length has increased to about 3nm, in better agreement with TEM observations.

This indicates that the Co-NPs have recrystallized during decantation. It should be mentioned that this transformation was not necessarily quantitative, and that  $\epsilon$ -Co-NPs were probably still present. They are not clearly visible because the contribution of the better-crystallized hcp Co-NPs is dominating in the WAXS response.

In contrary, the metal-metal distance near 0.35 nm was completely absent in case of Co-NPs prepared in  $C_1C_{12}ImNTf_2$ . This could be a clear indication for the domination of the non-compact  $\epsilon$ -Co phase in case of using long chain IL.

## ii. Magnetic properties:

To characterize the magnetic properties of the Co-NPs in ILs, SQUID measurements were undertaken using suspensions of Co-NPs elaborated in  $C_1C_4ImNTf_2$  and  $C_1C_{14}ImNTf_2$ . Prior to measuring the suspensions, the two ILs were tested. They were found to be diamagnetic with a low susceptibility, a good indication that they are chemically pure. For this reason, no significant contribution of the IL was expected to interfere with the response of the NPs. Nevertheless, some kind of transition was observed between 180 K. This could be related to the glass transition temperature of the IL (189 K, Figure 28).<sup>106</sup>

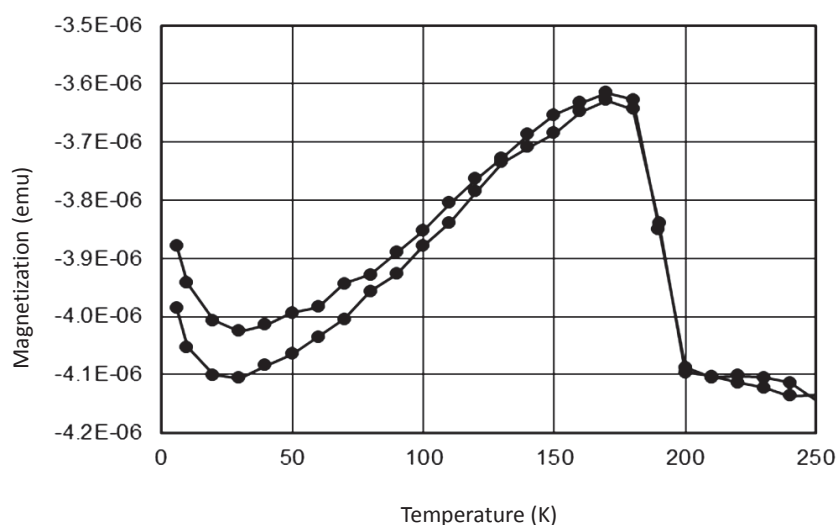


Figure 28 : Magnetization versus temperature for pure  $C_1C_4ImNTf_2$  sample.

The magnetization curve of Co-NPs synthesized in  $C_1C_4ImNTf_2$  recorded at 250K is plotted in Figure 29a. This curve is well centered and symmetrical with respect to a zero magnetic field. The fact that the magnetization curves remained symmetrical when the measurements were repeated at 10 K (Figure 30) is clear evidence that these Co-NPs are metallic. In addition, the saturation magnetization was measured at  $154 \text{ emu.g}^{-1}$ , which was close to the value of the bulk metal ( $163 \text{ emu.g}^{-1}$ ). This was a good indication that the NP surface was not chemically contaminated, as expected in this IL-based process.<sup>105</sup> Finally, this curve was successfully fitted with the Langevin function, in which the size of the NPs was the only adjustable parameter (the Co-NPs were superparamagnetic). This size was found to be 4.1 nm, in good agreement with TEM measurements.

The same conclusions can be drawn for Co-NPs grown in  $C_1C_{14}ImNTf_2$  (Figure 29b). The magnetic moment of Co atoms was  $169 \text{ emu.g}^{-1}$ , which is even closer to the value of bulk metal. Also, the Langevin fit confirmed that these NPs were smaller, with a diameter of 3.7nm ( $3.3 \pm 0.5 \text{ nm}$  as measured by TEM).

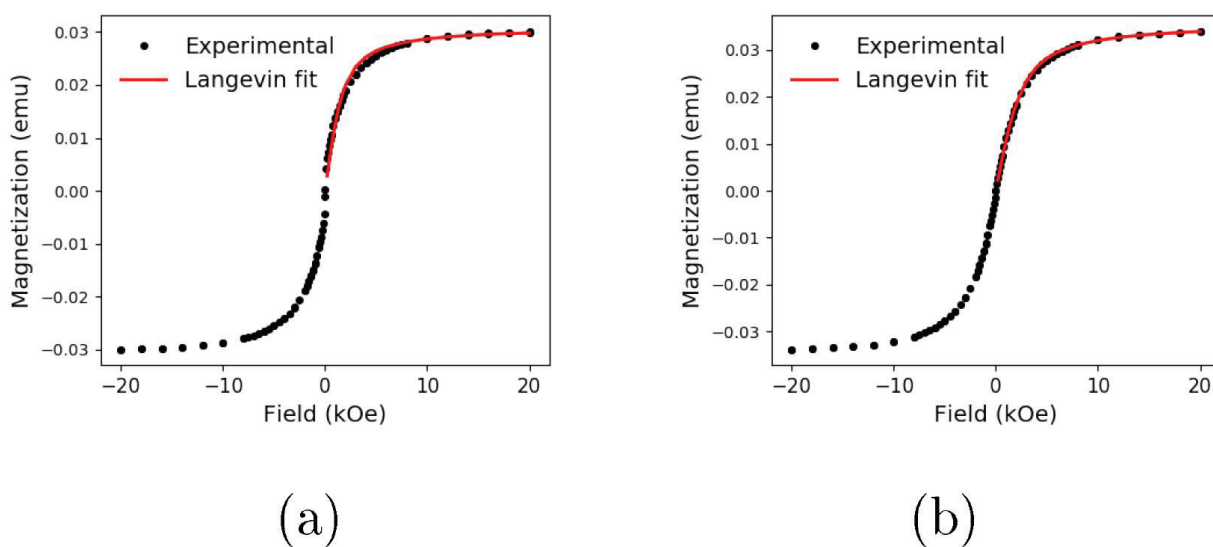


Figure 29 : Magnetization curves at 250K of Co-NPs synthesized in (a)  $C_1C_4ImNTf_2$  and (b)  $C_1C_{14}ImNTf_2$ .

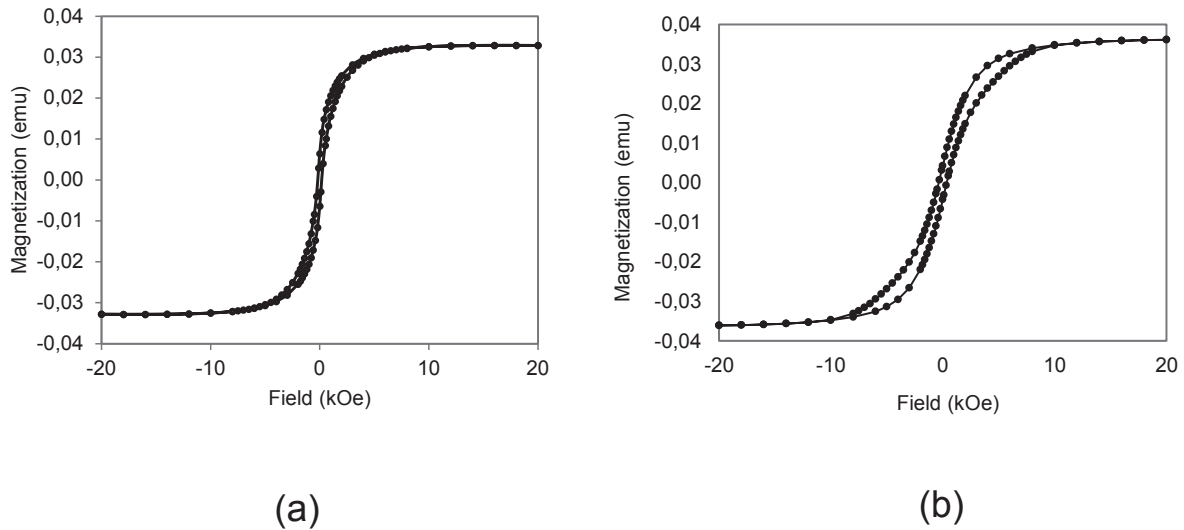


Figure 30 : Magnetization curves at 10K of Co-NPs synthesized in (a)  $C_1C_4ImNTf_2$  and (b)  $C_1C_{14}ImNTf_2$ .

The magnetic behavior of the Co-NPs in both  $C_1C_4ImNTf_2$  and  $C_1C_{14}ImNTf_2$  was further characterized by recording field cooled and zero-field cooled (FC-ZFC) curves (Figure 31). In both cases, the ZFC curve exhibits a clear maximum, corresponding to the blocking temperature  $T_b$ . The latter was only 7 K in  $C_1C_4ImNTf_2$ , whereas it reached 160 K in  $C_1C_{14}ImNTf_2$ . In both ILS, the Co-NPs are thus superparamagnetic at room temperature, as expected in this size range. However, considering that Co-NPs have similar diameters in both ILS, this difference in blocking temperature is unexpected, as is the fact that the smaller NPs in  $C_1C_{14}ImNTf_2$  exhibit a higher blocking temperature.

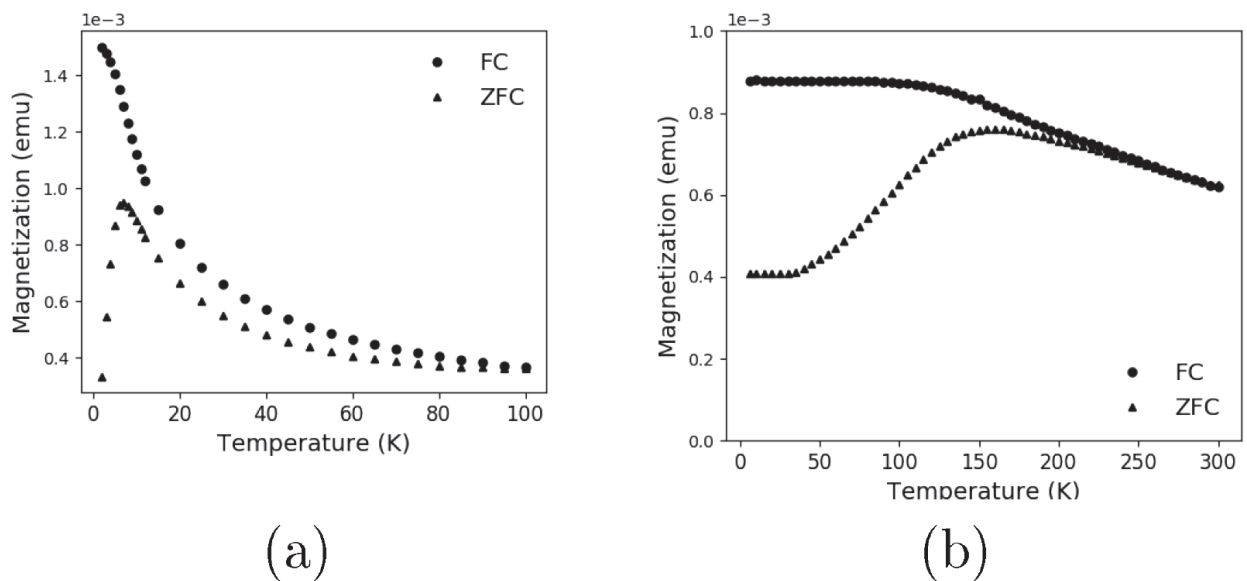


Figure 31 : FC-ZFC curves of Co-NPs synthesized in (a)  $C_1C_4ImNTf_2$  and (b)  $C_1C_{14}ImNTf_2$  recorded at 50 Oe.

In fact,  $T_b$  also depends on the magnetic anisotropy constant  $K$  of the NPs. The latter was deduced using the following relation:

$$K = \frac{25k_B T_b}{V_{NP}}$$

Where  $k_B$  is Boltzmann's constant and  $V_{NP}$  is the volume of the Co-NPs (as computed from the diameter derived from the Langevin fit). The resulting anisotropy constants are  $6.8 \times 10^5 \text{ erg.cm}^{-3}$  and  $2.0 \times 10^7 \text{ erg.cm}^{-3}$  for Co-NPs synthesized in  $C_1C_4\text{ImNTf}_2$  and  $C_1C_{14}\text{ImNTf}_2$ , respectively.

The magneto-crystalline anisotropy arises from the relativistic spin-orbit interaction, and gives rise to energetically-favored orientations for the magnetization relative to the crystal symmetry axis (see appendix 1). Therefore, highly symmetrical crystal structures give rise to quite low magneto-crystalline anisotropy (Table 6). The small anisotropy constant measured for Co-NPs in  $C_1C_4\text{ImNTf}_2$  can thus be accounted for by the quite high symmetry of either the cubic  $\epsilon$ -Co or hcp structures. However, this does not explain the large anisotropy measured with Co-NPs in  $C_1C_{14}\text{ImNTf}_2$ . Indeed, these NPs exhibit similar structure, size and shape as in  $C_1C_4\text{ImNTf}_2$ . Also, the chemical nature of both ILs is very similar. For all these reasons, no significant surface anisotropy is expected in  $C_1C_{14}\text{ImNTf}_2$ .

Table 6 : Anisotropy constants of Co

Structure	$K$ ( $\times 10^6 \text{ erg.cm}^{-3}$ )	Ref.
Bulk hcp	8.2	107
Bulk fcc	-0.6	108

A more plausible explanation to account for the unusual anisotropy constants of Co-NPs in  $C_1C_{14}\text{ImNTf}_2$  is related to the fact that the previously mentioned equation is valid only if the interaction between clusters is negligible. Considering the aggregation of Co-NPs (Figure 20), it is likely that some coupling occurs between the particles. Such a phenomenon is expected to affect the blocking temperature, and in turn the value of effective anisotropy deduced from that equation.

Inter-particle coupling could also be responsible for the weak remanence of the Co-NPs (0.12 at 10 K for Co-NPs in  $C_1C_{14}\text{ImNTf}_2$ , Figure 30).



### Magnetic coupling between Co-NPs

To further investigate the presence of such a coupling between Co-NPs, Isothermal Magnetic Remanence (IRM) and Demagnetization DC (DCD) measurements were undertaken. Since these measurements are not so common, they are presented here in details before going through data discussion:

We start by plotting 3 different curves:

- **M<sub>DCD</sub> – orange curve:**

The sample is de-magnetized at room temperature by applying a large, decreasing alternative magnetic field. It is then cooled down to 10 K. At this point the measured magnetization is zero because the individual magnetizations of the clusters point at random over a complete sphere. Then a positive magnetic field H is applied – the X axis in the graph – and removed. The magnetization M<sub>DCD</sub> at zero field is again measured. A larger H is applied and the measurement is repeated. The measured magnetization gradually increases as more and more clusters are dragged towards the half-sphere centered on the H direction by the applied field.

- **M<sub>IRM</sub> – blue curve:**

The sample is cooled down to 10 K with a 20 kOe positive applied field. The field is removed and the magnetization is measured. What is measured is the finite remanent magnetization of the clusters, which, if there was no coupling, would have their individual magnetization pointing at random in the half-sphere centered on the direction of the positive cooling field. The measurement proceeds as for M<sub>DCD</sub> except that the applied field is negative. The measured magnetization gradually decreases as more and more clusters are dragged towards the half-sphere centered on the H direction by the negative applied field.

Both responses can be combined into  $\Delta M$  according to the equation:

$$\Delta M = M_{DCD}(H) - (M_{IRM}(0) - 2 * M_{IRM}(H))$$

- **$\Delta M$  – grey curve:**

If there is no coupling, the curve is flat (*i.e.*,  $\Delta M=0$  for all H values). Otherwise, a negative (positive)  $\Delta M$  indicates an antiparallel (parallel) magnetic interaction.

This derives from the Wohlfarth theory for individual, uniform and uniaxial clusters.

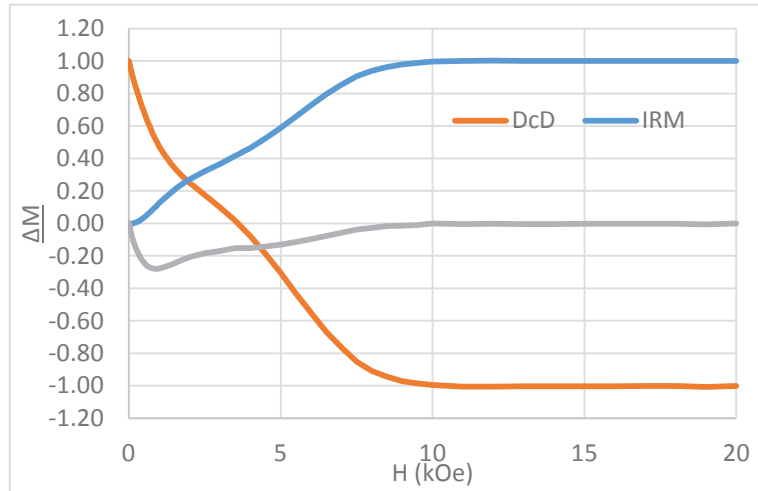


Figure 32 : Isothermal magnetic remanence and demagnetization DC measurements for Co-NPs synthesized in  $C_1C_{14}ImNTf_2$ .

The  $\Delta M$  deduced from our measurements corresponds to the grey curve in Figure 32. This curve clearly departs from 0, which demonstrates the existence of an antiparallel coupling between the Co-NPs. This curve, obtained for a suspension of Co-NPs in  $C_1C_{14}ImNTf_2$  is reproduced in Figure 33 (black circles) together with the corresponding response of Co-NPs in  $C_1C_4ImNTf_2$  (red triangles).

The shape of the black curve in Figure 33 suggests that this coupling has two components, one centered at 0.9 kOe and the other centered at about 5 kOe. Therefore, all experimental evidences converge in indicating that the Co-NPs in  $C_1C_{14}ImNTf_2$  undergo significant magnetic coupling.

Finally, qualitatively reduced coupling was found for the Co-NPs in  $C_1C_4ImNTf_2$ . In this case, a higher remanence of 0.2 at 10K was found (Figure 30). Also, the shape of the red curve in Figure 33 shows that the component at 5 kOe would be quenched. Such a diminution of coupling with respect to Co-NPs in  $C_1C_{14}ImNTf_2$  is consistent with the smaller anisotropy constant.

However, it needs to be pointed out that this result is quite surprising, considering that the Co-NPs in  $C_1C_4ImNTf_2$  are closer than their counterparts in  $C_1C_{14}ImNTf_2$ . For this reason, one would expect more magnetic interactions in  $C_1C_4ImNTf_2$ . Further experiments are certainly needed to elucidate this question.

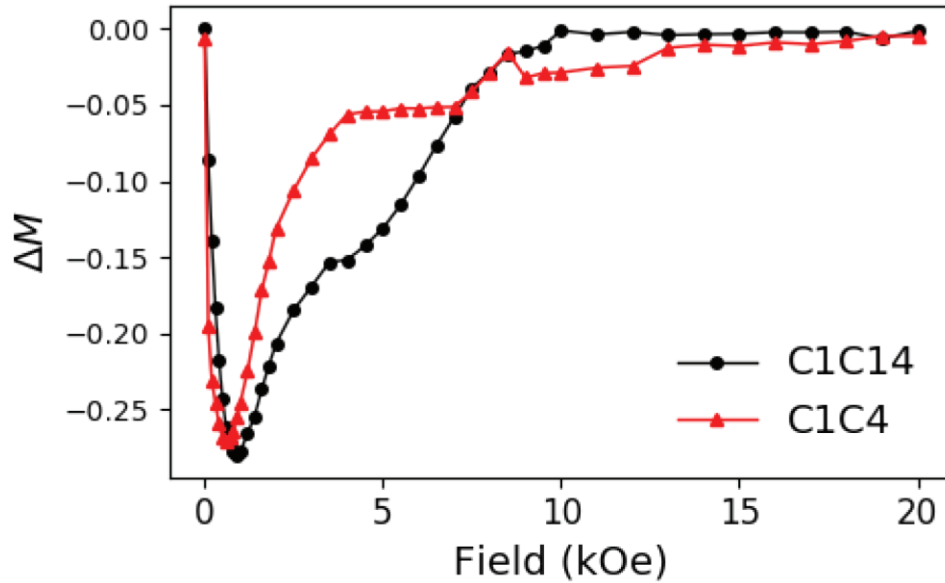


Figure 33 : IRM/DCD response of Co-NPs synthesized in  $C_1C_4\text{ImNTf}_2$  and  $C_1C_{14}\text{ImNTf}_2$ .

*Effect of precursor concentration on the magnetic properties of Co-NPs:*

To further investigate the concentration effect and if it could reduce coupling between Co-NPs, experiments with the previous 2 samples were repeated with suspensions synthesized from 20x diluted solutions. The sample prepared in  $C_1C_4\text{ImNTf}_2$  is called **Sample 1** while that prepared in  $C_1C_{14}\text{ImNTf}_2$  is called **Sample 2**.

For **sample 1**, the FC/ZFC curve measured at 50 Oe (Figure 34) is a little bit noisy, but indicates a very large maximum around 150 K, which is much higher than that of the original sample ( $T_b = 7$  K, see Figure 31a). Of course, this corresponds to a much higher anisotropy ( $1.0 \times 10^7 \text{ erg.cm}^{-3}$ ). A large maximum can be an indication of a large distribution in the anisotropy energy of the clusters. As this energy is a product of the intrinsic anisotropy times the volume of the clusters. This could reflect a large size distribution: the smaller clusters become superparamagnetic probably somewhere below 150 K, and the larger ones become superparamagnetic at higher temperatures.

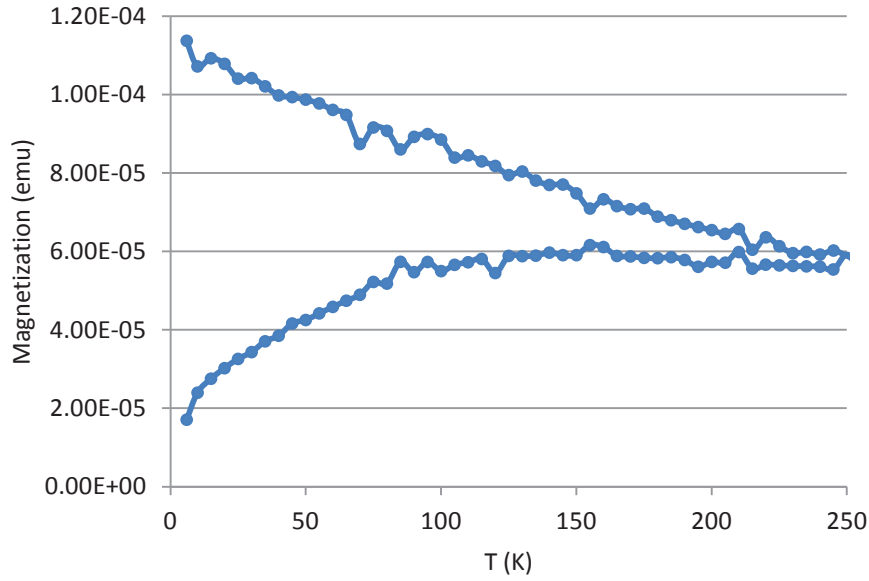


Figure 34 : FC/ZFC curve for Co-NPs suspended in  $C_1C_4ImNTf_2$  ( $0.0025 \text{ mol.L}^{-1}$ ), recorded under 50 Oe magnetic field.

From IRM/DcD measurements (Figure 35), we still have the antiferromagnetic coupling at  $0.7 - 1.0 \text{ kOe}$ .

For sample 2 (Figure 36), it is also similar to its corresponding original sample with a magnetic moment of  $181 \text{ emu.g}^{-1}$ , no oxides, a bit lower  $T_b$  of 105 K and anisotropy value of  $1.33 \times 10^7 \text{ erg.cm}^{-3}$ .

From the Langevin fit (Figure 37), the size of the Co-NPs is estimated at 3.7 nm which is similar to that of the undiluted sample and still comparable to the TEM values (3.3 nm).

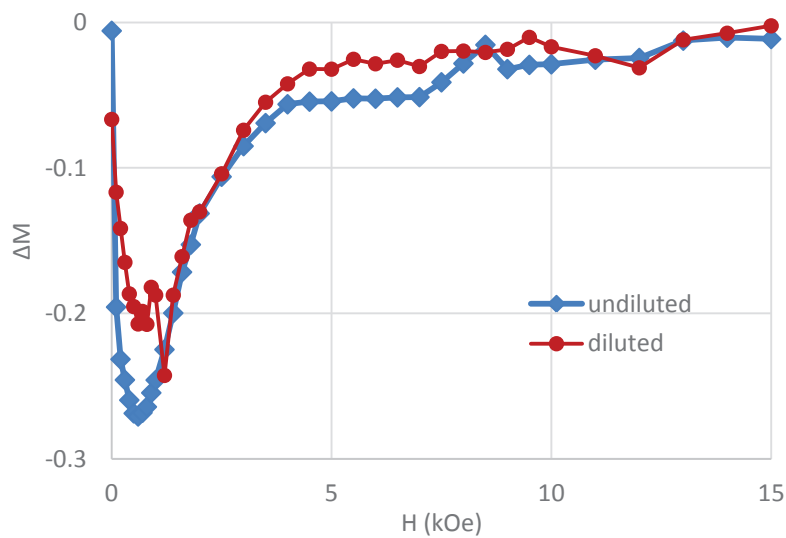


Figure 35 : IRM/DcD measurements for Co-NPs suspended in  $C_1C_4ImNTf_2$  ( $0.05 \text{ mol.L}^{-1}$ , blue,  $0.0025 \text{ mol.L}^{-1}$ , red) showing the  $\Delta M$  values plotted as a function of the applied magnetic field.

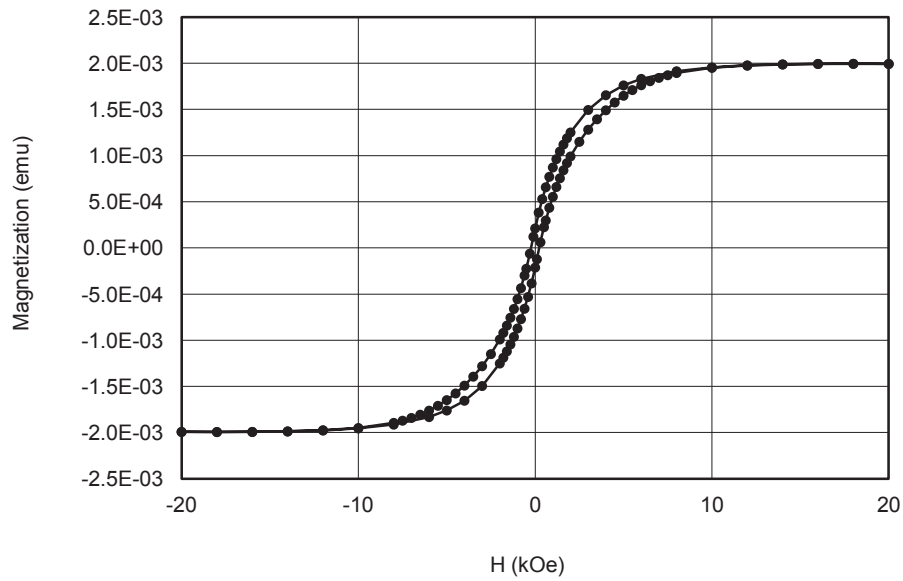


Figure 36 : Magnetization curve for Co-NPs suspended in  $C_{14}ImNTf_2$  ( $0.0025 \text{ mol.L}^{-1}$ ) measured at 10 K.

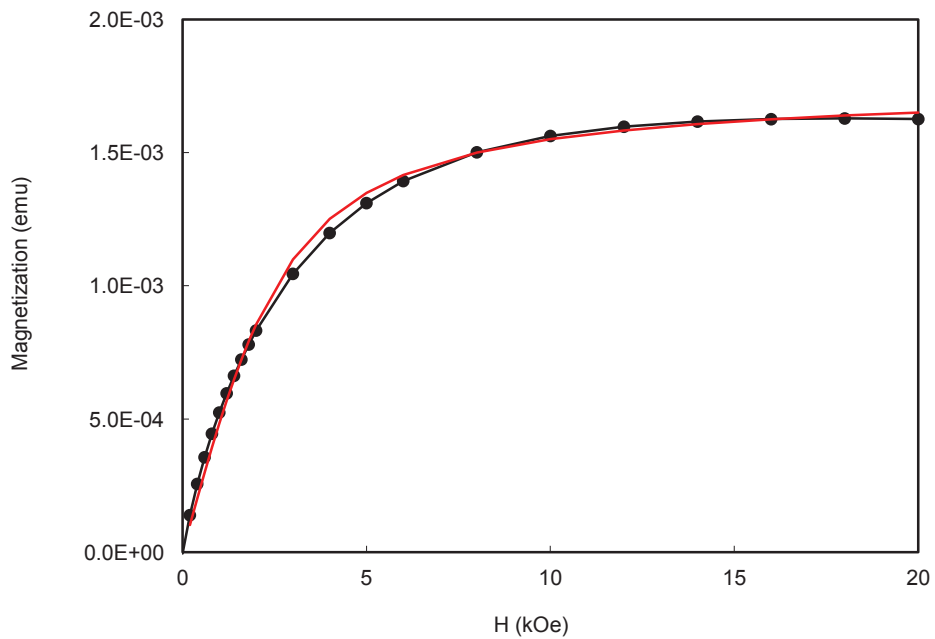


Figure 37 : Magnetization data for Co-NPs suspended in  $C_{14}ImNTf_2$  ( $0.0025 \text{ mol.L}^{-1}$ ) measured at 300 K (black) and the data fitting with Langevin model assuming 3.7 nm NPs (red).

IRM/DcD measurements (Figure 38) shows the disappearance of the antiferromagnetic coupling at 5 kOe as compared to the original sample indicating that it has something to do with sample dilution. On the other hand, the AF coupling around 0.7 - 1.0 kOe still exists.

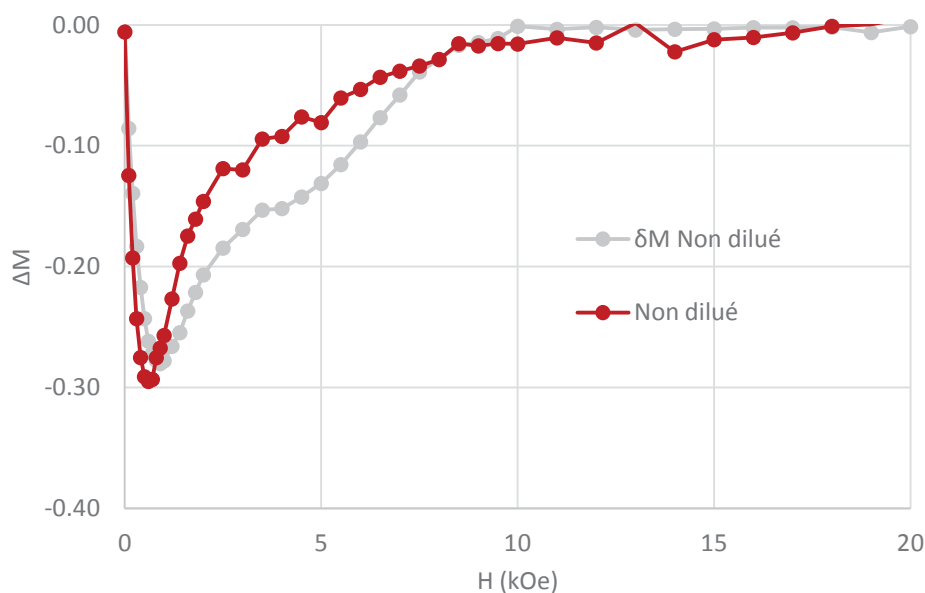


Figure 38 : IRM/DcD measurements for Co-NPs suspended in  $C_1C_{14}ImNTf_2$  ( $0.05 \text{ mol.L}^{-1}$ , grey and  $0.0025 \text{ mol.L}^{-1}$ , red) showing the  $\Delta M$  values plotted as a function of the applied magnetic field.

## I-B. V. Conclusion

Based on a detailed bibliographic study,  $Co(COD)(COE)$  has been verified to satisfy the various criteria for the synthesis of Co-NPs in ILs. It has a good solubility in these solvents, its decomposition temperature is less than  $100^\circ\text{C}$  and the main decomposition byproduct is cyclooctane, a volatile compound readily removed under vacuum. This was validated by a complete study involving TGA, DRIFT and GC-mass.

Co-NPs were accessible through the decomposition reaction of this OM under  $H_2$ . Their size could be tuned by varying the experimental conditions. For example, by increasing the reaction temperature from  $65^\circ\text{C}$  to  $100^\circ\text{C}$  and then to  $150^\circ\text{C}$ , the Co-NPs size increased from  $3.6 \pm 0.4 \text{ nm}$  to  $4.1 \pm 0.4 \text{ nm}$  then to  $7.0 \pm 0.8 \text{ nm}$ , respectively. The Co-NPs formed clusters, indicating that they were interacting. It is interesting to note that in an IL in which the imidazolium cation had a longer alkyl chain,  $C_1C_{14}ImNTf_2$ , the distance between adjacent NPs was larger.

The structure of these NPs was studied by HRTEM and WAXS showed that the Co-NPs consisted of a meta-stable allotrope of  $Co^{(0)}$  called  $\epsilon\text{-Co}$ . This cubic structure is not compact and could gradually evolve into the stable hcp structure at higher temperature.

The magnetic properties of Co-NPs were measured by SQUID. The magnetization curves confirmed that the NPs were as expected, not oxidized and superparamagnetic at room temperature. Their size estimated by a Langevin fit matched well with that measured in the TEM.

The blocking temperature was also measured by the FC-ZFC technique. This temperature was 7 K for Co-NPs synthesized in  $C_1C_4ImNTf_2$ , while it reached 160 K in the case of  $C_1C_{14}ImNTf_2$ . This difference was attributed to an anisotropy difference which probably originated from a dipole coupling of the NPs. However, this interpretation leads to the conclusion that this coupling was more pronounced in  $C_1C_{14}ImNTf_2$ , which is surprising because in this LI, Co-NPs were more distant from each other.

Finally, a new synthetic approach for Co-NPs was investigated, in which  $H_2$  was replaced by a solute reducing agent,  $(C_2H_5)_3SiH$ . This new method also made it possible to obtain small and monodisperse Co-NPs, whose structural and magnetic characterization is in progress.

## **Chapter II-A.**

---

### **State of the art:**

**Chemical synthesis and structural control  
of cobalt based bimetallic nanoparticles  
in different media.**





## II-A. I. General concepts of bimetallic nanostructures

Nanoscale systems and the size-dependent properties of materials have been of a great interest and opened up a lot of opportunities in the last few decades. The nanoparticles (NPs) have been at the core of these studies and it has been presented in details in the previous chapter.

Metallic nanoalloys offer a new dimension to this field, combining these nanoscale effects with the adaptability of metallic alloys. Hence, the variety of compositions and structures (size, morphology, atomic arrangement) bring a vast range of possibilities. Their complexity, however, requires a multidisciplinary approach to characterize and to study them.<sup>29</sup>

Most of the synthetic methods for monometallic NPs can be expanded to two metal systems. However, when NPs are produced using two different metals, there are several ways in which the metals can mix, and these processes, as well as the homogeneity and compatibility of the metals, have a great influence on the final outcome.<sup>29</sup> The four main types of possible structures are: core-shell alloys (in which one metal forms the core and the other metal forms a shell around this core, Figure 39-a), subcluster-segregated alloys (each metal forms its own subcluster and these share a mixed interface of some sort, also known as Janus-type alloys, Figure 39-b), mixed nanoalloys (either in an ordered manner or a fully random solid solution way, Figure 39-c), and multishell nano-alloys (onion-like or layered structure, similar to the core-shell but with multiple shells, Figure 39-d).<sup>109</sup>

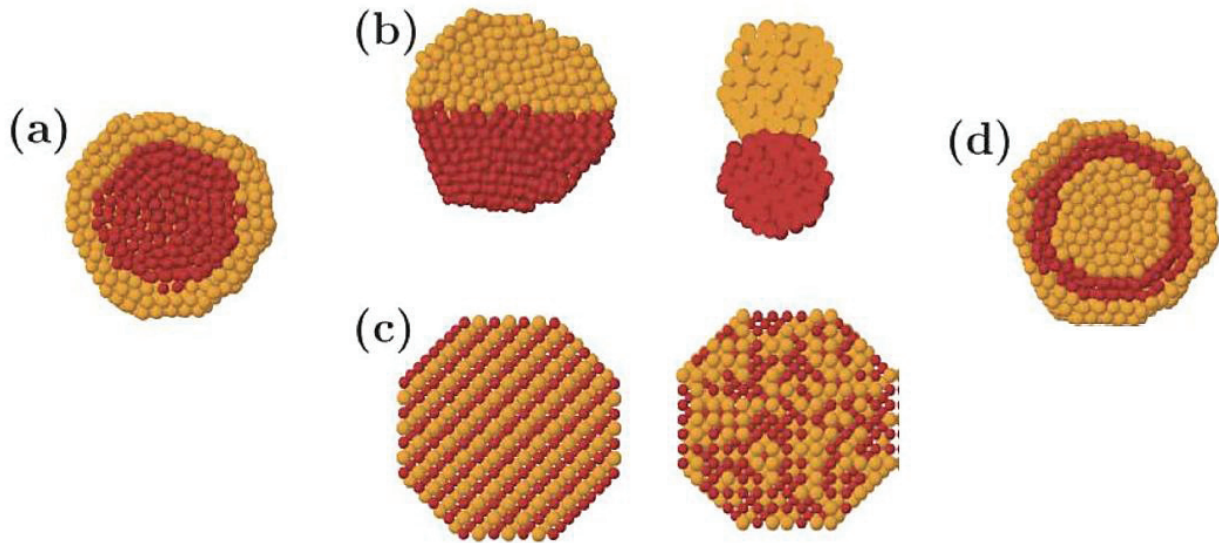


Figure 39 : The main types of alloying in nanoparticles; a) core-shell particles, b) subcluster-segregated alloys, c) mixed alloys (ordered or disordered), and d) multi-shell configuration.<sup>109</sup>

Due to the small size of nanoclusters, the arrangement of the atoms can also deviate from the conventional crystalline close-packed type structures and take on icosahedral, decahedral or tetrahedral based structures.

#### i. Structure determining factors

Several factors influence the final structure of the NPs:

- Relative bond strengths: Stronger heteronuclear bonds favor mixing while stronger homonuclear bonds favor segregation.
- Surface energies of elements: The element with the lower surface energy tends to occupy the surface.
- Relative atomic size: As the core is more sterically confined, smaller atom tend to occupy those positions.
- Charge transfer: Difference in electronegativity tends to favor electron transfer and mixing.
- Strength of binding to surfactants: The metal that interacts more strongly to the surfactants can be pulled out to the surface.
- In some cases some specific electronic or magnetic properties might also affect.<sup>109</sup>

The composition of the alloy can also influence the overall crystal structure.<sup>110</sup> Predicting the final structure of a nanoalloy can be very complicated. Despite the fact that the kinetic mixing process is frequently significantly faster at the nanoscale than in the bulk (and even faster in smaller NPs), the energetic landscape of bimetallic NPs is generally highly complicated. As a consequence, it can take these bimetallic NPs longer to reach equilibrium than it does for monometallic clusters. Furthermore, kinetic trapping effects have been identified to have strong effects on nanoalloy formation.<sup>109</sup>

Kinetics of nucleation can also play a very strong role in the formation and thus final structure of bimetallic NPs. In cases where organometallic salts or complexes are used as precursors, they must be reduced or decomposed to yield zero-valent metal nuclei. In case there is a significant difference in the rate of decomposition, an initial nucleus of the fast decomposing metal will be first formed, followed by growth of the slow-decomposing metal, leading to a core-shell structure. As less energy is required for heterogeneous nucleation than homogeneous nucleation, this growth is always favored over separate nucleation.<sup>111</sup> The difference in rate of decomposition can be used to design the composition of the bimetallic NPs based on the kinetics of the reaction and it is even possible to adjust the parameters of the reaction to yield metastable NPs, i.e. a core@shell structure that is the inverse of the thermodynamically stable one (see Figure 42 on p. 66).<sup>112, 113</sup>

Another potentially important parameter for the structure of NPs is the speed of the mixing process. This has been shown with in situ TEM studies of copper atom dissolution into gold clusters at the nanoscale.<sup>114, 115, 116</sup> It was found that at room temperature, Cu diffused into 4 nm Au clusters in rapid spontaneous mixing at a rate, 9 orders of magnitude larger than for the bulk material, forming a solid solution well below the bulk order-disorder temperature. By significantly lowering the temperature, diffusion was halted to form a two-phase structure with an Au core and a shell of Au-Cu solid solution. For larger particles, however, less mixing was found, i.e., with 10 nm clusters, Cu only diffused into the surface of the particle and at a size of 30 nm no dissolution was observed. This shows the importance of the low-temperature surface melting even if it is the negative heat of solution that acts as a driving force for this diffusion process. This type of rapid spontaneous mixing has also been observed in other systems; e.g., Au-Ni, Au-Zn, Au-Al, Au-Sn, and In-Sb.

Such an intermixing can also take place on boundaries of segregated nanoalloys. It has been found for a system of Au@Ag core-shell NPs that size dependent spontaneous interdiffusion takes place on the core-shell boundary in very small NPs (down to 2.5 nm). This was attributed to vacancy defects on the boundary, the number of which increases with decreasing particle size.<sup>109</sup>

## II-A. II. Co-based nanoparticles of particular interests

### i. Co-Pt NPs

To date, Pt-Co bimetallic nanoparticles with various structures and morphologies have been experimentally synthesized by chemical and physical approaches.<sup>17, 18, 117, 118, 119, 120, 121</sup> According to the atomic distributions of elements, these nanoparticles may be classified as chemically disordered alloys (solid solution), ordered intermetallics, and core-shell structures, (Figure 40), depending on the preparation strategy and route.

Numerous researchers have reported that Pt-Co (typical Pt<sub>3</sub>Co, PtCo, and PtCo<sub>3</sub>) alloy nanoparticles were chemically disordered, and most of them were coated by Pt-skin surface layer due to the thermally activated preferential surface segregation of Pt or preferential dissolution of the non-noble component during catalyst processing and operation of the fuel cell.<sup>14, 15, 16, 17, 18</sup> These nanoparticles all possess face-centered cubic (fcc) crystal phases with a concomitant lattice contraction for Pt due to the incorporation of Co atoms.

Meanwhile, structurally ordered intermetallic Pt-Co bimetallic nanoparticles have also been reported.<sup>17, 122, 123</sup> For example, ordered Pt<sub>3</sub>Co intermetallic cores (*L1<sub>2</sub>* structure, Figure 40), covered by a 2-3 atomic-layer thick Pt shell, exhibited over 200% increase in mass activity and over 300% increase in specific activity as compared with disordered Pt<sub>3</sub>Co alloy nanoparticles and the Pt/C catalysts.<sup>17</sup> Besides, the ordered Pt-Co intermetallic nanoparticles (*L1<sub>0</sub>* structure, Figure 40) have also been prepared experimentally.<sup>122, 123</sup> They exhibited a large coercivity owing to the rotation magnetization. The ordered Pt-Co intermetallic nanoalloy is an excellent system because it has both an excellent chemical stability, a high magnetocrystalline anisotropy and large coercivity resulting from the long-range order in these nanoparticles. This makes them one of the important candidates for future high-density magnetic storage media owing mainly to the existence of ordered intermetallic phases with exceptionally hard magnetic properties. The ordered Co-Pt nanoparticles have a large

magnetic anisotropy of about  $4.9 \times 10^7 \text{ erg.cm}^{-3}$ ,<sup>12, 13</sup> which makes it a potentially interesting material from a commercial point of view. From the practical application points of view, the magnetic data storage requires:

- (i) Small particle size with tight size distribution.
- (ii) *fcc* phase with high magnetocrystalline anisotropy and preferred (001) oriented crystal to overcome the superparamagnetism.
- (iii) Well-separated nanoparticles for reduced exchange coupling effects.

Hence these are three key challenges for practical data storage applications of  $L1_0$  phase Co-Pt nanoparticles nowadays.

Apart from the aforementioned two types of bimetallic nanoparticles, another type which has been successfully synthesized is the Co-core@Pt-shell (Co@Pt) structure.<sup>121, 124, 125, 126</sup> The electrochemical tests showed that the core-shell nanoparticles exhibit superior activity and durability for methanol oxidation than Pt-alloy catalysts.<sup>121, 126</sup>

In addition, the stable existence of the ordered intermetallics and core-shell structures has also been theoretically confirmed.<sup>127, 128, 129</sup>

As stated above, Pt-Co bimetallic nanoparticles present diverse structures and morphologies including disordered alloy, ordered intermetallics, and core@shell structures. Therefore, they could exhibit catalytic, electrical, magnetic, and optical properties remarkably different from those of their monometallic counterparts and that's why it is so important to be able to synthesize them in a very controlled manner and to be able to fully identify their structural and physical properties.

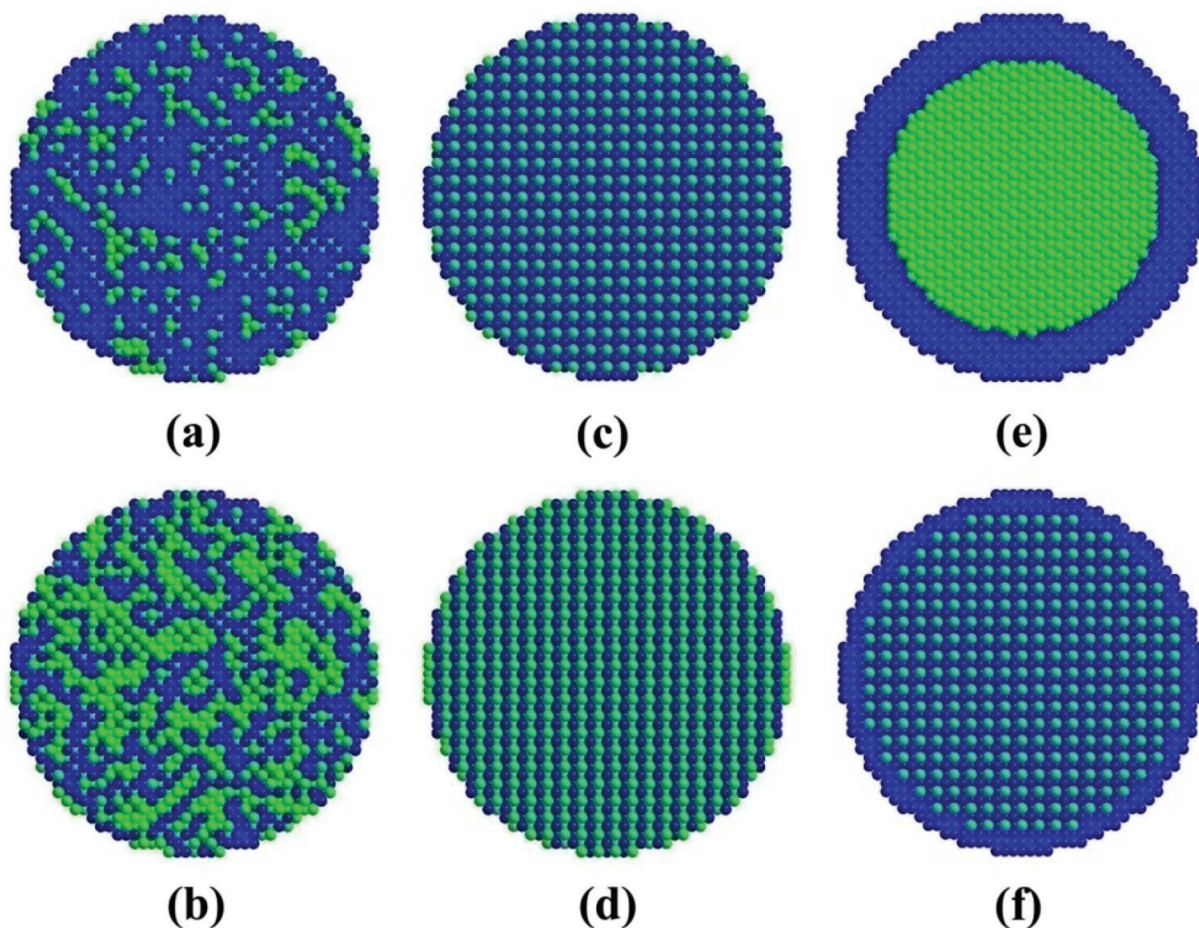


Figure 40 : Schematic illustration of Pt-Co bimetallic NPs: (a) disordered Pt<sub>3</sub>Co alloy, (b) disordered PtCo alloy, (c) ordered Pt<sub>3</sub>Co *L*<sub>12</sub> intermetallics, (d) ordered PtCo *L*<sub>10</sub> intermetallics, (e) Co@Pt core@shell structure, and (f) Pt<sub>3</sub>Co@Pt core@shell structure. Coloring denotes the type of atom: blue, Pt atom; bright green, Co atom (reproduced from ref. <sup>117</sup>).

One important notice for all these structurally controlled bimetallic NPs is that they were prepared either physically, <sup>12, 13, 117, 118, 122</sup> or chemically, applying either a polyol reduction technique, <sup>15, 17, 119, 120</sup> transmetalation reaction, <sup>14, 125</sup> or through the reduction of the corresponding metal salts with a strong reducing agent like NaBH<sub>4</sub>.<sup>16, 123, 124</sup>

Physical methods give an accurate access to the ordered intermetallic structures together with possible localization arrangement of the NPs on a solid support if it is combined with lithography techniques (which is required for memory storage applications).<sup>130</sup> On the other hand, the advantages of these techniques are always limited by the high costs and the needs of sophisticated equipments. They also miss the good control on NPs sizes below 10 nm. Chemical techniques are usually more cost effective and show better size control. Except for Dupont's work,<sup>60</sup> the organometallic approach was not much considered in the literature for

the synthesis of Co-Pt NPs and that's why it will be considered with more details in this chapter.

## ii. Co-Ru NPs

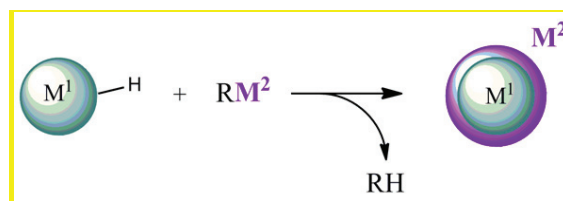
Another interesting class of Co-based bimetallic NPs is the Co-Ru NPs. Such bimetallic NPs find applications as catalysts for many reactions such as Fischer-Tropsch CO hydrogenation reaction,<sup>19</sup> nitroarene reduction reactions<sup>20</sup> and as an electrocatalysts for oxygen reduction in fuel cells.<sup>21</sup> For all these examples, mixing Ru with Co improved the catalyst performance. For example, in case of the Fischer-Tropsch reaction, the addition of small amounts of ruthenium to the standard  $\gamma$ -Al<sub>2</sub>O<sub>3</sub>-supported cobalt catalysts was advantageous in facilitating and improving the reduction of the cobalt. The amount of metal atoms exposed on the surface determined by H<sub>2</sub> chemisorption was also found to increase by a factor of 3 upon adding Ru which resulted in an equivalent increase in the rate of CO hydrogenation.

It should be mentioned that in all these examples, the Co-Ru NPs were supported or impregnated in a solid support such as zeolite,  $\gamma$ -Al<sub>2</sub>O<sub>3</sub> or activated carbon. To our knowledge, there was no mention of the use of a stable unsupported Co-Ru bimetallic suspension for catalysis applications. This is probably because of the ease of recycling such supported catalysts as compared to unsupported NPs. For that reason, Co@Ru core@shell NPs with a magnetic Co core and catalytic Ru shell could be, if it is experimentally accessible, an interesting structure to be studied as a possible recyclable catalyst that has not yet been reported in the literature.

As for Co-Pt NPs, the organometallic approach for the synthesis of Co-Ru NPs was not discussed in details in the literature. The concepts and advantages of this technique is going to be discussed in the following section.

In order to access such NPs, it is very important to have naked metal NPs with possible hydride formation on its surface. Such structures could catalyze the addition of a shell of the second metal (Scheme 5).<sup>131</sup>





Scheme 5 : Mechanism of formation of bimetallic nanoparticles through the reaction of a second metal precursor with  $[M]_s-H$ .

Thus, bimetallic NPs should be easily accessible in ILs as they afford metal NPs with naked surface. That was already achieved for Ru@Cu system as will be discussed later on.<sup>27</sup>

### II-A. III. Synthesis of bimetallic nanoparticles through the organometallic approach

As discussed earlier, bimetallic NPs can possess different structures showing different physical and chemical properties. This raises the challenge of controlling the chemical order of these NPs during their synthesis. Organometallic chemistry can afford some pathways to well control the chemical structure of these NPs.<sup>22</sup> The first approach, which is well represented in the literature, is the two-step “core then shell” synthesis.<sup>132</sup> This method is very practical. It includes the generation of well-defined NPs that will serve as seeds for the growth of a shell of another metal. It is even possible to successively decompose 2 metal precursors mixed in the same solution into core-shell structured NPs on the basis of a large difference in their kinetics of decomposition. For example, Rh@Fe NPs were obtained upon hydrogenation of a mixture of  $\{Fe[N(SiMe_3)_2]_2\}_2$  and  $[Rh(C_3H_5)_3]$ .<sup>113</sup> This is because the Rh precursor has faster decomposition kinetics than the Fe one under such conditions. On the contrary, using amine-borane as reducing agent can reverse the decomposition kinetics and thus reverse the chemical order into Fe@Rh NPs.<sup>112</sup> Such a kinetically controlled core-shell formation is very useful in case a passivating layer was needed to protect easily oxidized NPs. It also gives access to metastable core-shell structures that exhibit new properties. Similar results were also achieved for Ni@Pd NPs,<sup>133</sup> Cu@Ni and Ni@Cu NPs through typical organometallic approach.<sup>134</sup> In some cases, it could also give access to hollow metal capsules as well.<sup>135</sup> When the core consists of an easily oxidizing 3d metal, the second metal precursor could be able to oxidize the core during the second reaction step (transmetalization). Therefore, the use of a zero valent precursor is recommended in that case to minimize the transmetalization effect.

The second approach, on the other hand, takes advantage of this transmetallization process between large, first formed metallic cores (e.g. Co, Fe) and a noble metal precursor. As the redox process occurs, the size of the core decreases while the shell grows around it.<sup>136</sup> This approach is rather difficult to control and may lead to complete corrosion of the initial metallic core and formation of hollow metal spheres.<sup>137</sup>

An example is the synthesis of bimetallic FeBi nanospheres.<sup>138</sup> Even if these metals are immiscible in the bulk state and possess very different structural properties, the decomposition of their metallic precursors under amine-borane and H<sub>2</sub> leads to the formation of core-shell nanospheres in a Bi core and Fe shell. Such a thermodynamically and kinetically unexpected chemical order is the result of a transmetallation process that occurs at the very first stages of the synthesis and favors the formation of a metastable intermediate Fe-Bi amorphous alloy. The deposition of the remaining iron on the surface of the preformed Fe-Bi alloy is thus promoted leading to the formation of FeBi core-shell nanohybrids (Figure 41).

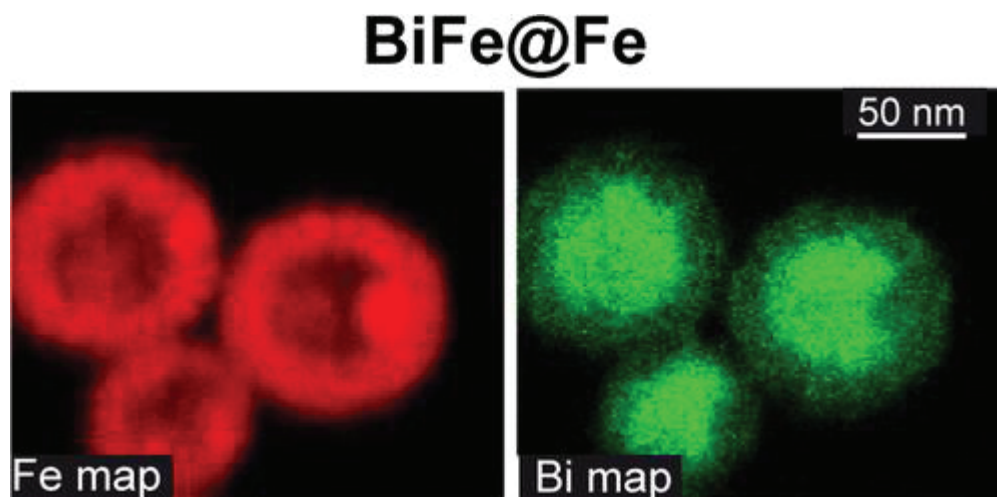


Figure 41 : Local elemental mapping of Fe-Bi nanospheres giving evidence for an iron-rich shell and a concentration of Bi atoms in the core region.<sup>138</sup>

Similarly, Rh@Fe<sup>76</sup> core@shell NPs were obtained upon hydrogenation of a mixture of [Fe[N(SiMe<sub>3</sub>)<sub>2</sub>]<sub>2</sub>]<sub>2</sub> and [Rh(C<sub>3</sub>H<sub>5</sub>)<sub>3</sub>]. In these conditions, Rh atoms are produced faster than the Fe ones. On the contrary, when an amine-borane is used as reducing agent, reversed kinetics of the decomposition and thus a reverse chemical order Fe@Rh are obtained (Figure 42).<sup>22</sup>

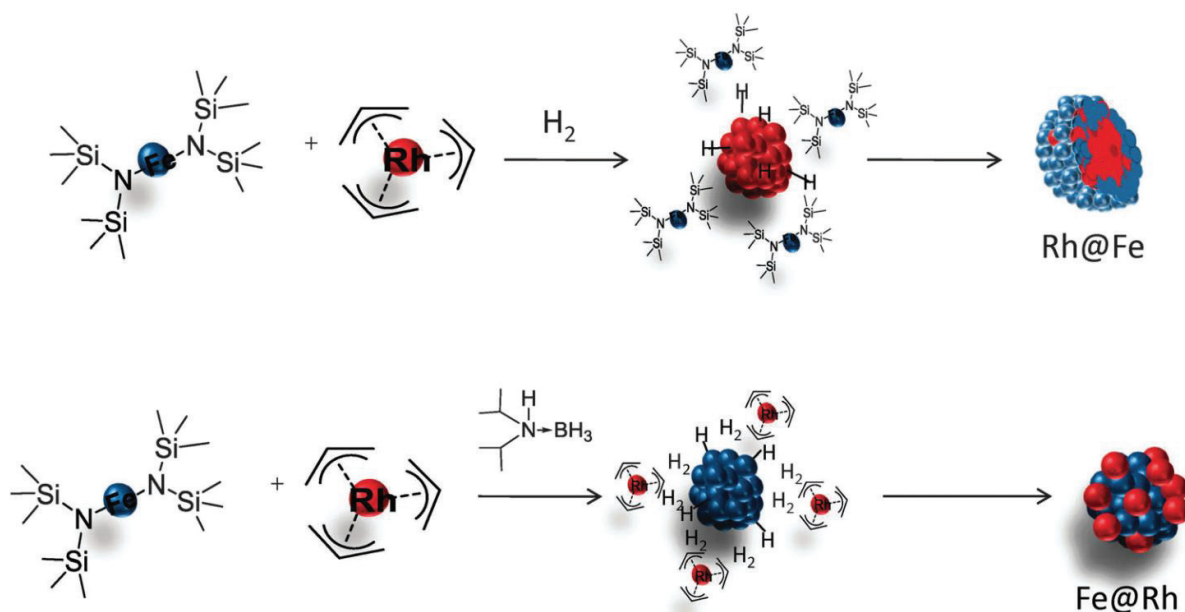


Figure 42 : Kinetics control of the chemical ordering in FeRh NPS (reproduced from ref.<sup>22</sup>).

Another example of the effect of the decomposition kinetics on the chemical order, is the controlled synthesis of RuPt nanosystems. When the 2 metal precursors, [Ru(COD)(COT)] and [Pt(dba)<sub>2</sub>], were simultaneously decomposed in the presence of polyvinylpyrrolidone as a stabilizer, RuPt nano-alloys with a fcc structure were obtained.<sup>139</sup> Upon changing the Pt precursor with [Pt(CH<sub>3</sub>)<sub>2</sub>(COD)], which exhibits a lower decomposition rate, it was possible to tune the chemical order and to achieve a core-shell structured RuPt NPs. This chemical ordering into core-shell RuPt NPs is the result of the decomposition kinetics, thermodynamics, and from the steric properties of the stabilizer as well (PVP has little or no chemical interaction with those metals).

In addition to the difference in kinetics of decomposition of the precursors, surface chemistry plays an important role in the final chemical ordering of the NPs.<sup>140</sup> Therefore, molecular chemistry can be a powerful tool to engineer the synthesis of complex nano-systems.

In this context, the electronic properties of the stabilizing ligand has been found to affect the size and chemical composition of RuPt NPs.<sup>141</sup> With the same metal precursors and reaction conditions as in the previous example, a strongly coordinating ligand (diphenylphosphinobutane) was used instead of the neutral sterically stabilizing agent (PVP). In that case, NPs with a ruthenium rich core and a disordered shell containing both ruthenium

and platinum were obtained (Figure 43). The complexity observed in the composition of these NPs arises from the high chemical affinity of the diphosphine ligand for both metals. This work proves how a simple ligand such as a diphosphine can cause a significant change in the chemical ordering in the formed NPs. Therefore, suitable selections of the metal precursor and of the stabilizer together with the choice of the decomposing agent are all necessary to well control the chemical order of bimetallic NPs.

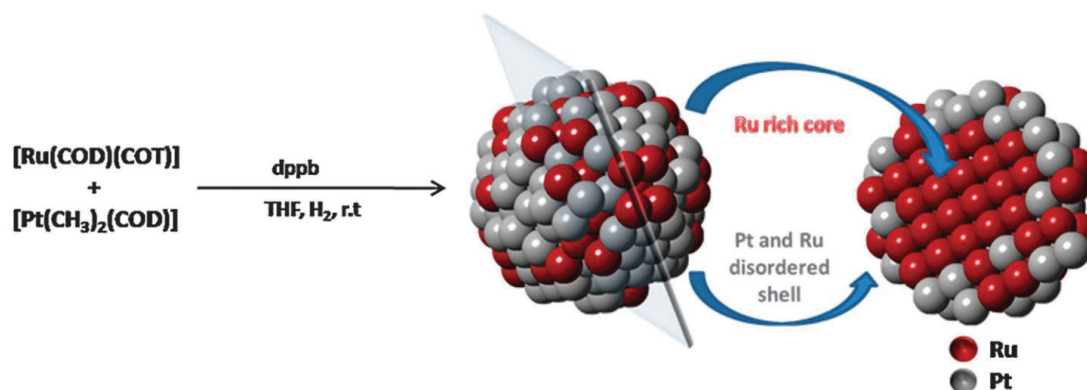


Figure 43 : Schematic representation of RuPt NPs synthesized from  $[\text{Ru}(\text{COD})(\text{COT})]$  and  $[\text{Pt}(\text{CH}_3)_2(\text{COD})]$  (reproduced from ref. <sup>141</sup>).

## II-A. IV. Bimetallic nanoparticles in ionic liquids

Despite the fact that the synthesis of bimetallic NPs in ionic liquids is not yet fully developed, some research has been already published for the synthesis of CoPt and CuRu NPs in IL using an organometallic approach.<sup>27, 60, 142</sup> Other results for RuTa, RuPt, CuNi and CuMn NPs from our lab are also very promising, not yet published and it is going to be introduced in this part as well.

### i. CoPt NPs

These NPs were prepared through a one-pot synthesis approach based on the spontaneous decomposition of [bis(cyclopentadienyl)cobalt(II)] and [tris(dibenzylideneacetone)-bisplatinum(0)] complexes in 1-n-butyl-3-methylimidazolium hexafluorophosphate at 150°C under hydrogen (10 bar) for 24 h.<sup>60</sup> The obtained bimetallic NPs were found to be small (4.4 nm), homogeneous in size ( $\pm 1.9$  nm) and well stabilized by the IL (Figure 44).

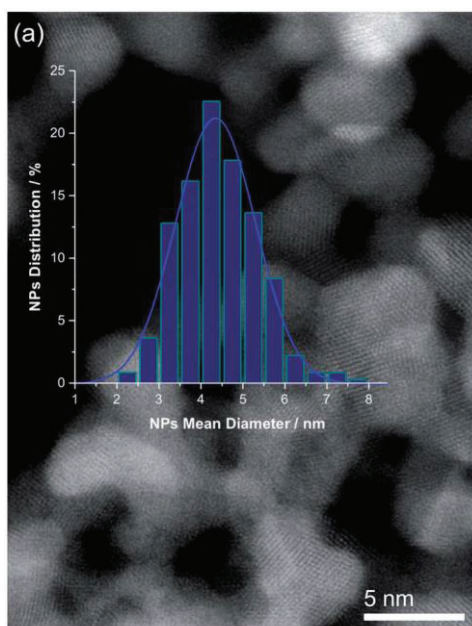


Figure 44 : HAADF-STEM image of a set of Co/Pt nanoparticles and the particle size distribution histogram.<sup>60</sup>

They possessed a core-shell like structures in which Pt was the main shell component and Pt concentration decreased in the inner-shells (CoPt<sub>3</sub>@Pt-like structure). The face-centered cubic crystal structure was confirmed by XRD (Figure 45). The five diffraction peaks matched with those of pure Pt metal with fcc structure, corresponding to the (111), (200), (220), (311) and (222) planes. The peak positions were shifted to higher angles, relative to Pt, which indicates that Co was incorporated into the Pt fcc structure to form an alloy phase with a concomitant lattice contraction (0.38%). The XRD pattern possessed also (100) and (110) peaks characteristic of an ordered, intermetallic CoPt<sub>3</sub>@Pt-like structure.

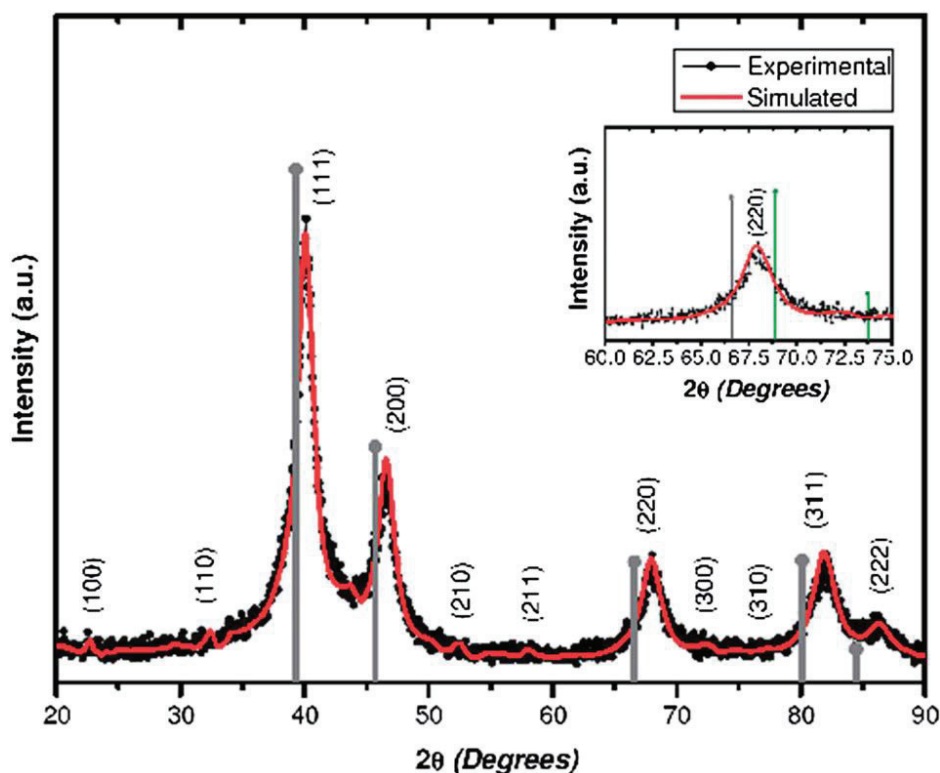


Figure 45 : XRD analysis of the bimetallic CoPt-NPs prepared in  $C_1C_4Im PF_6$  compared with bulk fcc Pt (gray lines). Inset: 220 reflections of bulk fcc Pt (gray line),  $CoPt_3@Pt$  like and  $CoPt_3$  (green line) structures (reproduced from ref. <sup>60</sup>).

## ii. RuCu NPs

Similar to CoPt NPs,<sup>60</sup> RuCo-NPs were successfully synthesized through the simultaneous decomposition of 2 metal precursors in an imidazolium based IL.<sup>27</sup> A solution of 0.05 mol/L Ru(COD)(COT) in  $C_1C_4ImNTf_2$  was mixed with an equimolar solution of mesitylcopper(I) (CuMes) and allowed to decompose under  $H_2$  at 100°C. Surprisingly, the obtained bimetallic NPs were smaller than that of the monometallic Ru and Cu NPs prepared under the same conditions but using single OM (2.5, 4.4, 5.1 nm respectively). The size of NPs was also found to be tuned upon changing the ratio of the 2 OM precursors while keeping the total concentration constant (Figure 46). These CuRu NP suspensions have been characterized by Anomalous Small-Angle X-ray Scattering (ASAXS) on the CRG-BM02 beam line at the European Synchrotron Radiation Facilities (ESRF), at energies slightly below the Ru K-edge (22.117 keV).

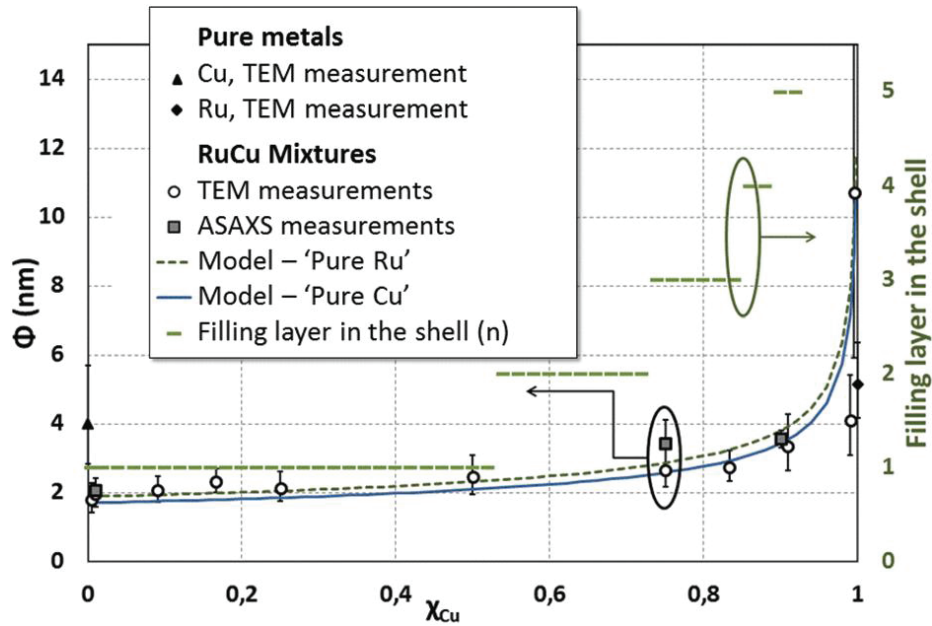


Figure 46 : Diameter evolution of the RuCuNPs with Cu content as measured by TEM and ASAXS, and comparison with the model developed in the present work (with 147 atoms in the core).<sup>27</sup>

Three suspensions with atomic fractions of Cu,  $\chi_{Cu}$ , equal to 0.1, 0.75 and 0.9 as well as the pure IL were measured at four energies, respectively 21.6, 21.94, 22.06 and 22.1 keV. Figure 47 shows the radial intensities measured for two capillaries containing pure ILs and NPs dispersed in IL ( $\chi_{Cu} = 0.9$ ).

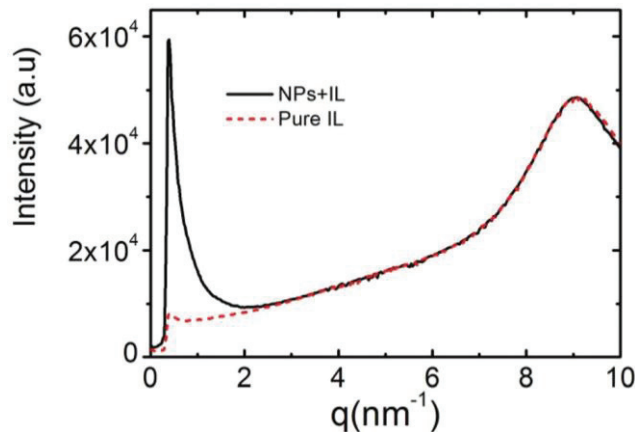


Figure 47 : Radial SAXS intensities as a function of the scattering vector,  $q$ , measured for the sample with  $\chi_{Cu} = 0.9$  (black curve) and pure IL (red dashed curve) ( $E = 22.1$  keV).

It appears clearly that below  $3 \text{ nm}^{-1}$  the intensity was dominated by the contribution of NPs whereas beyond this value the structure factor of IL was dominant with a first peak around  $9 \text{ nm}^{-1}$ . The intrinsic scattering intensities of NPs,  $I_{NP}(q)$ , were deduced from the total intensity,  $I_{IL+NP}$ , and the intensity of liquid,  $I_{IL}$ , corrected for sample transmission and

monitoring (Figure 48.a). The decrease of  $I_{NP}(q)$  with  $q$  was much faster for the Cu-rich NPs, as expected from the increase in size observed by TEM. The peak around  $0.4 \text{ nm}^{-1}$ , which for  $\chi_{Cu} = 0.1$  was well separated from the slower decrease starting from  $0.8 \text{ nm}^{-1}$ , was attributed to larger particles, likely agglomerates. The variation of  $I_{NP}(q)$  with the photon energy is shown in Figure 48.b for  $\chi_{Cu} = 0.1$ . The decrease of  $I_{NP}(q)$  when approaching the Ru K-edge results from the decrease of the form factor of the Ru atom,  $f_{Ru}$ ; namely,  $f_{Ru}$  decreases from 40.7 to 37.4 by changing  $E$  from 21.6 to 22.1 keV, while the form factor of Cu,  $f_{Cu}$  remains around 29.2.

For bimetallic NPs,  $I_{NP}(q, E)$  can be written as a function of the three partial structure factors,  $S_{ij}$  as follows:

$$I_{NP}(q, E) = \rho_{Ru}\rho_{Ru}(E)S_{RuRu}(q) + (\rho_{Ru}(E)\rho_{Cu} + \rho_{Ru}(E)\rho_{Cu})S_{RuCu}(q) + \rho_{Cu}\rho_{Cu}S_{CuCu}(q)$$

Where  $\rho_{Ru}$  and  $\rho_{Cu}$  are the electronic densities.<sup>143</sup> Therefore, the differential intensity,  $\Delta I_{NP}(q) = I_{NP}(q, E_1) - I_{NP}(q, E_2)$ , is only dependent on  $S_{RuRu}(q)$  and  $S_{RuCu}(q)$  and its behavior with  $q$  provides interesting information.<sup>143</sup>

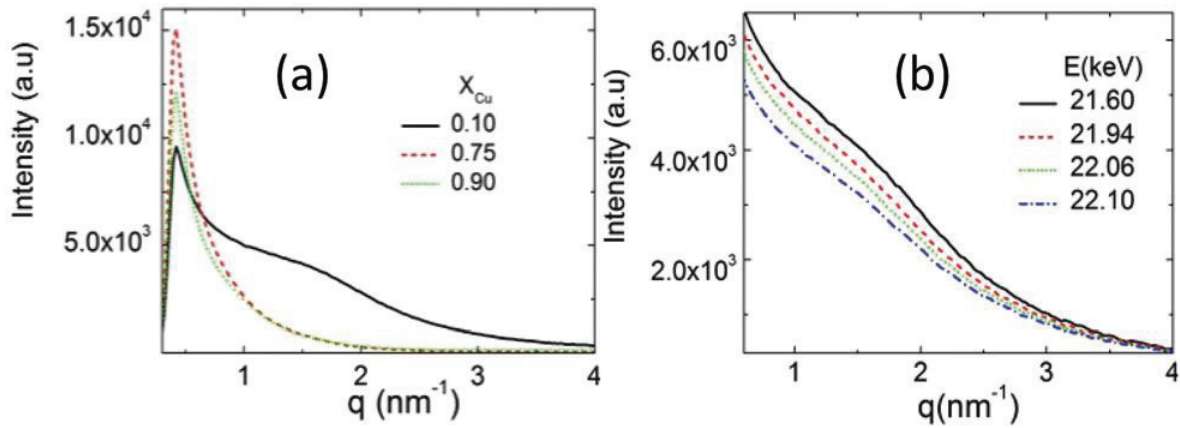


Figure 48 : (a) Change of the intrinsic scattering intensity of NPs,  $I_{NP}(q)$ , with the Cu atomic fraction at 22.10 keV. (b) Variation of  $I_{NP}(q)$  with the photon energy ( $\chi_{Cu} = 0.1$ ).

Figure 49 (a–c) show the total intensities  $I_{NP}(q)$  measured at 22.1 keV for the three Cu atomic fractions together with their corresponding differential intensities calculated between 21.6 and 22.1 keV after rescaling. It is striking that for  $\chi_{Cu} = 0.1$ ,  $I_{NP}(q)$  and  $\Delta I_{NP}(q)$  behave similarly, while for the two Cu-rich samples, the decrease of  $\Delta I_{NP}(q)$  with  $q$  is much slower than the corresponding total intensities. This feature strongly suggests that Ru and Cu atoms



in the nanoparticles are not randomly distributed. More precisely, the slower decrease of  $\Delta I_{NP}(q)$  with  $q$  indicates that the Ru atoms are distributed in smaller volumes in agreement with a core-shell morphology where Ru and Cu atoms would occupy preferably the core and the shell of NPs, respectively. Furthermore, the three  $\Delta I_{NP}(q)$  are really similar in the  $q$ -range  $[0.8-2 \text{ nm}^{-1}]$ , indicating a Ru core diameter almost identical in the three differently Cu enriched nanoparticles (Figure 49-d).

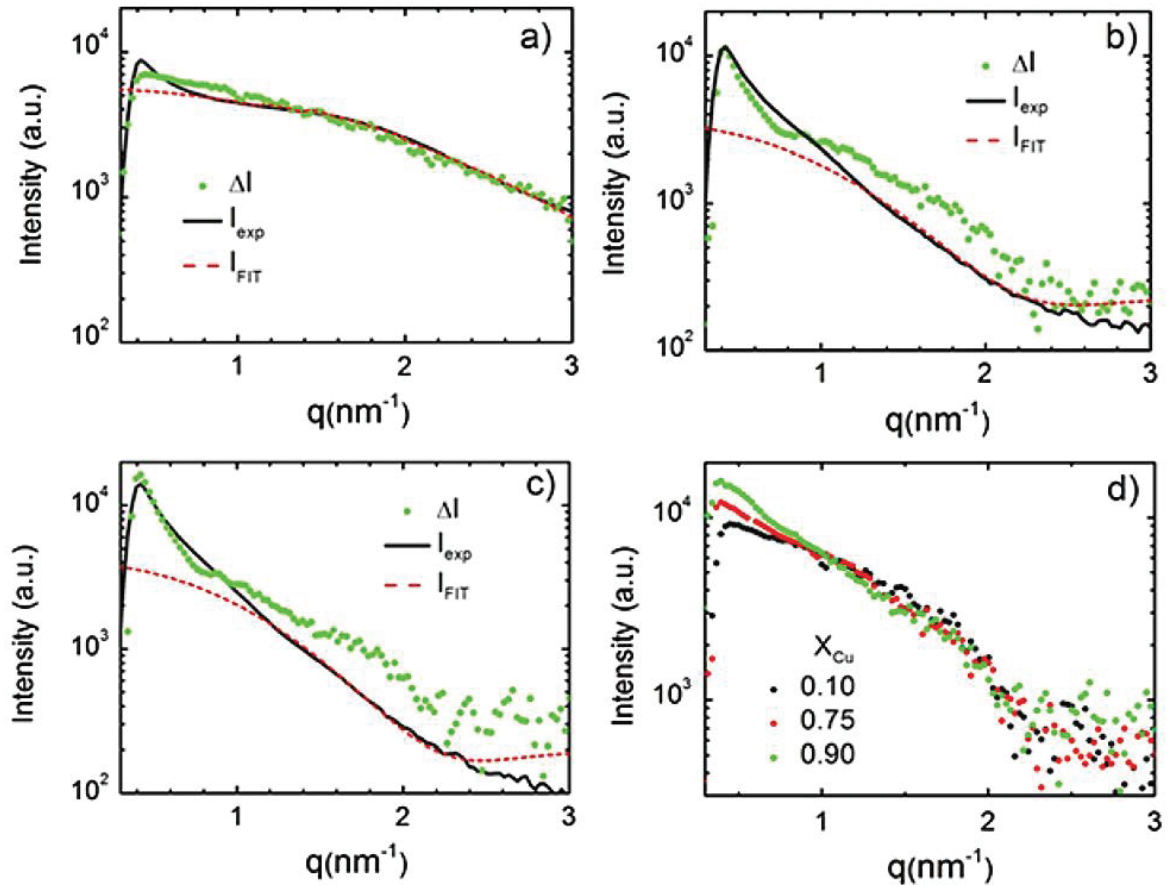


Figure 49 : Experimental (black solid line) and simulated (red dashed line) intensities obtained at 22.10 keV for (a)  $\chi_{Cu} = 0.1$ , (b)  $\chi_{Cu} = 0.75$  and (c)  $\chi_{Cu} = 0.9$ ; the green points are the differential intensities,  $I_{NP}(21.6 \text{ keV}) - I_{NP}(22.1 \text{ keV})$ , after rescaling with respect to  $I_{NP}(q)$ . (d) Comparison of the differential intensities obtained for the three compositions.

Based on such features, simulations of the intrinsic NPs intensities was done allowing the determination of the diameter of the Ru core and the thickness of the Cu shell. A value of 1.9 nm for the Ru core diameter was extracted, i.e. very close to the TEM value (see Table 7). Above  $0.8 \text{ nm}^{-1}$ , the corresponding simulated curve is in good agreement with the experimental one (Figure 49-a), since as already mentioned, below  $0.8 \text{ nm}^{-1}$  the strong increase of  $I_{NP}(q)$  towards the smaller  $q$ -values comes from larger clusters.

Table 7 : Geometrical parameters of the RuCu nanoparticles deduced from the ASAXS and TEM measurements for the three compositions.  $\Phi_{core}$  is the Ru core diameter,  $t_{shell}$  the Cu shell thickness,  $\Phi$  the resulting total diameter of NPs and their concentration in the IL deduced from both ASAXS and TEM.

$\chi_{Cu}$	ASAXS				TEM
	$\Phi$ (nm)	$\Phi_{core}$ (nm)	$t_{shell}$ (nm)	NPs concentration (NPs L <sup>-1</sup> )	$\Phi$ (nm)
0.10	$2.06 \pm 0.07$	1.9	—	$(1.1 \pm 0.3)10^{20}$	$2.0 \pm 0.4$
0.75	$3.4 \pm 0.7$	1.9	0.7	$(1.0 \pm 0.3)10^{19}$	$2.7 \pm 0.6$
0.90	$3.6 \pm 0.3$	1.9	0.79	$(2.0 \pm 0.3)10^{19}$	$3.4 \pm 0.8$

For the two other compositions, simulations were done keeping fixed the Ru core diameter at 1.9 nm and its Gaussian distribution at 0.4 nm leading to a reliable determination of the shell thicknesses. All the parameters are given in Table 7 and compared to the TEM values. For  $\chi_{Cu} = 0.1$  and 0.9, the agreement is relatively good, while for  $\chi_{Cu} = 0.75$  the total diameter of NPs deduced from ASAXS equal to  $3.4 \pm 0.7$  nm is larger, but still consistent with the value of  $2.7 \pm 0.6$  nm deduced by TEM. For this sample, the more pronounced agglomeration of NPs is probably responsible for the larger experimental error on the diameter measured by ASAXS.

From the transmission measurements and the values of the Ru core diameter and Cu shell thickness extracted from ASAXS, the concentrations of NPs in the IL could be deduced assuming that the atomic number densities of Ru and Cu in the core-shell particles are the ones of the pure metals and the molar density of IL remains unchanged in the presence of NPs. Again, for  $\chi_{Cu} = 0.1$  and 0.9, a good agreement between the values deduced from ASAXS and TEM is found. For  $\chi_{Cu} = 0.75$  the smaller density extracted from ASAXS could again be attributed to the more pronounced agglomeration of NPs.

As a conclusion, it was proved that the NPs adopt a Ru-core, a Cu-shell structure, with a constant Ru core diameter of 1.9 nm for all Ru : Cu compositions, while the Cu shell thickness increases with Cu content up to 0.9 nm. The formation of RuCu NPs thus proceeds through rapid decomposition of the Ru precursor into RuNPs of constant size followed by the reaction of the Cu precursor and agglomeration as a Cu shell explains why the bimetallic NPs possess smaller sizes as compared to the monometallic ones. Thus, as already observed in conventional solvents, the decomposition kinetics of the precursors gives access to core-shell NPs composed of two metals without chemical affinity.

To elucidate the mechanism leading to Cu growth on top of Ru-NPs, the two reactions (formation of Ru nuclei and decomposition of CuMes) were performed separately. In a first experiment, a suspension of 2 nm RuNPs (formed in  $C_1C_4ImNTf_2$  under  $H_2$  at 25 °C) was mixed with a solution of CuMes in the same IL and exposed to  $H_2$  at 100 °C for 4 h. After the reaction, the diameter of the NPs increased from 2.0 to 2.5 nm, with Cu around Ru. A second experiment was conducted using a suspension of Ru-NPs formed under  $D_2$  (instead of  $H_2$ ). In this case, the reaction of CuMes under argon released deuterated mesitylene. Finally, when Cu atoms were directly evaporated into a suspension of Ru-NPs in IL, distinct Cu-NPs were obtained, leaving the Ru-NPs unchanged. All these observations support the reaction of CuMes with [Ru]s-H. This reaction prevents further growth of Ru-NPs, stabilizing smaller NPs, even with a small amount of Cu (Figure 50).

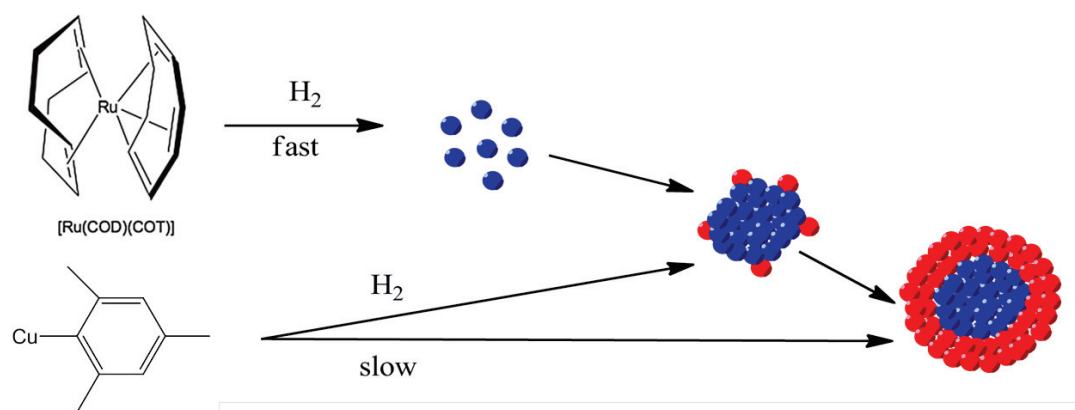


Figure 50 : Proposed mechanism for Ru@Cu NPs formation.

A simple model was devised to predict the size of obtained NPs (assuming a core-shell structure) and to compare it with the experimental one (from SAXS and TEM). In this model, a nested icosahedral structure is assumed for the metallic NPs. These icosahedral arrangements are composed of  $K$  layers of densely packed atoms, contain  $(10K^3 - 15K^2 + 11K - 3)/3$  atoms and their successive layers are formed by  $10K^2 - 20K + 12$  atoms. Each edge contains  $K$  atoms and has a length of approximately  $2Ka_{at}$  (where  $a_{at}$  is the radius of atoms in the icosahedron, with  $a_{Cu} = 0.132$  nm and  $a_{Ru} = 0.146$  nm). Thus the volume of icosahedral clusters is given by:

$$V_{ico} = \frac{5}{12}(3 + \sqrt{5})(2Ka_{at})^3$$

The diameter of spherical NPs can be related to the volume of a specific icosahedral cluster, as follows:

$$\Phi_{ico} = \left( \frac{6V_{ico}}{\pi} \right)^{1/3}$$

The size evolution of bimetallic NPs with composition can thus be modelled assuming that:

1. The Ru precursor is first fully decomposed into Ru cores, whose size is the same for all particles where  $0 < \chi_{Cu} < 1$ .
2. The particles grow by further decomposition of the Cu precursor, the shell being formed layer by layer.

Consequently, the bimetallic NPs are modelled by a core of  $N_{core}$  atoms of Ru ( $K_{core}$  layers), covered by  $n$  layers of Cu ( $n \geq 1$ ). This could be related to the atomic fraction (assuming full decomposition). At this stage, it is important to mention that the diameter values cannot be directly calculated from the previously mentioned equation because Cu atoms are significantly smaller than Ru atoms. Therefore, the diameter of the actual bimetallic NPs lies between two limiting cases:

1. The NPs are composed of a core of  $N_{core}$  Cu atoms, encapsulated with a shell composed of  $N_{shell}$  Cu atoms. This situation underestimates the actual size of the NPs.
2. Conversely, the NPs are composed of a core of  $N_{core}$  Ru atoms, encapsulated with a shell composed of  $N_{shell}$  Ru atoms. This situation overestimates the actual size of the NPs.

The theoretical value of  $\Phi$  were calculated upon the whole composition range for both limiting cases and it was found to be matching well with the experimental results (Figure 46).

## **II-A. V. Generalization to other bimetallic nanoparticles**

Following the previous results with bimetallic Ru-CuNPs from our Laboratory and other bimetallic NPs from Chaudret's group, if two organometallic precursors (OM<sub>1</sub> and OM<sub>2</sub>)

exhibit a different rate of decomposition, this chemical route should afford to size and structure controlled bimetallic  $M_1M_2$ NPs.

This chemical approach was generalized to other bimetallic systems. As Ru(COD)(COT) is easily decomposed, it was mixed with different organometallic precursors of Ni, Ta, Pt, whose decomposition kinetics are slower. Further experiments were also realized with Cu being co-decomposed with Ni, Mn precursors.

#### i. Ruthenium-core based nanoparticles <sup>144</sup>

##### Ruthenium-nickel NPs

Bis(1,5-cyclooctadiene) nickel, Ni(COD)<sub>2</sub> was used as a Ni precursor and 1-hexyl-3-methylimidazolium bis(trifluoromethylsulphonyl)imide, C<sub>1</sub>C<sub>6</sub>ImNTf<sub>2</sub>, as a solvent, due to the low solubility of Ni(COD)<sub>2</sub> in C<sub>1</sub>C<sub>4</sub>ImNTf<sub>2</sub>. Figure 51 shows the size of the obtained NPs as a function of the molar fraction of Ni ( $x_{Ni}$ ) varying from 0.09 to 0.91.

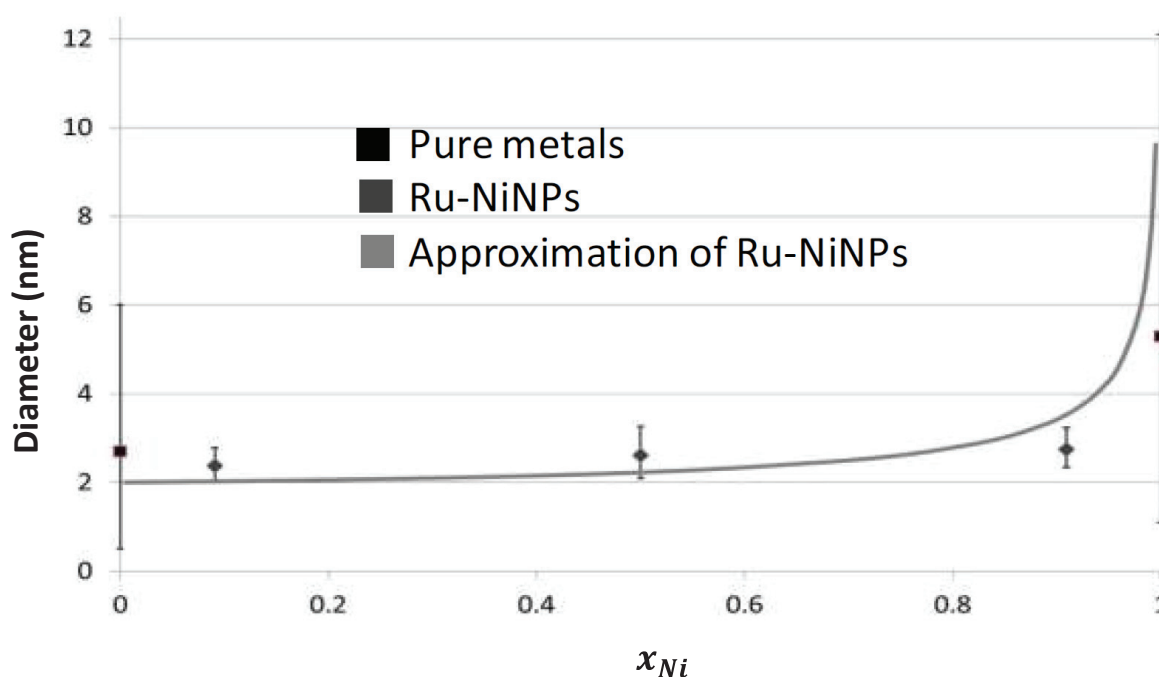


Figure 51 : Size and distribution of RuNi-NPs as a function of the molar fraction of Ni obtained at 100°C under 0.9 MPa of H<sub>2</sub> without stirring during 4 h in C<sub>1</sub>C<sub>6</sub>ImNTf<sub>2</sub>.

Note that in these attempts, the total metal concentration was reduced to  $1.8 \times 10^{-4}$  mol.L<sup>-1</sup>. This low concentration associated to the use of IL C<sub>1</sub>C<sub>6</sub>ImNTf<sub>2</sub> instead of C<sub>1</sub>C<sub>4</sub>ImNTf<sub>2</sub> induces a reduction of the size of Ru-NPs from 4 to 2.7 nm.

### Ruthenium-tantalum and ruthenium-platinum

Some attempts have been performed with tris(neopentyl)neopentylidenetantalum(V) ( $\text{Np}_3\text{Ta}=\text{CHCMe}_3$ ) and (1,5-cyclooctadiene) dimethylplatinum(II) ((COD)PtMe<sub>2</sub>) in  $\text{C}_1\text{C}_4\text{ImNTf}_2$ . Separate decomposition of these two OMs at 100°C under 0.9 MPa H<sub>2</sub> for 4 h affords bulk metal. Surprisingly, a 1:1 molar mixture of Ru(COD)(COT) and (COD)PtMe<sub>2</sub>, or Ru(COD)(COT) and  $\text{Np}_3\text{Ta}=\text{CHCMe}_3$  treated in  $\text{C}_1\text{C}_4\text{ImNTf}_2$  under the same conditions, yielded NPs with a mean size of  $2.6\pm 0.6\text{nm}$  and  $2.4\pm 0.8\text{ nm}$  respectively; compared to Ru-NPs of 4.0 nm.

Then, RuPt-NPs have been also synthesized in two steps. The size obtained of  $3.0\pm 0.7\text{nm}$  is nearly the same than RuPt-NPs formed in one step. As for RuCu-NPs, this proves that the decomposition of (COD)PtMe<sub>2</sub> occurs on the Ru-NPs surface.

To characterize the core-shell structure of RuTa-NPs embedded in  $\text{C}_1\text{C}_6\text{ImNTf}_2$ , anomalous SAXS measurements were performed below the Ru-K edge (22.117 keV) and the Ta-L<sub>III</sub> edge (9.881 keV) on the CRG-BM02 beamline.<sup>145</sup> Bimetallic NPs were prepared by successive decomposition of the precursors: (i) decomposition of the Ru (resp Ta) precursor, (ii) addition of a solution of the Ta (resp Ru) precursor, (iii) decomposition under H<sub>2</sub>. In both cases, the Ru content was 20% of the total metal content. Therefore, these bimetallic NPs are labelled Ru<sub>2</sub>Ta<sub>8</sub> (decomposition of Ru on Ta-NPs) and Ta<sub>8</sub>Ru<sub>2</sub> (decomposition of Ta on Ru-NPs). The ASAXS measurements were done at five energies: at the Ru-K edge (21.6, 21.94, 22.05, 22.09 and 22.106 keV) and the Ta-L<sub>III</sub> edge (9.68, 9.78, 9.844, 9.862 and 9.872 keV). In Figure 52.a, the scattered intensities of only the nanoparticles were obtained by subtracting the IL contribution (black curve) taking into account the transmissions of IL and IL+NPs. The curves obtained for E=21.6 keV reveal a strong increase of the intensity below  $0.4\text{ nm}^{-1}$  for the particles containing Ta. Such effect stems from the agglomeration of nanoparticles and is not taken into consideration in the analysis of the morphology of the bimetallic particles, which relies on the anomalous variation of the scattered intensities with energy. Compared to pure Ru-NPs (red curve), the intensities for pure Ta and bimetallic NPs are much larger and decrease more rapidly with  $q$  between  $0.5$  and  $2\text{ nm}^{-1}$ , indicating the presence of larger particles.

Moreover, the intensity for the Ru<sub>2</sub>Ta<sub>8</sub> sample is similar to the Ta signal for  $q$  smaller than  $1.25\text{ nm}^{-1}$  and to the Ru signal above, revealing two populations of Ru and Ta NPs. From

Guinier plots a linear behavior was found only for the Ru NPs leading to an average diameter of  $2.3 \text{ nm} \pm 0.2 \text{ nm}$ . For the Ta and  $\text{Ta}_8\text{Ru}_2$  NPs, a broad distribution of diameters ranging from 2 to 4 nm was found depending on the  $q$ -range. For the  $\text{Ta}_8\text{Ru}_2$ -NPs, Figure 52.b shows the variation of the radial intensity when approaching the Ru K-edge.

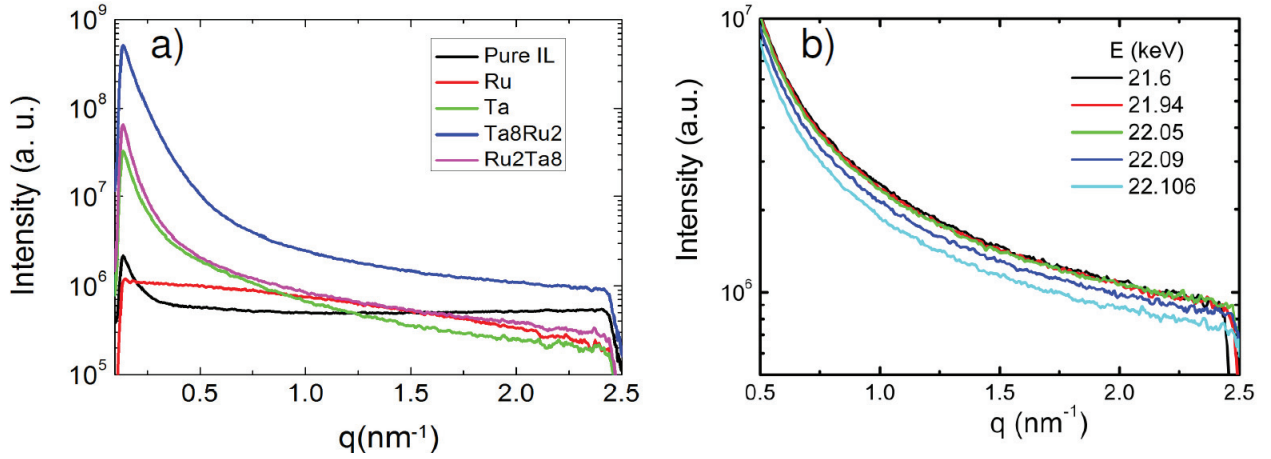


Figure 52 : a) Radial SAXS intensities as a function of the scattering vector,  $q$ , measured at  $E=21.6 \text{ keV}$  for pure IL, pure Ta and Ru NPs and two bimetallic NPs. b) For  $\text{Ta}_8\text{Ru}_2$  NPs, variation of the radial intensity with photon energy (K-Ru edge).

The intensity of a spherical particle with a Ru-core@Ta-shell structure is given by:

$$I(q) \approx [(3V_c(\xi_{Ru} - \xi_{Ta})J(qr_c))/qr_c + (3V_s(\xi_{Ta} - \xi_{IL})J(qr_s))/qr_s]^2$$

Where  $r_s = r_c + t_s$ .  $r_c$  is the core radius and  $t_s$  is the shell thickness,  $V_c$  and  $V_s$  are the volumes of the Ru core and the whole particle, respectively,  $\xi_i$  ( $i=\text{Ru, Ta, IL}$ ) are the electronic densities and  $j(x) = (\sin x - x \cos x)/x^2$ . The observed decrease with  $E$  is mostly due to the decrease of the cross-term  $(\xi_{Ru} - \xi_{Ta}) * (\xi_{Ta} - \xi_{IL}) * J(qr_c) * J(qr_s)$ . Using a core radius of 1.15 nm and a shell thickness of 0.55 nm (i.e. 2 ML of Ta), the intensities calculated for the different energies and integrated over a narrow  $q$ -range (1, 1.25 nm<sup>-1</sup>) lead to a variation between the two extreme energies of 6% and this figure holds for a monodisperse suspension. The experimental curves (Figure 52.b) would lead to a variation of the integrated intensity of 26%, i.e. much larger than 6%, but also larger than the value corresponding to a shell consisting of only one monolayer of Ta atoms equal to 9%. However, as shown in Figure 52.b, the decrease of the scattered intensity becomes more important from 22.09 keV. In contrast, the change in intensity between the three first energies is weaker and its magnitude order is in a relatively good agreement with the model assuming 2 ML of Ta. The

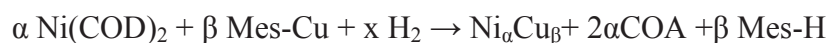
pronounced decrease of the scattered intensity above 22.05 keV can be attributed to a decrease of the number of particles in the beam. Indeed such effect was also observed at the Ta edge leading to an increase of the scattered intensity when approaching the Ta edge while a decrease is expected. Consequently no confirmation of the core-shell morphology can be brought by the Ta-edge measurements.

In summary, core-shell morphology for the Ta<sub>8</sub>Ru<sub>2</sub> nanoparticles is probable relying on the integrated intensities obtained at the Ru edge. As already shown for the Ru-Cu nanoparticles,<sup>27</sup> the differential intensity between I(E=21.6) and I(E=22.05) proportional to the cross-term would decrease more slowly than the total intensity dominated by the term  $(3V_s(\xi_{Ta} - \xi_{IL})J(qr_s))/qr_s^2$ .

## ii. Bimetallic Cu based nanoparticles<sup>144</sup>

### Ni-Cu NPs

In this section, the decomposition of Mes-Cu in the presence of Ni(COD)<sub>2</sub> is investigated. The reaction was performed at 100°C under 0.9 MPa H<sub>2</sub> for 4 h in C<sub>1</sub>C<sub>6</sub>ImNTf<sub>2</sub>. The molar fraction of Cu:  $\chi_{Cu} = \beta/(\alpha+\beta)$  was varied from 0.09 to 0.91 where  $\alpha$  and  $\beta$  corresponds to OM initial concentration for Ni and Cu, respectively.



Comparatively to Ni-NPs of 5.3 [4.2; 6.8] nm and Cu-NPs of 4.6 [3.6; 5.9] nm, the Ni-Cu mixture affords slightly smaller NPs (< 4 nm), for  $\chi_{Cu} = \beta/(\alpha+\beta)$  ranging between 0.09 and 0.83 (Figure 53). This effect is less pronounced since decomposition rates of the two precursors are close.

The binary phase diagram of Ni-Cu shows that alloy formation is possible whatever the Cu concentration. However, as the Ni surface energy value (1.7- 1.9 N.m<sup>-1</sup>) is higher than the Cu one (1.1 at 1.3 N.m<sup>-1</sup>), it could be expected that the Cu preferentially remains on Ni surface.



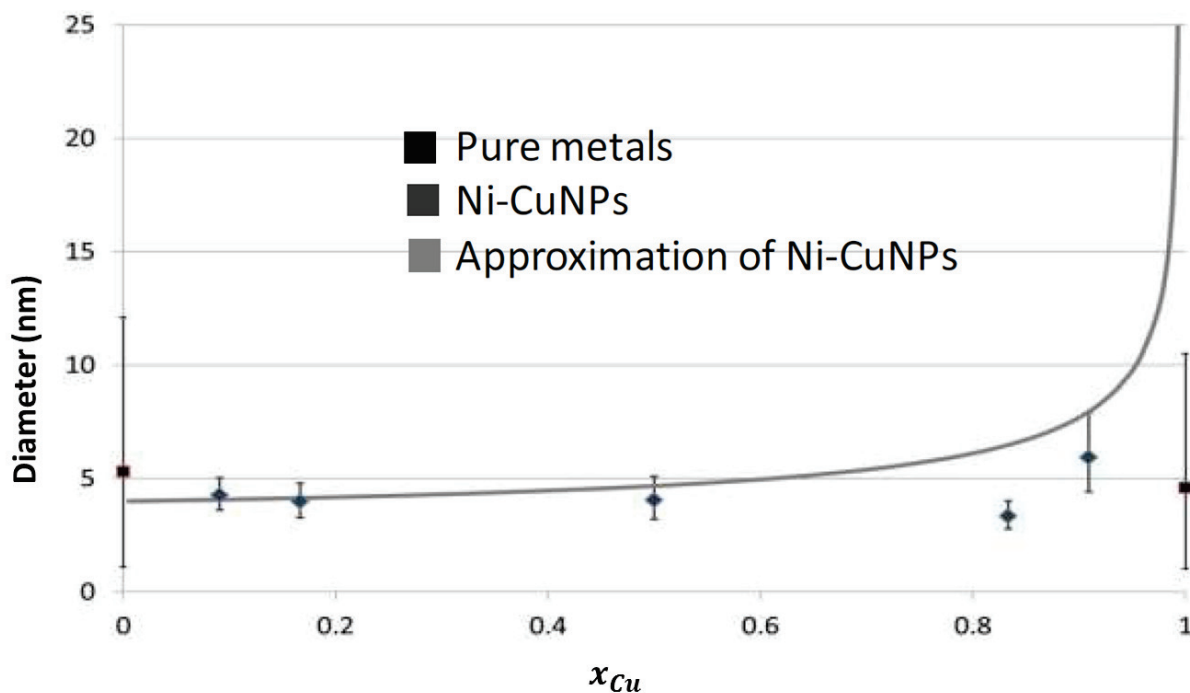


Figure 53 : Size and distribution of NiCu-NPs as a function of the molar fraction of Cu, obtained at 100 °C under 0.9 MPa of H<sub>2</sub> without stirring during 4 h.

In order to support this hypothesis, the catalytic activity of these bimetallic NPs has been studied in the isomerisation reaction of cyclic diene. Ni catalysts are active in the 1,5-cyclooctadiene (1,5-COD) isomerisation following the catalytic cycle depicted in Figure 54.<sup>146</sup> Contrarily, Cu is known to be inactive. This catalytic reaction was thus conducted in the presence of NiCu-NPs as a catalyst, in order to study the effect of  $\chi_{Cu}$  on the catalytic activity.

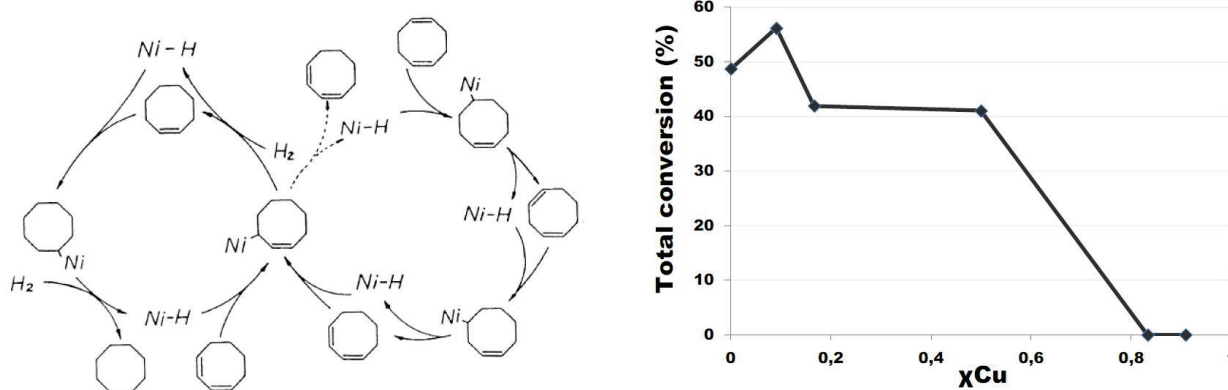


Figure 54 : Catalytic cycle of isomerisation and hydrogenation of 1,5-COD.<sup>146</sup> Conversion and selectivity in function of molar fraction of Cu in bimetallic Ni-CuNPs.

Increasing  $\chi_{\text{Cu}}$  induced a reduction of 1,5-COD conversion (Figure 54). For  $\chi_{\text{Cu}} = 83 \%$ , no more conversion is observed. This result provides evidence that Ni is less accessible when  $\chi_{\text{Cu}}$  increases, probably due to a Cu rich surface in NiCu-NPs.

### MnCu-NPs

Bimetallic MnCu-NPs are very interesting as they could enable, through a further annealing step, the synthesis of self-formed Mn barrier layer and copper seed layer needed in microelectronic devices.<sup>147</sup> In this part, the formation of MnCu-NPs from a mixture of organometallic precursors, Mes-Cu and bis(neopentyl)manganese, is reported. Again, the reduction occurred at 100°C under 0.9 MPa of H<sub>2</sub> without stirring in C<sub>1</sub>C<sub>4</sub>ImNTf<sub>2</sub> for 4 h.

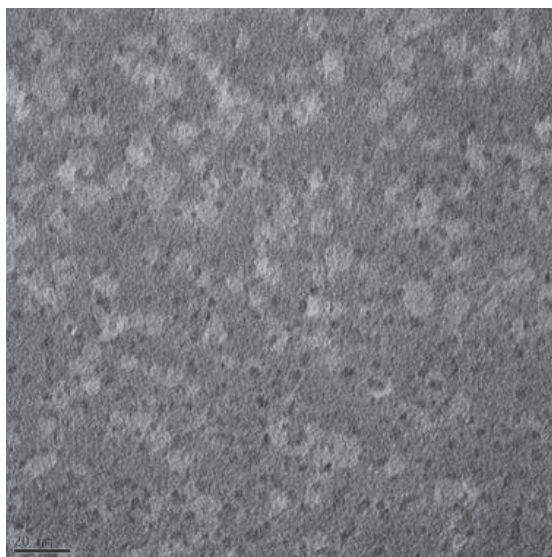


Figure 55 : TEM picture of Mn-CuNPs with 1:1 ratio of MnNp2 and Mes-Cu.

Note that in these conditions, pure OMs yielded Cu-NPs of 5.1 [4.2; 6.3] nm and Mn-NPs of 2.3 [1.8; 3.0] nm (Figure 56). When  $\chi_{\text{Cu}}$  varied between 0.09 and 0.91, the resulting NPs had a similar sizes (2.6 [2.1; 3.3] nm for  $\chi_{\text{Cu}} = 0.09$ ; 2.9 [2.3; 3.7] nm for  $\chi_{\text{Cu}} = 0.5$ ; 2.7 [2.1; 3.3] nm for  $\chi_{\text{Cu}} = 0.91$ ).

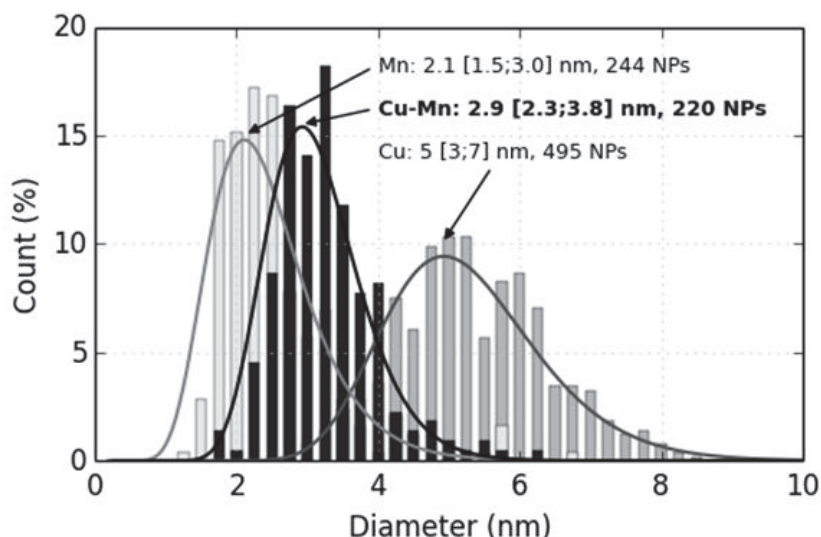


Figure 56 : Comparative size distribution histograms fitted by log-normal law of Mn-NPs, MnCu-NPs ( $\chi_{\text{Cu}} = 0.5$ ) and Cu-NPs obtained at 100 °C with  $5 \times 10^{-2}$  mol/L total concentration of precursors under 0.9 MPa of  $\text{H}_2$  without stirring during 4 hour in  $\text{C}_1\text{C}_4\text{ImNTf}_2$ .

In EDX analysis, these NPs proved to be composed of Mn and Cu. XPS analysis (Figure 57) showed that no metallic Mn typical peak at 638.6 eV was observed, and that the Cu  $2p_{3/2}$  (932.9 eV) and Cu LMM (914.6 eV) values correspond to  $\text{Cu}_2\text{O}$ . Mn oxide peaks were too broad and not well separated, preventing accurate determination of oxidation state. Hence, it was difficult to conclude from these analyses on the nature of MnCu-NPs. However, it has been shown that metallic Cu and metallic Mn-NPs were obtained under the same reaction conditions. Oxidation could occur during the transfer or the storage of NPs. In conclusion, the control of the NP size when  $\chi_{\text{Cu}}$  varied in the range between 0.09 and 0.91 and the analytical results let us suggest that there was formation of bimetallic MnCu-NPs which have been analyzed under oxidized state.

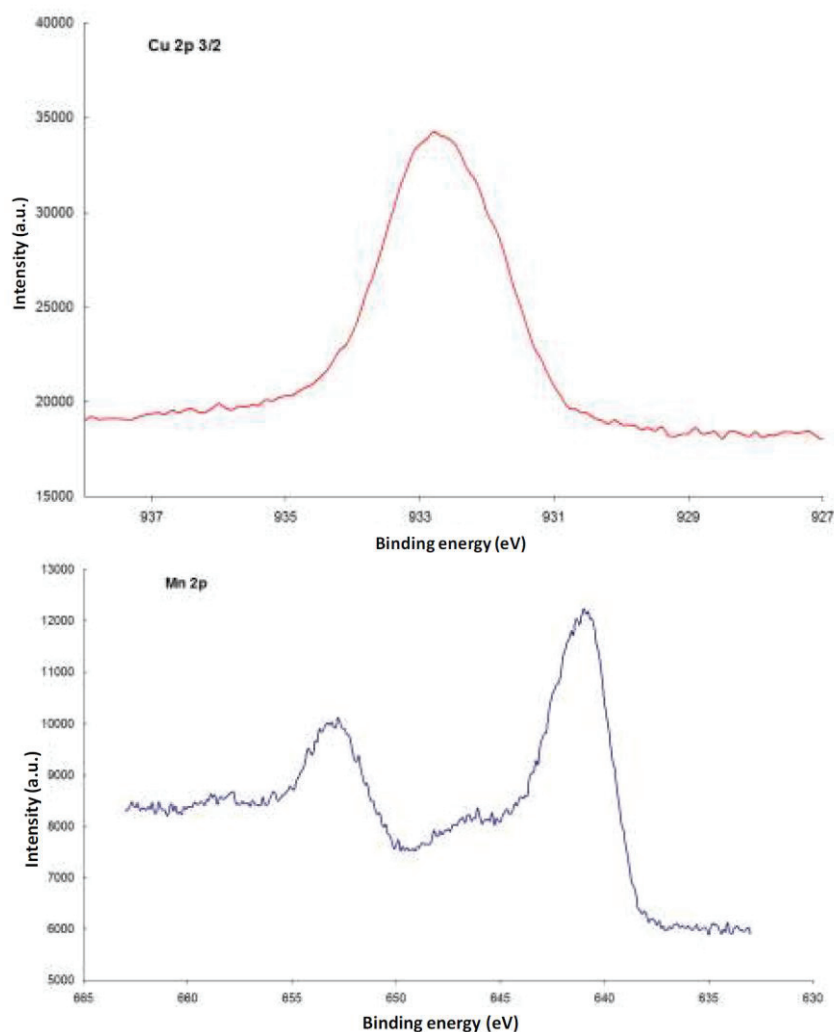


Figure 57 : XPS spectra of MnCu-NPs (ratio 1:1), top: Cu 2p<sub>3/2</sub> area, bottom: Mn2p area.

To conclude, an OM/IL approach is now well developed in our Laboratory that gave an easy access to many bimetallic NP systems with different structures. The challenging identification of the exact structure of these bimetallic systems was achieved by several advanced characterization tools like SAXS and several microscopy techniques. In light of these results, this OM/IL approach is going to be extended to include magnetic Co-based bimetallic systems which is the aim of the next chapter of this thesis.



# **Chapter II-B.**

---

## **Results:**

### **Synthesis and structural properties of bimetallic Co-based nanoparticles in ILs**



The decomposition of two OM precursors in solution in ILs, either successively or simultaneously, can lead to the formation of bimetallic NPs. In the previous chapter, it was shown that several bimetallic systems based on Co can exhibit useful properties for technological applications such as data storage or for catalysis. This chapter thus aims at demonstrating that the synthetic route in ILs is successful at forming Co-based NPs.

The examples depicted in the previous chapter demonstrate that the surface chemistry plays a key role in the formation of bimetallic NPs. More precisely, the presence of surface hydrides is needed on at least one of the two metals to initiate the decomposition of the second precursor and deposit the second metal on the first one. For this reason, the first question addressed in this chapter is: do our Co-NPs possess surface hydrides? It will be shown that such species are present on the Co-NPs. In the second part of this chapter, this reactivity is used to promote the synthesis of CoRu-NPs, both by one- and two-step approaches. Finally, a similar study is carried out to demonstrate the formation of bimetallic NPs in the CoPt system.

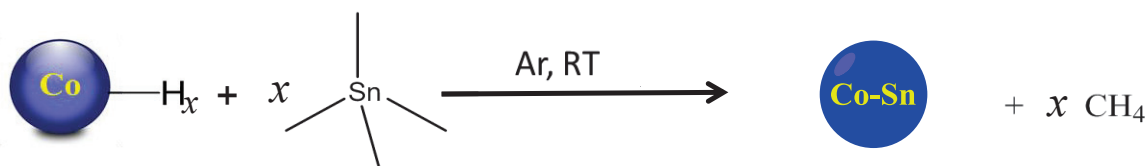
## **II-B. I. Surface chemistry of Co-NPs**

In chapter I-B, the Co-NPs were proven to be stable under H<sub>2</sub> atmosphere. As for Ru-NPs,<sup>90</sup> these results could suggest the presence of surface hydrides, [Co]<sub>surf.</sub>-H, stabilizing the Co-NPs and preventing their agglomeration. Similarly to a previous work on Ru-NPs,<sup>90</sup> and in order to assess and quantify the existence of [Co]<sub>surf.</sub>-H, two sets of experiments were considered, both under argon: the reaction of freshly prepared Co-NPs suspension with i) tetramethyltin, and ii) ethylene.

### **i. Reaction with tetramethyltin**

It is known that the hydrogenolysis reaction of Me<sub>x</sub>SnR<sub>4-x</sub> (0 ≤ x ≤ 4; R = methyl, *n*-butyl, *tert*-butyl, neopentyl, cyclohexyl) with metal surface hydrides leads to the evolution of MeH and RH in the gas phase.<sup>131</sup> In the presence of [Co]<sub>surf.</sub>-H, SnMe<sub>4</sub> should thus react and release methane according to the following schema:





To verify if this reaction occurs, a freshly synthesized Co-NPs suspension (0.4 MPa H<sub>2</sub>, 100°C, 0.05 mol.L<sup>-1</sup> Co(COD)(COE), in 2 ml of C<sub>1</sub>C<sub>4</sub>Im NTf<sub>2</sub>) was kept under Ar purging for 15 min. After addition of Me<sub>4</sub>Sn, the medium was kept at 50°C under stirring and static Ar pressure. After 24 h, all gaseous products were collected and analyzed by GC. The presence of methane was indeed confirmed and quantified (1.83x10<sup>-4</sup> mol.L<sup>-1</sup>). This result is a clear indication of the presence of [Co]<sub>surf.</sub>-H.

Furthermore, the modified NPs were analyzed by TEM. Images showed a little increase in their size from 4.1 ±0.4 to 4.7±0.3 nm. EDX and elemental mapping from STEM images proved the presence of little amounts of Sn on the Co-NPs colonies (Figure 58).

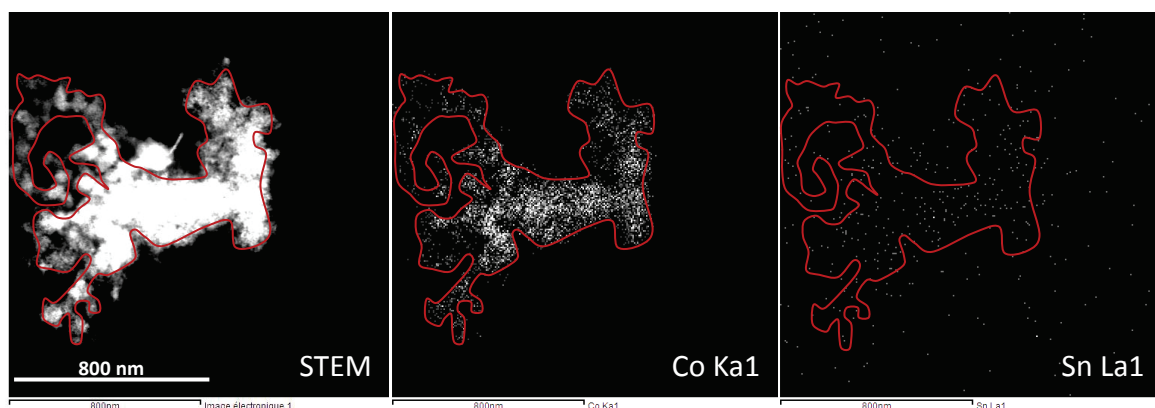
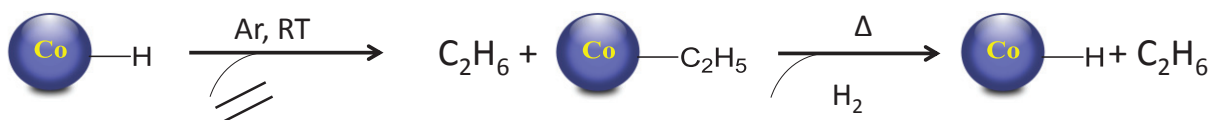


Figure 58 : STEM images for Co-NPs cluster after reaction with tetramethyltin (left), STEM elemental mapping image reproduced by EDX considering Co Ka1 intensities (middle), STEM elemental mapping image reproduced by EDX considering Sn La1 intensities (right).

## ii. Catalytic hydrogenation of ethylene

To confirm the existence of surface hydrides, the catalytic hydrogenation of ethylene under argon was performed.<sup>93</sup> A freshly synthesized Co-NPs suspension in C<sub>1</sub>C<sub>4</sub>ImNTf<sub>2</sub> was exposed to 11.4 KPa of C<sub>2</sub>H<sub>4</sub> at room temperature. An accurate gas manometer was used to

monitor the gas pressure evolution. The pressure was stabilized after 24 h. The gaseous products were then collected and analyzed by GC. To further collect the partially hydrogenated species such as (Co-C<sub>2</sub>H<sub>5</sub>), Scheme 6, 11.6 KPa of H<sub>2</sub> were introduced and the reactor was heated at 100°C until a stable pressure was reached (after 23 h). The collected gaseous species were identified and quantified as above. It was found that the total amount of ethane corresponded to a total concentration of  $1.65 \times 10^{-4}$  mol.L<sup>-1</sup> of [Co]<sub>surf</sub>-H.



Scheme 6: Reaction of ethylene gas with [Co]<sub>surf</sub>-H on freshly prepared Co-NPs.

Finally, this experiment confirmed the presence of [Co]<sub>surf</sub>-H species. However, both this and the previous results were consistent in detecting quite a small amount of these species, estimated to about 1% only of the available surface Co atoms in the system. As for Ru-NPs in which, exactly the same procedure was applied to report 0.6 H/Ru<sub>s</sub> as compared to 1-2 H/Ru<sub>s</sub> from the literature,<sup>90</sup> it should be noted that this method might not be so accurate in determining the exact amount of [Co]<sub>surf</sub>-H but indeed they are efficient enough to detect them. In the next section, it shall be examined if this low amount of surface reacting groups is sufficient to foster the formation of bimetallic NPs.

## II-B. II. Synthesis of Co-Ru bimetallic NPs

As Ru has been extensively studied and successfully used in several bimetallic systems (e.g. Ru-Cu and Ru-Ta),<sup>27, 142</sup> we follow this concept to develop a versatile synthetic route for bimetallic nanoparticles of Ru and Co.

### i. By successive decomposition of 2 metal precursors

Following the results of paragraph II.B.I, the most natural way to investigate the reactivity of the surface hydrides (either [Co]<sub>surf</sub>-H or [Ru]<sub>surf</sub>-H) is to tentatively decompose the second metal on pre-formed NPs of the first one. This approach is expected to result in the formation of either core@shell or nano-alloys structures. From a first sight on the CoRu phase diagram (Appendix 3), it seems that the core@shell structure is not the thermodynamically stable one. Despite so, such structure is not necessarily negligible, especially if the second

reaction step, involving the addition of the second metal, was performed at lower temperatures.

#### Reaction of Co-NPs with Ru-OM precursor to generate CoRu-NPs

Under argon, an equimolar solution of Ru(COD)(COT) in  $C_1C_4ImNTf_2$  was added to a freshly synthesized Co-NP suspension in  $C_1C_4ImNTf_2$  ( $4.1 \pm 0.5$  nm). The mixture was kept under stirring for 24 h at room temperature. The TEM images of the resulting NPs showed an increase in the NP-size to  $4.4 \pm 0.2$  nm after reaction with Ru(COD)(COT), Figure 59. Note that a blank experiment on the Co-NP suspension under the same reaction conditions but without adding Ru precursor showed no increase of the Co-NP size.

Furthermore, EDX and STEM observations (not shown here) prove the presence of 4-10 at% of Ru, together with Co. If we assume an icosahedral model for the Co-NPs with a covalent atomic radius of 0.126 nm for Co (see equations in section II-A.IV.ii), the total number of Co atoms and of layers for 4.1 nm Co-NPs are ~3000 Co atoms, and 10 atomic layers. From the Ru content derived from the EDX analysis, between 120 to 300 Ru atoms were present on (or in) each Co-NP. This low Ru amount does not represent a complete layer of Ru (if on the surface). This is probably related to the weak surface hydride coverage. Nevertheless, it clearly demonstrate that the  $[Co]_{surf}\text{-H}$  can decompose the Ru precursor to form CoRu-NPs.

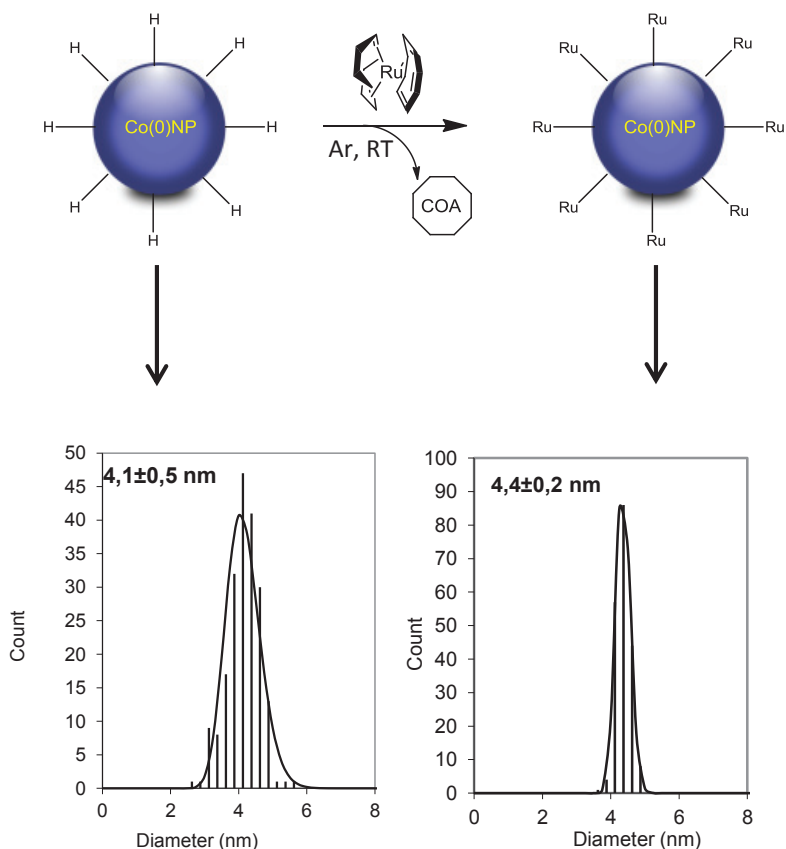


Figure 59 : Size distribution for Co-NPs obtained through the decomposition of Co(COD)(COE) under 0.4 MPa  $H_2$ , 100°C, 4 h, in  $C_1C_4ImNTf_2$ , before (left) and after (right) exposure to an equimolar solution of Ru(COD)(COT) for 24 h, at room temperature under Ar.

#### Reaction of Ru-NPs with Co-OM precursor to generate CoRu-NPs

Similar to Co-NPs, Ru-NPs possess surface hydrides and hence, they could react with our Co OM precursor.<sup>90, 93</sup>

In this part we report the reaction of a Co(COD)(COE) solution in  $C_1C_4ImNTf_2$  with a Ru-NP suspension in the same IL under Ar to afford RuCo-NPs.

The Ru NPs were synthesized in similar conditions than Co-NPs (2 mL of 0.05 mol.L<sup>-1</sup> solution of Ru(COD)(COT) 100°C, 0.4 MPa  $H_2$ , 4 h) and had a mean size of  $2.6 \pm 0.2$  nm. After a 24 h reaction with Co(COD)(COE), a single population of NPs with a mean size of  $3.7 \pm 0.2$  nm was observed in TEM images(Figure 60). Taking into account that the Ru-NP size remained unchanged under Ar at room temperature, the 1.1 nm increase in the size of the primary Ru-NPs could probably indicate the formation of a 0.55 nm thick Co shell on the surface of the initially formed Ru core (Figure 60).

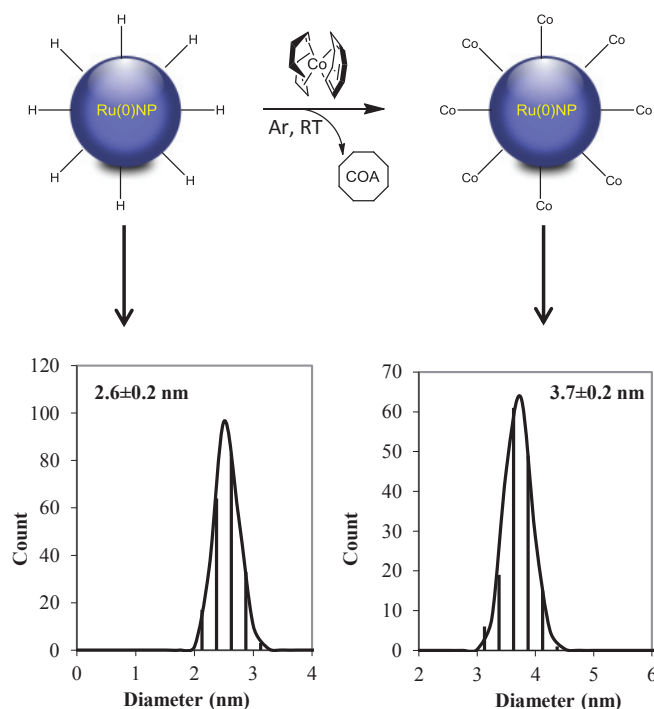


Figure 60 : Size distribution for Ru-NPs obtained through the decomposition of Ru(COD)(COT) under 0.4 MPa  $H_2$ , 100°C, 4 h, in  $C_1C_4ImNTf_2$ , before (left) and after (right) exposure to an equimolar solution of Co(COD)(COE) for 24 h at room temperature under Ar.

## ii. One-pot synthesis approach for RuCo-NPs

One-pot synthesis approaches are an advantageous way to synthesis NPs as they reduce the production steps and costs. The synthesis of CoRu NPs through a one-pot approach was attempted by mixing 2 solutions, 0.05 mol.L<sup>-1</sup> each, of Co(COD)(COE) and Ru(COD)(COT) in  $C_1C_4ImNTf_2$  in different volume ratios so as to keep the total volume fixed at 2 mL. In that way, the mole fraction of both metal precursors in the resultant solution was varied while keeping the total metal content fixed to 0.05 mol.L<sup>-1</sup>. These solutions were then allowed to decompose simultaneously under  $H_2$  atmosphere (0.4 MPa) during 4 hours at 100°C. In all cases, monodispersed NPs with a very narrow size distribution were obtained. Interestingly, their sizes depended on the Co/Ru ratio with an increase in size upon increasing the Co content (Figure 61).

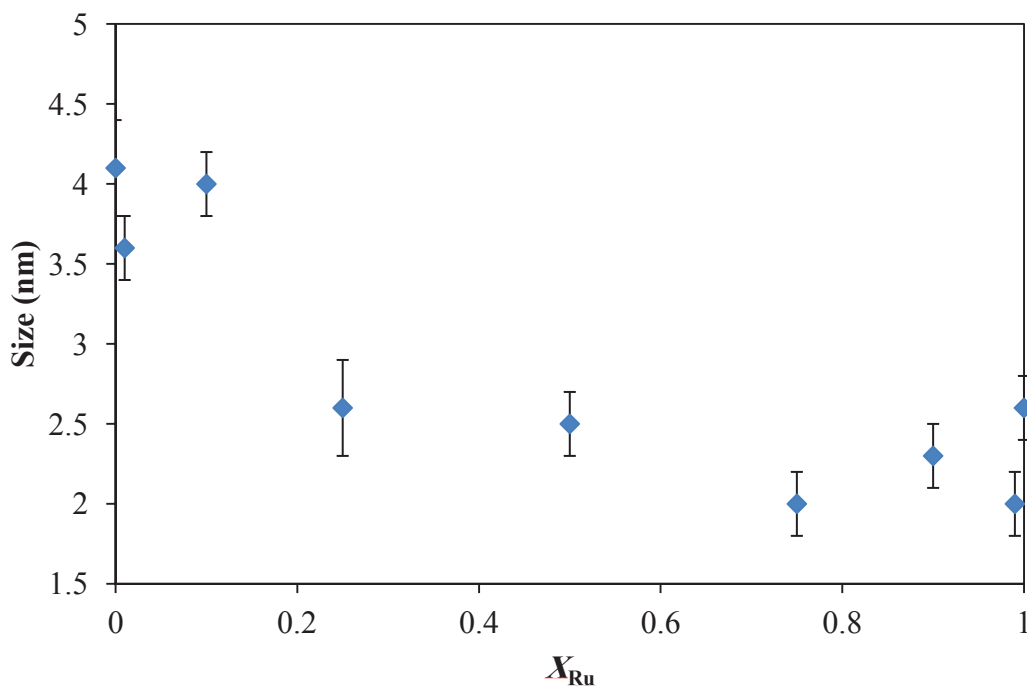


Figure 61 : Size of  $Co_{1-x}Ru_x$  NPs plotted as a function of the mole fraction of Ru ( $X_{Ru}$ ) in the initial solution mixture.

It is important to note that some of the NPs had a smaller size than the pure metals. This behavior, which has been observed in other bimetallic systems,<sup>27</sup> is a good indication for the formation of bimetallic NPs rather than the separate precipitation of the two metals.

### iii. Defining the structure of CoRu-NPs

In order to resolve the structure of the CoRu-NPs, ASAXS experiments were undertaken using the CRG-BM02 beamline at the ESRF (see appendix 4). Measurements were performed at various energies close to the Ru-K edge (22.117 keV) to be able to separate the contributions of the two metals, as was done for RuCu and RuTa systems (see paragraphs II-A.IV.ii and II-A.V.i, respectively). This approach had been successful at demonstrating the core-shell structures of these NPs.

For this study, two reference samples were considered: Co-NPs formed under the usual conditions ( $4.1 \pm 0.3$  nm) and Ru-NPs elaborated from Ru(COD)(COT) under the same conditions, at  $100^\circ\text{C}$  for 4 h in  $C_1C_4ImNTf_2$  ( $2.6 \pm 0.2$  nm). The latter sample was examined first to verify the accuracy of this series of experiments. The response of the Ru-NPs after correction for the apparatus and IL contributions is plotted in Figure 62. This curve is

comparable to the one measured in previous campaigns (see Figure 48, Figure 49, Figure 52). For low  $q$  values (below  $0.25 \text{ nm}^{-1}$  in this case), a peak of scattered intensity is indicative of the presence of agglomerates. A similar contribution of large objects is also present in the  $q$ -domain below  $1.0 \text{ nm}^{-1}$ . For this reason, this range was excluded from the analysis. Between  $1.0 \text{ nm}^{-1}$  and  $3.0 \text{ nm}^{-1}$  (which is typically the limit above which the IL response starts to dominate, see Figure 47), this response could be reasonably well fitted using a model of monodisperse spherical particles. For this fit, the scatter length densities of Ru and the IL were fixed at  $8.5 \times 10^{11} \text{ cm}^{-2}$  and  $1.2 \times 10^{11} \text{ cm}^{-2}$ , respectively. The best fit (red curve in Figure 62) was obtained with a NP diameter of  $2.4 \text{ nm}$  and concentration of  $3.1 \times 10^{19} \text{ cm}^{-3}$ . Both values are in fairly good agreement with TEM observations and expected mass balance of Ru.

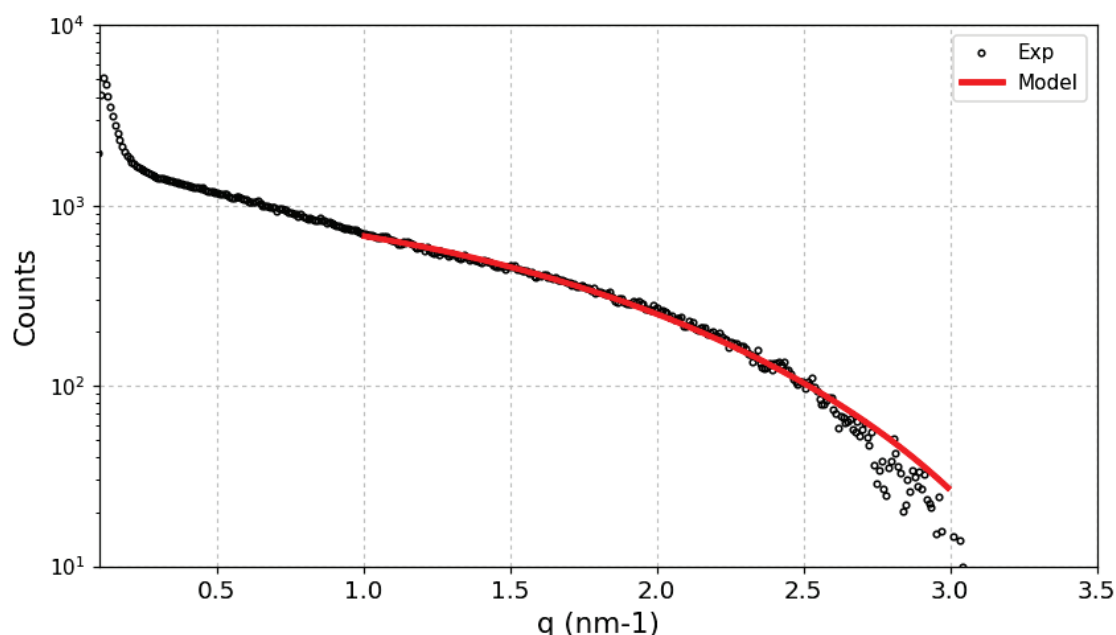


Figure 62 : Scattered intensity as a function of the scattering vector  $q$  measured at  $E = 21.6 \text{ keV}$  for the reference sample containing Ru-NPs. In red, the best fit obtained with a spherical particle model.

The same procedure was applied to the sample with Co-NPs. However, in this case, the scattered intensity could not be fitted with the same simple model. As compared to the expected response from spherical NPs, the scattered intensity curve was too flat (Figure 63). Considering the TEM picture in Figure 20, this deformation could arise from the aggregation of Co-NPs, which are not well dispersed like their Ru counterparts. Indeed, a similar deformation of the scattered intensity curves has been observed for concentrated suspension of latex NPs and was attributed to the interaction of the NPs.<sup>148</sup> To model such situations, the

usual strategy consists in introducing a so-called structure factor (or interference function). This factor (close to 1) modulates the form factor, which corresponds to the response of the uncorrelated NPs (like in the case of Ru-NPs) and contains the information about the size and internal structure of the NPs. To get access to the latter, it is thus needed to estimate the former. The structure factor is the Fourier transform of the radial distribution of NPs in the medium.

A conventional and well documented approach to calculate this structure factor is to use the Ornstein-Zernike equation with an adequate closure relation in which the interaction potential between NPs is implemented.<sup>149</sup> The most widespread closure relation is probably the Percus-Yevick approximation. When used with a hard sphere or sticky hard sphere potential, this model can be solved analytically. For both potential, the interaction energy is zero at long distance, and infinity (complete repulsion) below a given hard sphere radius that ought to be equal to or larger than the NP radius. In the case of sticky hard spheres, a potential well (attractive interaction) is introduced in the vicinity of the hard sphere surface (Figure 64). The depth of this potential is parametrized with the so-called stickiness coefficient  $\tau$ .<sup>150</sup> The closer this coefficient to zero, the deeper the potential well, the “stickier” the hard spheres.

In a first approximation, the hard-sphere model was used to fit the response of Co-NPs (scattering length density of Co  $7.0 \times 10^{11} \text{ cm}^{-2}$ ). In this fit, the NP radius and the hard sphere radius were considered as separate parameters. When both values were allowed to adjust, the NP radius always exceeded the hard sphere radius, which is unphysical. Interestingly enough, upon using a sticky hard sphere model, both radii adjusted to 1.3 nm. The concentration of NPs adjusted to  $1.6 \times 10^{20} \text{ cm}^{-3}$ , and the stickiness coefficient to 0.36. The corresponding curve is plotted in red in Figure 63, along with the separate contributions of the structure factor (in green) and the form factor (in blue).



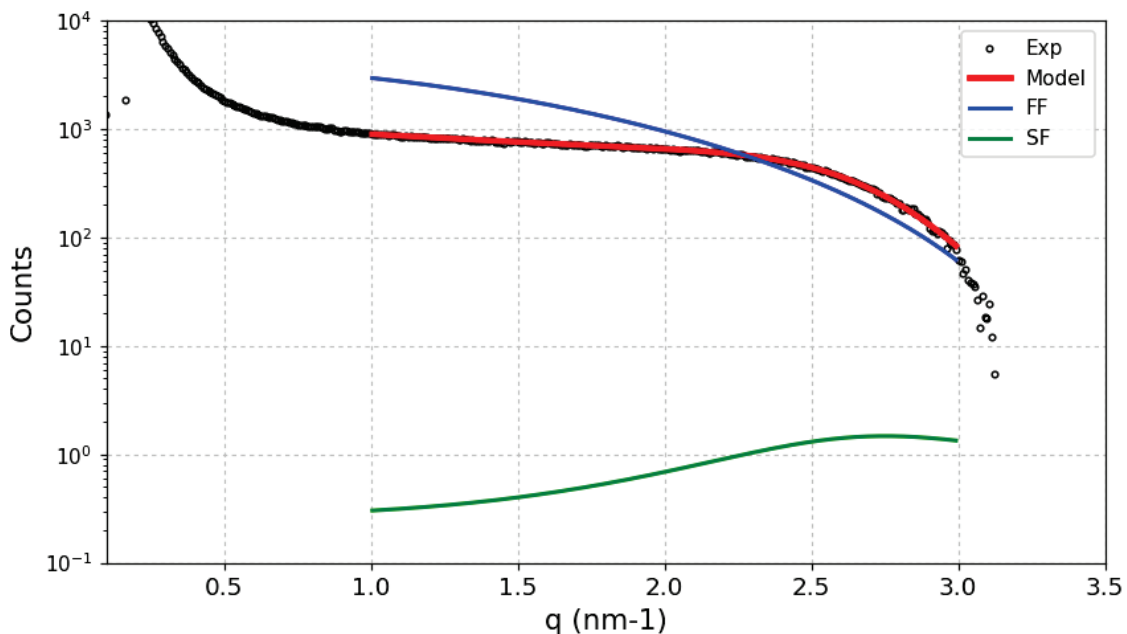


Figure 63 : Scattered intensity as a function of the scattering vector  $q$  measured at  $E = 21.6$  keV for the reference sample containing Co-NPs. In red the best fit obtained with a model of sticky hard spheres. In blue and green, the contributions of the form factor and structure factor, respectively.

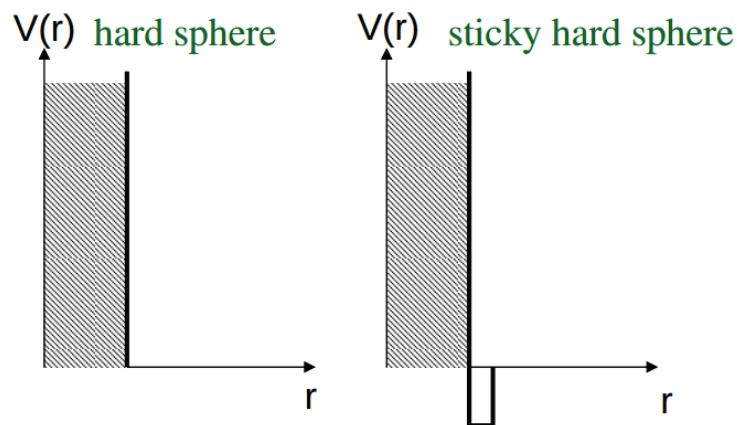


Figure 64 : Potential energy landscape  $V(r)$  for the (left) hard sphere and (right) sticky hard sphere models.

The fact that a sticky hard sphere model yields a better fit than simple hard spheres is consistent with the attractive interaction between Co-NPs as observed by TEM (Figure 20) and measured by SQUID (paragraph I-B.IV.ii). However, the size derived from this fit (2.6 nm) is significantly smaller than the size measured by both these techniques. Also, the NP concentration is higher than expected from the mass balance. For all these reasons, this result should be considered with care.

The interference between interacting NPs has also been observed in bimetallic CoRu-NPs. For instance, bimetallic NPs formed by the reaction of Co(COD)(COE) on Ru-NPs (such as those described in Figure 60) exhibited a clear correlation peak at about  $2 \text{ nm}^{-1}$ . It was possible to tentatively fit this curve using the same sticky hard sphere model. The best fit was obtained for NPs with a scattering length density of  $8.2 \times 10^{11} \text{ cm}^{-2}$  (intermediate between Ru and Cu, this parameter was allowed to adjust) and a diameter of 2.0 nm. The hard sphere diameter was much larger (3.5 nm), but the stickiness coefficient was again 0.37. However, this curve could also be fitted considering core-shell NPs (with a Ru diameter of 2.1 nm and a Co shell of about 0.5 nm) in a hard sphere configuration. To discriminate between the two models, their accuracy at other energies (closer to Ru edge) still has to be tested. However, it is worth to note that in all cases, the simple fact that the particles are interacting indicates that Co is present under its metallic (and magnetically active) form, because such interaction is not observed for pure Ru-NPs.

### **II-B. III. Synthesis of CoPt bimetallic NPs:**

The CoPt bimetallic system, which is of great importance for a variety of practical applications, has been studied following the same strategy as the CoRu system.

#### **i. By successive decomposition of 2 metal precursors**

In a first attempt, (COD)Pt(Me)<sub>2</sub> was considered as a Pt precursor. 1 mL of 0.05 mol.L<sup>-1</sup> solution of (COD)Pt(Me)<sub>2</sub> in C<sub>1</sub>C<sub>4</sub>ImNTf<sub>2</sub> was added to a suspension of freshly prepared Co-NPs of 4.8±0.4 nm (only purged with Ar for 15 min, not exposed to vacuum). The mixture was stirred and then kept under Ar for 24 h at room temperature. A first visual observation is that a metallic mirror was formed on the glass wall touching the solution surface. A gaseous aliquot was analyzed by GC-MS. Only traces of methane were detected corresponding to about 0.4% decomposition of the Pt precursor. Analyzing the formed NPs by TEM showed a uniform size distribution centered around 4.9 nm. Hence, no significant increase in the size of the initial Co-NPs was observed. On the other hand, EDX confirmed that the NPs were almost exclusively composed of Co with only traces of Pt (0.3 at%, could be either impregnated in the Co-NPs or it could be just traces of the IL containing dissolved Pt precursor). From all these observations, we conclude that (COD)Pt(Me)<sub>2</sub> is difficult to decompose under these reaction conditions and does not afford CoPt-NPs. Rather, it only decomposes partially to precipitate into a metallic mirror.

To confirm this, the previous experiment was repeated using  $D_2$  instead of  $H_2$  to decompose  $Co(COD)(COE)$  and form the Co-NPs. As a result, the Co-NPs are expected to possess a deuterated surface (instead of the typical surface hydrides) which, upon reacting with  $(COD)Pt(Me)_2$ , should afford the formation of deuterated methane ( $CH_3D$ ). Therefore, as in the previous experiment, a gaseous aliquot was analyzed in GC-MS. This analysis only showed the existence of methane and no evidences of deuterated methane. This rules out any surface reaction of  $[Co]-H$  with  $(COD)Pt(Me)_2$  to afford CoPt-NPs under our operating conditions.

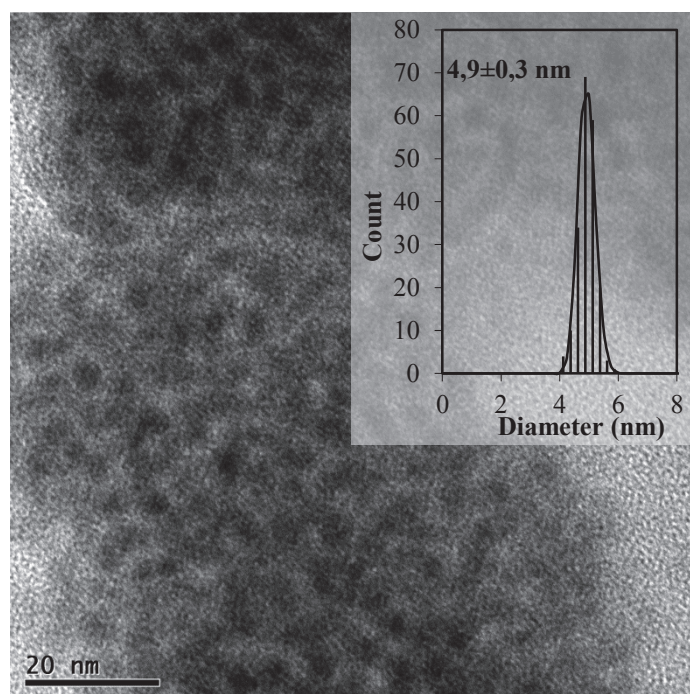


Figure 65 : TEM image and size distribution of Co-NPs obtained through the decomposition of  $Co(COD)(COE)$  under 0.4 MPa  $H_2$ , 100°C, 4 h, in  $C_1C_4ImNTf_2$ , after exposure to equimolar solution of  $(COD)Pt(Me)_2$  for 24 h, at room temperature under Ar.

In a second attempt,  $Pt(dba)_2$  was tested as a possible  $Pt^{(0)}$  precursor. In this attempt, and in order to monitor the reaction from the beginning, Co-NPs were again synthesized using  $D_2$  instead of  $H_2$  so as to label any possible surface reaction products. After purging the reactor for 15 min with Ar and then cooling down to 0°C, 1 mL of equimolar solution of  $Pt(dba)_2$  was added at a very slow rate while stirring to finally achieve an equimolar mixture of Co and Pt. The solution was then kept under static Ar at 20°C for 24 h. Then, all gaseous products were analyzed by GC. However, since dba is not so volatile, it was not detected. Therefore, the

liquid phase was also analyzed by high resolution mass spectrometry. Results showed only dba without any indication of either hydrogenated or deuterated derivatives. This indicates that under these conditions, no surface reaction occurred with the Co-NPs.

Finally, the NPs were analyzed by TEM to reveal the existence of NPs around 5 nm in diameter together with other 1 nm NPs (Figure 66).

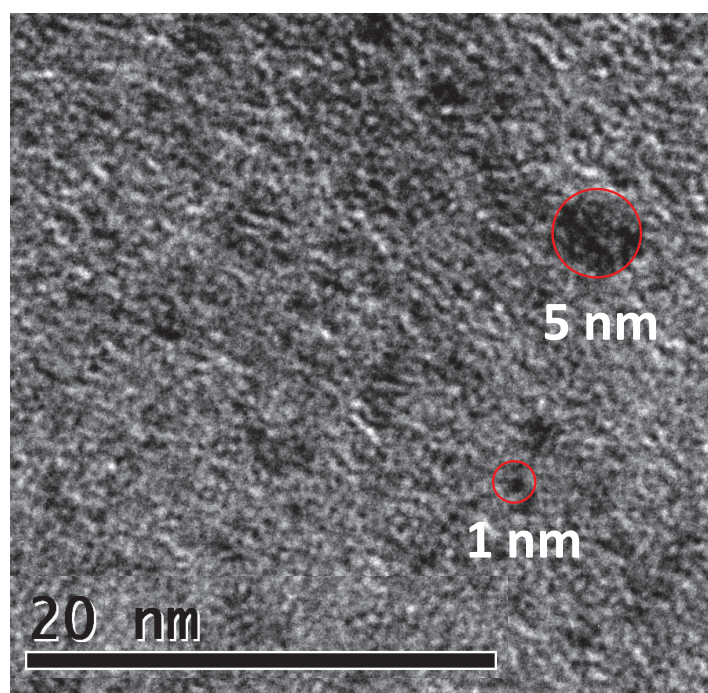


Figure 66 : TEM image of a suspension of Co-NPs in  $C_1C_4ImNTf_2$  after exposure to equimolar solution of  $Pt(dba)_2$  for 24 h at room temperature under Ar.

Upon switching to STEM mode (Figure 67), these small NPs appeared brighter, which shows that they were composed of a heavier element. To confirm this, quantitative EDX analysis was performed both on the overall sample and on a single small NP. The global EDX analysis showed identical amounts of Pt and Co (50 at % Co, 50 at % Pt). Since the excess IL solution was removed prior to analysis, this indicates a full decomposition of both OM precursors. Upon focusing on one 1 nm particle, only Pt was detected, with no trace of Co. All these observations clearly indicate that  $Co(COD)(COE)$  was fully decomposed into 5 nm Co-NPs.  $Pt(dba)_2$  was decomposed separately from the surface of Co-NPs to form very small distinct Pt-NPs. However, it cannot be excluded that some of the Pt OM reacted on the Co-NPs as well. In fact, based on a blank experiment for the stability of  $Pt(dba)_2$  in IL under the same conditions,  $Pt(dba)_2$  decomposes only in the presence of Co-NPs. This might indicate

that the decomposition of the precursor is indeed initiated by the [Co]-H. This could leave some Pt atoms on the Co-NPs, but also activate the decomposition of the rest of the Pt<sup>(0)</sup> OM to give separate Pt-NPs. This hypothesis matches well with the previously mentioned EDX results.

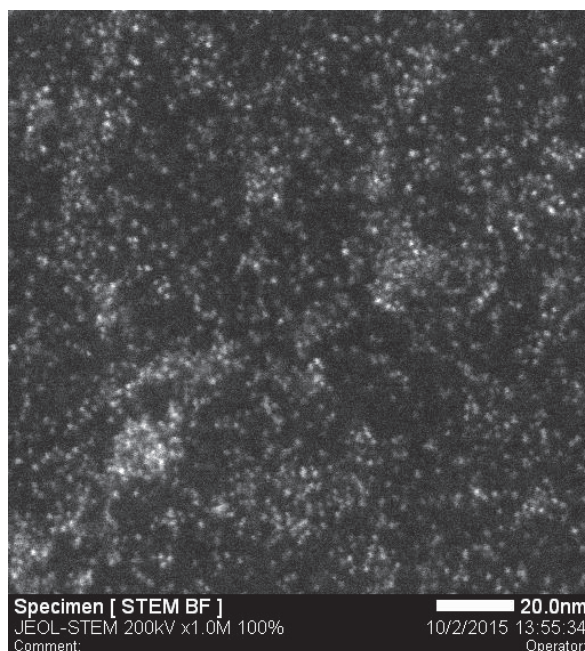


Figure 67 : STEM image of the same spot as in Figure 66 showing the existence of distinct tiny NPs of a heavier metal, probably Pt.

## ii. One-pot synthesis approach

From the previous section, it seems that the 2 step synthesis is not effective at forming bimetallic CoPt-NPs. Rather, it affords Co-NPs either with a mirror-like precipitate of Pt or distinct small Pt-NPs.

As an alternative, the one-pot synthesis approach was considered. In this set of experiments, we started first by considering a reference sample that was fully studied and characterized in the literature for the sake of comparison with our results. This reference sample was prepared exactly as reported in Chapter (II-A.IV.i) and it looked very similar in the TEM. Then, several Co-Pt solution mixtures were prepared by mixing different volumes of 2 solutions: 0.05 mol.L<sup>-1</sup> Co(COD)(COE) in C<sub>1</sub>C<sub>4</sub>ImNTf<sub>2</sub> and 0.05 mol.L<sup>-1</sup> Pt(dba)<sub>2</sub> in C<sub>1</sub>C<sub>4</sub>ImNTf<sub>2</sub>. The total volume of the mixtures was always fixed to 2 mL (total metal content of 0.05 mol.L<sup>-1</sup>). Each mixture was then allowed to decompose under 0.9 MPa of H<sub>2</sub> at 150°C for 24 h (same experimental conditions as for the reference sample).

For all samples, the at% values of Pt determined by global EDX were matching very well with the initial ratios of both metal precursors (Figure 68), indicating a full decomposition of both OM.

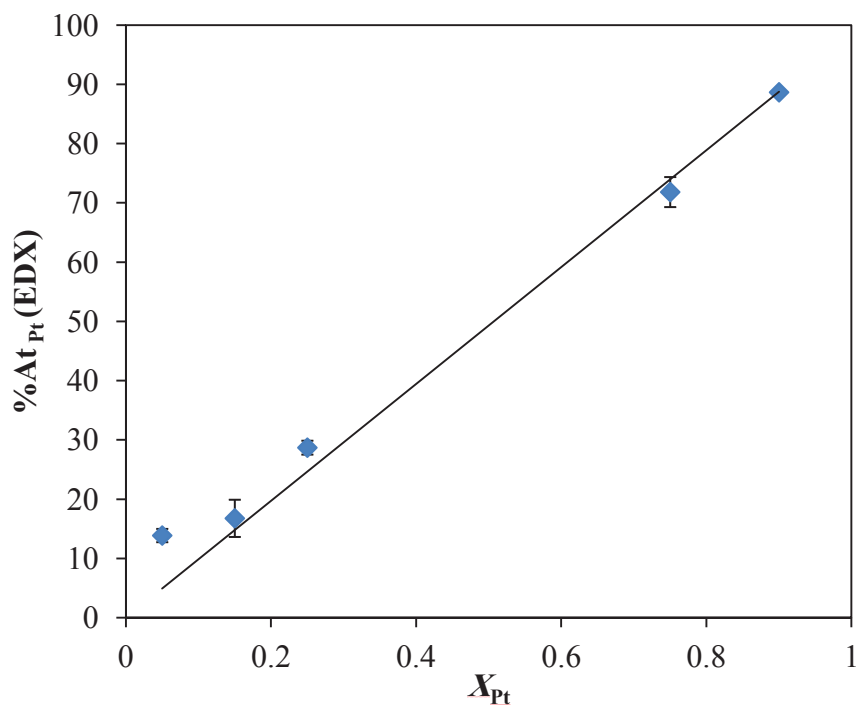


Figure 68 : Co content as measured by EDX, plotted as a function of  $X_{Pt}$  in the initial mixture.

Interestingly enough, for all the mixtures, a TEM analysis of the resulting NPs (Figure 69) showed a single and narrow size distribution. Upon moving from pure Co towards Pt, the average size gradually decreased from 4.1 nm (pure Co) to 2.6 nm ( $X_{Pt} = 0.9$ , Figure 70). It is important to note that the latter were even smaller than pure Pt-NPs ( $3.0 \pm 0.3$ nm).

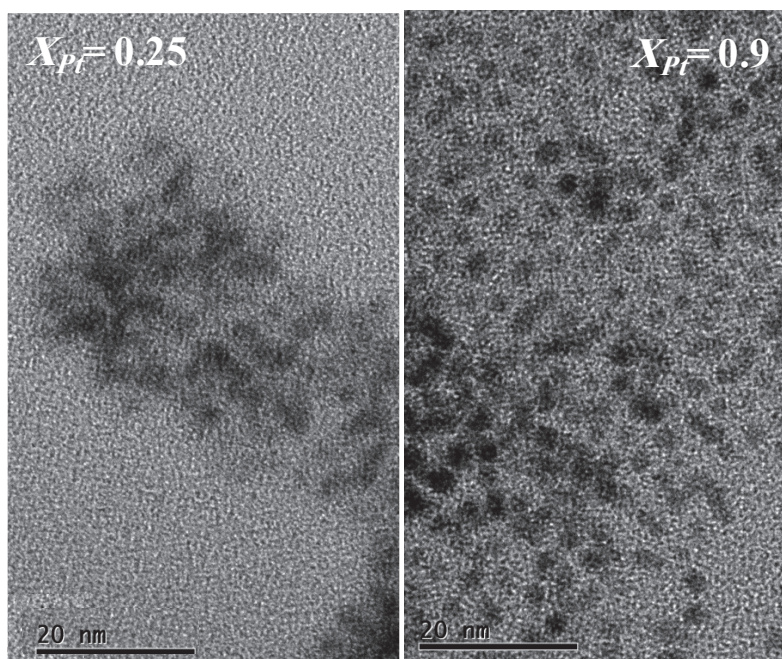


Figure 69 : TEM images of  $\text{Co}_{1-x}\text{Pt}_x$  NPs prepared by simultaneous decomposition of  $\text{Co}(\text{COD})(\text{COE})$  and  $\text{Pt}(\text{dba})_2$  in IL ( $X_{\text{Pt}}=0.25, 0.9$ ) under 0.9 MPa  $\text{H}_2$ , 150°C, 24 h.

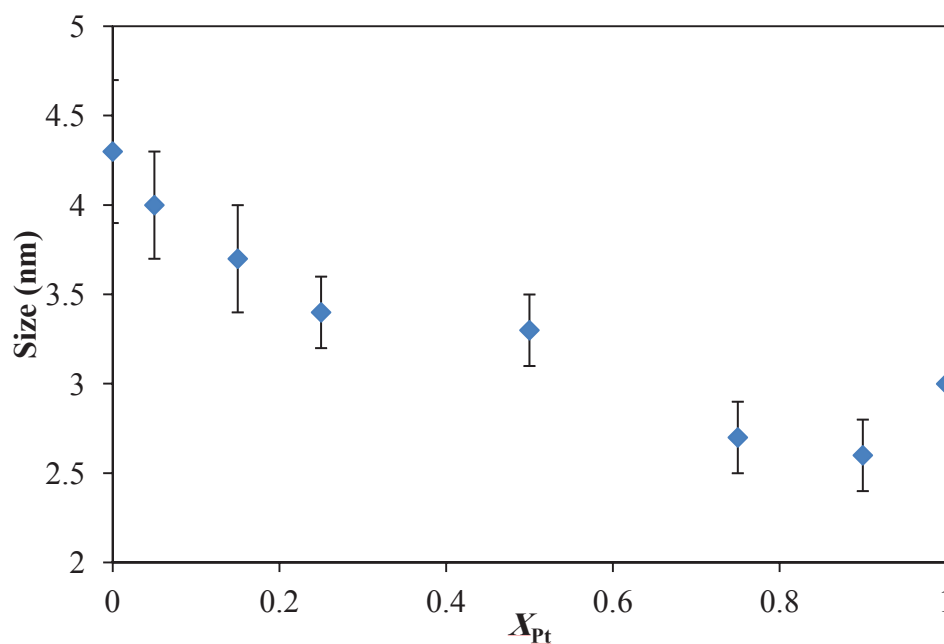


Figure 70 : Size of  $\text{Co}_{1-x}\text{Pt}_x$  NPs plotted as a function of the mole fraction of Pt ( $X_{\text{Pt}}$ ) in the initial solution mixture.

### iii. Defining the structure of CoPt NPs

Samples with CoPt-NPs were analyzed at ESRF during the same campaign as for the CoRu ones. The same general observation can be made that the anomalous effect must be decoupled from the interference function to resolve their structure. However, in the case of CoPt-NPs formed in one step from an equimolar mixture of  $\text{Co}(\text{COD})(\text{COE})$  and  $\text{Pt}(\text{dba})_2$ ,

quite a clear and steady evolution of the scattered intensity was observed as the energy was shifted towards the Pt-L<sub>III</sub> edge at 11.564 keV (Figure 71). As expected, the overall intensity steadily decreased as the energy approached the Pt edge. Interestingly enough, following the reasoning in paragraph II-A.IV.ii, the differential intensity between 11.34 and 11.56 keV compares well with the sample's response, except that it falls faster with  $q$ . This would indicate that Pt atoms are preferentially situated at the periphery of the NPs, like in a Co@Pt core@shell structure. However, more detailed analyses of these curves are needed to confirm this.

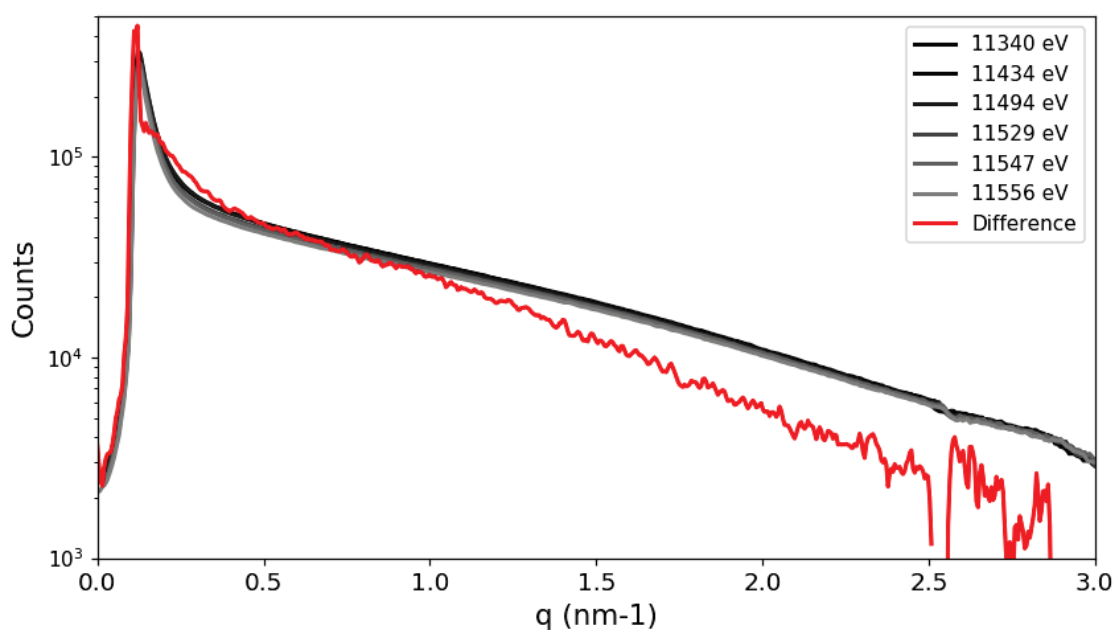


Figure 71 : Scattered intensity as a function of the scattering vector  $q$  measured at various energies close to the Pt-L<sub>III</sub> edge for the sample containing CoPt-NPs prepared in one step from an equimolar mixture of Co(COD)(COE) and Pt(dba)<sub>2</sub>. In red, the difference between the two extreme curves scaled to the initial response.

## II-B. IV. CoPt-NPs as hydrogenation catalysts

Since Pt-NPs are known to catalyze hydrogenation reactions of olefins, the formed bimetallic NPs were tested as catalysts for the hydrogenation of cyclohexadiene into cyclohexene and cyclohexane in the presence of H<sub>2</sub>. The catalyst activity and selectivity was monitored as a function of  $X_{Pt}$ . To allow the comparison between different catalysts, all catalytic reaction mixtures were diligently prepared in such a way that experimental parameters like the substrate-catalyst and substrate-ionic liquid ratio and therefore, viscosity and mass transport factors, remained constant.



In NP catalysis, as in heterogeneous catalysis, the reactions mainly take place at the surface of the NPs. As a result, the amount of surface metal atoms needed to be fixed for all experiments.

The dispersion (D) is defined as the ratio between surface atoms,  $M_{\text{surf}}$ , and the total number of atoms,  $M_{\text{T}}$  ( $D = M_{\text{surf}} / M_{\text{T}}$ ). Obviously, D increases when the size of the NPs decreases.<sup>93</sup> Suspensions of mono- and bimetallic NPs were synthesized from solutions with a total metal concentration of  $0.05 \text{ mol.L}^{-1}$ . For each suspension, the amount of surface atoms was estimated from the average diameter as measured by TEM, assuming an icosahedral model assuming  $a_{\text{Co}} = 0.126 \text{ nm}$  (see equations in section II-A.IV.ii). For instance, the following values were derived:

- Pure Co-NPs with a mean size of 4.3 nm:  $\text{Co}_{\text{surf.}} = 0.013 \text{ mol.L}^{-1}$ .
- CoPt-NPs with a mean size of 2.6 nm ( $X_{\text{Pt}} = 0.9$ ):  $\text{CoPt}_{\text{surf.}} = 0.022 \text{ mol.L}^{-1}$ .
- Pure Pt-NPs with a mean size of 3.0 nm:  $\text{Pt}_{\text{surf.}} = 0.02 \text{ mol.L}^{-1}$

To obtain the same amount of  $M_{\text{surf.}}$  ( $0.013 \text{ mol.L}^{-1}$ ) for all catalysts, an adequate quantity of IL was added to each suspension. In addition, the same substrate-ionic liquid ratio was kept throughout the experiments by fixing the volume of suspension to 0.5 mL. In each experiment,  $63 \mu\text{L}$  of cyclohexadiene (CYD) was added, *i.e.*  $\text{CYD} / M_{\text{surf.}}$  equal to 100. After 30 min under  $\text{H}_2$  (0.12 MPa), at room temperature, the medium was diluted in  $\text{CH}_3\text{CN}$ , and analyzed by GC. Figure 72 shows the evolution of the CYD conversion over  $X_{\text{Pt}}$ . Under these experimental conditions, Co-NPs were inactive, while the conversion rate gradually increased with Pt content to reach 50% for  $X_{\text{Pt}} = 0.5$ . For  $X_{\text{Pt}} \geq 0.5$  the conversion rate did no longer significantly evolve. Since the surface metal content was fixed for all samples and assuming the formation of a Pt layer at the surface of the NPs, this plateau in the conversion could be explained by an almost full coverage of the NP surface by Pt atoms. Indeed, the completion of the first layer of the Pt shell is expected to occur for  $X_{\text{Pt}} = 0.35$  (assuming  $a_{\text{Co}} = 0.126 \text{ nm}$ ,  $a_{\text{Pt}} = 0.129 \text{ nm}$ ). Once this first layer is complete, and owing to our experimental procedure, the concentration of  $\text{Pt}_{\text{surf.}}$  would be stable for  $X_{\text{Pt}} \geq 0.5$  affording a steady conversion rate.

The selectivity in cyclohexene defined as the cyclohexene/cyclohexane ratio, was maximal (75 %) for  $X_{\text{Pt}} = 0.05$ , then decreased sharply to 50 % for CoPt-NPs with  $X_{\text{Pt}} =$

0.5 (Figure 73). This tendency for  $X_{Pt} < 0.5$  could be related to the dilution of the active platinum surface atoms by inactive cobalt surface atoms when the Pt shell is incomplete.

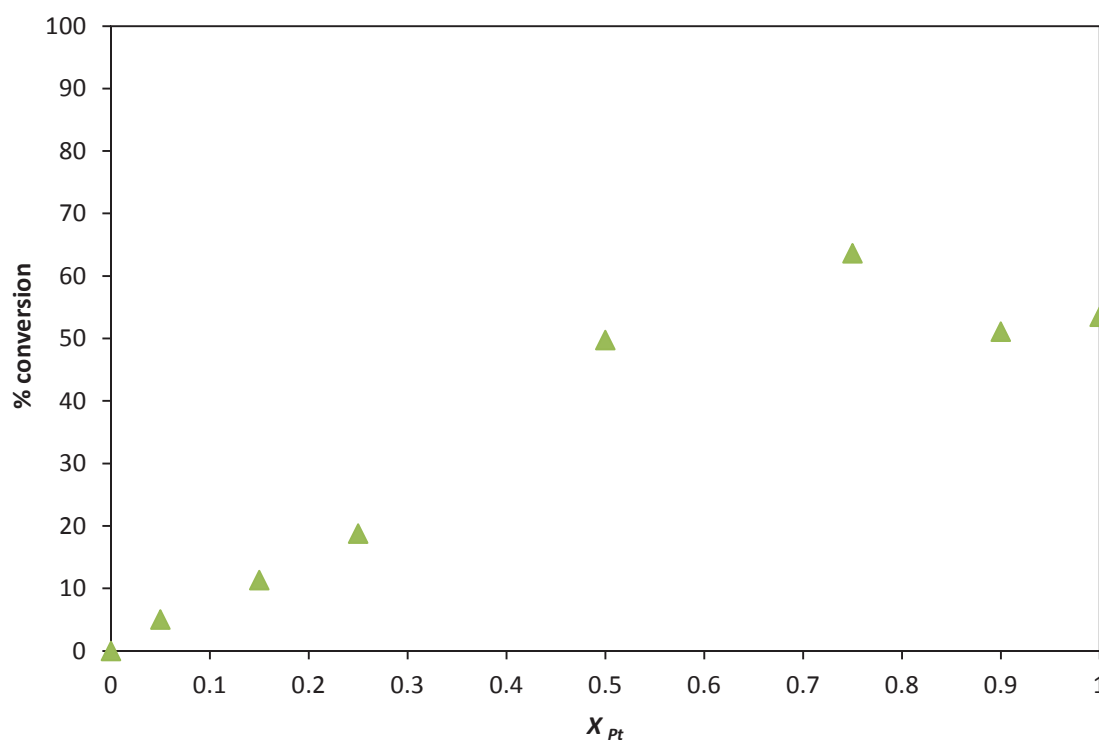


Figure 72 : Conversion of cyclohexadiene after 30 min under  $H_2$  (0.12 MPa), at room temperature plotted as a function of  $X_{Pt}$ .

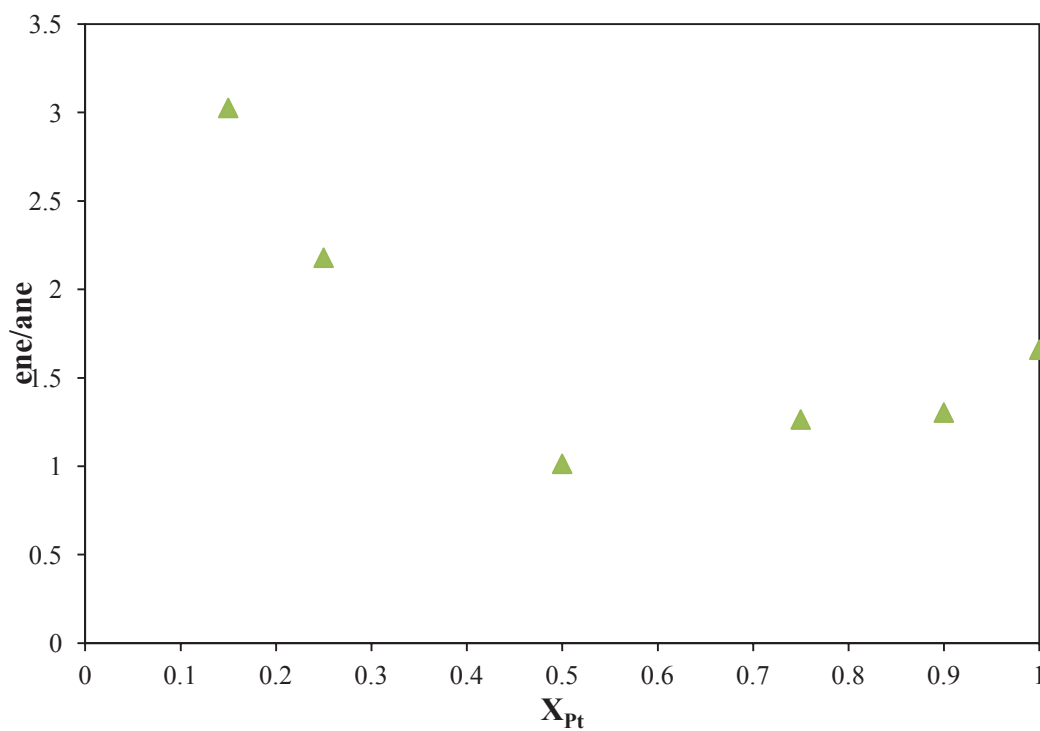


Figure 73 : cyclohexene/cyclohexane ratio as a function of  $X_{Pt}$ .

As a conclusion, the activity and selectivity of Co-NPs, Pt-NPs, and CoPt-NPs in the hydrogenation of cyclohexadiene are consistent with Dupont's work,<sup>60</sup> confirming that the generated NPs are bimetallic and that the Pt atoms are likely to be located on the NP surface.

## **II-B. V. Conclusion**

The successive or simultaneous decomposition of two OM precursors in an IL may lead to the formation of bimetallic NPs if the intermediate monometallic NPs have hydrides on their surface.<sup>27</sup> For this reason, the existence of [Co]-H was demonstrated by 2 experiments.

The first experiment consisted in exposing tetramethyltin to a freshly prepared suspension of Co-NPs in  $C_1C_4ImNTf_2$  under Ar. The presence of methane in the gaseous atmosphere was detected and quantified by GC. This methane production was attributed to the presence of surface hydrides on the Co-NPs.

In a second test, the catalytic properties of the Co-NPs with respect to ethylene hydrogenation were evaluated under Ar. Once again, a quantitative analysis of the gas phase revealed the formation of ethane, which resulted from the hydrogenation of ethylene by the surface hydrides of the Co-NPs.

Both experiments gave consistent results that were used to estimate the total concentration of surface hydrides to be  $1.7-1.8 \times 10^{-4}$  mol.  $L^{-1}$ . Even if this represents only a few % of Co atoms on the Co-NP surface, it was sufficient to initiate the deposition of Ru on the Co-NPs by adding Ru (COD) (COT) to the suspension. Indeed, TEM analysis showed a significant increase in the size of the NPs after the reaction. Similarly, a solution of Co(COD)(COE) reacted with a Ru-NPs suspension, which is known to have surface hydrides.<sup>90</sup>

In a final approach, the synthesis of CoRu-NPs was attempted by simultaneous decomposition of the two precursors in solution (one pot synthesis). Different Co/Ru ratios were tested, while fixing the total metal content. In all cases, monodispersed suspensions were obtained, some having a smaller NP size than the pure metals. This behavior, which has been observed in other bimetallic systems, is a good indication for the formation of bimetallic NPs rather than the separate precipitation of the two metals.

For the synthesis of CoPt-NPs, the most effective Pt precursor was  $\text{Pt}(\text{dba})_2$ , a  $\text{Pt}^{(0)}$  precursor. Initially, a two-step synthesis was attempted by adding  $\text{C}_1\text{C}_4\text{ImNTf}_2$  solution of  $\text{Pt}(\text{dba})_2$  to a suspension of Co-NPs in the same IL. After 24 h under Ar, TEM observations clearly showed the presence of two populations of NPs, one centered at 5 nm (probably Co or CoPt) and the other centered at 1 nm, which did not exist in the initial suspension. A STEM/EDX examination confirmed that the latter population corresponded to Pt-NPs.

To complete this study, a one-step synthesis was attempted. As in the case of the CoRu system, different Co/Pt ratios were tested, while maintaining the total metal content constant. Unlike the two-steps synthesis, monodispersed suspensions were obtained in all cases. Again, a monotonic variation in the size of the NPs against the metal composition was observed. For some bimetallic suspensions, the NP size was smaller than that of the two pure metals. This shows that bimetallic NPs have been obtained. To verify this, suspensions were analyzed by ASAXS at the ESRF. The results are still being exploited. Furthermore, these NPs have been tested as catalysts for the hydrogenation of cyclohexadiene. These tests showed that the reactivity increased sharply with the Pt content up to  $X_{\text{Pt}} = 0.5$ , then it saturated. This could correspond to the formation of a complete shell of Pt around the cores of Co for  $X_{\text{Pt}} \geq 0.5$ .



# Chapter III.

---

## Iron Nanoparticles (Fe-NPs)



Magnetic Iron and iron oxides nanoparticles have an extended use in many practical applications. For example, zero-valent iron (ZVI) finds large application as an efficient tool for removal of heavy metals and microorganisms from soils and water. The high magnetic moment of iron, its high saturation magnetization ( $MS$ ) at room temperature ( $218 \text{ emu}\cdot\text{g}^{-1}$ ) and high Curie temperature ( $770^\circ\text{C}$ ) makes  $\text{Fe}^{(0)}$ -NPs a very important candidate in magnetic fluids, energy storage and medical applications. Furthermore, the rhombohedral iron oxide (hematite,  $\alpha\text{-Fe}_2\text{O}_3$ ) is the most widely used magnetic material in industry, because the particle's morphology and size allow tuning their physical properties. Another very useful form of iron oxide is the cubic form (maghemite,  $\gamma\text{-Fe}_2\text{O}_3$ ). Its small nanoparticles ( $< 20 \text{ nm}$ ) are used in biomedical applications due to their superparamagnetism and biocompatibility.<sup>151</sup>

Some physical or chemical methods are already reported in the literature for the synthesis of  $\text{Fe}^{(0)}$ -NPs.<sup>151</sup> Monodisperse  $\text{Fe}^{(0)}$ -NPs with sizes under  $10 \text{ nm}$  were formed by reduction of  $\text{FeCl}_3$  in inverse micelles, by decomposition of an OM in the presence of a reducing agent ( $\text{H}_2$ ,  $\text{R}_3\text{B}\dots$ ) or by thermolysis of the OM.<sup>10, 105, 151, 152, 153, 154</sup>

### III.I. Synthesis of Fe-NPs from organometallic precursors

#### i. Synthesis of Fe-NPs in organic solvents

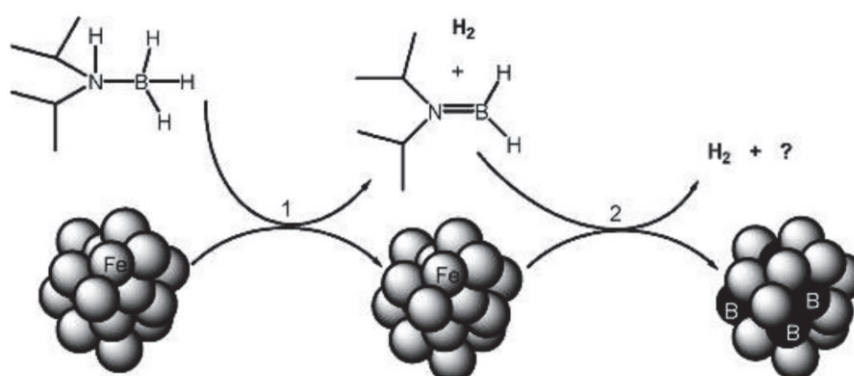
In organic solvent, Fe-NPs were usually synthesized by thermal, ultrasonic or photolytic decomposition of iron organometallic precursors like iron carbonyl compounds,  $[\text{Fe}(\text{CO})_5]$ ,  $\text{Fe}_2(\text{CO})_9$ , ferrocene,  $[\text{Fe}(\eta^5\text{-C}_5\text{H}_5)(\eta^5\text{-C}_6\text{H}_7)]$  or bis(bis(trimethylsilylamido)iron),  $[\text{Fe}[\text{N}(\text{SiMe}_3)_2]_2]_2$ .

Generally, the reduction of  $\text{Fe}^{(II)}$  into  $\text{Fe}^{(0)}$ -NPs requires high temperature ( $>100^\circ\text{C}$ ) and long reaction durations ( $> 12\text{h}$ , Table 8). In most studies under such conditions,  $\text{Fe}^{(0)}$ -NPs were immediately oxidized and surfactants were always needed to protect the generated nanoparticles against aggregation and oxidation, Table 8.

The Fe-NPs generated in organic solvents from  $[\text{Fe}[\text{N}(\text{SiMe}_3)_2]_2]_2$  required either reducing atmosphere ( $\text{H}_2$ ) and/or additives ( $i\text{Pr}_2\text{NH}\text{-BH}_3$  or  $i\text{Pr}_2\text{NBH}_2$ , Table 8, entries 4-6, 8, 9, 13).<sup>105, 153, 155, 156, 157, 158</sup> Under  $\text{H}_2$  ( $0.4 \text{ MPa}$ ), in the presence of long chain amines and/or carboxylic acids (hexadecyl amine; oleic or palmitic acids) as ligands, the Fe-NP size was  $8.3$  and  $10.7 \text{ nm}$ , for temperatures of  $100$  and  $150^\circ\text{C}$ , respectively (Table 8, entries 4, 6). Varying the hexadecyl amine/palmitic acid ratio (from 0 to 1.8 equivalent) and the reaction time (from 2 to 21 days), it was also possible to change the NP sizes from  $1.5$  to  $27 \text{ nm}$ , and their



morphology from nano-spheres to nano-cubes or stars (Table 8, entry 13).<sup>154</sup> In all cases, the Fe-NPs exhibited a bcc structure and a magnetism of 210 emu.g<sup>-1</sup>. Smaller Fe-NPs (1.5 to 4 nm) were generated depending on the amount of *i*Pr<sub>2</sub>NHBH<sub>3</sub> and the reaction temperature (the size increased with the amount of *i*Pr<sub>2</sub>NHBH<sub>3</sub>, Table 8, entries 5, 7-9). Note that this reducing compound acted also as a stabilizing agent of Fe-NPs, (Table 8, entries 7, 8).<sup>157</sup> These smaller Fe-NPs exhibited higher magnetism than the larger ones. An original polytetrahedral structure was proposed.<sup>59</sup> The main drawback of using *i*Pr<sub>2</sub>NHBH<sub>3</sub> was the inclusion of boron atoms, as shown by EXAFS and Mossbauer spectrometry. This resulted from the reaction of the amino-borane byproduct onto the surface of the primarily formed Fe-NPs (Scheme 7).



Scheme 7 : Proposed steps for boron incorporation.<sup>157</sup>

Under similar experimental conditions, Fe( $\eta^5$ -C<sub>5</sub>H<sub>5</sub>)( $\eta^5$ -C<sub>6</sub>H<sub>7</sub>) yielded larger Fe-NPs (14 to 16 nm) with a broad size distribution, (Table 8, entry 3). Even if no boron contamination was detected, their weaker magnetic moment (150 emu.g<sup>-1</sup>) suggested the presence of residual ligands on the NP- surface.<sup>155, 159</sup>

Fe(CO)<sub>5</sub>, a volatile and unstable compound, was easily decomposed into Fe-NPs upon heating, sonication or microwave irradiation under inert atmosphere . For example, Fe-NPs of 8 nm were formed under ultrasonic irradiation of a solution of Fe(CO)<sub>5</sub> in hexadecane in the presence of oleic acid, (Table 8, entry 1).<sup>160, 161</sup> Upon adding a polymer and anisole, two NP populations were formed, a smaller one (1.8-1.9 nm) with a very narrow size distribution ( $\pm 0.1$ nm) and a larger one  $> 8$ nm, (Table 8, entry 2).<sup>105, 156, 161</sup> In all cases with this carbonyl precursor, there are always some risks to get some metal carbides.<sup>58</sup> Indeed, these Fe-NPs exhibited a significantly weaker magnetic moment (101 emu.g<sup>-1</sup>) attributed to the coordination of carbonyl ligands on the NP surface, as previously noticed in the case of Co-NPs formed from the corresponding carbonyl precursor.<sup>50</sup>

Table 8 : Size, shape, crystal structure and magnetic moment of Fe-NPs prepared through the decomposition of various Fe precursors under different experimental conditions.

Entry	P (MPa)	$\Theta$ (°C)	Precursor	Medium	Duration	Size / Shape	Structure	Magnetism (emu.g <sup>-1</sup> )	Ref
1	--	Ultrasonic irradiation, 30 °C	Fe(CO) <sub>5</sub>	Hexadecane/oleic acid	1 h	8 nm	bcc	101	160
2	--	Sonication at R.T	Fe(CO) <sub>5</sub>	Anisol / PPO		1,9±0,1 (together with larger particles >8nm)	bcc (+ fcc for larger particles)	---	161
3	0.2	130 110	[Fe(C <sub>5</sub> H <sub>5</sub> )(C <sub>6</sub> H <sub>7</sub> ) <sub>2</sub> ]	oleic acid / mesitylene	2 days 3 days	16±1,5 nm 14.2±1.8	bcc	150	155 159
4	0.4	150	[Fe[N(SiMe <sub>3</sub> ) <sub>2</sub> ] <sub>2</sub> ] <sub>2</sub>	Mesitylene/ hexadecylamine + oleic acid	48 h	8.3 nm nanocubes	bcc	212	162
5	0.4	110		organic polymer matrix	12 h	1,8 nm nanoparticles	Polytetrahedral structure	259	105, 156
6		150	[Fe[N(SiMe <sub>3</sub> ) <sub>2</sub> ] <sub>2</sub> ] <sub>2</sub>	long chain acid and amine ligands	48 h	8.4 nm nanocubes	bcc	214	
7	No	R. T	[Fe[N(SiMe <sub>3</sub> ) <sub>2</sub> ] <sub>2</sub> ] <sub>2</sub>	Toluene/2.2 equiv. <i>i</i> Pr <sub>2</sub> NHBH <sub>3</sub>	overnight	3–3.5 nm	Polytetrahedral structure	---	157
8	0.4	110	[Fe[N(SiMe <sub>3</sub> ) <sub>2</sub> ] <sub>2</sub> ] <sub>2</sub>	Toluene/0.16-1.6 equiv. <i>i</i> Pr <sub>2</sub> NHBH <sub>3</sub>		2.8, 3.4, 3.5, 4 nm ( <i>i</i> Pr <sub>2</sub> NHBH <sub>3</sub> )			
9	0.4	150	[Fe[N(SiMe <sub>3</sub> ) <sub>2</sub> ] <sub>2</sub> ] <sub>2</sub>	mesitylene	12 h	1.5±0.2 nm	Polytetrahedral structure		153, 158
10		150			2 days	8,7±0.5 nm	bcc	212	
11	No	135	[Fe[N(SiMe <sub>3</sub> ) <sub>2</sub> ] <sub>2</sub> ] <sub>2</sub>	Mesitylene/ hexadecylammonium chloride+ hexadecylamine	4 days	10.4±0.8 nm			163
12		120			7 days	10.7±0.5 nm			
13	0.4	100 - 150	[Fe[N(SiMe <sub>3</sub> ) <sub>2</sub> ] <sub>2</sub> ] <sub>2</sub>	Mesitylene/ hexadecylamine+ palmitic acid (0-1,8 equiv)	2 – 21 days	1.5 to 27 nm spheres, cubes, or stars	bcc	---	154

## ii. Synthesis of Fe-NPs in ionic liquids

Several attempts have been reported in the literature for the preparation of Fe-NPs in ILs, using PVD (Table 9, entry 1),<sup>71</sup> decomposition of iron(0) organometallic precursors (Table 9, entries 2–7) or reduction of iron(III) salts (Table 9, entries 8–10). Fe(CO)<sub>5</sub> was the most commonly used precursor. With this precursor, the generated NPs were mainly oxidized and their size and shape showed some dependence on the chosen IL and the reduction conditions with no general tendency (Table 9, entries 2-5). The formation of Fe<sup>(0)</sup>-NPs was only reported

in  $C_1C_4ImBF_4$  at  $250^\circ C$  under argon (Table 9, entry 6). However, no convincing analytic data were reported confirming the zero valence of Fe.

Iron monoxide NPs, FeO-NPs, were formed during the decomposition of  $Fe(COT)_2$  under 0.5 MPa  $H_2$  at  $75^\circ C$  in  $C_1C_4ImNTf_2$  (Table 9, entry 7). Dupont, *et al*<sup>164</sup> attributed this to the presence of residual water confined in the IL, less than 300 ppm.<sup>165</sup>

Another synthetic approach was based on the chemical reduction of  $Fe^{(III)}$  salts (Table 9, entries 8-10). While the microwave hydrothermal synthesis from  $Fe(NO_3)_3 \cdot 9H_2O$  in  $C_1C_4ImBF_4$  afforded  $\alpha$ -FeOOH (Table 9, entry 8), the authors claimed the formation of Fe-NPs by reduction of  $FeCl_3 \cdot 6H_2O$  (Table 9, entries 9, 10) even in the presence of water (Table 9, entry 10). It should be noted that the later results were obtained in fluorinated ILs ( $C_1C_1C_4ImNTf_2$ ,  $C_1C_{cyanopropyl}ImNTf_2$ ,  $C_1C_1C_{cyanopropyl}ImNTf_2$ ,  $C_1C_nImPF_6$ ,  $C_1C_nImBF_4$ ), even if some of them are known to produce HF in the presence of water.

Additionally, Janiak, *et al*<sup>166</sup> observed that the decomposition of iron amidinate,  $Fe[MeC(NiPr)_2]_2$ ,  $Fe(AMD)_2$ , in fluorinated ILs yielded a mixture of large  $FeF_2$ -NPs (~70 nm) and smaller Fe-NPs with a broad size distribution (from 7 to 12 nm) while only Fe-NPs were observed when or non-fluorinated ILs were used. This result increased the doubts on the nature of the Fe-NPs obtained from  $FeCl_3$  in fluorinated ILs (Table 9, entry 10).

As a conclusion, by contrast with organic solvents, the formation of  $Fe^{(0)}$ -NPs in ILs was not straightforward as the few reported attempts to date show some uncertainties. Additionally, there was a lack of data concerning the magnetic properties of  $Fe^{(0)}$ -NPs prepared in ILs.

Table 9 : Size and oxidation state of Fe-NPs prepared through the decomposition of various Fe precursors in several ILs.

Entry	Precursor	IL	Exp Cond	NPs	Size (nm)	Characterization	Ref
1	Fe	C <sub>1</sub> C <sub>4</sub> ImNTf <sub>2</sub>	PVD	Fe <sup>(0)</sup>	??		71, 167
2	Fe(CO) <sub>5</sub>	C <sub>1</sub> C <sub>2</sub> ImBF <sub>4</sub>	Ultrasonication, 0°C, air	Fe <sub>2</sub> O <sub>3</sub>	2-6	XRD, XPS, SEM, TEM, VSM	168
3	Fe(CO) <sub>5</sub>	C <sub>1</sub> C <sub>8</sub> ImBF <sub>4</sub>	Δ 90°C, air	Fe <sub>2</sub> O <sub>3</sub>	length 30±9.7, width 5.7±1.8	XPS, TEM, IR	169
4	Fe(CO) <sub>5</sub>	C <sub>1</sub> C <sub>4</sub> ImNTf <sub>2</sub>	Δ 280°C, Ar	Fe <sub>2</sub> O <sub>3</sub>	10.6±1.6	PXRD, TEM, IR, TGA	170
5	Fe(CO) <sub>5</sub>	C <sub>1</sub> C <sub>4</sub> ImBF <sub>4</sub>	250°C, air	Fe <sub>2</sub> O <sub>3</sub>	4.2±1.1	TEM, TED, DLS	152
6	Fe(CO) <sub>5</sub>	C <sub>1</sub> C <sub>4</sub> ImBF <sub>4</sub>	250°C, Ar	Fe <sup>(0)</sup>	5.2±1.6	TEM, TED, DLS	152, 164
7	Fe(COT) <sub>2</sub>	C <sub>1</sub> C <sub>4</sub> ImNTf <sub>2</sub>	0.5 MPa H <sub>2</sub> , 75°C	FeO	5.3±1.6	TEM, XANES, EXAFS	164
8	Fe(NO <sub>3</sub> ) <sub>3</sub> ·9H <sub>2</sub> O	C <sub>1</sub> C <sub>4</sub> ImBF <sub>4</sub>	Microwave hydrothermal preparation, 160°C	α- FeOOH	~1000	PXRD, SEM, TEM, PPMS, BET	171
9	FeCl <sub>3</sub>	C <sub>1</sub> C <sub>1</sub> C <sub>4</sub> ImNTf <sub>2</sub> C <sub>1</sub> C <sub>BCN</sub> ImNTf <sub>2</sub> , C <sub>1</sub> C <sub>1</sub> C <sub>BCN</sub> ImNTf <sub>2</sub>	Stirring with EtMgCl in THF, R.T, Ar	Fe <sup>(0)</sup>	~5	TEM	172
10	FeCl <sub>3</sub> ·6H <sub>2</sub> O	C <sub>1</sub> C <sub>n</sub> ImPF <sub>6</sub> , C <sub>1</sub> C <sub>n</sub> ImBF <sub>4</sub>	Reduction by NaBH <sub>4</sub> in IL/water medium	Fe <sup>(0)</sup>	20±4	PXRD, TEM	173
11	[Fe(AMD) <sub>2</sub> ] <sub>2</sub>	BF <sub>4</sub> , NTf <sub>2</sub> , TfO ILs	Microwave heating (240°C)	FeF <sub>2</sub>	68-72	PXRD, TEM, EDX	166
		C <sub>1</sub> C <sub>4</sub> ImTos		Fe <sup>(0)</sup>	7-12		

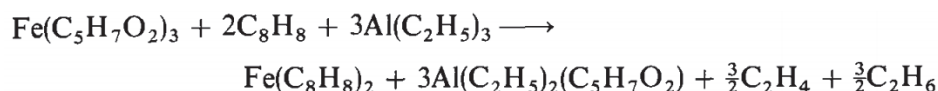
### III.II. Selection and synthesis of Fe organometallic precursors

From the literature survey, several iron precursors thus show some concerns such as the possible carbide formation in case of Fe<sup>(0)</sup> carbonyls and the difficult reduction of Fe<sup>(III)</sup> salts. Organometallic precursors are probably better candidates. Among them, bis(1,3,5,7-cyclooctatetraene) iron(0), Fe(COT)<sub>2</sub>, and bis(bis(trimethylsilylamido) Iron (II),

$\{\text{Fe}^{\text{II}}[\text{N}(\text{SiMe}_3)_2]_2\}_2$ , were selected for this study as possible precursors for the synthesis of Fe-NPs in ILs. Indeed, the decomposition of these precursors under  $\text{H}_2$  is expected to generate either fully or partially volatile hydrogenated hydrocarbons as by-products. These volatile compounds can be easily removed under vacuum. To determine the optimal decomposition conditions under hydrogen, their thermal stability was monitored by coupled DRIFT and GC–mass techniques first in the solid state (pure precursor), then in solution in the considered IL. Based on these results, the experimental conditions (time and temperature) were adapted for each precursor. The Fe-NPs syntheses were conducted in  $\text{C}_1\text{C}_4\text{ImNTf}_2$  IL, as well as in  $\text{C}_1\text{C}_2\text{ImNTf}_2$ ,  $\text{C}_1\text{C}_2\text{ImB}(\text{CN})_4$  and  $\text{C}_1\text{C}_2\text{ImFAP}$ . Preliminary characterizations were performed by TEM, EDX and HRTEM techniques. Magnetism and WAXS experiments are still need to be considered in the future.

**i. Bis(1,3,5,7-Cyclooctatetraene) iron(0),  $\text{Fe}(\text{COT})_2$**

$\text{Fe}(\text{COT})_2$ , is usually prepared through the reduction of anhydrous iron(III) chloride with the isopropyl Grignard reagent in the presence of cyclooctatetraene.<sup>174</sup>



Obtained as a black crystalline solid,  $\text{Fe}(\text{COT})_2$  is unstable toward atmospheric oxygen. It can be stored for several weeks in an inert atmosphere at room temperature, and for several months at  $-40^\circ\text{C}$  without significant decomposition.  $\text{Fe}(\text{COT})_2$  is soluble in diethyl ether and common aliphatic and aromatic solvents but is less stable in solution and decomposes at room temperature within a few days even in rigorously inert atmosphere. Chlorinated hydrocarbons rapidly decompose  $\text{Fe}(\text{COT})_2$ . Its solid-state structure established by x-ray crystallography shows that the Fe atom is five-coordinated and is linked through  $\pi$ -bonds to six carbon atoms of one ring and four of the other.<sup>174</sup>

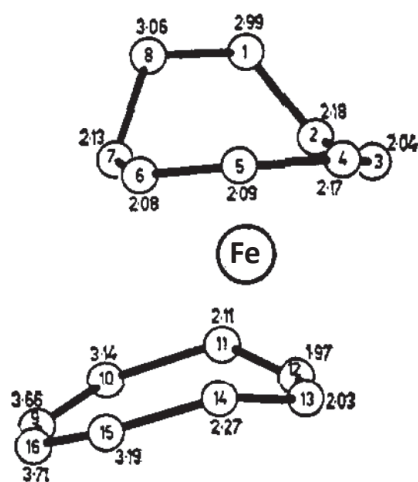
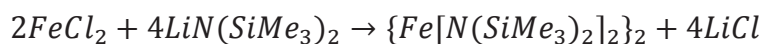


Figure 74 : crystal structure of  $\text{Fe}(\text{COT})_2$  as reproduced from ref.<sup>175</sup>

**ii. Bis(bistrimethylsilylamido)Iron(II),  $\{\text{Fe}^{\text{II}}[\text{N}(\text{SiMe}_3)_2]_2\}_2$**  (Collaboration Pr S. Daniele)

$\{\text{Fe}^{\text{II}}[\text{N}(\text{SiMe}_3)_2]_2\}_2$  used in this work has been synthesized by K. Soussi, a former PhD student from Pr. S. Daniele's Laboratory

$\{\text{Fe}^{\text{II}}[\text{N}(\text{SiMe}_3)_2]_2\}_2$  was prepared by the reaction of  $\text{FeCl}_2$  with lithium bis(trimethylsilyl) amide  $\text{LiN}(\text{SiMe}_3)_2$  in ether and then purified by distillation at 90-100°C (0.01 mmHg) as a green oil that crystallize at room temperature.<sup>176, 177, 178</sup>



$\{\text{Fe}^{\text{II}}[\text{N}(\text{SiMe}_3)_2]_2\}_2$  is an extremely air and moisture sensitive light-green solid (m. p. 36-38°C). It is very soluble in hexane and toluene, while THF binds to the iron center to produce a three-coordinated THF adduct  $\{(\text{THF})\text{Fe}[\text{N}(\text{SiMe}_3)_2]_2\}$ . The product crystallize as a dimer (Figure 75),<sup>177</sup> while the monomeric form dominates in solution at room temperature.

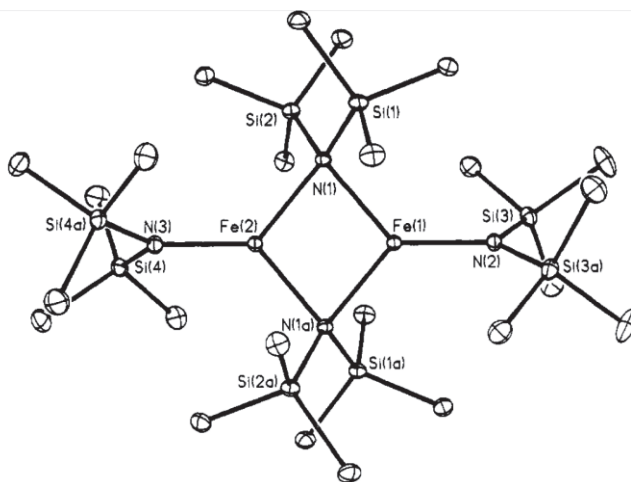


Figure 75 : crystal structure of  $\{\text{Fe}^{\text{II}}[\text{N}(\text{SiMe}_3)_2]_2\}_2$  as reproduced from ref.<sup>177</sup>

### III.III. Synthesis of Fe-NPs from the Fe(COT)<sub>2</sub>

#### i. Thermal decomposition of Fe(COT)<sub>2</sub> under H<sub>2</sub>

As for Co(COD)(COE), Fe(COT)<sub>2</sub> was expected to decompose under H<sub>2</sub>, affording Fe-NPs in addition to some hydrogenated derivatives of cyclooctatetraene. In order to confirm this reaction and to identify the best decomposition conditions, the thermal stability of Fe(COT)<sub>2</sub> under H<sub>2</sub> was first studied, both in the solid phase and in solution in IL.

The reaction of the solid Fe(COT)<sub>2</sub> under H<sub>2</sub> at room temperature was tentatively monitored by DRIFT. However, because of its black color, no clear IR spectrum could be obtained due to saturation. Consequently, the reaction was monitored by GC-MS. The GC-MS spectrum (Figure 76, a) represents the evolution of the integrated peak areas of the evolved compounds, under 0.4 MPa of H<sub>2</sub>, at 25°C as a function of time. During the first 2h, only cyclooctatetraene and cyclooctatriene were present. The cyclooctatetraene peak area was roughly constant while the cyclooctatriene peak area increased monotonously. After 2h, a sharp decrease of the cyclooctatetraene and cyclooctatriene was observed together with the appearance of new peaks corresponding to cyclooctene and cyclooctane. The latter indicate the hydrogenation of the cyclooctatetraene and cyclooctatriene ligands. Such hydrogenation reaction, in these experimental conditions, ought to be catalyzed by zero-valent metallic species like Co, Pt or Fe.<sup>158, 179, 180</sup> Hence, this hydrogenation reaction could indicate the formation of metallic Fe<sup>(0)</sup> as a result of the reaction of Fe(COT)<sub>2</sub> with H<sub>2</sub>.

To investigate if the same behavior was maintained in IL solution, the reaction of a solution of Fe(COT)<sub>2</sub> ( $2.5 \times 10^{-3} \text{ mol.L}^{-1}$ ) in C<sub>1</sub>C<sub>4</sub>ImNTf<sub>2</sub>, heated at 150°C, under 0.4MPa H<sub>2</sub> was monitored by GC-mass (Figure 76, b). The chosen experimental conditions were identical to those reported by Dupont.<sup>164</sup> As compared to the solid phase, the apparition of the products was faster due to the higher temperature, but their order of appearance was the same. During the initial reaction stages, only cyclooctatetraene (grey curve) and cyclooctatriene (green curve) were observed. After 30 min, partially hydrogenated cyclooctadiene and cyclooctene were formed. For all these unsaturated products, the peak areas reached a maximum after 2h, and then all sharply decreased. Simultaneously, the peak area of cyclooctane which was initially the smallest, remained fairly steady until 4h. After that point, its peak area increased sharply, suggesting a large conversion of all derivatives into cyclooctane, (Figure 76, b). Nevertheless, it should be noted that the hydrogenation rates were

much slower in solution. This might be related to the fact that less  $\text{Fe}^{(0)}$  was formed as compared with the solid case.

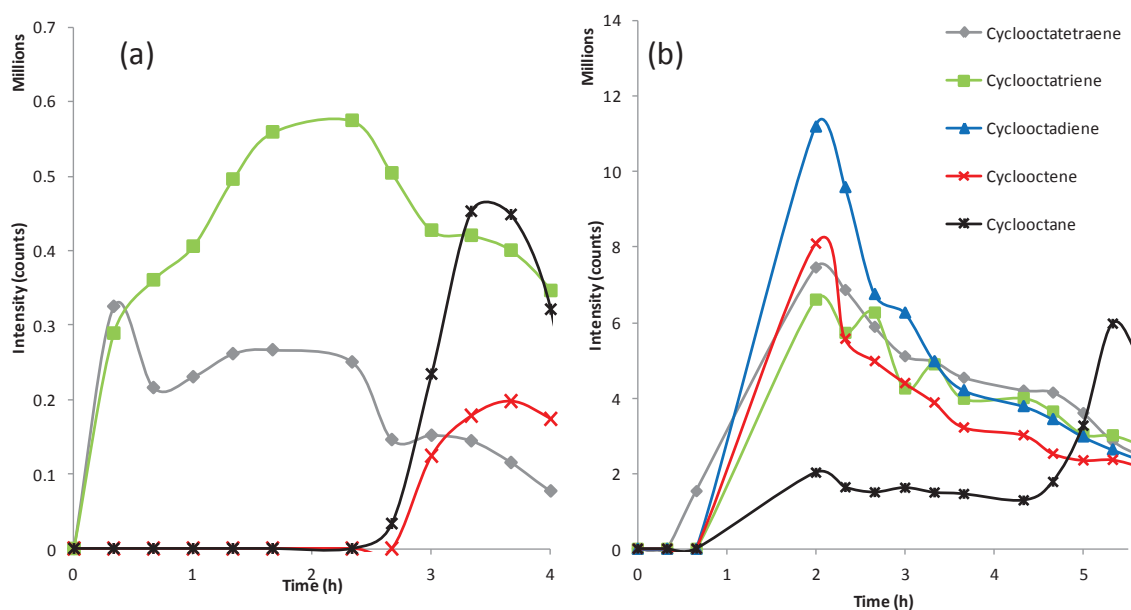


Figure 76 : Integrated GC-MS peak areas of different  $\text{H}_2$  decomposition byproducts of (a) solid  $\text{Fe}(\text{COT})_2$ , (0.4 MPa  $\text{H}_2$ , 25°C) and (b) solution of  $\text{Fe}(\text{COT})_2$  ( $2.5 \times 10^{-3} \text{ mol.L}^{-1}$ ) in  $\text{C}_1\text{C}_4\text{ImNTf}_2$ , (0.4 MPa  $\text{H}_2$ , 150°C), plotted versus time.

## ii. Reaction of $\text{Fe}(\text{COT})_2$ solutions with $\text{H}_2$

Based on these results, Fe-NPs formation was attempted through the decomposition of solutions of  $\text{Fe}(\text{COT})_2$  in  $\text{C}_1\text{C}_4\text{ImNTf}_2$ . Since  $\text{Fe}(\text{COT})_2$  has a low solubility in  $\text{C}_1\text{C}_4\text{ImNTf}_2$ , adding pentane and heating up were necessary to obtain a partial solubility, Figure 77-left. Finally, solutions with concentrations between  $2.5 \times 10^{-2}$  and  $5 \times 10^{-3} \text{ mol.L}^{-1}$  could be obtained. Taking into account the above results concerning the thermal decomposition under  $\text{H}_2$ , the suspension was warmed at 150°C under 0.4 MPa of  $\text{H}_2$ . After 48 h, the solution became brownish with black precipitate (Figure 77-right).

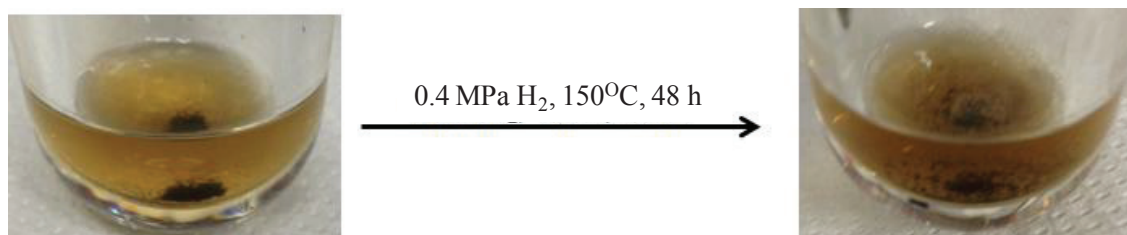


Figure 77 :  $2.5 \times 10^{-2} \text{ mol.L}^{-1}$  solution of  $\text{Fe}(\text{COT})_2$  in  $\text{C}_1\text{C}_4\text{ImNTf}_2$ , before (left) and after (right) the reaction with 0.4 MPa  $\text{H}_2$  for 48 h at 150°C.



The gaseous phase was collected after 4h and 48h from the start of the reaction. In both cases, the collected products were dissolved in acetonitrile and analyzed by GC. The chromatogram of the collected volatile products after 4h reaction time showed the presence of peaks identified as both cyclooctatetraene and cyclooctatriene. After 48 h, the gaseous phase contained only cyclooctane. These results are consistent with those of the thermal decomposition studies under  $H_2$  discussed above.

Furthermore, the TEM images in (Figure 78) shows that small monodispersed NPs of  $4.4\pm 0.5$  nm were formed.

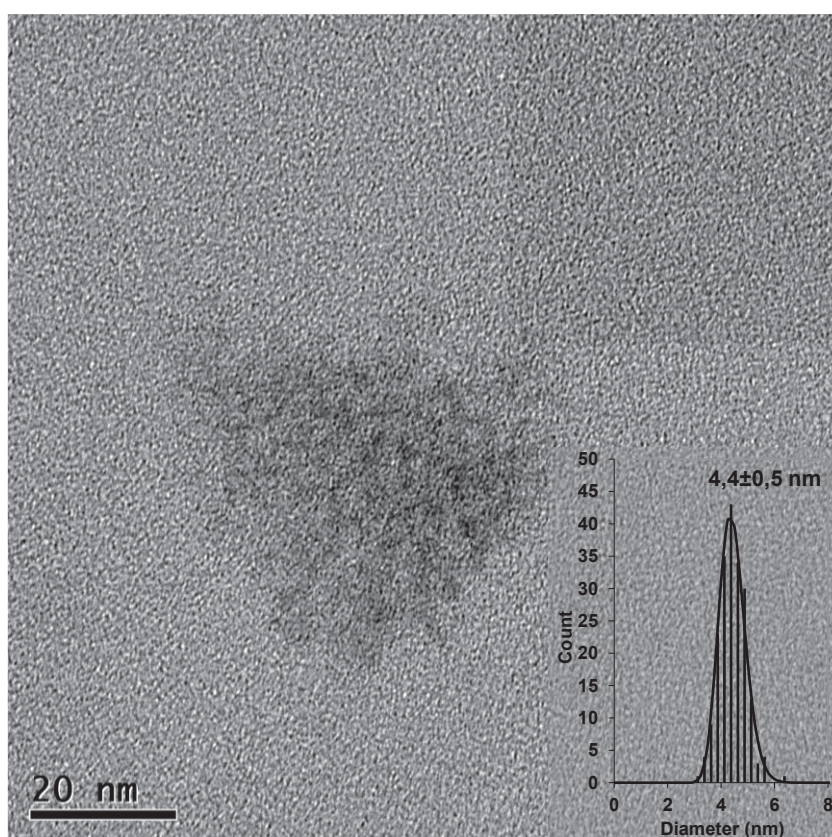


Figure 78 : TEM images of Fe-NPs ( $4.4\pm 0.5$ nm) prepared through the decomposition of  $5 \times 10^{-3}$  mol.L<sup>-1</sup> solution of  $Fe(COT)_2$  in  $C_1C_4ImNTf_2$  under 0.4MPa  $H_2$  for 48 h at 150°C.

### iii. Characterization of Fe-NPs

Upon switching into HRTEM, it was possible to get the fast Fourier transform patterns of these NPs and to compare them with all the known crystal structures of  $Fe^{(0)}$ , as well as with all the oxide, sulfide, fluoride, nitride and carbide forms of iron (Figure 79). Surprisingly, the lattice parameters were not matching with any of these forms of iron. Instead, they fit well with a tetragonal structure with lattice parameters of  $a = 6.8 \text{ \AA}$ ,  $c = 6.1 \text{ \AA}$ .

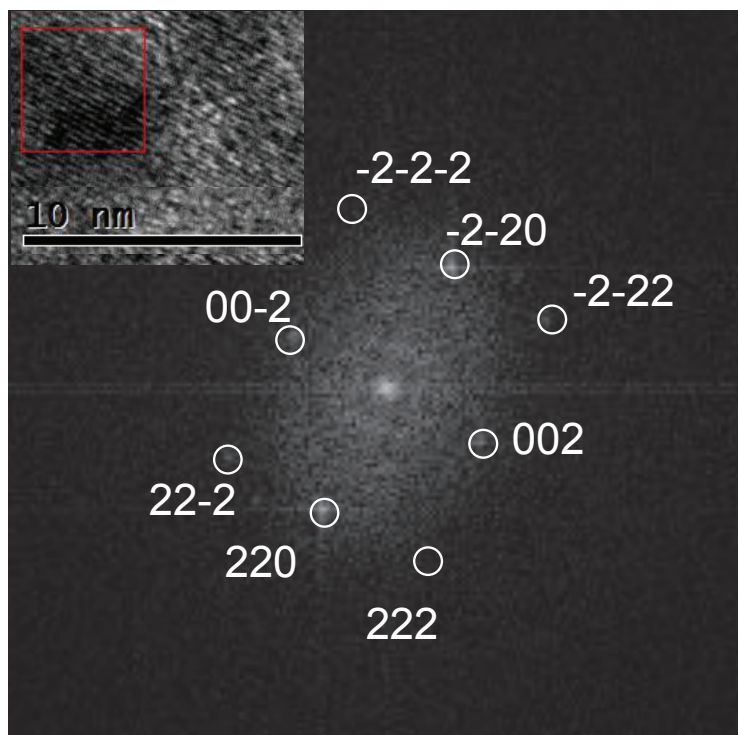


Figure 79 : HRTEM image of Fe-NP generated by the decomposition of  $\text{Fe}(\text{COT})_2$  in  $\text{C}_1\text{C}_4\text{ImNTf}_2$  and the FFT of the particle indexed by a tetragonal structure along the (-110) zone axis with lattice parameters of  $a=6.8\text{\AA}$ ,  $c=6.1\text{\AA}$ .

In order to explain that, 3 different possibilities were considered. The first assumption is the possible oxidation of the initially formed Fe-NPs by the  $\text{NTf}_2$  anion. Indeed, zero-valent iron can reduce sulfoxide functional groups. In order to verify that assumption, the synthesis of Fe-NPs was repeated again under exactly the same conditions but using ILs with different anions,  $\text{C}_1\text{C}_2\text{ImNTf}_2$ ,  $\text{C}_1\text{C}_2\text{ImB}(\text{CN})_4$ ,  $\text{C}_1\text{C}_2\text{ImFAP}$  where  $\text{B}(\text{CN})_4$  = tetracyanoborate, FAP = trifluorophosphate. The  $\text{B}(\text{CN})_4$  and FAP anions were chosen because they are not expected to act as oxidizing agents for the NPs while the  $\text{C}_1\text{C}_2\text{ImNTf}_2$  was considered as a control sample. At first sight, there was a difference in the size of the NPs obtained in these 3 ILs,  $4.5\pm 0.4$ ,  $5.5\pm 0.4$  and  $11.6\pm 0.8$  for  $\text{C}_1\text{C}_2\text{ImB}(\text{CN})_4$ ,  $\text{C}_1\text{C}_2\text{ImFAP}$  and  $\text{C}_1\text{C}_2\text{ImNTf}_2$  respectively (Figure 80). Back to the crystal structure, NPs formed in  $\text{C}_1\text{C}_2\text{ImB}(\text{CN})_4$  showed crystal parameters fitting with a cubic  $\text{Fe}_2\text{O}_3$  phase (Figure 81), indicating that it is not the IL anion that affects the oxidation state of the formed Fe-NPs.

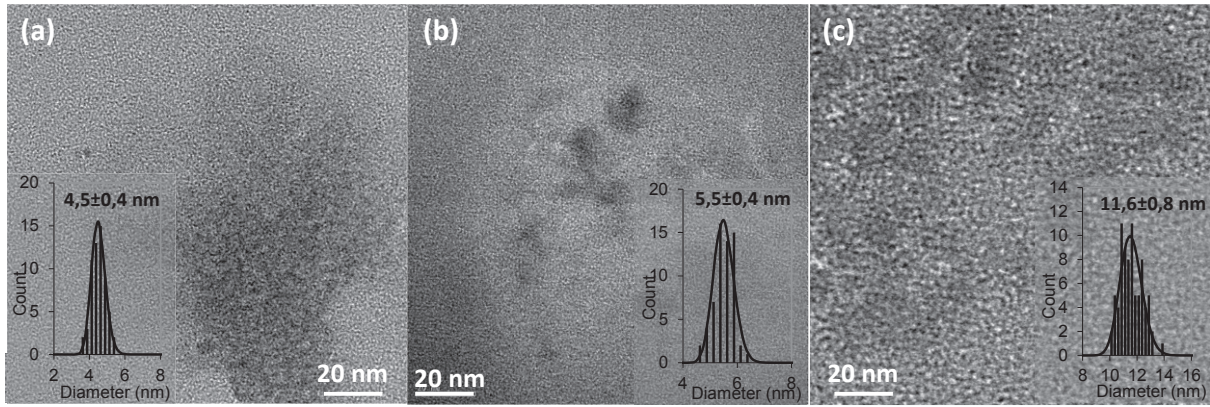


Figure 80 : TEM images for Fe-NPs prepared from the decomposition of  $\text{Fe}(\text{COT})_2$  in (a)  $\text{C}_1\text{C}_2\text{ImB}(\text{CN})_4$ , (b)  $\text{C}_1\text{C}_2\text{ImFAP}$  and (c)  $\text{C}_1\text{C}_2\text{ImNTf}_2$ .

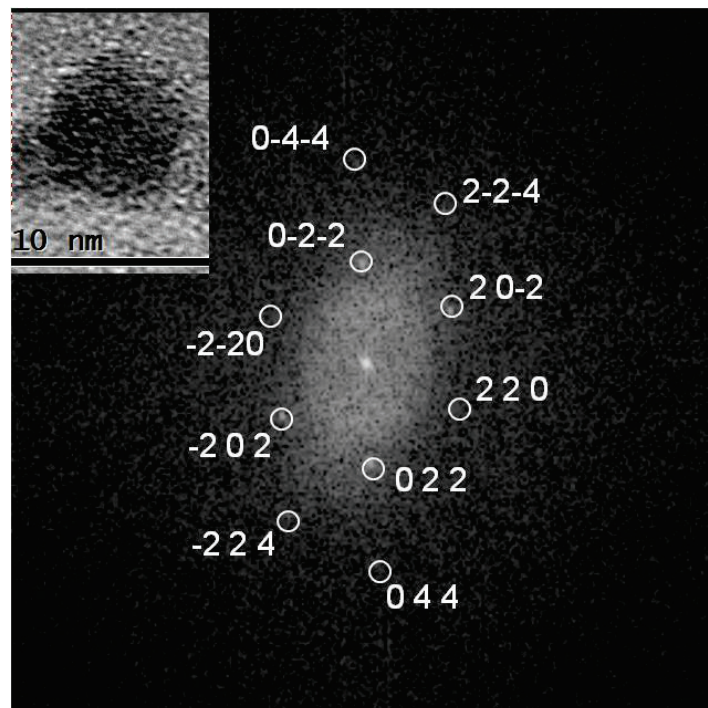


Figure 81 : HRTEM image of  $\text{Fe}_2\text{O}_3$ -NP generated by the decomposition of  $\text{Fe}(\text{COT})_2$  in  $\text{C}_1\text{C}_2\text{ImB}(\text{CN})_4$  and the FFT of the particle indexed by a cubic  $\text{Fe}_2\text{O}_3$  structure along the (1-11) zone axis with a lattice parameter of  $8.3\text{\AA}$ .

The second assumption is the possible oxidation of the Fe-NPs by residual water molecules that are confined within the IL structure. This phenomenon was reported by Dupont, *et al*<sup>164</sup> as responsible for the formation of FeO-NPs from  $\text{Fe}(\text{COT})_2$  in  $\text{C}_1\text{C}_4\text{ImNTf}_2$  under similar reducing conditions. In our point of view, this assumption could be probable in the case of NPs prepared in  $\text{C}_1\text{C}_2\text{ImB}(\text{CN})_4$  as they are clearly matching with a cubic  $\text{Fe}_2\text{O}_3$  structure. Even so, it is still questionable in the case of NPs prepared in  $\text{C}_1\text{C}_4\text{ImNTf}_2$  as they are not matching with any of the known iron oxide structures. In addition, zero-valent Co-NPs

as well as zero-valent Ta-NPs,<sup>181</sup> which are highly sensitive towards oxidation, were successfully prepared under similar conditions and in the same IL medium. They were stable for long periods in such media without being oxidized.

The last option could be that these are in fact metallic Fe-NPs but with an uncommon, non-compact structure of Fe, similar to the  $\epsilon$ -Co structure (Figure 79), which is not documented in crystallographic databases. In fact, a similar case was previously reported by Margeat, *et al.*,<sup>105</sup> for Fe<sup>(0)</sup>-NPs prepared by the thermal decomposition of  $\{\text{Fe}[\text{N}(\text{SiMe}_3)_2]_2\}_2$  in organic solvents. In their work, the WAXS-RDF analysis did not show the peak at 0.35 nm corresponding to a compact structure. Based on these results together with HRTEM and the Mossbauer experiments, they attributed this to an unordered polytetrahedral structure of metallic Fe that shows a WAXS-RDF response perfectly matching with that obtained from Co-NPs with an  $\epsilon$ -Co structure.

To conclude, the existence of a non-compact form of metallic Fe could be probable but this still has to be confirmed by WAXS, SQUID and Mossbauer techniques in order to distinguish it from iron oxides.

### III.IV. Synthesis of Fe-NPs from $\{\text{Fe}[\text{N}(\text{SiMe}_3)_2]_2\}_2$

This OM was chosen because it has been reported in the literature to decompose under H<sub>2</sub> in organic solvents to afford Fe-NPs (Table 8, run 4-13).<sup>39, 91, 92, 94, 95, 96, 100, 101</sup>

#### i. Thermal decomposition of $\{\text{Fe}[\text{N}(\text{SiMe}_3)_2]_2\}_2$ under H<sub>2</sub>

Similar to Fe(COT)<sub>2</sub>, the decomposition of solid  $\{\text{Fe}[\text{N}(\text{SiMe}_3)_2]_2\}_2$  under H<sub>2</sub> was first monitored by GC-MS, either as a pure compound or in solution in C<sub>1</sub>C<sub>4</sub>ImNTf<sub>2</sub> in order to recognize the reaction and the decomposition conditions. For the pure phase, 0.4 MPa of H<sub>2</sub> was applied at room temperature and the temperature was then raised by 1°C/min to 100°C then kept constant for 5 h. No volatile byproduct was detected until the temperature reached 65°C after *c.a.* 45 min (Figure 82, a). The only compounds detected were identified as (Me<sub>3</sub>Si)<sub>2</sub>O and Me<sub>3</sub>SiOH. Note that as these compounds were unexpected, but could be produced by a reaction of the volatile (Me<sub>3</sub>Si)<sub>2</sub>NH with the GC column. To verify this, a blank sample of (Me<sub>3</sub>Si)<sub>2</sub>NH in acetone was injected into the same GC column. Both (Me<sub>3</sub>Si)<sub>2</sub>O and Me<sub>3</sub>SiOH peaks were detected as well, confirming the interaction with the

column material. Therefore, the sum of these peak areas was used as an indication for the progress of the reaction as represented in Figure 82a.

Their peak areas were found to increase sharply with temperature. The curve reached a peak 30 min after the temperature was stabilized at 100°C (i.e. 2 h from the start of the experiment). As a conclusion, pure  $\{\text{Fe}[\text{N}(\text{SiMe}_3)_2]_2\}_2$  was determined to start decomposing at 65°C under  $\text{H}_2$ . This reaction was fast as the precursor was full decomposed after 2 h.

The decomposition of  $\{\text{Fe}[\text{N}(\text{SiMe}_3)_2]_2\}_2$  was then studied in solution in  $\text{C}_1\text{C}_4\text{ImNTf}_2$  ( $2.5 \times 10^{-2} \text{ mol.L}^{-1}$ , 0.4 MPa  $\text{H}_2$  and 100°C). The same products,  $(\text{Me}_3\text{Si})_2\text{O}$  and  $\text{Me}_3\text{SiOH}$ , were again observed (Figure 83, b). Following the evolution of the peak areas with time, the precursor in solution could be considered as fully decomposed after 2 h. (Figure 82b). Note that the residual pentane observed in this case is due to its use to facilitate the dissolution of  $\{\text{Fe}[\text{N}(\text{SiMe}_3)_2]_2\}_2$  in IL.

As a conclusion,  $\{\text{Fe}[\text{N}(\text{SiMe}_3)_2]_2\}_2$  was decomposing in  $\text{C}_1\text{C}_4\text{ImNTf}_2$  under 0.4 MPa  $\text{H}_2$  at 100°C. Minimum duration of 2 h is required to complete the reaction. Therefore, these decomposition conditions were applied in the subsequent section to prepare the Fe-NPs from this compound.

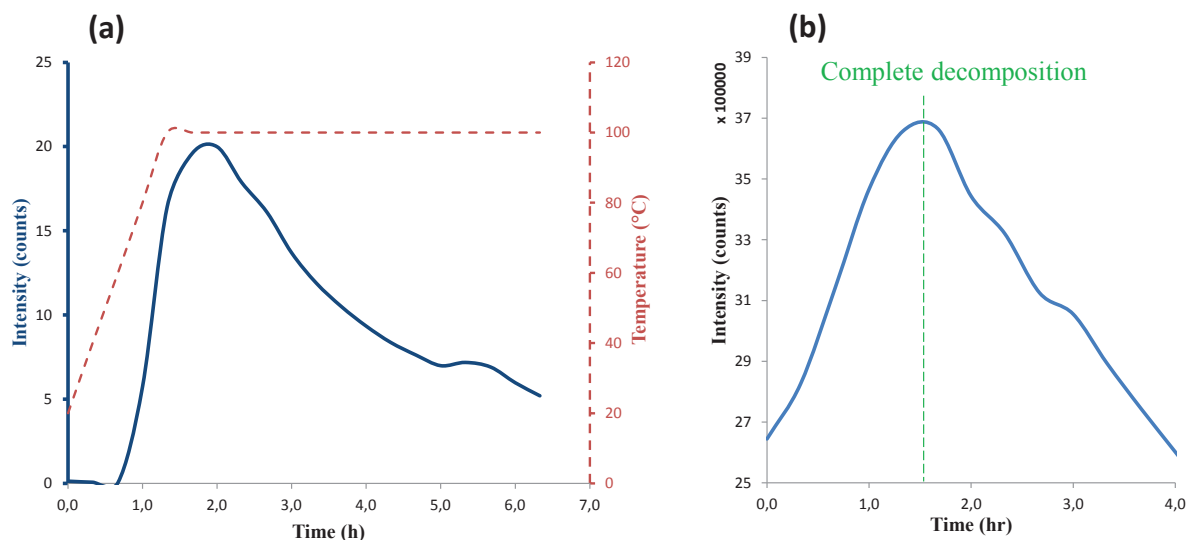


Figure 82 : Sum of integrated GC-MS peak areas of different  $\text{H}_2$  decomposition byproducts during the reaction of  $\text{H}_2$  (0.4MPa) with  $\{\text{Fe}^{\text{II}}[\text{N}(\text{SiMe}_3)_2]_2\}_2$  (a) in pure form starting at 25°C while raising T 1°C/min to 100°C and then keeping it constant for 5h, (b) in  $\text{C}_1\text{C}_4\text{ImNTf}_2$  solution ( $2.5 \times 10^{-2} \text{ mol.L}^{-1}$ , 100°C), plotted versus time.

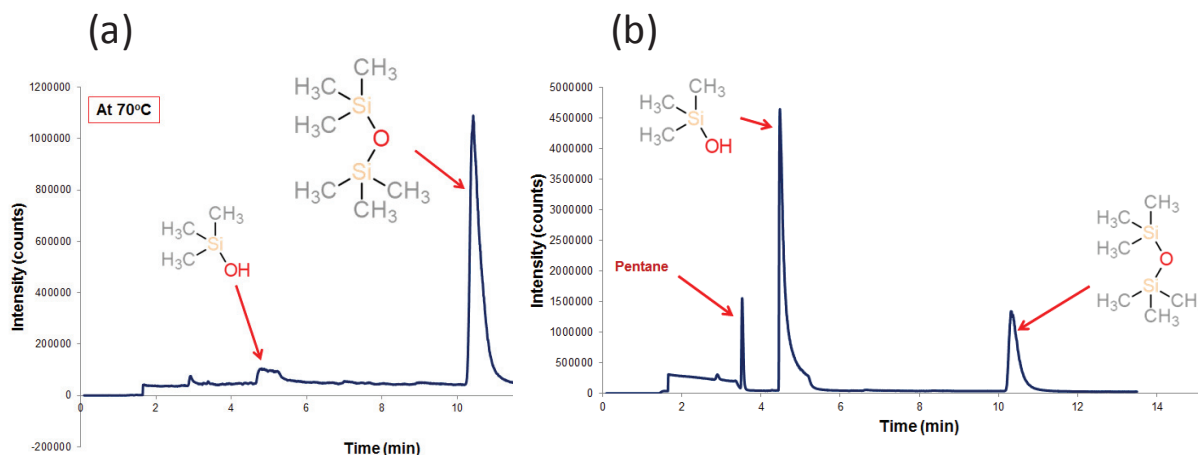


Figure 83 : GC-MS chromatograph recorded during the reaction with  $\text{H}_2$  (0.4MPa) of (a) solid  $\{\text{Fe}[\text{N}(\text{SiMe}_3)_2]_2\}_2$  (corresponding to  $70^\circ\text{C}$  reaction temperature) and (b)  $\{\text{Fe}[\text{N}(\text{SiMe}_3)_2]_2\}_2$  solution in  $\text{C}_1\text{C}_4\text{ImNTf}_2$  ( $2.5 \times 10^{-2} \text{ mole.L}^{-1}$ ,  $100^\circ\text{C}$ , after 1h of reaction).

## ii. Reaction of $\{\text{Fe}[\text{N}(\text{SiMe}_3)_2]_2\}_2$ solutions with $\text{H}_2$

In a first experiment, a  $2.5 \times 10^{-2} \text{ mol.L}^{-1}$  solution of  $\{\text{Fe}[\text{N}(\text{SiMe}_3)_2]_2\}_2$  in  $\text{C}_1\text{C}_4\text{ImNTf}_2$  was decomposed under 0.4MPa of  $\text{H}_2$  at  $100^\circ\text{C}$  for 4 h. After the reaction, the solution turned very black in color (Figure 84).

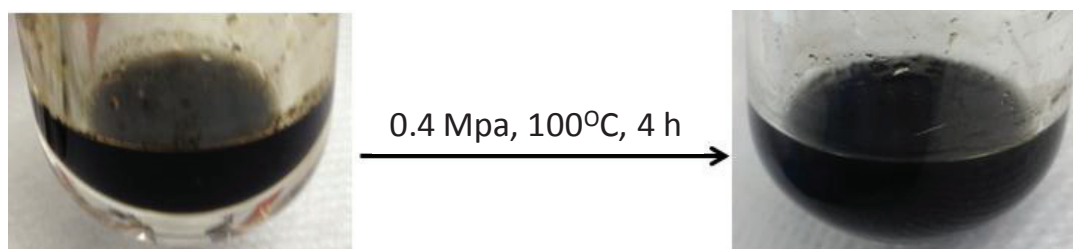


Figure 84 :  $2.5 \times 10^{-2} \text{ mol.L}^{-1}$  solution of  $\{\text{Fe}[\text{N}(\text{SiMe}_3)_2]_2\}_2$  in  $\text{C}_1\text{C}_4\text{ImNTf}_2$ , left: before and right: after, the reaction with 0.4MPa  $\text{H}_2$  for 4 h at  $100^\circ\text{C}$ .

Volatile products were also collected, dissolved in acetone and analyzed by GC. It should be noted that the GC column used in that case was different than that of the in situ-GC. It did not exhibit any reaction with the  $(\text{Me}_3\text{Si})_2\text{NH}$ . In that case, the obtained chromatogram confirms the formation of  $(\text{Me}_3\text{Si})_2\text{NH}$  as the main decomposition product together with traces of  $(\text{Me}_3\text{Si})_2\text{O}$  (Figure 85).

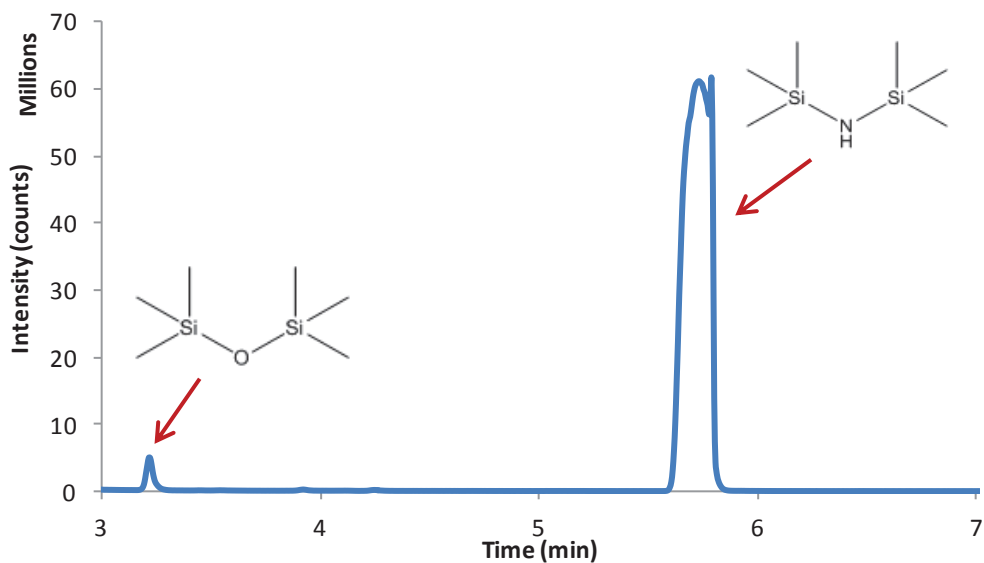


Figure 85 : GC chromatogram of the volatile byproducts resulting from the reaction of  $2.5 \times 10^{-2} \text{ mol.L}^{-1}$  solution of  $\{\text{Fe}[\text{N}(\text{SiMe}_3)_2]_2\}_2$  in  $\text{C}_1\text{C}_4\text{ImNTf}_2$  with  $0.4 \text{ MPa H}_2$  for 4h at  $100^\circ\text{C}$ .

In TEM, the formation of very small and monodispersed ( $4.1 \pm 0.4 \text{ nm}$ ) NPs was observed (Figure 86).

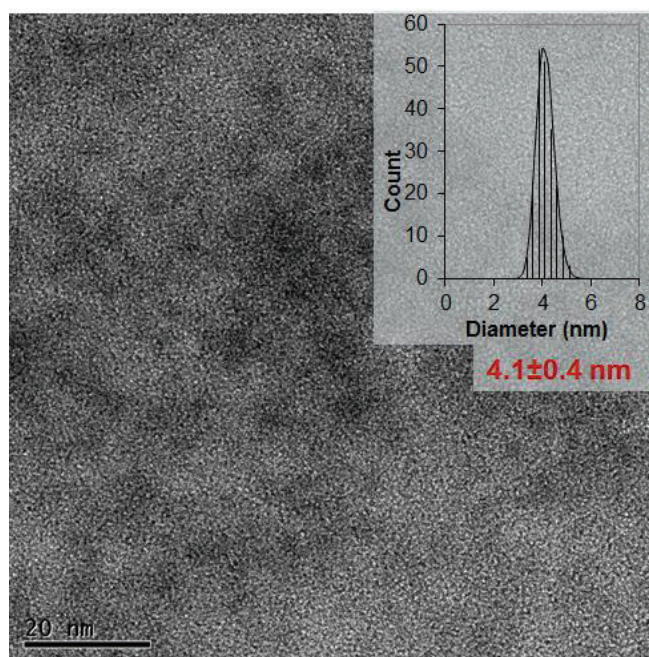


Figure 86 : TEM image of NPs prepared through the decomposition of  $2.5 \times 10^{-2} \text{ mol.L}^{-1}$  solution of  $\{\text{Fe}[\text{N}(\text{SiMe}_3)_2]_2\}_2$  in  $\text{C}_1\text{C}_4\text{ImNTf}_2$  under  $0.4 \text{ MPa}$  of  $\text{H}_2$  at  $100^\circ\text{C}$  for 4 h.

### iii. Characterization of Fe-NPs

Interestingly enough, HRTEM analysis suggested that these NPs are matching perfectly with Fe<sup>(0)</sup> possessing a fcc structure with a lattice parameter of 3.52Å (Figure 87). It is worth mentioning that the coexistence of Fe<sub>2</sub>O<sub>3</sub>-NPs with a tetragonal structure was also observed by HRTEM (Figure 88). These results are quite surprising as compared to the results from Fe(COT)<sub>2</sub>. Basically, Fe(COT)<sub>2</sub> is more stable towards oxidation and decomposition as compared to the extremely air sensitive {Fe[N(SiMe<sub>3</sub>)<sub>2</sub>]<sub>2</sub>}<sub>2</sub>. Therefore, the formation of Fe<sup>(0)</sup>-NPs expected to be more probable with Fe(COT)<sub>2</sub> rather than {Fe[N(SiMe<sub>3</sub>)<sub>2</sub>]<sub>2</sub>}<sub>2</sub>. The fact that Fe<sup>(0)</sup>-NPs were observed in the latter case should be attributed to the amine byproduct, (Me<sub>3</sub>Si)<sub>2</sub>NH, that could act as a ligand to stabilize the formed NPs, as previously reported by Lacroix, *et. al.*<sup>153</sup> In the same time, this compound would partially prevent the Fe-NPs oxidation.

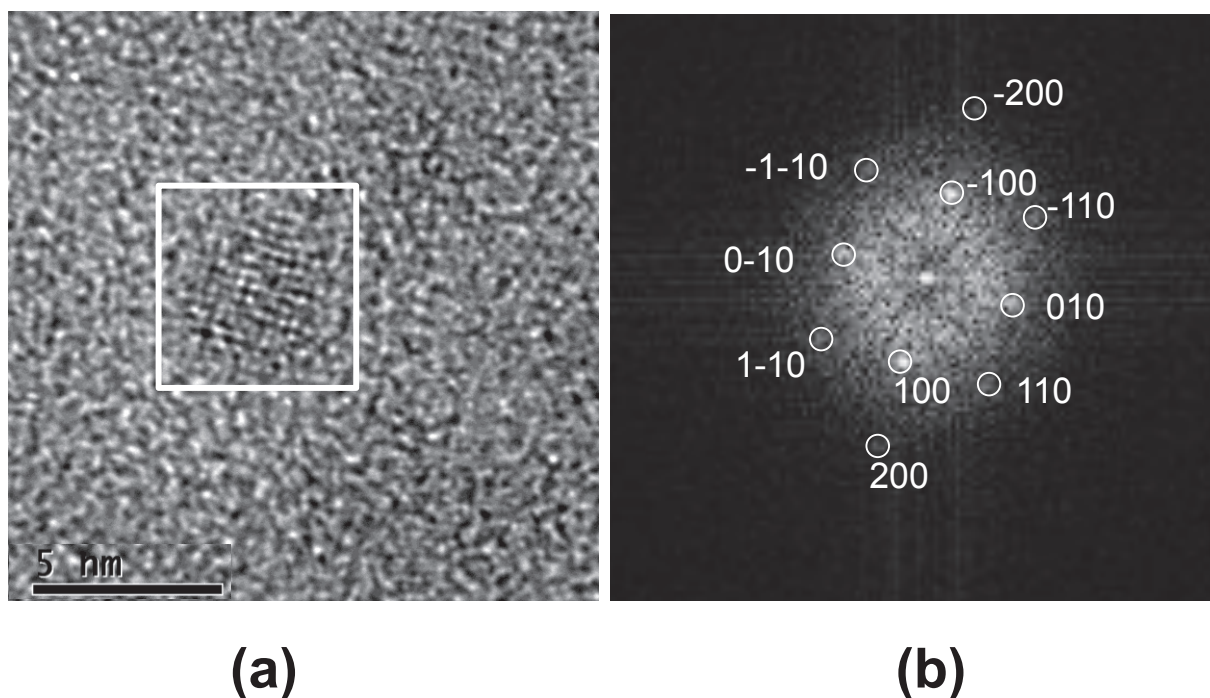


Figure 87 : (a) Exemplary HRTEM image of Fe-NPs generated by the decomposition of {Fe[N(SiMe<sub>3</sub>)<sub>2</sub>]<sub>2</sub>}<sub>2</sub> in C<sub>1</sub>C<sub>4</sub>ImNTf<sub>2</sub> under 0.4MPa of H<sub>2</sub> for 4h, 100°C and (b) FFT of the particle in the white square indexed by a fcc structure along the (001) zone axis with a lattice parameter of 3.52Å corresponding to fcc Fe.



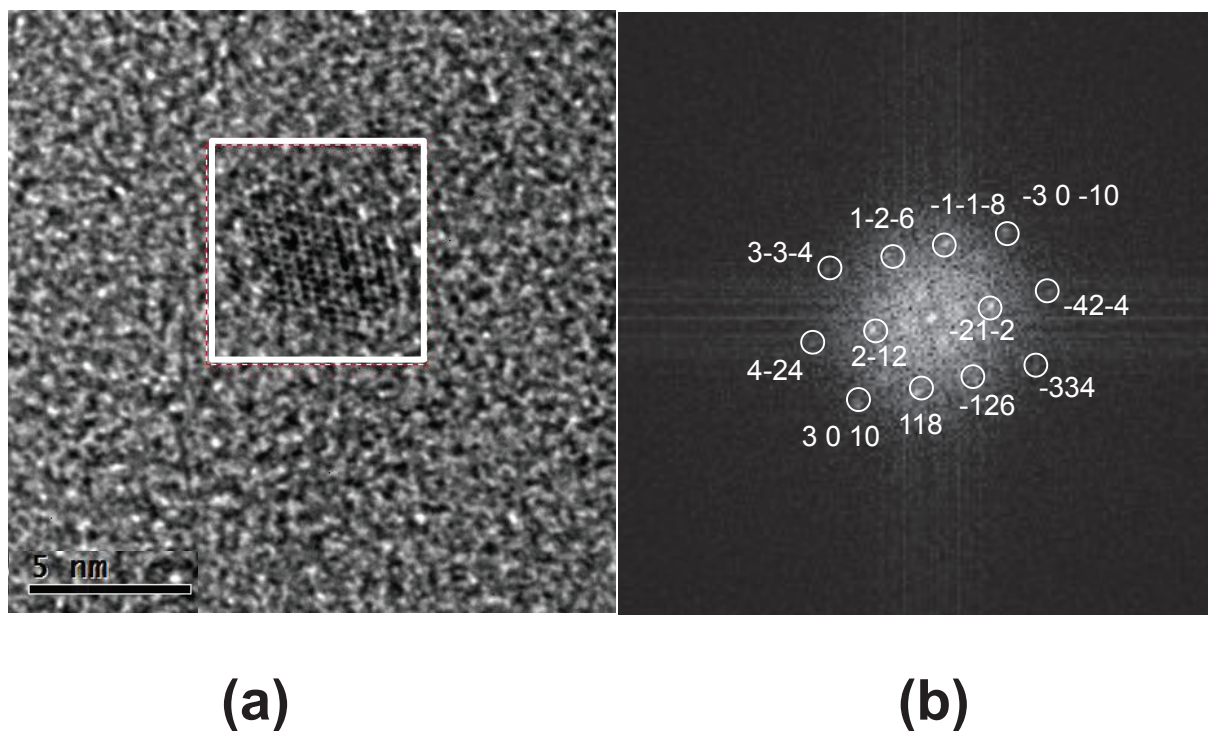


Figure 88 : (a) HRTEM image of  $\text{Fe}_2\text{O}_3$ -NPs coexisting with the Fe-NPs from Figure 87 and (b) FFT of the particle in the white square indexed by a tetragonal  $\text{Fe}_2\text{O}_3$  structure along the (10 14 -3) zone axis.

In light of the previous findings, the study was extended to include the different parameters affecting the size of formed Fe-NPs. An important factor that was identified is the initial concentration of the precursor. Increasing the concentration to the double ( $5 \times 10^{-2} \text{ mol.L}^{-1}$ ) resulted in smaller NPs ( $2.9 \pm 0.2 \text{ nm}$ ). This is probably due to the faster nucleation kinetics.<sup>182</sup> Furthermore, as for Co-NPs, the decomposition temperature was found to affect the NP size (Table 10). The Fe-NPs size increased upon increasing the temperature. This could be related to the evaporation of  $(\text{Me}_3\text{Si})_2\text{NH}$  (b.p.  $126^\circ\text{C}$ ) limiting its stabilization effect, *vide supra*.

Table 10 : Variation of Fe NPs size with the reaction temperature

Concentration (mol.L <sup>-1</sup> )	IL	Temperature	Pressure	Duration	Color after reaction	NP size (nm)
$5 \times 10^{-2}$	$\text{C}_1\text{C}_4\text{ImNTf}_2$	$65^\circ\text{C}$	0.4 MPa	4 h	Brown	$2.8 \pm 0.2$
$5 \times 10^{-2}$	$\text{C}_1\text{C}_4\text{ImNTf}_2$	$100^\circ\text{C}$	0.4 MPa	4 h	Black	$2.9 \pm 0.2$
$5 \times 10^{-2}$	$\text{C}_1\text{C}_4\text{ImNTf}_2$	$150^\circ\text{C}$	0.4 MPa	4 h	Black	$3.9 \pm 0.3$

As a conclusion, the decomposition of  $\{\text{Fe}[\text{N}(\text{SiMe}_3)_2]_2\}_2$  by  $\text{H}_2$  in  $\text{C}_1\text{C}_4\text{ImNTf}_2$  was studied under different conditions. In all cases, small NPs were obtained with the formation of  $(\text{Me}_3\text{Si})_2\text{NH}$  as the main byproduct. Both the precursor concentration and the reaction temperature were found to affect the size of resulting NPs. HRTEM analysis of the resulting NPs evidenced the formation of metallic fcc  $\text{Fe}^{(0)}$ -NPs together with the coexistence of other NPs with a tetragonal structure characteristic for  $\text{Fe}_2\text{O}_3$ . Further characterizations are still required to consolidate these conclusions.

### III.V. Conclusion

For the synthesis of Fe-NPs, two OM precursors were evaluated,  $\text{Fe}(\text{COT})_2$  and  $\{\text{Fe}[\text{N}(\text{SiMe}_3)_2]_2\}_2$ . Thermal decomposition studies combined with GC analysis showed that both of them can decompose under  $\text{H}_2$  at moderate temperatures in ILs. In both cases, small NPs (<5 nm) were obtained with a narrow size distribution.

Some NPs formed from  $\text{Fe}(\text{COT})_2$  were analyzed by HRTEM. Their structure was found to match with a tetragonal lattice of  $a = 6.8 \text{ \AA}$ ,  $c = 6.1 \text{ \AA}$  that did not correspond to any of the known structures of iron or its compounds. One possible hypothesis is that these are metallic Fe-NPs but they possess an uncommon, non-compact form of Fe that resembles the  $\epsilon$ -Co structure, which is not documented in crystallographic databases. Additionally, the nature of the anion was found to influence the size of the NPs, which was  $4.5 \pm 0.4 \text{ nm}$  in  $\text{C}_1\text{C}_2\text{ImB}(\text{CN})_4$  and  $5.5 \pm 0.4 \text{ nm}$  in  $\text{C}_1\text{C}_2\text{ImFAP}$ , against  $11.6 \pm 0.8 \text{ nm}$  in  $\text{C}_1\text{C}_2\text{ImNTf}_2$ .

In the case of  $\{\text{Fe}[\text{N}(\text{SiMe}_3)_2]_2\}_2$ , some  $\text{Fe}^{(0)}$ -NPs were detected in HRTEM with a cubic structure with the lattice parameter matching with the fcc form of  $\text{Fe}^{(0)}$ . However, some NPs were oxidized with a  $\text{Fe}_2\text{O}_3$  structure. This partial oxidation should be attributed to the residual water confined in the IL structure. The fact that  $\text{Fe}^{(0)}$ -NPs were observed with this precursor could be related to the formation of the amine byproduct,  $(\text{Me}_3\text{Si})_2\text{NH}$ , acting as a ligand to stabilize the  $\text{Fe}^{(0)}$ -NPs avoiding their oxidation.

For both precursors, additional characterizations are necessary to definitely conclude about the structure (WAXS, Mossbauer spectroscopy) and the magnetic properties (SQUID) of these NPs.



# Chapter IV.

---

## Experimental Part



## IV.I. Synthesis of NPs

### i. Materials

All operations have been performed in the strict absence of oxygen and water under a purified argon atmosphere using glove box (MBraun) or vacuum-line techniques. Distilled water, freshly distilled toluene (> 99 %, Sigma Aldrich) and freshly distilled dichloromethane (> 99 %, Sigma Aldrich) were used for purification of ILs. Tetramethyltin (95%, Sigma Aldrich), 1-Butyl-3-methylimidazolium chloride [ $C_1C_4ImCl$ ], Bis(trifluoromethane)-sulfonimide lithium [ $LiNTf_2$ ] (CAS No. 90076-65-6, Solvionic),  $(\eta^4-1,5\text{-cyclooctadiene})(\eta^6-1,3,5\text{-cyclooctatriene})\text{ruthenium}(0)$ ,  $Ru(COD)(COT)$ ,  $(\eta^4-1,5\text{-cyclooctadiene})(\eta^3\text{-cyclooctadienyl})\text{cobalt}(I)$  and bis(cyclooctatetraene)iron  $Fe(COT)_2$  (Nanomeps and Aldrich), were kept in a glove box and used as received. For  $\{Fe[N(SiMe_3)_2]_2\}_2$ , was prepared by K. Soussi, and it was received as a dark green solution in pentane. Bis(dibenzylideneacetone)platinum(0)  $Pt(dba)_2$  was prepared in the laboratory as described in reference <sup>183</sup>.

### ii. NMR spectroscopy

Solution NMR spectra were recorded on Bruker Avance 300 MHz spectrometer for  $^1H$  and  $^{13}C$ .

### iii. GC analysis

The products were quantitatively analyzed by gas chromatography on a P6890 chromatograph equipped with a flame ionization detector (FID) and an  $Al_2O_3/KCl$  column ( $L = 50$  m,  $\phi_{int} = 0.32$  mm, film thickness = 5  $\mu m$ ). The injector and detector temperature was 230° C, and the injection volume was 1  $\mu L$ . The temperature was fixed at 190° C.

### iv. Synthesis of ionic liquids

1-Butyl-3-methylimidazolium bis(trifluoromethylsulfonyl)imide [ $C_1C_4Im NTf_2$ ] was prepared from the corresponding chloride salt. First, 70 g of 1-butyl-3-methylimidazolium chloride, [ $C_1C_4ImCl$ ], were dissolved in 100 mL distilled water. Into this solution, a solution of 1.1 equivalent of bis(trifluoromethane)sulfonimide lithium [ $LiNTf_2$ ] (CAS No. 90076-65-6) in 100 mL of distilled water, was added. The mixture was stirred overnight at room temperature to allow the exchange of chloride anion with the  $NTf_2$  anion. The lower phase was then collected and washed repeatedly with water until no chloride traces remained in the

washing (silver nitrate was used to test the presence of chloride). Dichloromethane was then added into the mixture in order to facilitate liquid-liquid separation. After evaporation of dichloromethane, activated charcoal was added, stirred for 10 minutes and then filtered off through a short neutral alumina column (alumina was dried overnight in oven at 110 °C), in order to obtain a colorless liquid. [C<sub>1</sub>C<sub>4</sub>Im NTf<sub>2</sub>] was dried under 10<sup>-2</sup> bar for 8 h, then overnight under high vacuum (10<sup>-5</sup> mbar) and stored inside the glove box under argon.

<sup>1</sup>H-NMR (CD<sub>2</sub>Cl<sub>2</sub>): δ (ppm) : 8.66 (s, 1H, C<sub>2</sub>H); 7.29 (d, 1H, C<sub>4</sub>H); 7.27 (d, 1H, C<sub>5</sub>H); 4.17 (t, 2H, NCH<sub>2</sub>); 3.93 (s, 3H, NCH<sub>3</sub>); 1.86 (qt, 2H, CH<sub>2</sub>CH<sub>2</sub>CH<sub>2</sub>); 1.37 (st, 2H, CH<sub>2</sub>CH<sub>2</sub>CH<sub>3</sub>); 0.97 (t, 3H, CH<sub>2</sub>CH<sub>3</sub>).

<sup>13</sup>C-NMR (CD<sub>2</sub>Cl<sub>2</sub>) : δ(ppm) : 136.10 (C<sub>2</sub>H); 124.05 (C<sub>4</sub>H); 122.70 (C<sub>5</sub>H); 118.07 (CF<sub>3</sub>); 50.34 (NCH<sub>2</sub>); 36.66 (NCH<sub>3</sub>); 32.22 (CH<sub>2</sub>CH<sub>2</sub>CH<sub>2</sub>); 19.66 (CH<sub>2</sub>CH<sub>2</sub>CH<sub>3</sub>); 13.34 (CH<sub>2</sub>CH<sub>3</sub>).

Electrospray HR-Mass spectrometry, MS (+ve): m/z 139.12 (100% - C<sub>1</sub>C<sub>4</sub>Im<sup>+</sup>), MS (-ve): m/z 279.92 (100% - NTf<sub>2</sub>)

## v. Thermal analysis

### a. *In situ drift analysis of pure solid*

For diffuse reflectance infrared Fourier transform spectroscopy (DRIFT) analysis, an exact weight of the precursor (10-15 mg) was first weighed in an aluminum crucible and transferred in a Harrick high temperature cell that was tightly closed under argon inside the glove box and then fixed into a Thermo Scientific Nicolet 6700 FT-IR equipment. The sample was initially purged for 20 min under 20 mL.min<sup>-1</sup> of argon. It was then put under 0.4MPa of H<sub>2</sub> gas (purging at 2mL/min flow rate) and heated up at 1°C/min heating rate till 150°C. It was then kept at this temperature for 6h to insure complete decomposition. An IR spectrum was recorded every minute to follow up the decomposition of the precursor. Every 30 min, a gaseous injection is induced into a 20 m CP-PoraBOND Q column to separate the products that were then analyzed using a GC-MS (Agilent GC 6850 MS 5975C).

### b. *Thermal decomposition analysis in IL*

The OM precursor was first dissolved in 2.5 mL IL in a Schlenk tube upon stirring for 45min under argon to give a concentration of 5 x 10<sup>-2</sup> mol.L<sup>-1</sup>. 2 mL of this solution were

cannuled into a metallic autoclave kept under argon flow. The autoclave was then heated up under argon flow until the selected temperature was reached. 0.4MPa of H<sub>2</sub> were then applied. The H<sub>2</sub> pressure was kept constant through H<sub>2</sub> flow rate of 2mL.min<sup>-1</sup>. Every 20 min, a gaseous injection was induced into a 20 m CP-PoraBOND Q column to separate the products that were then analyzed using an online GC-MS (Agilent GC 6850 MS 5975C).

*c. Thermogravimetric analysis*

Thermogravimetric Analysis (TGA) was performed using a Mettler Toledo TGA DSC1. The instrument was calibrated using indium, zinc and aluminum samples. First, an exact amount of the compound (7-10 mg) was weighed in a 100μL aluminum pan that was then sealed inside an Ar-filled glove box. The sample was then heated under an argon flow of 30 mL.min<sup>-1</sup>. Dynamic TGA experiments were performed using a temperature increase from 25 to 500°C at temperature ramp rate of 5°C.min<sup>-1</sup>. The start temperature (T<sub>start</sub>) was determined from the first derivative of the weight loss vs time curve  $|dw/dT|$  and was defined as the temperature at which  $|dw/dT|$  is larger than 10<sup>-4</sup> mg.s<sup>-1</sup>. Each experiment was performed twice and upon subtraction from an argon background.

**vi. Synthesis of monometallic NPs**

*a. General procedure for Co-NPs*

Co(COD)(COE) was weighed in a clean dry Schlenk tube in the glove box, dissolved in 0.1 mL of pentane (degassed through 3 cycles of vacuum-argon) and stirred for 10 min. C<sub>1</sub>C<sub>4</sub>Im NTf<sub>2</sub> ( 2.5 mL) were added. The mixture was kept under stirring at room temperature until complete dissolution affording a dark brown solution. 2 mL of this organometallic solution were canuled into an autoclave under argon. At this step, the reaction medium was warmed to the desired temperature without stirring. After gas purge, the autoclave was pressurized at 0.4 MPa of H<sub>2</sub> during 10 min and kept at the selected temperature (100 and 150 °C) during 0.5, 1, 2, 4 and 24h. Then, the resulting dark suspension was placed under vacuum to eliminate the volatile by-products (mainly cyclooctane) and stored under argon in a glove box.

In some cases, the cyclooctane was condensed at -198°C in order to determine its amount by GC to get an idea about the degree of conversion of the OM precursor.



Under the selected standard conditions (0.4MPa H<sub>2</sub>, 100°C, 4h), Co-NP mean size was 4.1±0.4 nm corresponding to ~ 2900 Co atoms per NP with ~ 800 Co<sub>surf.</sub> atoms, i.e. a dispersion of 0.29. The Co-NPs concentration in this case was 1.74x10<sup>-5</sup> mol.L<sup>-1</sup>.

#### *b. Fe-NPs*

Following the same procedure than for Co-NPs, Fe-NPs were synthesized from:

- Fe(COD)<sub>2</sub>, 13.2mg (0.05 mmol) in C<sub>1</sub>C<sub>4</sub>Im NTf<sub>2</sub> (2 mL) under H<sub>2</sub> pressure of 0.4MPa at 150 °C during 48h.
- {Fe[N(SiMe<sub>3</sub>)<sub>2</sub>]<sub>2</sub>}<sub>2</sub>, 97.5mg (0.129 mmol) in C<sub>1</sub>C<sub>4</sub>Im NTf<sub>2</sub> (2 mL) under H<sub>2</sub> pressure of 0.4MPa at 65, 100 and 150°C during 4h

### **vii. Synthesis of bimetallic NPs**

#### *a. CoRu-NPs*

CoRu-NPs were prepared through the decomposition of Co(COD)(COE) and Ru(COD)(COT) metal precursors in C<sub>1</sub>C<sub>4</sub>ImNTf<sub>2</sub> under 0.4MPa H<sub>2</sub>. The CoRu NPs with a cobalt molar ratio,  $\chi_{Co}$  = 1; 0.9; 0.75; 0.5; 0.25; 0.1; 0, were generated through two approaches:

- A one-pot synthesis in which, initial solutions of 0.05 mol.L<sup>-1</sup> concentration of the separate metal precursors were prepared in C<sub>1</sub>C<sub>4</sub>ImNTf<sub>2</sub>. In a glass autoclave, diverse volumes of these solutions were mixed to fix the selected  $\chi_{Co}$  value, the total liquid volume at 2 mL, and the total metal concentration at 0.05 mol.L<sup>-1</sup>. Then the mixture was kept under 0.4 MPa of H<sub>2</sub> at 100°C for 4 h. At the end of the reaction, the resulting dark suspension was placed under vacuum to eliminate the volatile by-products and stored under argon in a glove box.
- The successive decomposition of 2 metal precursors approach in which, two separate metal NPs suspensions of either Co-NPs or Ru-NPs were first prepared as in paragraph *vi-a*. The suspensions were cooled down to room temperature under argon flushing for 15 minutes. To these suspensions, either 1 mL of an equimolar solution of Ru(COD)(COT) or 1 mL of an equimolar solution of Co(COD)(COE) were added respectively. Each solution was kept for 24h under argon at room temperature. The resulting solutions containing Co@Ru [resp.

Ru@Co] NPs were then put under vacuum for 10 min to remove volatile byproducts and stored under argon inside the glove box.

#### *b. CoPt-NPs*

CoPt-NPs were prepared through the simultaneous decomposition of Co(COD)(COE) and Pt(dba)<sub>2</sub> metal precursors in C<sub>1</sub>C<sub>4</sub>ImNTf<sub>2</sub> under 0.9MPa H<sub>2</sub> at 150°C for 24h. To obtain diverse Co molar ratio ( $\chi_{\text{Co}} = 1; 0.95; 0.85; 0.75; 0.5; 0.25; 0.1; 0$ ), the initial solutions of separate metal precursors in 0.05 mol.L<sup>-1</sup> concentration were prepared in C<sub>1</sub>C<sub>4</sub>ImNTf<sub>2</sub>. Adjusted volumes of these solutions were mixed in an autoclave in order to fix the total volume at 2 mL and the total metal concentration at 0.05 mol.L<sup>-1</sup>, whatever was the  $\chi_{\text{Co}}$  value. The resulting black solution was cooled down to room temperature, kept under vacuum for 10 min to remove volatile byproducts and stored under argon in the glove box.

## **IV.II. Determination of hydrides onto the surface of Co-NPs**

### **i. Reaction with SnMe<sub>4</sub>**

Freshly prepared Co-NPs in C<sub>1</sub>C<sub>4</sub>ImNTf<sub>2</sub> were kept under Ar purging for 15 min to remove volatile byproducts and H<sub>2</sub> atmosphere. Then, SnMe<sub>4</sub> (0.7 mol.L<sup>-1</sup>) was added to the Co-NPs suspension, immediately the formation of bubbles was observed. The system was stirred 24 h under static Ar at 50°C. At the end, all volatile byproducts were collected under vacuum in a flask cooled by liquid N<sub>2</sub>. In three gaseous aliquots of 300  $\mu$ L analyzed by GC, methane was present. Using calibration curves, the average amount of evolved methane was found equal to  $3.65 \times 10^{-7}$  mole per aliquot *i.e.* a total methane concentration of  $1.83 \times 10^{-4}$  mole.L<sup>-1</sup> *i.e.* a ratio surface hydride/ cobalt surface  $[H_{\text{surf.}}]/[Co_{\text{surf.}}]$  of 0.01.

### **ii. Hydrogenation of ethylene by Co-NPs in the IL**

A 2 mL sample of the Co-NPs solution in the IL was introduced under argon into a Schlenk of known volume. The system was kept under flow of argon for 24h. The Ar was replaced by ethylene (P initial = 11.4 KPa) . The media was stirred at room temperature until the internal pressure become constant~24 h. A decrease of the internal pressure was observed, and the composition of the gas phase was analyzed by GC. Then P<sub>H<sub>2</sub></sub> of 11.6 KPa was applied and the temperature increased to 100 °C till a constant internal pressure was maintained (23 h). At the end, the composition of the gas phase was again analyzed by GC. From this experiment, the total number of moles of H was found to be  $6.82 \times 10^{-7}$  moles/2 mL corresponding to a concentration of  $[H_{\text{surf.}}]$  equal to  $1.65 \times 10^{-4}$  mol.L<sup>-1</sup>

### IV.III. Catalytic hydrogenation of cyclohexadiene

0.5 mL of Co-NP, Pt-NP and CoPt-NP suspensions in  $C_1C_4ImNTf_2$  with ( $\chi_{Co} = 1; 0.95; 0.85; 0.75; 0.5; 0.25; 0.1; 0$ ), were tested as catalyst for the hydrogenation of cyclohexadiene under  $P_{H_2}$  of 0.12 MPa. For Co-NPs, the mean size was 4.3 nm affording a concentration of  $Co_{surf.}$  atoms of  $0.013 \text{ mol.L}^{-1}$ . For the CoPt-NPs with a mean size of 3.0 nm, the concentration of  $(CoPt)_{surf.}$  atoms was  $0.020 \text{ mol.L}^{-1}$  while for pure Pt-NPs with a mean size of 2.5 nm, the concentration of  $Pt_{surf.}$  was  $0.022 \text{ mol.L}^{-1}$ . To obtain the same amount of  $M_{surf.}$  for all the tested catalysts, the added quantity of IL was adapted in order to get the same  $M_{surf.}$  concentration in the same total volume of IL. Following this procedure, for each experiment there was a total volume of 0.5 mL with a surface metal concentration of  $1.3 \times 10^{-2} \text{ mol.L}^{-1}$  and,  $63 \mu\text{L}$  of cyclohexadiene (CYD) were added, *i.e.* a ratio  $CYD / M_{surf.}$  equal to 100.

In a Schlenk tube, the solution was stirred 12 h, under Ar, to insure homogeneity and then put under vacuum for 30 min,  $30^\circ\text{C}$ , at this time,  $H_2$  (0.12 MPa) was applied. The reaction was stopped after 30 minutes and 10 mL of acetonitrile (containing  $1 \text{ mol.L}^{-1}$  of toluene as internal reference for GC) were added.  $1 \mu\text{L}$  of this solution was analyzed in GC. For high accuracy, blank samples are also considered for GC analysis. These blank samples were containing either the same components but without NPs ( $63 \mu\text{L}$  cyclohexadiene + 0.5 mL pure IL + toluene/acetonitrile solution), or  $63 \mu\text{L}$  cyclohexadiene + 1 eq of cyclohexane in the same solution environment.

### IV.IV. Transmission electron microscopy (TEM) / High resolution transmission electron microscopy (HRTEM)

All samples were analyzed by transmission electron microscopy (TEM) using a MET JEOL 2100FEF (field effect gun energy filtering) microscope at the “Centre Technologiques des Microstructures”, CT $\mu$ , Villeurbanne, France.

The analysis was performed in the IL media. First, a thin film of NPs suspension in IL was deposited on a copper mesh 200 grid coated with a layer of formvar/carbon. The grid was then dried gently with a filter paper. The liquid films were observed using an acceleration voltage of 200 kV. Size histograms and average size were determined by measuring the diameter of minimum of 200 particles per sample. Their size distribution was fitted by a lognormal law, and is described with the following notation: mean size [lower limit; upper

limit] nm, where upper and lower limits correspond to plus and minus two standard deviations of the lognormal fit, respectively.

High resolution transmission electron microscopy, HRTEM, analysis coupled with electron dispersive X-Ray analysis, EDX, was also performed on some NPs using the same microscope. Subsequently, the HRTEM images and their crystal structure were determined from the diffraction pattern seen in the Fourier Transform images.

#### IV.V. Wide angle X-ray scattering (WAXS):

X-ray techniques are the most valuable methods to characterize crystalline materials. For example, X-Ray powder diffraction, XRD, allows the phase analysis, the lattice parameters and substance identification by comparison with reference compounds in databases, such as JCPDS or ICSD. The principle of X-ray diffraction is based on the irradiation of a crystalline powder sample by monochromatic X-ray photons and the subsequent elastic scattering of the photons by atoms in a periodic lattice. The scattered photons exhibit a constructive interference (Figure 89). The angles, under which the photons leave the crystal, are characteristic for each crystal lattice plane. This dependence is described by Bragg's Law:

$$\lambda = 2 \cdot d \cdot \sin(\theta)$$

Where  $\lambda$  is the wavelength of the X-ray photons,  $d$  is the distance between two lattice planes of the same orientation in the crystal, and  $\theta$  is the angle between the reflected X-ray and the lattice plane.

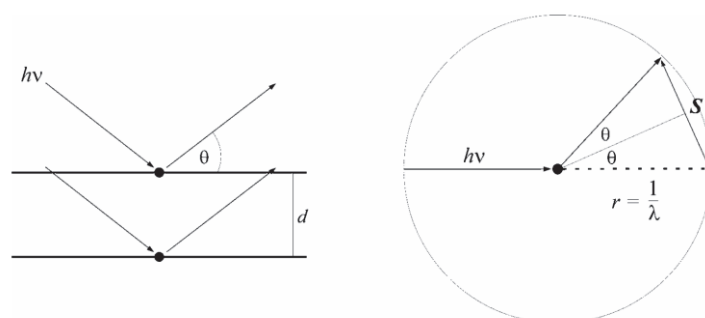


Figure 89 : Schematic illustration of the diffraction of X-rays on a lattice plane of a crystalline material (left), and illustration of the scattering vector in the reciprocal space (right).

However, with decreasing crystallite size, e.g. in nanoparticles, the reflections become broader and if the crystallites become too small, they have no long-range order, and must be regarded as either amorphous or nanocrystalline. Consequently, the X-rays are not diffracted in phase, and there is no constructive periodic interference of the reflected X-rays, but rather a diffuse scattering in all directions of space.

Thus, the XRD pattern of such a sample would exhibit no reflections at all. For that reason, the wide angle X-ray scattering measurement technique can be employed to examine the structure of such materials with a crystallite size of less than 4 nm. The radius of the Ewald sphere of diffracted or scattered photons, respectively, is in reciprocal relationship to the irradiated X-ray wavelength (Figure 89, right). Thus, the samples are typically irradiated with photons of lower wavelengths, e.g. Mo-K $\alpha$  or synchrotron radiation, which causes a better resolution of scattering signals at low  $\theta$  angles, which contain substantial structural information on the sample. In WAXS measurements, the scattered photons are detected in dependence of the scattering vector S:

$$S = \frac{4\pi \sin(\theta)}{\lambda}$$

The detector moves in equidistant S steps (unit: nm $^{-1}$ ) in the reciprocal space to collect all scattered X-rays. The resulting scattering diagram in the reciprocal space, where the scattering vector is plotted against the intensity of the scattered X-rays, is equivalent to a diffraction pattern and can be converted to  $2\theta$ . If the particles are nanocrystalline, this pattern can already be used for a pattern structure search, as it is common in XRD data evaluation. For an extraction of structural information such as particle size, the crystal lattice and atom-atom distances, the scattering contribution of the glass of the capillary, of other components within the sample (e.g. a polymer-, framework- or mesoporous matrix, or a colloid surfactant, in which the nanoparticle are embedded), and fluorescence, cannot be neglected and must be subtracted from the total scattering intensity. After the data reduction steps, the reduced intensity function  $i(S)$  is obtained, which contains the interatomic distances in the sample. By Fourier transformation of  $i(S)$ , the Radial Distribution Function (RDF)  $F(r)$  is obtained, *i.e.* the occurrence diagram of the interatomic distances inside the nanoparticle.

$$F(r) = \frac{2\pi}{r} \int_{S_{min}}^{S_{max}} S \cdot i(S) \cdot \sin(r \cdot S) ds$$

The obtained RDF exhibit a set of local maximums, which correspond to the metal-metal distances in the nano-crystallite. The coherence length of the RDF gives information about the particle size. The extracted RDF can be used for an identification of the sample by comparison with the calculated RDF of a reference sample.

In this work, the WAXS measurements were performed by Dr. Pierre Lecante at the Centre d'Elaboration des Matériaux et d'Etudes Structurales, CNRS, Toulouse. The samples were prepared in the glovebox in quartz capillaries (diameter 1.5 mm) irradiated with graphite monochromated Mo-K $\alpha$ -radiation (0.71069 Å), using a two-axis diffractometer. The data collection time was 20 h for a set of 457 measurements in the range of 0° <  $\theta$  < 65°, for equidistant S values.

#### **IV.VI. Anomalous Small Angle X-ray Scattering (ASAXS)**

ASAXS measurements for Co-Ru and Co-Pt NPs suspended in [C<sub>1</sub>C<sub>4</sub>Im][NTf<sub>2</sub>] ionic liquid were performed below the Ru-K edge (22.117keV) and the Pt-L<sub>III</sub> edge (11.564 keV) on the CRG-BM02 beamline of the synchrotron at the ESRF in Grenoble. Samples with different compositions were compared;  $\chi_{Co} = 1; 0.9; 0.75; 0.5; 0.25; 0.1; 0$  for CoRu-NPs and  $\chi_{Co} = 1; 0.95; 0.85; 0.75; 0.5; 0.25; 0.1; 0$  for CoPt NPs, as well as a blank sample of neat C<sub>1</sub>C<sub>4</sub>ImNTf<sub>2</sub>. These NPs suspensions were contained in quartz capillaries of 1.5mm diameter and 10 cm length with wall thickness of 10  $\mu$ m. The capillaries sealed under argon were mounted perpendicularly on a multiple sample holder (Figure 90).

Accurate positioning of capillaries in the beam was ensured by two stepping motors(Y,Z). A distance of 1360 mm (for Ru edge, 810 mm for Pt edge) between the sample and CCD camera allows us to measure up to the first peak of the IL structure factor. The size of the beam focused on the CCD camera was 326  $\mu$ m high and 239  $\mu$ m wide for Ru-edge measurements and 312  $\mu$ m by 325  $\mu$ m for Pt edge measurements. The ASAXS set-up was under primary vacuum excepted around the sample holder. The tubes before and after the sample holder were closed by mica windows which produce negligible scattering compared to kapton foils. A photomultiplier (PM) with a removable kapton foil was mounted after the

samples for sample alignment and transmission measurements. The direct beam was stopped by a Pb disk of 2 mm diameter centered on a kapton foil placed inside the beam-stop chamber just before the CCD camera.

Five energy values were considered for Ru-K edge measurements (21.6; 21.94; 22.05; 22.089; 22.106 KeV) while for the Pt-L<sub>II</sub> measurements, the energy values used were 11.34; 11.434; 11.494; 11.529; 11.547; 11.556 KeV.

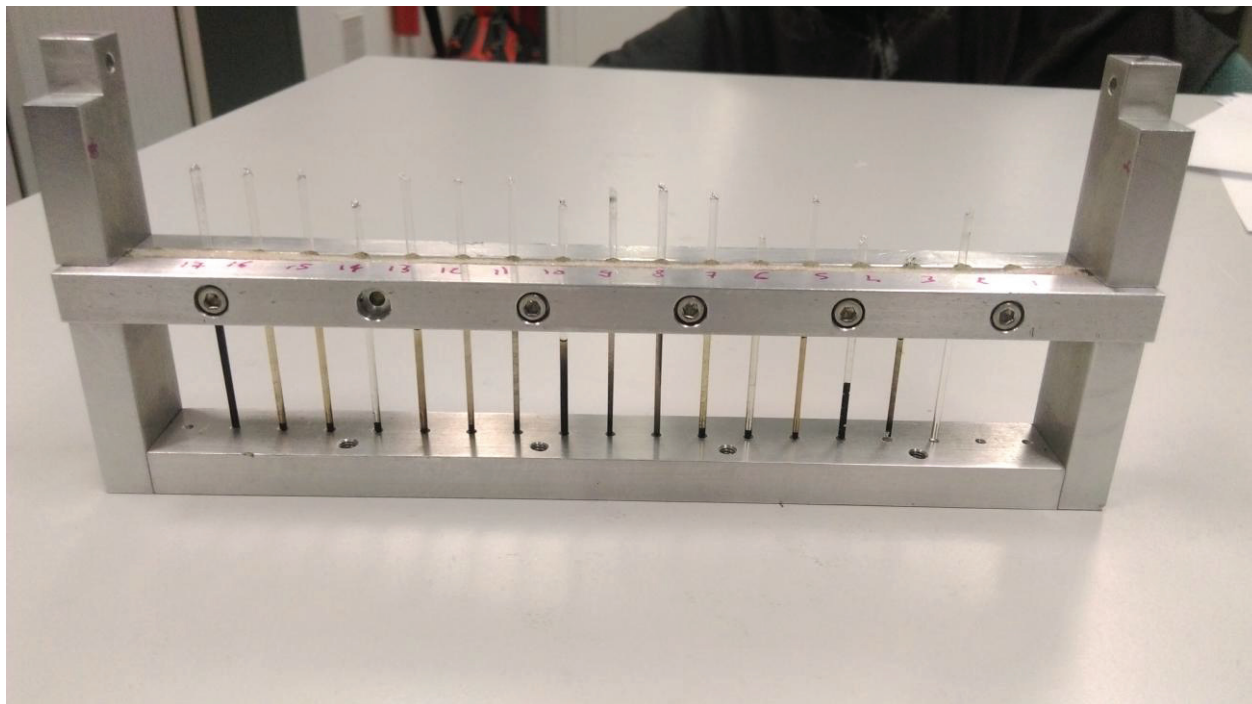


Figure 90 : Sealed capillaries in a multiple sample holder for ASAXS experiment.

#### **IV.VII. Magnetic measurement (SQUID)**

SQUID (Superconducting QUantum Interference Device) is the main component of Quantum Design's Magnetic Property Measurement System (MPMS) which is a highly integrated instrument system, designed to study the magnetism in matter. The magnetic signature of a material reflects its intrinsic spin and orbital angular momentum.

The principal components of this measurement system are:

- Temperature Control System: Precisely control the sample temperature from 2 K to 400 K.
- Magnet Control System: Current from a power supply is set to provide magnetic fields from zero to  $\pm 7$  tesla.
- Superconducting SQUID amplifier system: The rf SQUID detector is the heart of the magnetic moment detection system.
- Sample Handling System.
- Computer Operating System.

A SQUID is the most sensitive device available for measuring magnetic fields, and, although the SQUID in the MPMS is the source of the instrument's remarkable sensitivity, it does not detect directly the magnetic field from the sample. Instead, the sample moves through a system of superconducting detection coils which are connected to the SQUID with superconducting wires, allowing the current from the detection coils to inductively couple to the SQUID sensor. When properly configured, the SQUID electronics produces an output voltage which is strictly proportional to the current flowing in the SQUID input coil. Hence, the thin film SQUID device essentially functions as an extremely sensitive current-voltage convertor.

A measurement is performed in the MPMS by moving a sample through the superconducting detection coils, which are located outside the sample chamber and at the center of the magnet (Figure 91). As the sample moves through the coils, the magnetic moment of the sample induces an electric current in the detection coils. Because the detection coils, the connecting wires, and the SQUID input coil form a closed superconducting loop, any change of magnetic flux in the detection coils produces a change in the persistent current in the detection circuit, which is proportional to the change in magnetic flux. Since the SQUID functions as a highly linear current-voltage convertor, the variations in the current in the detection coils cause corresponding variations in the SQUID output voltage which is proportional to the magnetic moment of the sample. In a fully calibrated system, measurements of the voltage variations from the SQUID detector as the sample is moved through the detection coils provide a highly accurate measurement of the sample's magnetic



moment. The system can be accurately calibrated using a small piece of material of known mass and magnetic susceptibility.

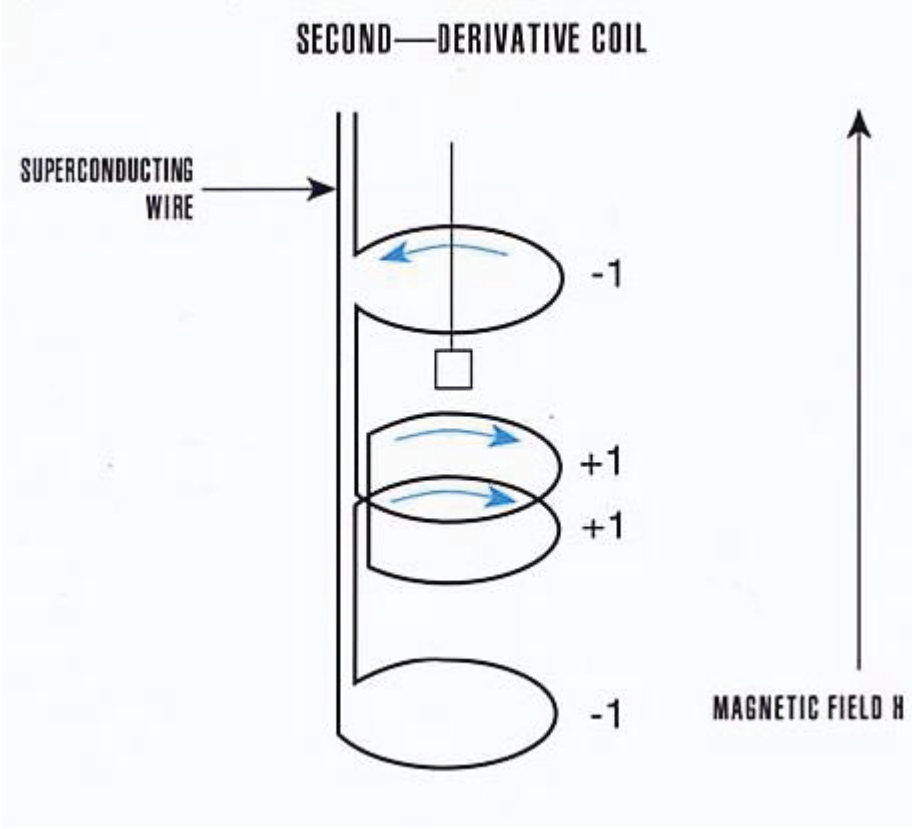


Figure 91 : Graphical illustration for SQUID measurements.

# Conclusion and outlook

---



## I. Synthesis of monometallic NPs in ILs

### i. Synthesis of Co-NPs

Based on a detailed bibliographic study, several OM precursors have been identified. Among them, (1,5-cyclooctadiene)(cyclooctadienyl)Cobalt (I), Co(COD)(COE) has been verified to satisfy the various criteria for the synthesis of Co-NPs:

- It has good solubility in ILs.
- Its decomposition temperature is less than 100 ° C.
- The main byproduct of the reaction is cyclooctane, a volatile compound readily removed under vacuum.

To validate the last two points, a complete study was carried out by TGA, DRIFT and GC-mass.

Co-NPs were accessible through the decomposition reaction of this OM under H<sub>2</sub>. Their size could be tuned by varying the experimental conditions. For example, by increasing the reaction temperature from 65°C to 100°C and then to 150°C, the size of the Co-NPs increased from 3.6 ± 0.4 nm to 4.1 ± 0.4 nm then to 7.0 ± 0.8 nm, respectively. The Co-NPs formed clusters, indicating that they were interacting (Figure 92). It is interesting to note that in an IL in which the imidazolium cation has a longer alkyl chain, C<sub>1</sub>C<sub>14</sub>ImNTf<sub>2</sub>, the distance between adjacent NPs was larger.

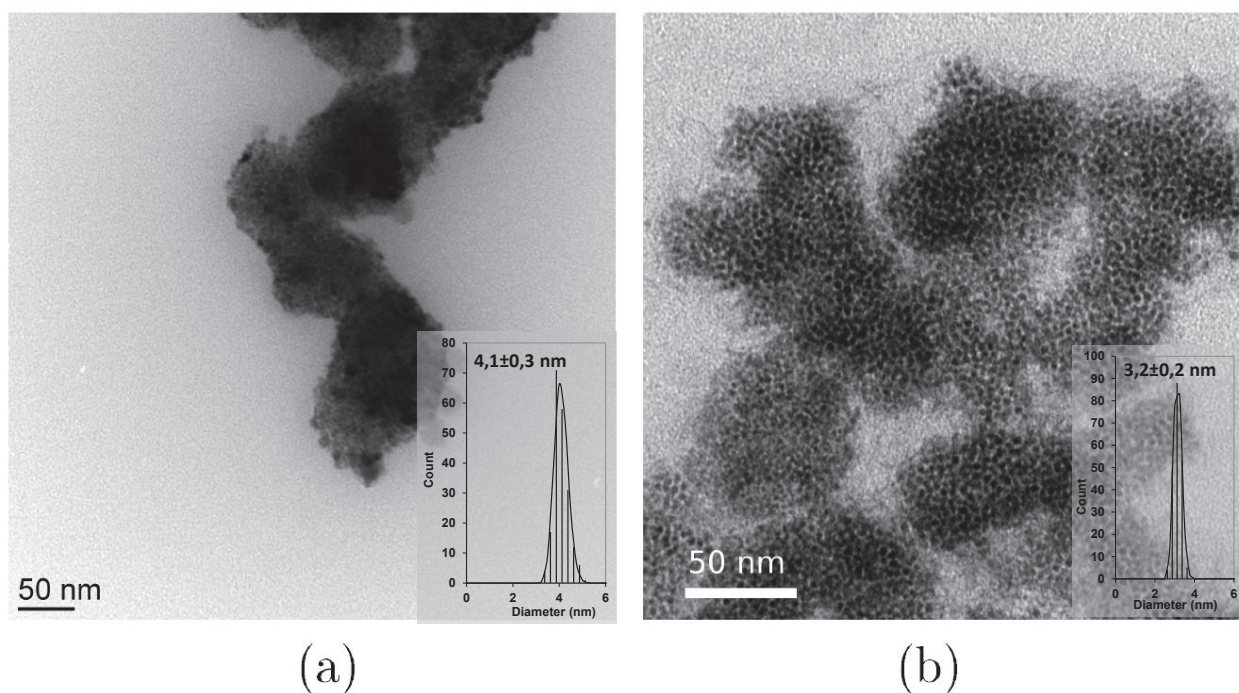


Figure 92 : TEM images for Co-NPs generated at 100°C, 0.4 M Pa of H<sub>2</sub> in (a) C<sub>1</sub>C<sub>4</sub>ImNTf<sub>2</sub>, (b) C<sub>1</sub>C<sub>14</sub>ImNTf<sub>2</sub>.

The structure of these NPs has been studied by HRTEM and WAXS. These two techniques showed that the Co-NPs consisted of a meta-stable allotrope of  $\text{Co}^{(0)}$  called  $\epsilon\text{-Co}$ . This cubic structure is not compact and gradually evolved into the stable hcp structure (Figure 93).

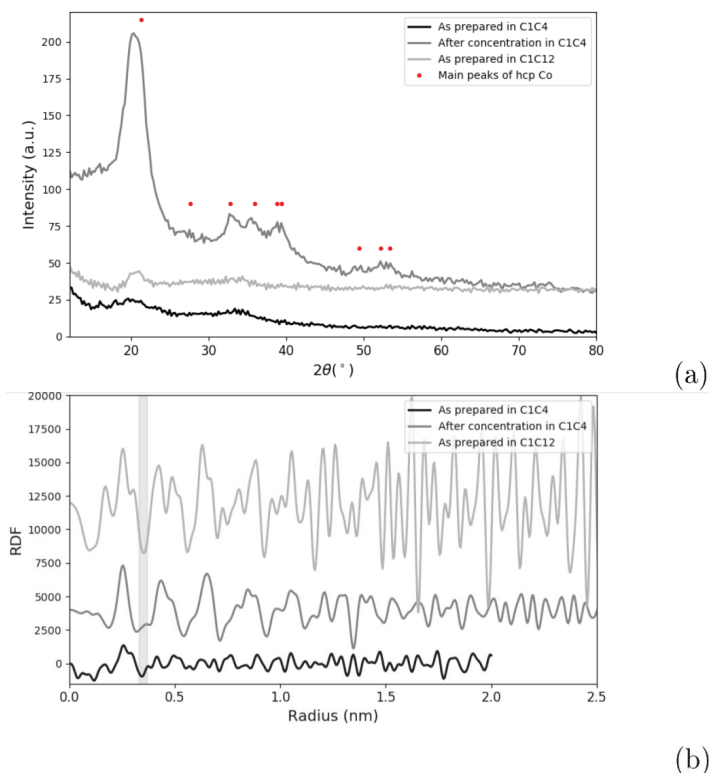
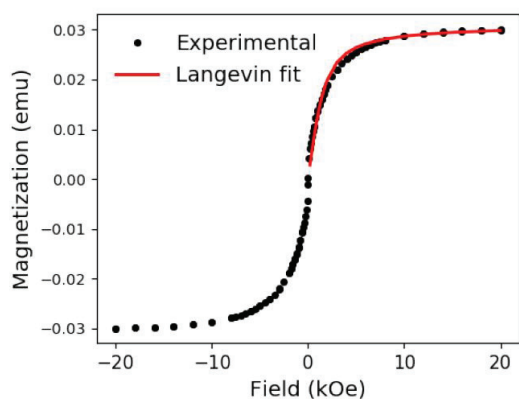


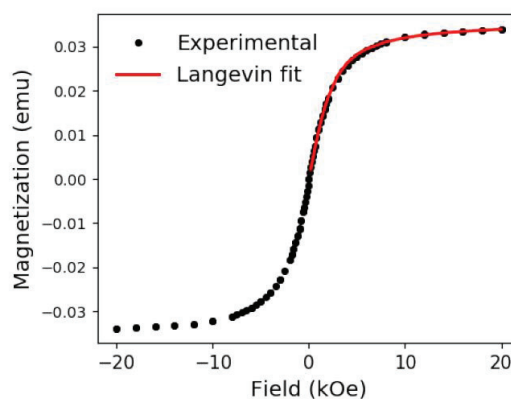
Figure 93 : (a) Scattering curves and (b) corresponding radial distribution functions (RDF) of Co-NPs as prepared in  $\text{C}_1\text{C}_4\text{ImNTf}_2$  and in  $\text{C}_1\text{C}_{12}\text{ImNTf}_2$ , and after decantation over a magnet in  $\text{C}_1\text{C}_4\text{ImNTf}_2$ .

The magnetic properties of Co-NPs were measured by SQUID. The magnetization curves confirmed that the NPs were as expected, not oxidized and superparamagnetic at room temperature (Figure 94). Their size estimated by a Langevin fit matched well with that measured in the TEM.

The blocking temperature was also measured by the FC-ZFC technique (it corresponds to the maximum of the ZFC curve, Figure 95). This temperature was 7 K for Co-NPs synthesized in the  $\text{C}_1\text{C}_4\text{ImNTf}_2$ , while it reached 160 K in the case of  $\text{C}_1\text{C}_{14}\text{ImNTf}_2$ . This difference was attributed to an anisotropy difference which probably originated from a dipole coupling of the NPs. However, this interpretation leads to the conclusion that this coupling was more pronounced in the  $\text{C}_1\text{C}_{14}\text{ImNTf}_2$ , which is surprising because in this IL, Co-NPs were more distant from each other (see Figure 92-b).

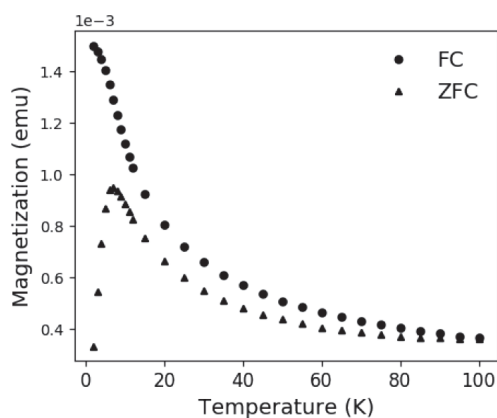


(a)

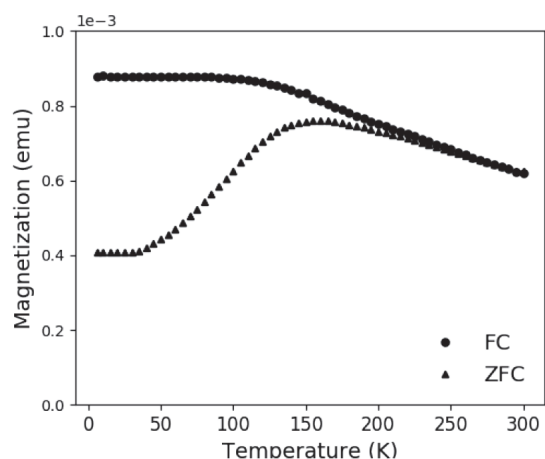


(b)

Figure 94 : Magnetization curves at 250K of CoNPs synthesized in (a)  $C_1C_4ImNTf_2$  and (b)  $C_1C_{14}ImNTf_2$ .



(a)



(b)

Figure 95 : FC-ZFC curves of Co-NPs synthesized in (a)  $C_1C_4ImNTf_2$  and (b)  $C_1C_{14}ImNTf_2$  recorded at 50 Oe.

Finally, a new synthetic approach for Co-NPs was investigated, in which,  $H_2$  was replaced by a liquid reducing agent,  $(C_2H_5)_3SiH$ . This new method also made it possible to obtain small and monodisperse Co-NPs, whose structural and magnetic characterization is in progress.

## ii. Synthesis of Fe-NPs

For the synthesis of Fe-NPs, two OM precursors were evaluated,  $Fe(COT)_2$  and  $\{Fe[N(SiMe_3)_2]_2\}_2$ . These two compounds were decomposed under  $H_2$  in  $C_1C_4ImNTf_2$ . In both cases, small NPs (<5 nm) were obtained with a narrow size distribution.

Some NPs formed from  $\text{Fe}(\text{COT})_2$  were analyzed by HRTEM. Their structure was found to match with a tetragonal lattice of  $a = 6.8 \text{ \AA}$ ,  $c = 6.1 \text{ \AA}$  that was not corresponding to any of the known structures of iron and its compounds. One possible hypothesis is that they were metallic Fe-NPs but with an uncommon, non-compact form of Fe, that resembles the  $\epsilon$ -Co structure. Additionally, the nature of the anion was found to influence the size of NPs, which was  $4.5 \pm 0.4 \text{ nm}$  in  $\text{C}_1\text{C}_2\text{ImB}(\text{CN})_4$  and  $5.5 \pm 0.4 \text{ nm}$  in  $\text{C}_1\text{C}_2\text{ImFAP}$ , against  $11.6 \pm 0.8 \text{ nm}$  in  $\text{C}_1\text{C}_2\text{ImNTf}_2$ .

In the case of  $\{\text{Fe}[\text{N}(\text{SiMe}_3)_2]_2\}_2$ , some NPs observed in HRTEM had a cubic structure with the lattice parameter matching with the fcc form of  $\text{Fe}^{(0)}$ . However, some NPs had a structure assigned to  $\text{Fe}_2\text{O}_3$ . This partial oxidation could be explained by the presence of residual water in the IL. The fact that  $\text{Fe}^{(0)}$ -NPs were observed with this precursor could be related to the formation of the amine byproduct,  $(\text{Me}_3\text{Si})_2\text{NH}$ , that could act as a ligand to stabilize the formed NPs and to partially protect them against oxidation.

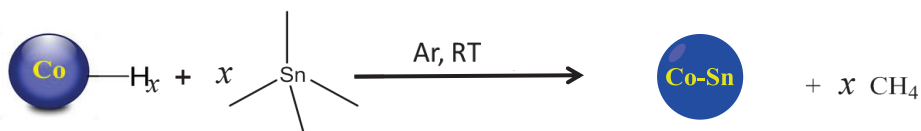
For both precursors, additional characterizations are necessary to definitely conclude about the structure (WAXS, Mossbauer spectroscopy) and the magnetic properties (SQUID) of these NPs.

## II. Synthesis of bimetallic NPs in ILs

### i. Surface chemistry of Co-NPs

The successive or simultaneous decomposition of two OM precursors in an IL may lead to the formation of bimetallic NPs even in the case of immiscible metals. This is in particular possible when the intermediate monometallic NPs have hydrides on their surface.<sup>27</sup> For this reason, the first step towards the synthesis of bimetallic NPs containing Co was to investigate the existence of such hydrides on the surface of Co-NPs.

A first experiment was conducted, which consisted in exposing tetramethyltin to a freshly prepared suspension of Co-NPs in  $\text{C}_1\text{C}_4\text{ImNTf}_2$  under Ar. The presence of methane in the gaseous atmosphere was detected and quantified by GC. This methane production was attributed to the presence of surface hydrides on the Co-NPs.



In a second test, the catalytic properties of the Co-NPs with respect to ethylene hydrogenation were evaluated under Ar. Once again, a quantitative analysis of the gas phase revealed the formation of ethane, which results from the hydrogenation of ethylene by the surface hydrides of the Co-NPs.

## ii. Synthesis of CoRu-NPs

Both experiments gave consistent results leading to an estimated total concentration of surface hydrides of  $1.7\text{-}1.8 \times 10^{-4} \text{ mol. L}^{-1}$ . Even if this represents only a few at% of Co surface atoms, it was sufficient to initiate the deposition of Ru on the Co-NPs by adding Ru (COD) (COT) to the suspension. Indeed, TEM analysis showed a significant increase in the size of the NPs after the reaction.

Similarly, a solution of Co(COD)(COE) reacted with a Ru-NPs suspension, which is known to have even more surface hydrides (Figure 96).<sup>90</sup>

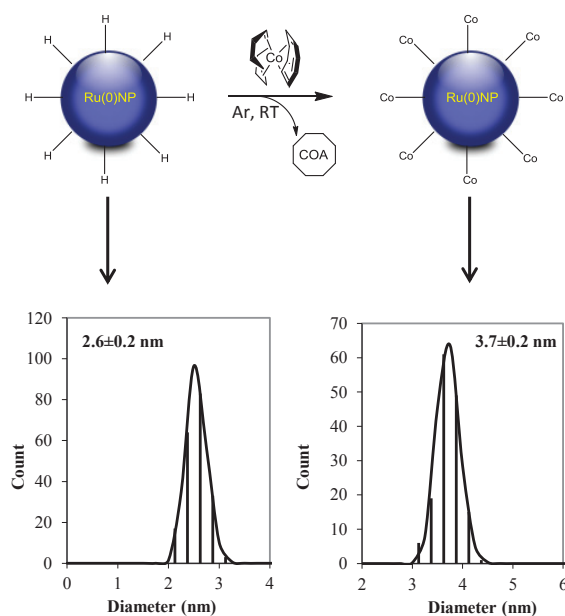


Figure 96 : Size distribution for Ru-NPs obtained through the decomposition of Ru(COD)(COT) under 0.4 MPa  $\text{H}_2$ ,  $100^\circ\text{C}$ , 4 h, in  $\text{C}_1\text{C}_4\text{ImNTf}_2$ , before (left) and after (right) exposure to an equimolar solution of Co(COD)(COE) for 24 h at room temperature under Ar.



These two reactions are therefore supposed to have afforded core@shell NPs of Co@Ru and Ru@Co respectively. To confirm this structure, suspensions were analyzed by anomalous SAXS (ASAXS) in the ESRF. However, due to the presence of an interference arising from the interaction between agglomerated NPs, the elucidation of the internal structure of the NPs by the anomalous effect is more complex than in previous systems such as RuCu. Therefore, this work is still under progress.

In a final approach, the synthesis of CoRu-NPs was attempted by simultaneous decomposition of the two precursors in solution (one pot synthesis). Different Co/Ru ratios were tested, while fixing the total metal content. In all cases, monodispersed suspensions were obtained, some with smaller size than pure metals. This behavior, which has been observed in other bimetallic systems, is a good indication for the formation of bimetallic NPs rather than the separate precipitation of the two metals.

### iii. Synthesis of CoPt-NPs

For the synthesis of CoPt-NPs, the Pt precursor used was Pt(dba)<sub>2</sub>, a Pt<sup>(0)</sup> precursor that is easier to decompose than other Pt<sup>(II)</sup> precursors (eg, PtMe<sub>2</sub>COD). Initially, a two-step synthesis was attempted by adding a solution of Pt(dba)<sub>2</sub> in C<sub>1</sub>C<sub>4</sub>ImNTf<sub>2</sub> to a suspension of Co-NPs in the same IL. After 24 h under Ar, the TEM observations clearly showed the presence of two populations of NPs, one centered at 5 nm (size of the starting Co-NPs) and the other centered at 1 nm, which did not exist in the initial suspension. A STEM examination confirmed that the latter population corresponded to Pt-NPs. In contrary to the CoRu system, it seems that in this case, Pt did not associate with Co. Even though, the deposition of a small portion of the Pt on the Co-NPs cannot be excluded.

To complete this study, a one-step synthesis was attempted. As for the CoRu system, different Co/Pt ratios were tested, while maintaining the total metal content constant. Unlike the two-step synthesis, monodispersed suspensions were obtained in all cases. Again, a monotonic variation in the size of the NPs against the metal composition was observed. For some bimetallic suspensions, the NP size was smaller than that of the pure metals (Figure 97). This indicates that bimetallic NPs have been obtained. To verify this, suspensions were analyzed by ASAXS at the ESRF. The results are still being exploited, but preliminary results suggest that for equimolar CoPt-NPs, Pt would be preferentially distributed at the periphery of the NPs, as expected in a Co@Pt core@shell structure. To support this, these NPs have been

tested as catalysts for the hydrogenation of cyclohexadiene. These tests showed that the reactivity increased sharply with the Pt content up to  $X_{Pt} = 0.5$ , then saturated. This could correspond to the formation of a complete shell of Pt around the cores of Co for  $X_{Pt} \geq 0.5$ .

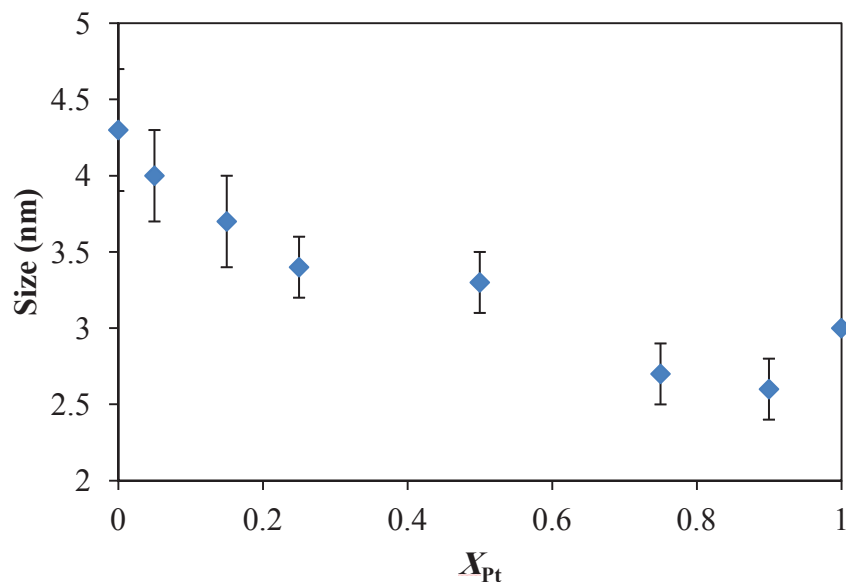


Figure 97 : Size of  $Co_xPt_{1-x}$  NPs plotted as a function of the mole fraction of Pt ( $X_{Pt}$ ) in the initial solution mixture.

In final words, this work confirms that ILs are smart and versatile media for the synthesis of magnetic mono and bimetallic NPs with controlled size and structure. In this study, the synthesis of Co, CoRu and CoPt-NPs was successfully achieved.

One important result in this work is the successful decomposition of  $Co(COD)(COE)$  into Co-NPs by the Si-H group in  $Et_3SiH$ . This paves the way to an even more controllable synthesis of Co-NPs. This reaction could also be used to promote the deposition of Co-NPs on Si wafers treated for instance with HF (to introduce surface Si-H functional groups) by simple reaction with a solution of  $Co(COD)(COE)$  under inert atmosphere.

However, this research also highlighted the recent challenges in determining the exact crystal structure of small NPs (<10nm). HRTEM analysis can be useful in a first approach, but WAXS has proven a more reliable tool. Indeed, while larger NP (or even bulk) structures are well represented in the literature, it sometimes lack the specific data for very small NPs, as in the case of the Fe-NPs generated from  $Fe(COT)_2$ .

Another added challenge in case of magnetic NPs is the possible magnetic interaction between the NPs that resulted in some magnetic coupling as revealed in the SQUID measurement. Such interaction added some complexity for the ASAXS data fitting.

It is important to first tackle these questions to then be able to tune the synthesis to foster the formation of specific well controlled bimetallic structures like, for instance, the ordered  $\text{Co}_1\text{Pt}_1$  structure which is a very interesting material for hard memory storage applications or core@shell Co@M-NPs for catalytic and energy applications.

# **Résumé substantiel en français**

---

**Mise au point d'un procédé de synthèse  
de nanoparticules métalliques magnétiques  
utilisant des liquides ioniques**



## I. Introduction

### i. Intérêt et applications des nanoparticules (NPs) magnétiques

Les nanoparticules (NPs) métalliques constituent un domaine de recherche extrêmement actif car ces objets possèdent des propriétés électriques, optiques, thermiques et magnétiques inhabituelles sous l'effet combiné de phénomènes quantiques et du grand nombre d'atomes de surface. Pour cette raison, les NPs métalliques suscitent un grand intérêt pour divers domaines d'application. Généralement, ces applications nécessitent de fabriquer des NPs de petite taille (inférieure à 10 nm), avec un contrôle précis de leur taille, de leur composition et de leur morphologie, et ce en quantité significative.<sup>1</sup> En particulier, les NPs de métaux magnétiques offrent de nombreux avantages dans une grande variété d'applications (Schéma 1).<sup>2</sup>

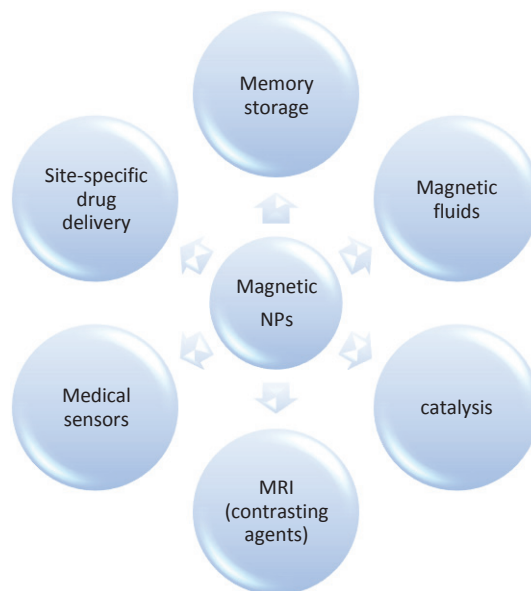


Schéma 1 : Différents domaines d'application des NPs magnétiques

Bien entendu, les NPs magnétiques peuvent être utilisées dans diverses applications technologiques telles que le stockage de données,<sup>3</sup> la spintronique<sup>4</sup> ou les fluides magnétiques (ferrofluides).<sup>5</sup> Elles peuvent également être utilisées dans le domaine médical, en particulier dans les outils de diagnostic. Certaines sont de très bons agents de contraste en imagerie par résonance magnétique pour le diagnostic du cancer.<sup>6</sup> Elles peuvent également traiter certaines formes de cette maladie par destruction thermique localisée de la tumeur sous l'effet d'une excitation par un champ magnétique alternatif de fréquence et d'amplitude adéquates.<sup>7</sup> Une autre possibilité consiste à les utiliser comme vecteur d'un traitement ciblé de la tumeur.<sup>8</sup>

Par ailleurs, certaines NPs magnétiques telles que les Co-NPs sont très prometteuses dans le domaine de la catalyse.<sup>9</sup> Par exemple, elles peuvent être utilisées dans le procédé de Fischer-Tropsch pour convertir CO et H<sub>2</sub> en hydrocarbures liquides.<sup>10</sup> Dans cette application, les Co-NPs ont montré une sélectivité accrue par rapport aux catalyseurs conventionnels concurrents. Un autre usage moins direct des NPs magnétiques en catalyse consiste à les utiliser en tant que support magnétique chimiquement inerte du catalyseur proprement dit. Elles facilitent alors le recyclage de ce dernier, car elles permettent de l'extraire facilement du milieu réactionnel par application d'un champ magnétique externe. Par exemple, un complexe de Mn(III) supporté sur des Co-NPs a été utilisé avec succès pour oxyder des alcools et des sulfures, puis recyclé avec un très bon rendement.<sup>11</sup>

Pour la plupart de ces applications, de meilleures performances sont obtenues lorsque le métal magnétique (le cobalt par exemple) est allié avec un second métal. En effet, cette association avec d'autres métaux tels que le platine ou le ruthénium modifie les propriétés physiques des NPs de manière bénéfique. Par exemple, le composé intermétallique ordonné CoPt est un excellent candidat pour les futurs dispositifs de stockage magnétique de données à très haute densité. En effet, ce composé possède une bonne stabilité chimique, une forte anisotropie magnétocristalline et un champ coercitif élevé, ce qui lui confère des propriétés d'aimant « dur » exceptionnelles.<sup>148, 149</sup> D'autres NPs bimétalliques associant Co et Pt peuvent également être d'excellents catalyseurs pour les piles à combustible.<sup>14, 15, 16, 17, 18</sup> De même, les CoRu-NPs sont des catalyseurs appliqués dans de nombreuses réactions telles que l'hydrogénation de CO par la réaction de Fischer-Tropsch,<sup>19</sup> la réduction des nitroarènes<sup>20</sup> ou l'électrocatalyse de la réduction de l'oxygène dans les piles à combustible.<sup>21</sup> Dans tous ces exemples, l'association de Ru à Co améliore significativement les performances du catalyseur.

## II. Synthèse des NPs métalliques par voie chimique

Pour la plupart de ces applications, des NPs monodisperses en taille sont nécessaires, dont le diamètre peut varier de quelques nm à quelques dizaines de nm. Les procédés chimiques en solution sont bien adaptés à la synthèse de tels objets, que ce soit à partir de sels métalliques ou de précurseurs organométalliques (OM).<sup>22, 23</sup> Cependant, ces procédés nécessitent la mise en œuvre d'agents stabilisants, tels que des ligands ou des polymères, qui en se fixant à la surface des NPs permettent de limiter leur croissance (contrôler leur taille) et

de prévenir leur agglomération (stabiliser les suspensions). Or, dans de nombreuses applications, cette contamination de surface des NPs compromet leurs performances.

Ces dernières années, il a été démontré que cette voie de synthèse peut être appliquée dans des solvants d'un genre particulier, les liquides ioniques (LIs). Dans ce cas, des NPs monodisperses et stables peuvent être obtenues directement, sans ajout d'un agent stabilisant.<sup>24</sup> Les LIs sont des sels possédant un très bas point de fusion (typiquement inférieur à 100°C) et qui possèdent des propriétés uniques : ils ne s'évaporent pratiquement pas, sont chimiquement et thermiquement très stables et possèdent une conductivité électrique appréciable.<sup>25</sup> Surtout, ils jouent également le rôle d'agents stabilisants durant la synthèse de NPs métalliques. Ils permettent ainsi d'obtenir des NPs de taille bien contrôlée, sans contaminer leur surface.

Cette voie de synthèse a été particulièrement étudiée dans notre Laboratoire durant ces dernières années dans les LIs de la famille 1-butyl-3-alkyl-imidazolium bis(trifluoromethanesulphonyl)imide ( $C_1C_n\text{ImNTf}_2$ , Schéma 2).<sup>26</sup> Elle a permis d'obtenir des NPs de nombreux métaux tels que Cu, Ru, Pt, Mn, Ni et même Ta. Il a également été démontré que des NPs bimétalliques de structure contrôlée peuvent être obtenues par cette voie.<sup>27</sup> L'objectif de cette thèse est donc d'obtenir par ce procédé simple et relativement peu coûteux des NPs mono- et bimétalliques magnétiques à base de Co et de Fe, et de les caractériser sur le plan structural et magnétique.

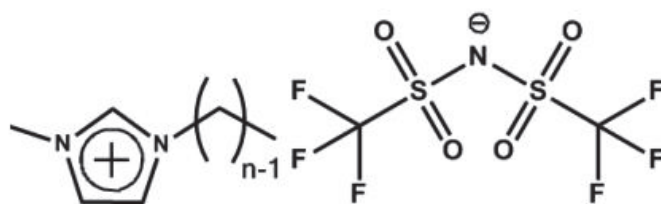


Schéma 2 : Formule développée des LIs 1-butyl-3-alkyl-imidazolium bis(trifluoromethanesulphonyl)imide ( $C_1C_n\text{ImNTf}_2$ )

### III. Synthèse de NPs monométalliques dans les LIs

#### i. Synthèse de Co-NPs

Sur la base d'une étude bibliographique la plus exhaustive possible, un précurseur OM a été identifié parmi plusieurs candidats, le (1,5-cyclooctadiène)(cyclooctadiényl) Cobalt(I),



Co(COD)(COE). Il a été vérifié que ce composé satisfait aux différents critères pour la synthèse des NPs :

- Il possède une bonne solubilité dans les LIs,
- Sa température de décomposition est inférieure à 100°C,
- Le sous-produit de la réaction est le cyclo-octane, un composé volatil facilement éliminé dans la phase gazeuse.

Pour valider ces deux derniers points, une étude complète a été menée par ATG, DRIFT et GC-masse.

Cette réaction a permis de former des Co-NPs, dont la taille a pu être modifiée en variant les conditions expérimentales. Par exemple, en augmentant la température de réaction de 65°C à 100°C puis à 150°C, la taille des Co-NPs a augmenté de 3,6±0,4 nm à 4,1±0,4 nm puis 7,0±0,8 nm, respectivement. Les Co-NPs formaient des assemblées, ce qui indique qu'elles étaient en interaction (Figure 98). Il est intéressant de noter que dans un LI dont le cation imidazolium possède une chaîne alkyle longue, le C<sub>1</sub>C<sub>14</sub>ImNTf<sub>2</sub>, la distance séparant les NPs voisines était plus élevée.

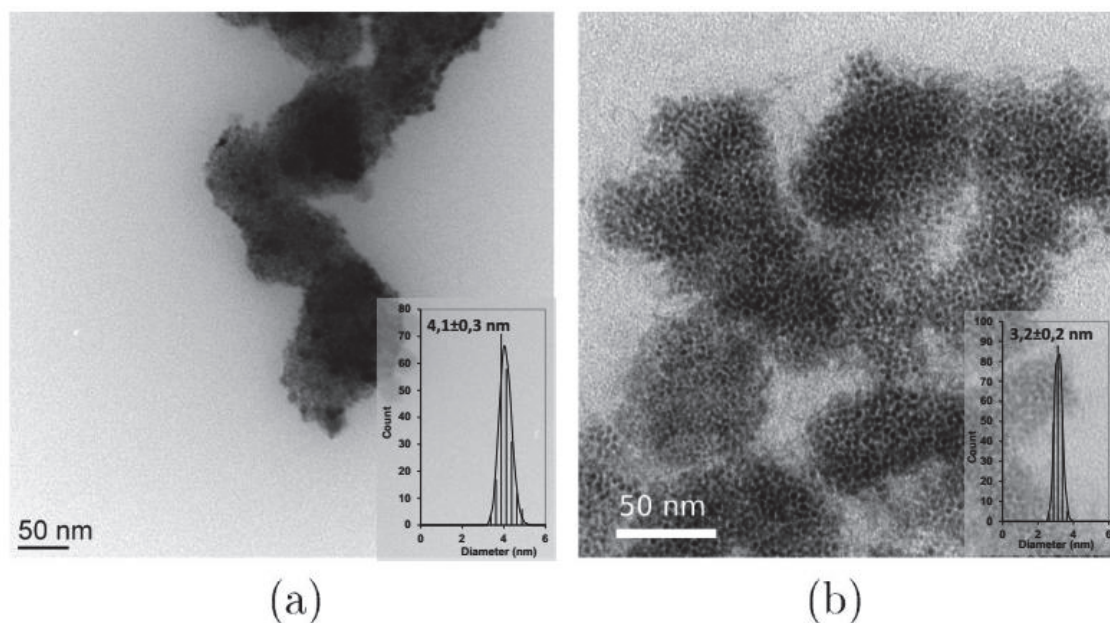


Figure 98 : images TEM de Co-NPs formées à 100°C, sous 0,4MPa de H<sub>2</sub> dans (a) C<sub>1</sub>C<sub>4</sub>ImNTf<sub>2</sub> et (b) C<sub>1</sub>C<sub>14</sub>ImNTf<sub>2</sub>.

La structure de ces NPs a été étudiée par HRTEM et par WAXS. Ces deux techniques ont montré que les Co-NPs étaient constituées d'un allotrope métastable de Co(0) appelé  $\epsilon$ -Co. Cette structure cubique n'est pas compacte : les Co-NPs ont donc progressivement évolué vers la structure hcp, qui est l'allotrope stable de Co(0) (Figure 99).

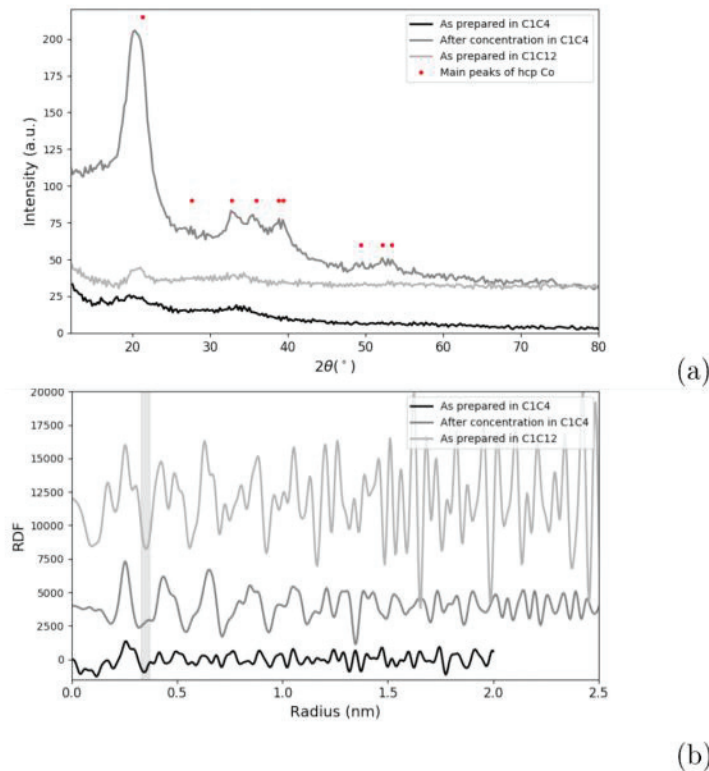


Figure 99 : (a) courbes de diffusion et (b) distributions radiales (RDF) correspondantes pour des Co-NPs préparées dans  $C_1C_4ImNTf_2$ , dans  $C_1C_{14}ImNTf_2$  et après décantation sur un aimant dans  $C_1C_4ImNTf_2$ .

Les caractéristiques magnétiques des Co-NPs ont été mesurées au SQUID. Les courbes d'aimantation ont confirmé que les NPs étaient formées de Co(0). Ces NPs étaient, comme attendu, superparamagnétiques à température ambiante (Figure 100). Leur taille estimée par fit de Langevin correspondait bien à celle mesurée au TEM.

La température de blocage a été également mesurée par la technique de FC-ZFC (elle correspond au maximum de la courbe ZFC, Figure 101). Cette température était de 7 K pour des Co-NPs synthétisées dans le  $C_1C_4ImNTf_2$ , tandis qu'elle atteignait 160 K dans le  $C_1C_{14}ImNTf_2$ . Cette différence a été attribuée à une différence d'anisotropie qui trouve probablement son origine dans un couplage dipolaire des NPs. Toutefois, cette interprétation conduit à conclure que ce couplage était plus prononcé dans le  $C_1C_{14}ImNTf_2$ , ce qui est

surprenant car dans ce LI, les Co-NPs étaient plus éloignées les unes des autres (voir Figure 98b).

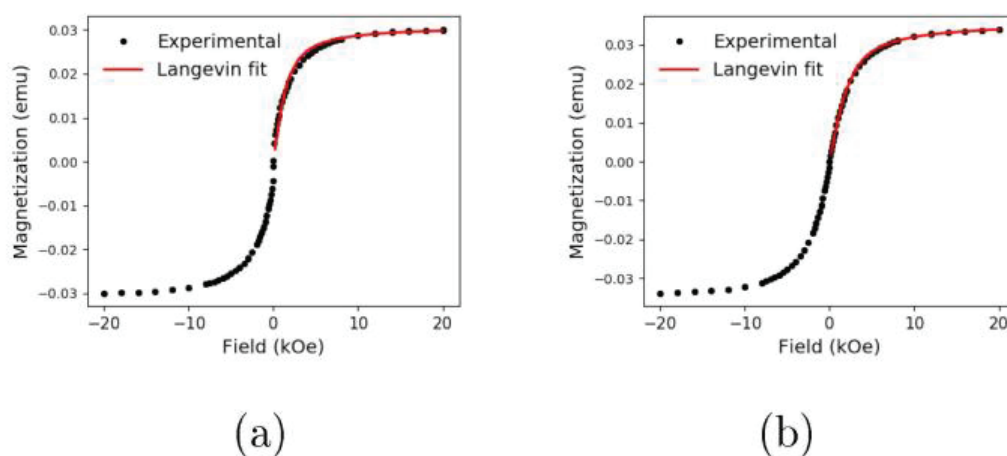


Figure 100 : Courbes d'aimantation à 250 K de Co-NPs synthétisées dans (a)  $C_1C_4ImNTf_2$  et (b)  $C_1C_{14}ImNTf_2$ .

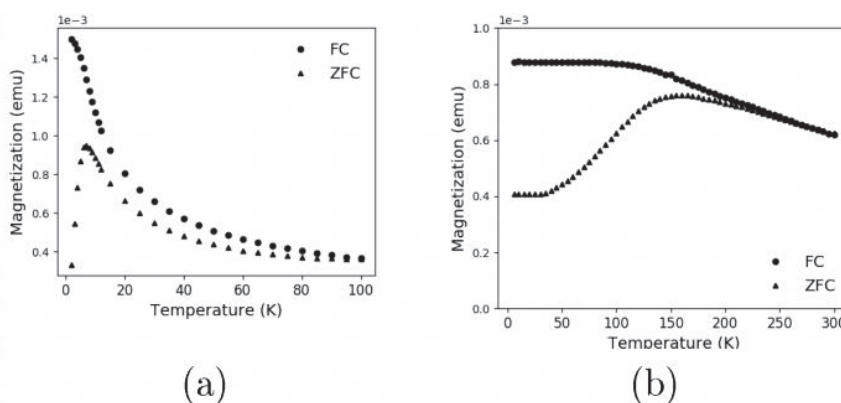


Figure 101 : Courbes FC-ZFC de Co-NPs synthétisées dans (a)  $C_1C_4ImNTf_2$  et (b)  $C_1C_{14}ImNTf_2$ .

Enfin, une modification de la synthèse des Co-NPs a été étudiée, qui consiste à remplacer le  $H_2$  par un agent réducteur en solution dans le LI,  $Et_3SiH$ . Cette variante du procédé a également permis d'obtenir des Co-NPs petites et monodisperses, dont la caractérisation structurale et magnétique est en cours.

## ii. Synthèse de Fe-NPs

Pour la synthèse de Fe-NPs, deux précurseurs OM ont été évalués,  $Fe(COT)_2$  et  $\{Fe[N(Me_3Si)_2]_2\}_2$ . Ces deux composés ont pu être décomposés sous  $H_2$  dans le  $C_1C_4ImNTf_2$ . Dans les deux cas, de petites NPs ( $< 5$  nm) ont été obtenues avec une distribution de tailles resserrée.

Quelques NPs formées à partir de  $\text{Fe}(\text{COT})_2$  ont été analysées par HRTEM. Elles étaient bien cristallisées, et leur structure correspondait à la maille tétragonale de  $\text{Fe}_2\text{O}_3$ . Ce résultat est surprenant, dans la mesure où toutes les synthèses ont été conduites à l'abri de l'air sous atmosphère inerte. L'anion  $\text{NTf}_2$ , qui contient des atomes d'oxygène, n'est a priori pas responsable de cette oxydation, qui a également été observée pour des NPs synthétisées dans des LIs avec des anions différents :  $\text{C}_1\text{C}_2\text{ImB}(\text{CN})_4$  et  $\text{C}_1\text{C}_2\text{ImFAP}$ . Il est en revanche possible que cette oxydation résulte de la présence d'eau résiduelle dans le LI. Dans tous les cas, il convient de noter que la nature de l'anion a influencé la taille des NPs, qui était de  $4,5 \pm 0,4$  nm dans  $\text{C}_1\text{C}_2\text{ImB}(\text{CN})_4$  et  $5,5 \pm 0,4$  nm dans  $\text{C}_1\text{C}_2\text{ImFAP}$ , contre  $11,6 \pm 0,8$  nm dans  $\text{C}_1\text{C}_2\text{ImNTf}_2$ .

Dans le cas de  $\{\text{Fe}[\text{N}(\text{Me}_3\text{Si})_3]_2\}_2$ , certaines NPs observées au HRTEM avaient une structure cubique dont le paramètre de maille coïncide avec la forme fcc de  $\text{Fe}(0)$ . Il semble donc que le métal a donc pu être obtenu dans ce cas. Cependant et à nouveau, certaines NPs possédaient une structure attribuée à  $\text{Fe}_2\text{O}_3$ . Cette oxydation partielle pourrait également être expliquée par la présence d'eau résiduelle dans le LI.

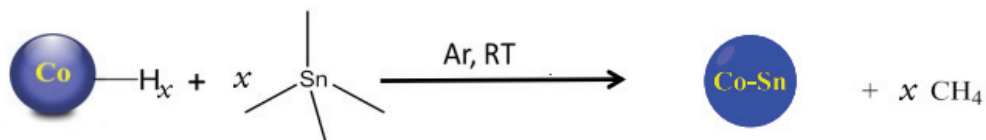
Pour les deux précurseurs, des caractérisations complémentaires sont nécessaires pour conclure définitivement quant à la structure (WAXS, spectroscopie Mossbauer) et aux propriétés magnétiques (SQUID) de ces NPs.

## IV. Synthèse de NPs bimétalliques dans les LIs

### i. Chimie de surface des Co-NPs

La décomposition successive ou simultanée de deux précurseurs OM dans un LI peut conduire à la formation de NPs bimétalliques même dans le cas de métaux immiscibles, pour peu que les NPs monométalliques intermédiaires portent des hydrures de surface.<sup>27</sup> Pour cette raison, la première tâche en vue de la synthèse de NPs bimétalliques contenant du Co a été la vérification de la présence de ces hydrures à la surface des Co-NPs.

Un premier test a été mené, qui a consisté à exposer du tétraméthyle-étain à une suspension de Co-NPs fraîchement préparée dans  $\text{C}_1\text{C}_4\text{ImNTf}_2$ . L'apparition de méthane dans l'atmosphère gazeuse a été détectée et quantifiée par GC. Cette production de méthane a été attribuée à la présence sur les Co-NPs d'hydrures de surface, qui conduisent à la réaction suivante :



Lors d'un second test, les propriétés catalytiques des Co-NPs vis-à-vis de l'hydrogénation de l'éthylène ont été évaluées. Une fois encore, une analyse quantitative de la phase gazeuse a permis de mettre en évidence la formation d'éthane, qui résulte de l'hydrogénation de l'éthylène par les hydrures de surface des Co-NPs.

## ii. Synthèse de CoRu-NPs

Les deux tests ont donné des résultats concordants qui ont permis d'estimer la concentration totale en hydrures de surface à  $1,7-1,8 \cdot 10^{-4} \text{ mol.L}^{-1}$ . Cela ne représente que quelques % des atomes de Co de surface des Co-NPs, mais a été suffisant pour initier le dépôt de Ru sur les Co-NPs par addition de Ru(COD)(COT) dans la suspension. En effet, l'analyse TEM a montré un accroissement significatif de la taille des NPs après la réaction (Figure 102).

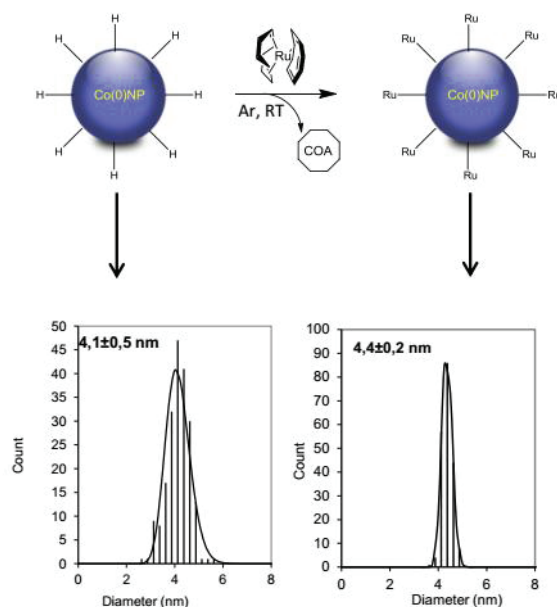


Figure 102 : Distribution de tailles de Co-NPs synthétisées par décomposition de Co(COD)(COE) à 100°C, sous 0,4 MPa de H<sub>2</sub> dans C<sub>1</sub>C<sub>4</sub>ImNTf<sub>2</sub> (à gauche) avant et (à droite) après exposition à une solution équimolaire de Ru(COD)(COT) pendant 24 h à température ambiante sous Ar.

De manière symétrique, une solution de Co(COD)(COE) a réagi sur une suspension de RuNPs, qui sont connues pour posséder des hydrures de surface (Figure 103).<sup>90</sup>

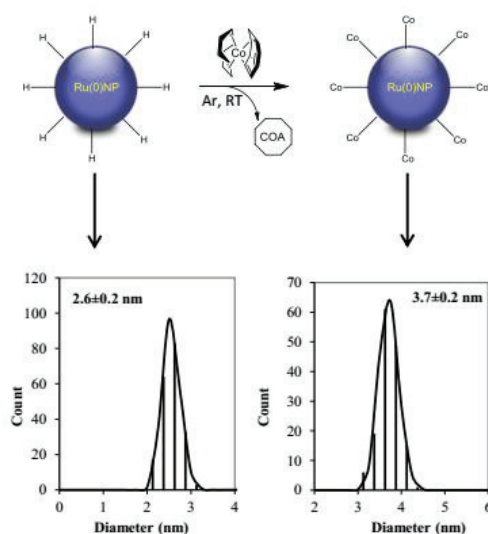


Figure 103 : Distribution de tailles de Ru-NPs synthétisées par décomposition de Ru(COD)(COT) à 100°C, sous 0,4 MPa de H<sub>2</sub> dans C<sub>1</sub>C<sub>4</sub>ImNTf<sub>2</sub> (à gauche) avant et (à droite) après exposition à une solution équimolaire de Co(COD)(COE) pendant 24 h à température ambiante sous Ar.

Ces deux réactions sont donc supposées avoir formé des NPs cœur@coquille, respectivement Co@Ru et Ru@Co. Pour vérifier cette structure, des suspensions ont été analysées par SAXS anomal (ASAXS) à l'ESRF. Les résultats sont encore en cours d'exploitation.

Dans une dernière approche, une synthèse de NPs bimétalliques de Co et de Ru a été tentée en une seule étape, par décomposition simultanée des deux précurseurs en solution dans C<sub>1</sub>C<sub>4</sub>ImNTf<sub>2</sub>. Différents ratios de Co/Ru ont été testés, en maintenant constante la teneur totale en métal. Dans tous les cas, des suspensions monodisperses ont été obtenues, avec pour certaines une taille de NPs inférieure à celle des métaux purs. De plus, une augmentation monotone de la taille des NPs a été observée avec la teneur en Co dans le milieu (Figure 104). Ce comportement, qui a été observé dans d'autres systèmes, est une bonne indication de la formation de NPs bimétalliques plutôt que de la précipitation séparée des deux métaux.

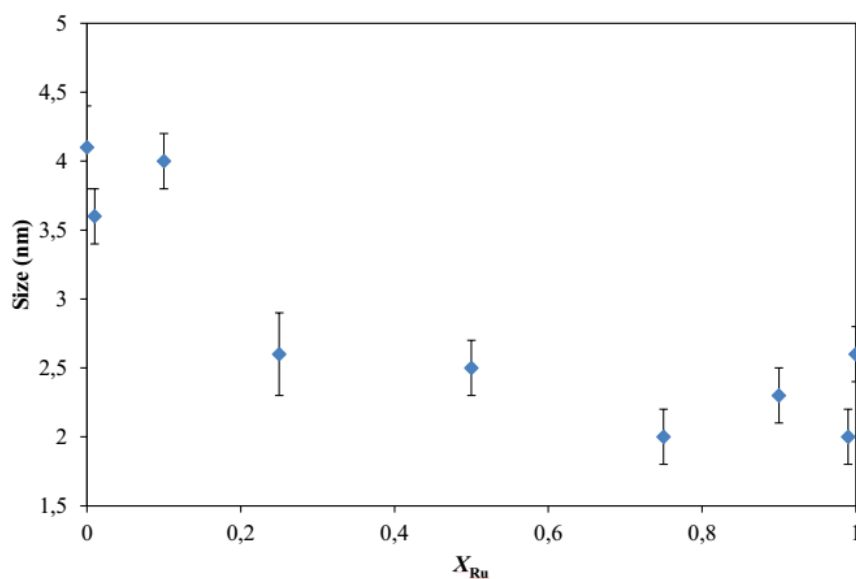


Figure 104 : Taille des NPs par décomposition simultanée de Co(COD)(COE) et Ru(COD)(COT) dans des mélanges  $Co_{1-x}Ru_x$  en fonction de la teneur en Ru dans le milieu.

### iii. Synthèse de CoPt-NPs

Pour la synthèse de CoPt-NPs, le précurseur de Pt retenu est le  $Pt(dba)_2$ , un précurseur de Pt(0) plus facile à décomposer que d'autres précurseurs de Pt(II) tels que  $PtMe_2COD$ . Dans un premier temps, une synthèse en deux étapes a été tentée en ajoutant à une suspension de Co-NPs dans  $C_1C_4ImNTf_2$  à une solution de  $Pt(dba)_2$  dans le même LI. Après 24 h sous Ar, les observations TEM ont clairement montré la présence de deux populations de NPs, l'une vers 5 nm (taille des Co-NPs de départ) et l'autre vers 1 nm, qui n'existait pas dans la suspension initiale (Figure 105-a). Un examen au STEM a confirmé que cette dernière population correspondait à des Pt-NPs (Figure 105-b). Finalement, et contrairement au système CoRu, il semble donc que dans ce cas, le Pt ne s'est pas associé au Co.

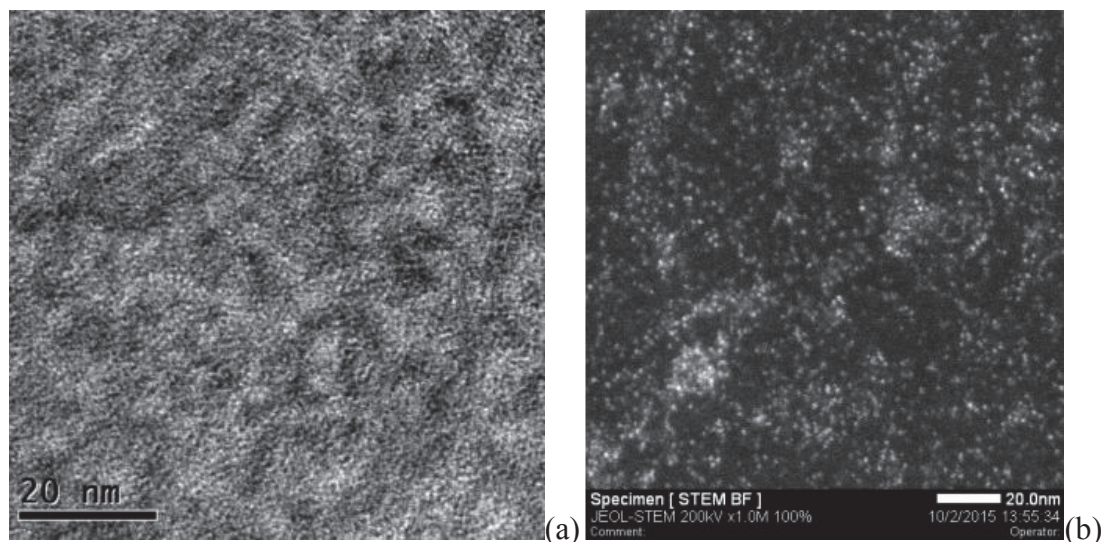


Figure 105 : (a) Image TEM et (b) image STEM d'une suspension obtenue par réaction entre une suspension de Co-NPs dans  $C_1C_4ImNTf_2$  et une solution de  $Pt(dba)_2$  dans le même LI.

Pour compléter cette étude, une synthèse en une étape a été tentée, comme dans le système précédent. Comme précédemment, différents ratios de Co/Pt ont été testés, en maintenant constante la teneur totale en métal. Contrairement à la synthèse en deux étapes, des suspensions monodisperses ont été obtenues dans tous les cas. A nouveau, une variation monotone de la taille des NPs en fonction de la composition a été observée, ainsi que l'existence de suspensions dont les NPs sont plus petites que celles des deux métaux séparément (Figure 106). Il semble donc que dans ce cas, des NPs bimétalliques ont bien été obtenues. Pour le vérifier, des suspensions ont été analysées par SAXS à l'ESRF. Les résultats sont encore en cours d'exploitation. Par ailleurs, ces NPs ont été testées pour la catalyse de l'hydrogénation du cyclohexadiène. Ces tests ont montré que la réactivité augmentait fortement avec la teneur en Pt jusqu'à  $X_{Pt}=0,5$ , puis saturait. Cela pourrait correspondre à la formation à partir de cette composition d'une coquille complète de Pt autour des cœurs de Co.



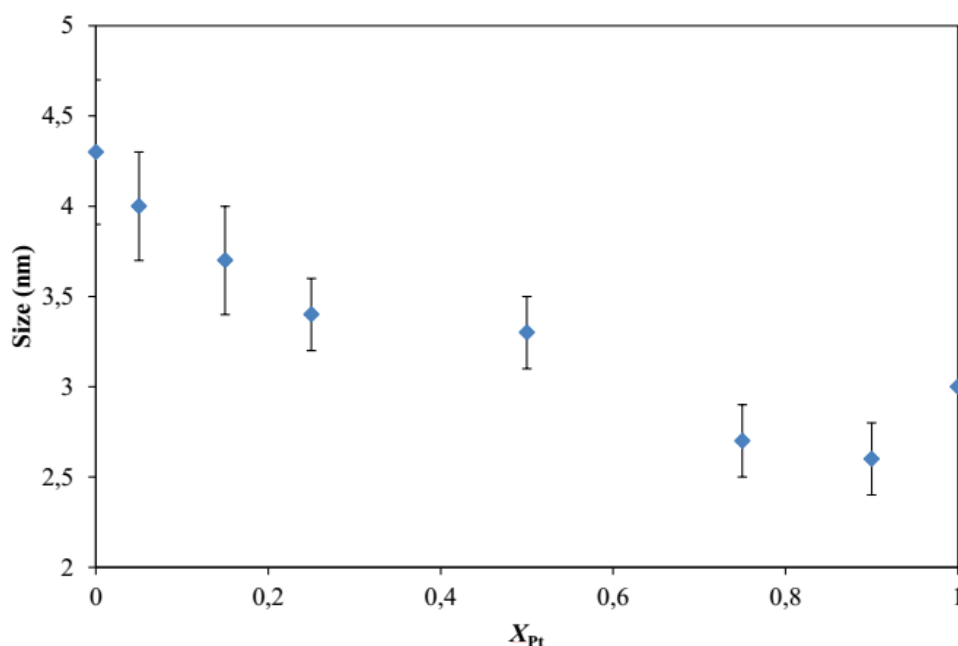


Figure 106 : Taille des NPs par décomposition simultanée de Co(COD)(COE) et Pt(dba)<sub>2</sub> dans des mélanges Co<sub>1-x</sub>Pt<sub>x</sub> en fonction de la teneur en Pt dans le milieu.

## V. Conclusion

En conclusion, ce travail démontre que les LIs constituent un milieu de choix pour réaliser la synthèse de NPs magnétiques par un procédé simple, peu onéreux, mais performant. Pour cela, des précurseurs OM adéquats ont été identifiés et mis en œuvre. Un procédé d'élaboration fiable et reproductible et de Co-NPs monodisperses de taille réglable a été en particulier développé. Ces NPs ont pu être complètement caractérisées sur le plan structural. Elles adoptent une phase métastable appelée  $\epsilon$ -Co qui évolue vers la structure hcp, qui est l'allotrope stable de Co(0). Les propriétés magnétiques de ces NPs ont également été mesurées. Elles sont comme attendu superparamagnétiques à température ambiante. Cependant, les mesures indiquent qu'elles sont en interaction, ce qui modifie leur réponse magnétique (température de blocage notamment).

Une tentative d'adaptation de ce procédé pour la synthèse de Fe-NPs a également été menée. Dans certains cas, des NPs de Fe(0) ont pu être obtenues, mais des NPs oxydées de Fe<sub>2</sub>O<sub>3</sub> ont toujours été observées. Cette oxydation est probablement due à la présence d'eau résiduelle dans le LI.

Finalement, des NPs bimétalliques de Co ont pu être synthétisées avec succès. Cela résulte probablement de la présence sur les Co-NPs d'hydrures de surface. Dans le cas de CoRu, des synthèses en deux étapes (réaction du précurseur de Ru sur les Co-NPs et inversement) semblent avoir conduit à l'obtention de NPs bimétalliques. En revanche, dans le cas de CoPt, cette stratégie a clairement conduit à la précipitation de Pt-NPs indépendamment du Co. Pour les deux systèmes, la co-décomposition des deux précurseurs (Co et Pt ou Ru) semble dans tous les cas avoir résulté dans la formation de NPs bimétalliques. La structure de toutes ces NPs est en cours d'analyse. Leurs propriétés magnétiques doivent encore être mesurées. Cependant, des premiers tests montrent d'ores et déjà qu'elles pourront probablement trouver des applications en catalyse.



# References

1. Goesmann, H.; Feldmann, C. Nanoparticulate Functional Materials. *Angewandte Chemie International Edition* **2010**, *49* (8), 1362-1395.
2. Frey, N.; Sun, S. Magnetic Nanoparticle for Information Storage Applications. In *Inorganic Nanoparticles*; CRC Press: New York, 2010, pp 33-68.
3. Galloway, J. M.; Talbot, J. E.; Critchley, K.; Miles, J. J.; Bramble, J. P. Developing Biotemplated Data Storage: Room Temperature Biomineralization of L10 CoPt Magnetic Nanoparticles. *Advanced Functional Materials* **2015**, *25* (29), 4590-4600.
4. Wang, C.; Meyer, J.; Teichert, N.; Auge, A.; Rausch, E.; Balke, B.; Hütten, A.; Fecher, G. H.; Felser, C. Heusler nanoparticles for spintronics and ferromagnetic shape memory alloys. *Journal of Vacuum Science & Technology B, Nanotechnology and Microelectronics: Materials, Processing, Measurement, and Phenomena* **2014**, *32* (2), 020802.
5. Genc, S.; Derin, B. Synthesis and rheology of ferrofluids: a review. *Current Opinion in Chemical Engineering* **2014**, *3*, 118-124.
6. Parkes, L. M.; Hodgson, R.; Lu, L. T.; Tung, L. D.; Robinson, I.; Fernig, D. G.; Thanh, N. T. K. Cobalt nanoparticles as a novel magnetic resonance contrast agent—relaxivities at 1.5 and 3 Tesla. *Contrast Media & Molecular Imaging* **2008**, *3* (4), 150-156.
7. Obaidat, I.; Issa, B.; Haik, Y. Magnetic Properties of Magnetic Nanoparticles for Efficient Hyperthermia. *Nanomaterials* **2015**, *5* (1), 63.
8. Chattopadhyay, S.; Dash, S. K.; Ghosh, T.; Das, D.; Pramanik, P.; Roy, S. Surface modification of cobalt oxide nanoparticles using phosphonomethyl iminodiacetic acid followed by folic acid: a biocompatible vehicle for targeted anticancer drug delivery. *Cancer Nanotechnology* **2013**, *4* (4-5), 103-116.
9. Hudson, R.; Feng, Y.; Varma, R. S.; Moores, A. Bare magnetic nanoparticles: sustainable synthesis and applications in catalytic organic transformations. *Green Chemistry* **2014**, *16* (10), 4493-4505.
10. Gual, A.; Godard, C.; Castillon, S.; Curulla-Ferré, D.; Claver, C. Colloidal Ru, Co and Fe-nanoparticles. Synthesis and application as nanocatalysts in the Fischer Tropsch process. *Catalysis Today* **2012**, *183* (1), 154-171.
11. Judy Azar, A. R.; Safaei, E.; Mohebbi, S. A novel Schiff base of Mn(III) complex supported on magnetic cobalt nanoparticles as a highly efficient retrievable heterogeneous catalyst in oxidation of alcohols and sulfides compounds. *Materials Research Bulletin* **2015**, *70*, 753-761.
12. Pan, Z.; Rawat, R. S.; Lin, J.; Karamat, S.; Lee, P. C. K.; Springham, S. V.; Tan, A. T. L. Direct Synthesis of L10-Phase Nanostructured CoPt Using Dense Plasma Focus Device Operating in Non-optimized Focus Mode. *MRS Proceedings* **2011**, *1250*.
13. Weller, D.; Moser, A.; Folks, L.; Best, M. E.; Wen, L.; Toney, M. F.; Schwickert, M.; Thiele, J. U.; Doerner, M. F. High  $K_{eff}$  materials approach to 100 Gbits/in<sup>2</sup>. *IEEE Transactions on Magnetics* **2000**, *36* (1), 10-15.
14. Cai, Y. X.; Wolfkuhler, D.; Myalitsin, A.; Perlich, J.; Meyer, A.; Klinke, C. Tunable Electrical Transport through Annealed Monolayers of Monodisperse Cobalt–Platinum Nanoparticles. *ACS Nano* **2011**, *5*, 67.
15. Jiang, S. J.; Ma, Y. W.; Jian, G. Q.; Tao, H. S.; Wang, X. Z.; Fan, Y. M.; Lu, Y. N.; Hu, Z.; Chen, Y. Facile Construction of Pt–Co/CNx Nanotube Electrocatalysts and Their Application to the Oxygen Reduction Reaction. *Advanced Materials* **2009**, *21*, 4953.
16. Vinayan, B. P.; Jafri, R. I.; Nagar, R.; Rajalakshmi, N.; Sethupathi, K.; Ramaprabhu, S. Catalytic Activity of Platinum–Cobalt Alloy Nanoparticles Decorated Functionalized Multiwalled Carbon Nanotubes for Oxygen Reduction Reaction in PEMFC. *International Journal of Hydrogen Energy* **2012**, *37*, 412.

17. Wang, G. H.; Hilgert, J.; Richter, F. H.; Wang, F.; Bongard, H. J.; Spliethoff, B.; Weidenthaler, C.; Schuth, F. Platinum–Cobalt Bimetallic Nanoparticles in Hollow Carbon Nanospheres for Hydrogenolysis of 5–Hydroxymethylfurfural. *Nature Materials* **2014**, *13*, 293.
18. Xin, H. L.; Alayoglu, S.; Tao, R.; Genc, A.; Wang, C. M.; Kovarik, L.; Stach, E. A.; Wang, L. W.; Salmeron, M.; Somorjai, G. A.; Zheng, H. M. Revealing the Atomic Restructuring of Pt–Co Nanoparticles. *Nano Letters* **2014**, *14*, 3203.
19. Tavasoli, A.; Taghavi, S. Performance enhancement of bimetallic Co–Ru/CNTs nano catalysts using microemulsion technique. *Journal of Energy Chemistry* **2013**, *22* (5), 747-754.
20. Udumula, V.; Tyler, J. H.; Davis, D. A.; Wang, H.; Linford, M. R.; Minson, P. S.; Michaelis, D. J. Dual Optimization Approach to Bimetallic Nanoparticle Catalysis: Impact of M1/M2 Ratio and Supporting Polymer Structure on Reactivity. *ACS Catalysis* **2015**, *5* (6), 3457-3462.
21. Gucci, L.; Boskovic, G.; Kiss, E. Bimetallic Cobalt Based Catalysts. *Catalysis Reviews* **2010**, *52* (2), 133-203.
22. Amiens, C.; Chaudret, B.; Ciuculescu-Pradines, D.; Colliere, V.; Fajerweg, K.; Fau, P.; Kahn, M.; Maisonnat, A.; Soulantica, K.; Philippot, K. Organometallic approach for the synthesis of nanostructures. *New Journal of Chemistry* **2013**, *37* (11), 3374-3401.
23. Lu, L.-Y.; Yu, L.-N.; Xu, X.-G.; Jiang, Y. Monodisperse magnetic metallic nanoparticles: synthesis, performance enhancement, and advanced applications. *Rare Metals* **2013**, *32* (4), 323-331.
24. Dupont, J.; Meneghetti, M. R. On the stabilisation and surface properties of soluble transition-metal nanoparticles in non-functionalised imidazolium-based ionic liquids. *Current Opinion in Colloid & Interface Science* **2013**, *18* (1), 54-60.
25. Hayes, R.; Warr, G. G.; Atkin, R. Structure and Nanostructure in Ionic Liquids. *Chemical Reviews* **2015**, *115* (13), 6357-6426.
26. S. Campbell, P.; H.G. Pechtl, M.; C. Santini, C.; Haumesser, P.-H. Ruthenium Nanoparticles in Ionic Liquids - A Saga. *Current Organic Chemistry* **2013**, *17* (4), 414-429.
27. Helgadottir, I.; Freychet, G.; Arquilliere, P.; Maret, M.; Gergaud, P.; Haumesser, P. H.; Santini, C. C. Ru-core/Cu-shell bimetallic nanoparticles with controlled size formed in one-pot synthesis. *Nanoscale* **2014**, *6* (24), 14856-14862.
28. Schmid, G. *Nanoparticles: From Theory to Application*; Wiley-VCH Verlag GmbH & Co. KGaA2005.
29. Alloyeau, D.; Mottet, C.; Ricolleau, C. *Nanoalloys: Synthesis, Structure and Properties*; Springer London2012.
30. Helmut, B.; Kyatanahalli S, N. CHAPTER 2 - Metal Nanoclusters: Synthesis and Strategies for their Size Control A2 - CORAIN, B. In *Metal Nanoclusters in Catalysis and Materials Science*, Schmid, G.; Toshima, N., Eds.; Elsevier: Amsterdam, 2008, pp 21-48.
31. Scariot, M.; Silva, D. O.; Scholten, J. D.; Machado, G.; Teixeira, S. R.; Novak, M. A.; Ebeling, G.; Dupont, J. Cobalt Nanocubes in Ionic Liquids: Synthesis and Properties. *Angewandte Chemie* **2008**, *120* (47), 9215-9218.
32. Dengler, M.; Saatchi, K.; Dailey, J. P.; Matsubara, J.; Mikelberg, F. S.; Häfeli, U. O.; Yeung, S. N. Targeted Delivery of Magnetic Cobalt Nanoparticles to the Eye Following Systemic Administration. *AIP Conference Proceedings* **2010**, *1311* (1), 329-336.
33. Mohapatra, S.; Rout, S. R.; Maiti, S.; Maiti, T. K.; Panda, A. B. Monodisperse mesoporous cobalt ferrite nanoparticles: synthesis and application in targeted delivery of antitumor drugs. *Journal of Materials Chemistry* **2011**, *21* (25), 9185-9193.
34. Hong, J. S.; Pyun, J.; Park, Y. W.; Kim, C. S.; Shim, I. B. Oxidation Effect in Cobalt Nanoparticles Magnetic Fluids. *IEEE Transactions on Magnetics* **2009**, *45* (6), 2464-2466.
35. Scherer, C.; Figueiredo Neto, A. M. Ferrofluids: properties and applications. *Brazilian Journal of Physics* **2005**, *35*, 718-727.
36. Sant, S. B. Nanoparticles: From Theory to Applications. *Materials and Manufacturing Processes* **2012**, *27* (12), 1462-1463.

37. Meng, H.; Zhao, F.; Zhang, Z. Preparation of cobalt nanoparticles by direct current arc plasma evaporation method. *International Journal of Refractory Metals and Hard Materials* **2012**, *31* (0), 224-229.
38. Balzani, V. Nanoscience and Nanotechnology: A Personal View of a Chemist. *Small* **2005**, *1* (3), 278-283.
39. Amiens, C.; Chaudret, B. ORGANOMETALLIC SYNTHESIS OF NANOPARTICLES. *Modern Physics Letters B* **2007**, *21* (18), 1133-1141.
40. Salman, S. A.; Usami, T.; Kuroda, K.; Okido, M. Synthesis and Characterization of Cobalt Nanoparticles Using Hydrazine and Citric Acid. *Journal of Nanotechnology* **2014**, *2014*, 6.
41. Sun, S.; Murray, C. B. Synthesis of monodisperse cobalt nanocrystals and their assembly into magnetic superlattices (invited). *Journal of Applied Physics* **1999**, *85* (8), 4325-4330.
42. Natalie, A. F.; Shouheng, S. Magnetic Nanoparticle for Information Storage Applications. In *Inorganic Nanoparticles: Synthesis, Applications, and Perspectives*; CRC Press, 2010, pp 33-68.
43. Legrand, J.; Ngo, A. T.; Petit, C.; Pileni, M. P. Domain Shapes and Superlattices Made of Cobalt Nanocrystals. *Advanced Materials* **2001**, *13* (1), 58-62.
44. Petit, C.; Russier, V.; Pileni, M. P. Effect of the Structure of Cobalt Nanocrystal Organization on the Collective Magnetic Properties. *The Journal of Physical Chemistry B* **2003**, *107* (38), 10333-10336.
45. Petit, C.; Wang, Z. L.; Pileni, M. P. Seven-Nanometer Hexagonal Close Packed Cobalt Nanocrystals for High-Temperature Magnetic Applications through a Novel Annealing Process. *The Journal of Physical Chemistry B* **2005**, *109* (32), 15309-15316.
46. Dumestre, F.; Chaudret, B.; Amiens, C.; Fromen, M.-C.; Casanove, M.-J.; Renaud, P.; Zurcher, P. Shape Control of Thermodynamically Stable Cobalt Nanorods through Organometallic Chemistry. *Angewandte Chemie International Edition* **2002**, *41* (22), 4286-4289.
47. Verelst, M.; Ely, T. O.; Amiens, C.; Snoeck, E.; Lecante, P.; Mosset, A.; Respaud, M.; Broto, J. M.; Chaudret, B. Synthesis and Characterization of CoO, Co<sub>3</sub>O<sub>4</sub>, and Mixed Co/CoO Nanoparticles. *Chemistry of Materials* **1999**, *11* (10), 2702-2708.
48. Dumestre, F.; Martinez, S.; Zitoun, D.; Fromen, M.-C.; Casanove, M.-J.; Lecante, P.; Respaud, M.; Serres, A.; Benfield, R. E.; Amiens, C.; Chaudret, B. Magnetic nanoparticles through organometallic synthesis: evolution of the magnetic properties from isolated nanoparticles to organised nanostructures. *Faraday Discussions* **2004**, *125* (0), 265-278.
49. Osuna, J.; de Caro, D.; Amiens, C.; Chaudret, B.; Snoeck, E.; Respaud, M.; Broto, J.-M.; Fert, A. Synthesis, Characterization, and Magnetic Properties of Cobalt Nanoparticles from an Organometallic Precursor. *The Journal of Physical Chemistry* **1996**, *100* (35), 14571-14574.
50. Ely, T. O.; Pan, C.; Amiens, C.; Chaudret, B.; Dassenoy, F.; Lecante, P.; Casanove, M. J.; Mosset, A.; Respaud, M.; Broto, J. M. Nanoscale Bimetallic Co<sub>x</sub>Pt<sub>1-x</sub> Particles Dispersed in Poly(vinylpyrrolidone): Synthesis from Organometallic Precursors and Characterization. *The Journal of Physical Chemistry B* **2000**, *104* (4), 695-702.
51. Comesana-Hermo, M.; Estivill, R.; Ciuculescu, D.; Li, Z.-A.; Spasova, M.; Farle, M.; Amiens, C. Effect of a Side Reaction Involving Structural Changes of the Surfactants on the Shape Control of Cobalt Nanoparticles. *Langmuir* **2014**, *30* (15), 4474-4482.
52. Respaud, M.; Broto, J. M.; Rakoto, H.; Fert, A. R.; Thomas, L.; Barbara, B.; Verelst, M.; Snoeck, E.; Lecante, P.; Mosset, A.; Osuna, J.; Ely, T. O.; Amiens, C.; Chaudret, B. Surface effects on the magnetic properties of ultrafine cobalt particles. *Physical Review B* **1998**, *57* (5), 2925-2935.
53. Behrens, S.; Essig, S. A facile procedure for magnetic fluids using room temperature ionic liquids. *Journal of Materials Chemistry* **2012**, *22* (9), 3811-3816.
54. Silva, D. O.; Scholten, J. D.; Gelesky, M. A.; Teixeira, S. R.; Dos Santos, A. C. B.; Souza-Aguiar, E. F.; Dupont, J. Catalytic Gas-to-Liquid Processing Using Cobalt Nanoparticles Dispersed in Imidazolium Ionic Liquids. *ChemSusChem* **2008**, *1* (4), 291-294.
55. Vollmer, C.; Redel, E.; Abu-Shandi, K.; Thomann, R.; Manyar, H.; Hardacre, C.; Janiak, C. Microwave Irradiation for the Facile Synthesis of Transition-Metal Nanoparticles (NPs) in Ionic Liquids

(ILs) from Metal–Carbonyl Precursors and Ru-, Rh-, and Ir-NP/IL Dispersions as Biphasic Liquid–Liquid Hydrogenation Nanocatalysts for Cyclohexene. *Chemistry – A European Journal* **2010**, *16* (12), 3849-3858.

56. Chaudret, B.; Philippot, K. Organometallic Nanoparticles of Metals or Metal Oxides. *Oil & Gas Science and Technology - Rev. IFP* **2007**, *62* (6), 799-817.

57. Vollmer, C.; Janiak, C. Naked metal nanoparticles from metal carbonyls in ionic liquids: Easy synthesis and stabilization. *Coordination Chemistry Reviews* **2011**, *255*, 2039-2057.

58. Tuxen, A.; Carenco, S.; Chintapalli, M.; Chuang, C.-H.; Escudero, C.; Pach, E.; Jiang, P.; Borondics, F.; Beberwyck, B.; Alivisatos, A. P.; Thornton, G.; Pong, W.-F.; Guo, J.; Perez, R.; Besenbacher, F.; Salmeron, M. Size-Dependent Dissociation of Carbon Monoxide on Cobalt Nanoparticles. *Journal of the American Chemical Society* **2013**, *135* (6), 2273-2278.

59. Margeat, O.; Amiens, C.; Chaudret, B.; Lecante, P.; Benfield, R. E. Chemical Control of Structural and Magnetic Properties of Cobalt Nanoparticles. *Chemistry of Materials* **2004**, *17* (1), 107-111.

60. Silva, D. O.; Luza, L.; Gual, A.; Baptista, D. L.; Bernardi, F.; Zapata, M. J. M.; Morais, J.; Dupont, J. Straightforward synthesis of bimetallic Co/Pt nanoparticles in ionic liquid: atomic rearrangement driven by reduction-sulfidation processes and Fischer-Tropsch catalysis. *Nanoscale* **2014**, *6* (15), 9085-9092.

61. Liakakos, N.; Cormary, B.; Li, X.; Lecante, P.; Respaud, M.; Maron, L.; Falqui, A.; Genovese, A.; Vendier, L.; Koinis, S.; Chaudret, B.; Soulantica, K. The Big Impact of a Small Detail: Cobalt Nanocrystal Polymorphism as a Result of Precursor Addition Rate during Stock Solution Preparation. *Journal of the American Chemical Society* **2012**, *134* (43), 17922-17931.

62. Gosser, L. W.; Cushing, M. A.; Berke, H.; Stengelin, S.  $\pi$ -Cyclooctenyl- $\pi$ -L,5-Cycloocta-Dienecobalt. In *Inorganic Syntheses*; John Wiley & Sons, Inc.: USA, 2007, pp 112-115.

63. Otsuka, S.; Rossi, M. Synthesis, structure, and properties of [small pi]-cyclo-octenyl-[small pi]-cyclo-octa-1,5-dienecobalt. *Journal of the Chemical Society A: Inorganic, Physical, Theoretical* **1968**, (0), 2630-2633.

64. Koda, S.; Takenaka, A.; Watanabe, S.; Tokunosuk, S. The Crystal and Molecular Structure of  $\pi$ -Cyclooctenyl- $\pi$ -cycloocta-1,5-dienecobalt,  $\text{Co}(\text{C}_8\text{H}_{13}) (\text{C}_8\text{H}_{12})$ . *Bulletin of the Chemical Society of Japan* **1971**, *44* (3), 653-658.

65. Benn, R.; Cibura, K.; Hofmann, P.; Jonas, K.; Rufinska, A. Cobalt-59 NMR spectroscopy of organocobalt(I) and -cobalt(III) compounds and its relation to chemical properties of the complexes. *Organometallics* **1985**, *4* (12), 2214-2221.

66. Comesana-Hermo, M.; Ciuculescu, D.; Li, Z.-A.; Stienen, S.; Spasova, M.; Farle, M.; Amiens, C. Stable single domain Co nanodisks: synthesis, structure and magnetism. *Journal of Materials Chemistry* **2012**, *22* (16), 8043-8047.

67. Verelst, M.; Snoeck, E.; Ely, T. O.; Lecante, P.; Amiens, C.; Roucau, C.; Mosset, A.; Chaudret, B. Wide Angles X-Ray Scattering (W.A.X.S.) and H.R.E.M. Studies on Nanoscale Cobalt and Cobalt Colloids. *Materials Science Forum, Trans Tech Publications, Switzerland* **1998**, 269-272.

68. Abbott, A. P.; Ryder, K.; Licence, P.; Taylor, A. W. What Is an Ionic Liquid? In *Ionic Liquids Completely UnCOILed*; John Wiley & Sons, Inc, 2015, pp 1-12.

69. Dupont, J.; Scholten, J. D. On the structural and surface properties of transition-metal nanoparticles in ionic liquids. *Chemical Society Reviews* **2010**, *39* (5), 1780-1804.

70. Migowski, P.; Dupont, J. Catalytic Applications of Metal Nanoparticles in Imidazolium Ionic Liquids. *Chemistry – A European Journal* **2007**, *13* (1), 32-39.

71. Vieth, G. M.; Dudney, N. J.; Dai, S. Method to prepare nanoparticles suspension in ionic liquids 20080271570, 2008.

72. Katayama, Y.; Fukui, R.; Miura, T. Electrodeposition of Cobalt from an Imide-Type Room-Temperature Ionic Liquid. *Journal of The Electrochemical Society* **2007**, *154* (10), D534-D537.

73. Katayama, Y.; Fukui, R.; Miura, T. Electrochemical Preparation of Cobalt Nano-particles in an Ionic Liquid. *Electrochemistry* **2013**, *81* (7), 532-534.

74. Jin, H.; O'Hare, B.; Dong, J.; Arzhantsev, S.; Baker, G. A.; Wishart, J. F.; Benesi, A. J.; Maroncelli, M. Physical Properties of Ionic Liquids Consisting of the 1-Butyl-3-Methylimidazolium Cation with Various Anions and the Bis(trifluoromethylsulfonyl)imide Anion with Various Cations. *The Journal of Physical Chemistry B* **2008**, *112* (1), 81-92.
75. Machado, G.; Scholten, J. D.; Vargas, T.; Teixeira, S. R.; Ronchi, L. H.; Dupont, J. Structural aspects of transition-metal nanoparticles in imidazolium ionic liquids. *International Journal of Nanotechnology* **2007**, *4*, 541-563.
76. Rao, C. N. R.; Vivekchand, S. R. C.; Biswas, K.; Govindaraj, A. Synthesis of inorganic nanomaterials. *Dalton Transactions* **2007**, (34), 3728-3749.
77. Slattery, J. M.; Daguene, C.; Dyson, P. J.; Schubert, T. J. S.; Krossing, I. How to Predict the Physical Properties of Ionic Liquids: A Volume-Based Approach. *Angewandte Chemie International Edition* **2007**, *46* (28), 5384-5388.
78. Wasserscheid, P.; Keim, W. Ionic Liquids—New “Solutions” for Transition Metal Catalysis. *Angewandte Chemie International Edition* **2000**, *39* (21), 3772-3789.
79. Gutel, T.; Santini, C. C.; Philippot, K.; Padua, A.; Pelzer, K.; Chaudret, B.; Chauvin, Y.; Basset, J.-M. Organized 3D-alkyl imidazolium ionic liquids could be used to control the size of in situ generated ruthenium nanoparticles? *Journal of Materials Chemistry* **2009**, *19* (22), 3624-3631.
80. Tokuda, H.; Hayamizu, K.; Ishii, K.; Susan, M. A. B. H.; Watanabe, M. Physicochemical Properties and Structures of Room Temperature Ionic Liquids. 1. Variation of Anionic Species. *The Journal of Physical Chemistry B* **2004**, *108* (42), 16593-16600.
81. Antonietti, M.; Kuang, D.; Smarsly, B.; Zhou, Y. Ionic Liquids for the Convenient Synthesis of Functional Nanoparticles and Other Inorganic Nanostructures. *Angewandte Chemie International Edition* **2004**, *43* (38), 4988-4992.
82. Redel, E.; Thomann, R.; Janiak, C. Use of ionic liquids (ILs) for the IL-anion size-dependent formation of Cr, Mo and W nanoparticles from metal carbonyl M(CO)<sub>6</sub> precursors. *Chemical Communications* **2008**, (15), 1789-1791.
83. Redel, E.; Thomann, R.; Janiak, C. First Correlation of Nanoparticle Size-Dependent Formation with the Ionic Liquid Anion Molecular Volume. *Inorganic Chemistry* **2008**, *47* (1), 14-16.
84. Verwey, E. J. W. Theory of the Stability of Lyophobic Colloids. *The Journal of Physical and Colloid Chemistry* **1947**, *51* (3), 631-636.
85. Marcus, Y. Ionic and molar volumes of room temperature ionic liquids. *Journal of Molecular Liquids* **2015**, *209*, 289-293.
86. Dinega, D. P.; Bawendi, M. G. A Solution-Phase Chemical Approach to a New Crystal Structure of Cobalt. *Angewandte Chemie International Edition* **1999**, *38* (12), 1788-1791.
87. Dassenoy, F.; Casanove, M.-J.; Lecante, P.; Verelst, M.; Snoeck, E.; Mosset, A.; Ely, T. O.; Amiens, C.; Chaudret, B. Experimental evidence of structural evolution in ultrafine cobalt particles stabilized in different polymers—From a polytetrahedral arrangement to the hexagonal structure. *The Journal of Chemical Physics* **2000**, *112* (18), 8137-8145.
88. Li, Z.-q.; Gu, B.-l. Electronic-structure calculations of cobalt clusters. *Physical Review B* **1993**, *47* (20), 13611-13614.
89. Yang, M.; Campbell, P. S.; Santini, C. C.; Mudring, A.-V. Small nickel nanoparticle arrays from long chain imidazolium ionic liquids. *Nanoscale* **2014**, *6* (6), 3367-3375.
90. Campbell, P. S.; Santini, C. C.; Bouchu, D.; Fenet, B.; Philippot, K.; Chaudret, B.; Padua, A. A. H.; Chauvin, Y. A novel stabilisation model for ruthenium nanoparticles in imidazolium ionic liquids: in situ spectroscopic and labelling evidence. *Physical Chemistry Chemical Physics* **2010**, *12* (16), 4217-4223.
91. Arquillière, P.; Haumesser, P. H.; Santini, C. C. Copper nanoparticles generated in situ in imidazolium based ionic liquids. *Microelectronic Engineering* **2012**, *92* (0), 149-151.
92. Gutel, T.; Garcia-Anton, J.; Pelzer, K.; Philippot, K.; Santini, C. C.; Chauvin, Y.; Chaudret, B.; Basset, J.-M. Influence of the self-organization of ionic liquids on the size of ruthenium nanoparticles: effect of the temperature and stirring. *Journal of Materials Chemistry* **2007**, *17* (31), 3290-3292.



93. Campbell, P. S.; Santini, C. C.; Bayard, F. o.; Chauvin, Y.; Collière, V.; Podgoršek, A.; Costa Gomes, M. F.; Saji, J. Olefin hydrogenation by ruthenium nanoparticles in ionic liquid media: Does size matter? *Journal of Catalysis* **2010**, *275* (1), 99-107.
94. Fredlake, C. P.; Crosthwaite, J. M.; Hert, D. G.; Aki, S. N. V. K.; Brennecke, J. F. Thermophysical Properties of Imidazolium-Based Ionic Liquids. *Journal of Chemical & Engineering Data* **2004**, *49* (4), 954-964.
95. Vyazovkin, S. Thermogravimetric Analysis. In *Characterization of Materials*; John Wiley & Sons, Inc.: USA, 2002.
96. Kroon, M. C.; Buijs, W.; Peters, C. J.; Witkamp, G.-J. Quantum chemical aided prediction of the thermal decomposition mechanisms and temperatures of ionic liquids. *Thermochimica Acta* **2007**, *465* (1), 40-47.
97. Heck, R. F.; Heck, R. F. Chapter VI - Reactions of Dienes, Trienes, and Tetraenes with Transition Metal Compounds. In *Organotransition Metal Chemistry a Mechanistic Approach*; Academic Press, 1974, p 118.
98. Otsuka, S.; Taketomi, T. Bicyclo[3,3,0]octa-2,4-dien-1-yl(cyclo-octa-1,5-diene)cobalt. *Journal of the Chemical Society, Dalton Transactions* **1972**, (17), 1879-1882.
99. LaMer, V. K.; Dinegar, R. H. Theory, Production and Mechanism of Formation of Monodispersed Hydrosols. *Journal of the American Chemical Society* **1950**, *72* (11), 4847-4854.
100. Migowski, P.; Machado, G.; Texeira, S. R.; Alves, M. C. M.; Morais, J.; Traverse, A.; Dupont, J. Synthesis and characterization of nickel nanoparticles dispersed in imidazolium ionic liquids. *Physical Chemistry Chemical Physics* **2007**, *9* (34), 4814-4821.
101. Ji, Q.; Acharya, S.; Richards, G. J.; Zhang, S.; Vieaud, J.; Hill, J. P.; Ariga, K. Alkyl Imidazolium Ionic-Liquid-Mediated Formation of Gold Particle Superstructures. *Langmuir* **2013**, *29* (24), 7186-7194.
102. Darwich, W.; Santini, C. C.; Haumesser, P. H.; Gaillard, F. An Efficient, Versatile, and Safe Access to Supported Metallic Nanoparticles on Porous Silicon with Ionic Liquids. *International journal of molecular sciences* **2016**, *17* (6), 876.
103. Laurent, P.; Baudouin, D.; Fenet, B.; Veyre, L.; Donet, S.; Coperet, C.; Thieuleux, C. Facile preparation of small and narrowly distributed platinum nanoparticles in the absence of H<sub>2</sub> from Pt(II) and Pt(0) molecular precursors using trihydrogen(octyl)silane. *New Journal of Chemistry* **2014**, *38* (12), 5952-5956.
104. Shevchenko, E. V.; Talapin, D. V.; Schnablegger, H.; Kornowski, A.; Festin, Ö.; Svedlindh, P.; Haase, M.; Weller, H. Study of Nucleation and Growth in the Organometallic Synthesis of Magnetic Alloy Nanocrystals: The Role of Nucleation Rate in Size Control of CoPt<sub>3</sub> Nanocrystals. *Journal of the American Chemical Society* **2003**, *125* (30), 9090-9101.
105. Margeat, O.; Dumestre, F.; Amiens, C.; Chaudret, B.; Lecante, P.; Respaud, M. Synthesis of iron nanoparticles: Size effects, shape control and organisation. *Progress in Solid State Chemistry* **2005**, *33* (2-4), 71-79.
106. Herath, M. B.; Hickman, T.; Creager, S. E.; DesMarteau, D. D. A new fluorinated anion for room-temperature ionic liquids. *Journal of Fluorine Chemistry* **2011**, *132* (1), 52-56.
107. Paige, D. M.; Szpunar, B.; Tanner, B. K. The magnetocrystalline anisotropy of cobalt. *Journal of Magnetism and Magnetic Materials* **1984**, *44* (3), 239-248.
108. Suzuki, T.; Weller, D.; Chang, C. A.; Savoy, R.; Huang, T.; Gurney, B. A.; Speriosu, V. Magnetic and magneto-optic properties of thick face-centered-cubic Co single-crystal films. *Applied Physics Letters* **1994**, *64* (20), 2736-2738.
109. Ferrando, R.; Jellinek, J.; Johnston, R. L. Nanoalloys: From Theory to Applications of Alloy Clusters and Nanoparticles. *Chemical Reviews* **2008**, *108* (3), 845-910.
110. Pan, C.; Dassenoy, F.; Casanove, M.-J.; Philippot, K.; Amiens, C.; Lecante, P.; Mosset, A.; Chaudret, B. A New Synthetic Method toward Bimetallic Ruthenium Platinum Nanoparticles; Composition Induced Structural Changes. *The Journal of Physical Chemistry B* **1999**, *103* (46), 10098-10101.

111. Wang, D.; Li, Y. Bimetallic Nanocrystals: Liquid-Phase Synthesis and Catalytic Applications. *Advanced Materials* **2011**, *23* (9), 1044-1060.
112. Atamena, N.; Ciuculescu, D.; Alcaraz, G.; Smekhova, A.; Wilhelm, F.; Rogalev, A.; Chaudret, B.; Lecante, P.; Benfield, R. E.; Amiens, C. Organometallic control at the nanoscale: a new, one-pot method to decorate a magnetic nanoparticle surface with noble metal atoms. *Chemical Communications* **2010**, *46* (14), 2453-2455.
113. Ciuculescu, D.; Amiens, C.; Respaud, M.; Falqui, A.; Lecante, P.; Benfield, R. E.; Jiang, L.; Fauth, K.; Chaudret, B. One-Pot Synthesis of Core-Shell FeRh Nanoparticles. *Chemistry of Materials* **2007**, *19* (19), 4624-4626.
114. Yasuda, H.; Mori, H. Cluster-size dependence of alloying behavior in gold clusters. *Zeitschrift für Physik D Atoms, Molecules and Clusters* **1994**, *31* (1), 131-134.
115. Yasuda, H.; Mori, H.; Komatsu, M.; Takeda, K. Spontaneous alloying of copper atoms into gold clusters at reduced temperatures. *Journal of Applied Physics* **1993**, *73* (3), 1100-1103.
116. Yasuda, H.; Mori, H.; Komatsu, M.; Takeda, K.; Fujita, H. In Situ Observation of Spontaneous Alloying in Atom Clusters. *Journal of Electron Microscopy* **1992**, *41* (4), 267-269.
117. Huang, R.; Shao, G.-F.; Zhang, Y.; Wen, Y.-H. Thermal Stability of Platinum-Cobalt Bimetallic Nanoparticles: Chemically Disordered Alloys, Ordered Intermetallics, and Core-Shell Structures. *ACS Applied Materials & Interfaces* **2017**, *9* (14), 12486-12493.
118. Stamenkovic, V. R.; Mun, B. J. S.; Mayrhofer, K. J. J.; Ross, P. N.; Markovic, N. M. Effect of Surface Composition on Electronic Structure, Stability, and Electrocatalytic Properties of Pt-Transition Metal Alloys: Pt-Skin versus Pt-Skeleton Surfaces. *Journal of the American Chemical Society* **2006**, *128*, 8813.
119. Vinayan, B. P.; Nagar, R.; Rajalakshmi, N.; Ramaprabhu, S. Novel Platinum-Cobalt Alloy Nanoparticles Dispersed on Nitrogen-Doped Graphene as a Cathode Electrocatalyst for PEMFC Applications. *Advanced Functional Materials* **2012**, *22*, 3519.
120. Wang, D. L.; Xin, H. L. L.; Hovden, R.; Wang, H. S.; Yu, Y. C.; Muller, D. A.; DiSalvo, F. J.; Abruna, H. D. Structurally Ordered Intermetallic Platinum-Cobalt Core-Shell Nanoparticles with Enhanced Activity and Stability as Oxygen Reduction Electrocatalysts. *Nature Materials* **2012**, *12*, 81.
121. Zhang, M. M.; Li, Y.; Yan, Z. X.; Jing, J. J.; Xie, J. M.; Chen, M. Improved Catalytic Activity of Cobalt Core-Platinum Shell Nanoparticles Supported on Surface Functionalized Graphene for Methanol Electro-Oxidation. *Electrochimica Acta* **2015**, *158*, 81.
122. Alloyeau, D.; Ricolleau, C.; Mottet, C.; Oikawa, T.; Langlois, C.; Le Bouar, Y.; Braidy, N.; Loiseau, A. Size and Shape Effects on the Order-Disorder Phase Transition in CoPt Nanoparticles. *Nature Materials* **2009**, *8*, 940.
123. Klem, M. T.; Willits, D.; Solis, D. J.; Belcher, A. M.; Young, M.; Douglas, T. Bio-inspired Synthesis of Protein-Encapsulated CoPt Nanoparticles. *Advanced Functional Materials* **2005**, *15*, 1489.
124. Kuttiyiel, K. A.; Choi, Y. M.; Hwang, S. M.; Park, G. G.; Yang, T. H.; Su, D.; Sasaki, K.; Liu, P.; Adzic, R. R. Enhancement of the Oxygen Reduction on Nitride Stabilized Pt-M (M = Fe, Co, and Ni) Core-Shell Nanoparticle Electrocatalysts. *Nano Energy* **2015**, *13*, 442.
125. Park, J. I.; Cheon, J. Synthesis of "Solid Solution" and "Core-Shell" Type Cobalt-Platinum Magnetic Nanoparticles via Transmetalation Reactions. *Journal of the American Chemical Society* **2001**, *123*, 5743.
126. Zhang, X. T.; Wang, H.; Key, J. L.; Linkov, V.; Ji, S.; Wang, X. L.; Lei, Z. Q.; Wang, R. F. Strain Effect of Core-Shell Co@Pt/C Nanoparticle Catalyst with Enhanced Electrocatalytic Activity for Methanol Oxidation. *Journal of The Electrochemical Society* **2012**, *159*, B270.
127. Gruner, M. E.; Rollmann, G.; Entel, P.; Farle, M. Multiply Twinned Morphologies of FePt and CoPt Nanoparticles. *Physical Review Letters* **2008**, *100*, 087203.
128. Kettner, M.; Schneider, W. B.; Auer, A. A. Computational Study of Pt/Co Core-Shell Nanoparticles: Segregation, Adsorbates and Catalyst Activity. *The Journal of Physical Chemistry C* **2012**, *116*, 15432.

129. Rossi, G.; Ferrando, R.; Mottet, C. Structure and Chemical Ordering in CoPt Nanoalloys. *Faraday Discussions* **2008**, *138*, 193.
130. Dong, Q.; Qu, W.; Liang, W.; Guo, K.; Xue, H.; Guo, Y.; Meng, Z.; Ho, C.-L.; Leung, C.-W.; Wong, W.-Y. Metallopolymer precursors to L10-CoPt nanoparticles: synthesis, characterization, nanopatterning and potential application. *Nanoscale* **2016**, *8* (13), 7068-7074.
131. Taoufik, M.; Cordonnier, M.-A.; Santini, C. C.; Basset, J.-M.; Candy, J.-P. Surface organometallic chemistry on metals: controlled hydrogenolysis of Me<sub>4</sub>Sn, Me<sub>3</sub>SnR, Me<sub>2</sub>SnR<sub>2</sub>, MeSnBu<sub>3</sub> and SnBu<sub>4</sub> (R = methyl, n-butyl, tert-butyl, neopentyl, cyclohexyl) onto metallic rhodium supported on silica. *New Journal of Chemistry* **2004**, *28* (12), 1531-1537.
132. Sobal, N. S.; Ebels, U.; Möhwald, H.; Giersig, M. Synthesis of Core-Shell PtCo Nanocrystals. *The Journal of Physical Chemistry B* **2003**, *107* (30), 7351-7354.
133. Son, S. U.; Jang, Y.; Park, J.; Na, H. B.; Park, H. M.; Yun, H. J.; Lee, J.; Hyeon, T. Designed Synthesis of Atom-Economical Pd/Ni Bimetallic Nanoparticle-Based Catalysts for Sonogashira Coupling Reactions. *Journal of the American Chemical Society* **2004**, *126* (16), 5026-5027.
134. Carroll, K. J.; Calvin, S.; Ekiert, T. F.; Unruh, K. M.; Carpenter, E. E. Selective Nucleation and Growth of Cu and Ni Core/Shell Nanoparticles. *Chemistry of Materials* **2010**, *22* (7), 2175-2177.
135. Vasquez, Y.; Sra, A. K.; Schaak, R. E. One-Pot Synthesis of Hollow Superparamagnetic CoPt Nanospheres. *Journal of the American Chemical Society* **2005**, *127* (36), 12504-12505.
136. Bao, Y.; Calderon, H.; Krishnan, K. M. Synthesis and Characterization of Magnetic-Optical Co-Au Core-Shell Nanoparticles. *The Journal of Physical Chemistry C* **2007**, *111* (5), 1941-1944.
137. Sun, Q.; Wang, S.; Wang, R. Well-Aligned CoPt Hollow Nanochains Synthesized in Water at Room Temperature. *The Journal of Physical Chemistry C* **2012**, *116* (9), 5352-5357.
138. Mattei, J. G.; Pelletier, F.; Ciuculescu, D.; Lecante, P.; Dupin, J. C.; Yaacoub, N.; Allouche, J.; Greneche, J. M.; Gonbeau, D.; Amiens, C.; Casanove, M. J. Formation of Bimetallic FeBi Nanostructured Particles: Investigation of a Complex Growth Mechanism. *The Journal of Physical Chemistry C* **2013**, *117* (3), 1477-1484.
139. Dassenoy, F.; Casanove, M. J.; Lecante, P.; Pan, C.; Philippot, K.; Amiens, C.; Chaudret, B. Size and composition effects in polymer-protected ultrafine bimetallic Pt<sub>x</sub>Ru<sub>1-x</sub> (0<x<1) particles. *Physical Review B* **2001**, *63* (23), 235407.
140. Bradley, J. S.; Hill, E. W.; Chaudret, B.; Duteil, A. Surface Chemistry on Colloidal Metals. Reversible Adsorbate-Induced Surface Composition Changes in Colloidal Palladium-Copper Alloys. *Langmuir* **1995**, *11* (3), 693-695.
141. Lara, P.; Ayval, T.; Casanove, M.-J.; Lecante, P.; Mayoral, A.; Fazzini, P.-F.; Philippot, K.; Chaudret, B. On the influence of diphosphine ligands on the chemical order in small RuPt nanoparticles: combined structural and surface reactivity studies. *Dalton Transactions* **2013**, *42* (2), 372-382.
142. Arquilliere, P.; Haumesser, P. H.; Helgadottir, I.; Santini, C. Composition for the synthesis of bimetallic nanoparticles in an ionic liquid and associated method US patent 9017448 B2, 2012.
143. Andrezza, P.; Khelfane, H.; Lyon, O.; Andrezza-Vignolle, C.; Ramos, A. Y.; Samah, M. Trends in anomalous small-angle X-ray scattering in grazing incidence for supported nanoalloyed and core-shell metallic nanoparticles. *The European Physical Journal Special Topics* **2012**, *208* (1), 231-244.
144. ARQUILLIERE, P. NANOPARTICULES MONO- ET BIMETALLIQUES POUR LA METALLISATION DE MICROVIAS PAR UN PROCEDE INNOVANT UTILISANT LES LIQUIDES IONIQUES. PhD, UNIVERSITE CLAUDE BERNARD LYON 12012.
145. GERGAUD, P.; FREYCHET, G.; HAUMESSER, P. H.; SANTINI, C. C.; ARQUILLIERE, P.; DARWICH, W. Anomalous SAXS study of bimetallic Ru-Ta nanoparticles. 2014.
146. Chow, Y. L.; Li, H. Light-promoted catalysis of nickel hydride complexes in the isomerization and hydrogenation of cis,cis-1,5-cyclooctadiene: mechanistic studies. *Canadian Journal of Chemistry* **1986**, *64* (11), 2229-2231.
147. Koike, J.; Wada, M. Self-forming diffusion barrier layer in Cu-Mn alloy metallization. *Applied Physics Letters* **2005**, *87* (4), 041911.

148. Lurio, L. B.; Lumma, D.; Sandy, A. R.; Borthwick, M. A.; Falus, P.; Mochrie, S. G. J.; Pelletier, J. F.; Sutton, M.; Regan, L.; Malik, A.; Stephenson, G. B. Absence of Scaling for the Intermediate Scattering Function of a Hard-Sphere Suspension: Static and Dynamic X-Ray Scattering from Concentrated Polystyrene Latex Spheres. *Physical Review Letters* **2000**, *84* (4), 785-788.
149. Li, T.; Senesi, A. J.; Lee, B. Small Angle X-ray Scattering for Nanoparticle Research. *Chemical Reviews* **2016**, *116* (18), 11128-11180.
150. Baxter, R. J. Percus–Yevick Equation for Hard Spheres with Surface Adhesion. *The Journal of Chemical Physics* **1968**, *49* (6), 2770-2774.
151. Huber, D. L. Synthesis, Properties, and Applications of Iron Nanoparticles. *Small* **2005**, *1* (5), 482-501.
152. Krämer, J.; Redel, E.; Thomann, R.; Janiak, C. Use of Ionic Liquids for the Synthesis of Iron, Ruthenium, and Osmium Nanoparticles from Their Metal Carbonyl Precursors. *Organometallics* **2008**, *27* (9), 1976-1978.
153. Lacroix, L.-M.; Lachaize, S.; Falqui, A.; Blon, T.; Carrey, J.; Respaud, M.; Dumestre, F.; Amiens, C.; Margeat, O.; Chaudret, B.; Lecante, P.; Snoeck, E. Ultrasmall iron nanoparticles: Effect of size reduction on anisotropy and magnetization. *Journal of Applied Physics* **2008**, *103* (7), 07D521.
154. Lacroix, L.-M.; Lachaize, S.; Falqui, A.; Respaud, M.; Chaudret, B. Iron Nanoparticle Growth in Organic Superstructures. *Journal of the American Chemical Society* **2009**, *131* (2), 549-557.
155. Cheong, S.; Ferguson, P.; Feindel, K. W.; Hermans, I. F.; Callaghan, P. T.; Meyer, C.; Slocombe, A.; Su, C.-H.; Cheng, F.-Y.; Yeh, C.-S.; Ingham, B.; Toney, M. F.; Tilley, R. D. Simple Synthesis and Functionalization of Iron Nanoparticles for Magnetic Resonance Imaging. *Angewandte Chemie International Edition* **2011**, *50* (18), 4206-4209.
156. Margeat, O.; Respaud, M.; Amiens, C.; Lecante, P.; Chaudret, B. Ultrafine metallic Fe nanoparticles: synthesis, structure and magnetism. *Beilstein Journal of Nanotechnology* **2010**, *1*, 108-118.
157. Pelletier, F.; Ciuculescu, D.; Mattei, J.-G.; Lecante, P.; Casanove, M.-J.; Yaacoub, N.; Greneche, J.-M.; Schmitz-Antoniak, C.; Amiens, C. On the Use of Amine–Borane Complexes To Synthesize Iron Nanoparticles. *Chemistry – A European Journal* **2013**, *19* (19), 6021-6026.
158. Kelsen, V.; Wendt, B.; Werkmeister, S.; Junge, K.; Beller, M.; Chaudret, B. The use of ultrasmall iron(0) nanoparticles as catalysts for the selective hydrogenation of unsaturated C-C bonds. *Chemical Communications* **2013**, *49* (33), 3416-3418.
159. Cheong, S.; Ferguson, P.; Hermans, I. F.; Jameson, G. N. L.; Prabakar, S.; Herman, D. A. J.; Tilley, R. D. Synthesis and Stability of Highly Crystalline and Stable Iron/Iron Oxide Core/Shell Nanoparticles for Biomedical Applications. *ChemPlusChem* **2012**, *77* (2), 135-140.
160. Suslick, K. S.; Fang, M.; Hyeon, T. Sonochemical Synthesis of Iron Colloids. *Journal of the American Chemical Society* **1996**, *118* (47), 11960-11961.
161. de Caro, D.; Ely, T. O.; Mari, A.; Chaudret, B.; Snoeck, E.; Respaud, M.; Broto, J.-M.; Fert, A. Synthesis, Characterization, and Magnetic Studies of Nonagglomerated Zerovalent Iron Particles. Unexpected Size Dependence of the Structure. *Chemistry of Materials* **1996**, *8* (8), 1987-1991.
162. Dumestre, F.; Chaudret, B.; Amiens, C.; Renaud, P.; Fejes, P. Superlattices of Iron Nanocubes Synthesized from Fe[N(SiMe<sub>3</sub>)<sub>2</sub>]<sub>2</sub>. *Science* **2004**, *303* (5659), 821-823.
163. Meffre, A.; Lachaize, S.; Gatel, C.; Respaud, M.; Chaudret, B. Use of long chain amine as a reducing agent for the synthesis of high quality monodisperse iron(0) nanoparticles. *Journal of Materials Chemistry* **2011**, *21* (35), 13464-13469.
164. Leal, B. C.; Scholten, J. D.; Alves, M. C. M.; Morais, J.; de Pedro, I.; Fernandez Barquin, L.; Dupont, J. Interacting Superparamagnetic Iron(II) Oxide Nanoparticles: Synthesis and Characterization in Ionic Liquids. *Inorganic Chemistry* **2016**, *55* (2), 865-870.
165. Armstrong, J. P.; Hurst, C.; Jones, R. G.; Licence, P.; Lovelock, K. R. J.; Satterley, C. J.; Villar-Garcia, I. J. Vapourisation of ionic liquids. *Physical Chemistry Chemical Physics* **2007**, *9* (8), 982-990.

166. Schütte, K.; Barthel, J.; Endres, M.; Siebels, M.; Smarsly, B. M.; Yue, J.; Janiak, C. Synthesis of Metal Nanoparticles and Metal Fluoride Nanoparticles from Metal Amidinate Precursors in 1-Butyl-3-Methylimidazolium Ionic Liquids and Propylene Carbonate. *ChemistryOpen* **2017**, *6* (1), 137-148.
167. Vieth, G. M.; Dudney, N. J.; Dai, S. Method to prepare nanoparticles suspension in ionic liquids US patent 20080271570, 2008.
168. Zhang, S.; Zhang, Y.; Wang, Y.; Liu, S.; Deng, Y. Sonochemical formation of iron oxide nanoparticles in ionic liquids for magnetic liquid marble. *Physical Chemistry Chemical Physics* **2012**, *14* (15), 5132-5138.
169. Lee, C.-M.; Jeong, H.-J.; Lim, S. T.; Sohn, M.-H.; Kim, D. W. Synthesis of Iron Oxide Nanoparticles with Control over Shape Using Imidazolium-Based Ionic Liquids. *ACS Applied Materials & Interfaces* **2010**, *2* (3), 756-759.
170. Wang, Y.; Maksimuk, S.; Shen, R.; Yang, H. Synthesis of iron oxide nanoparticles using a freshly-made or recycled imidazolium-based ionic liquid. *Green Chemistry* **2007**, *9* (10), 1051-1056.
171. Cao, S.-W.; Zhu, Y.-J. Iron oxide hollow spheres: Microwave-hydrothermal ionic liquid preparation, formation mechanism, crystal phase and morphology control and properties. *Acta Materialia* **2009**, *57* (7), 2154-2165.
172. Gieshoff, T. N.; Welther, A.; Kessler, M. T.; Pechtl, M. H. G.; Jacobi von Wangelin, A. Stereoselective iron-catalyzed alkyne hydrogenation in ionic liquids. *Chemical Communications* **2014**, *50* (18), 2261-2264.
173. Zhao, Y.; Cui, G.; Wang, J.; Fan, M. Effects of Ionic Liquids on the Characteristics of Synthesized Nano Fe(0) Particles. *Inorganic Chemistry* **2009**, *48* (21), 10435-10441.
174. Gerlach, D. H.; Schunn, R. A.; Bennett, M. A.; Tomkins, I. B.; Turney, T. W. Bis(1,3,5,7-cyclooctatetraene)iron(0). In *Inorganic Syntheses*; John Wiley & Sons, Inc., 2007, pp 1-4.
175. Allegra, G.; Colombo, A.; Immirzi, A.; Bassi, I. W. The crystal structure of bis(cyclooctatetraene)iron. *Journal of the American Chemical Society* **1968**, *90* (16), 4455-4456.
176. Andersen, R. A.; Faegri, K.; Green, J. C.; Haaland, A.; Lappert, M. F.; Leung, W. P.; Rypdal, K. Synthesis of bis[bis(trimethylsilyl)amido]iron(II). Structure and bonding in  $M[N(SiMe_3)_2]_2$  ( $M =$  manganese, iron, cobalt): two-coordinate transition-metal amides. *Inorganic Chemistry* **1988**, *27* (10), 1782-1786.
177. Olmstead, M. M.; Power, P. P.; Shoner, S. C. Three-coordinate iron complexes: x-ray structural characterization of the iron amide-bridged dimers  $[Fe(NR_2)_2]_2$  ( $R = SiMe_3, C_6H_5$ ) and the adduct  $Fe[N(SiMe_3)_2]_2(THF)$  and determination of the association energy of the monomer  $Fe[N(SiMe_3)_2]_2$  in solution. *Inorganic Chemistry* **1991**, *30* (11), 2547-2551.
178. Rauchfuss, T. B. Bio-Inspired Iron and Nickel Complexes. In *Inorganic Syntheses*; John Wiley & Sons, Inc.: New Jersey, 2010, pp 129-147.
179. Michalek, F.; Lagunas, A.; Jimeno, C.; Pericas, M. A. Synthesis of functional cobalt nanoparticles for catalytic applications. Use in asymmetric transfer hydrogenation of ketones. *Journal of Materials Chemistry* **2008**, *18* (39), 4692-4697.
180. Crampton, A. S.; Rötzer, M. D.; Schweinberger, F. F.; Yoon, B.; Landman, U.; Heiz, U. Ethylene hydrogenation on supported Ni, Pd and Pt nanoparticles: Catalyst activity, deactivation and the d-band model. *Journal of Catalysis* **2016**, *333*, 51-58.
181. Helgadottir, I. S.; Arquillière, P. P.; Campbell, P. S.; Santini, C. C.; Haumesser, P. H. Novel Chemical Route to Size-Controlled Ta(0) and Ru-Ta Nanoparticles in Ionic Liquids. *MRS Proceedings* **2012**, *1473*.
182. Haumesser, P.-H. 2 - Phase Transition: Nucleation, Growth, Aggregation and Coalescence. In *Nucleation and Growth of Metals*; Elsevier, 2016, pp 13-58.
183. Moseley, K.; Maitlis, P. M. Bis- and tris-(dibenzylideneacetone)platinum and the stabilization of zerovalent complexes by an unsaturated ketone. *Journal of the Chemical Society D: Chemical Communications* **1971**, (16), 982-983.
184. Jana, N. R.; Chen, Y.; Peng, X. Size- and Shape-Controlled Magnetic (Cr, Mn, Fe, Co, Ni) Oxide Nanocrystals via a Simple and General Approach. *Chemistry of Materials* **2004**, *16* (20), 3931-3935.

185. Chen, M.; Liu, J. P.; Sun, S. One-Step Synthesis of FePt Nanoparticles with Tunable Size. *Journal of the American Chemical Society* **2004**, *126* (27), 8394-8395.
186. Sun, S.; Zeng, H.; Robinson, D. B.; Raoux, S.; Rice, P. M.; Wang, S. X.; Li, G. Monodisperse MFe<sub>2</sub>O<sub>4</sub> (M = Fe, Co, Mn) Nanoparticles. *Journal of the American Chemical Society* **2004**, *126* (1), 273-279.
187. Weissleder, R.; Mahmood, U. Molecular Imaging. *Radiology* **2001**, *219* (2), 316-333.
188. Rudin, M.; Weissleder, R. Molecular imaging in drug discovery and development. *Nature Reviews Drug Discovery* **2003**, *2* (2), 123-131.
189. Gu, H.; Zheng, R.; Zhang, X.; Xu, B. Facile One-Pot Synthesis of Bifunctional Heterodimers of Nanoparticles: A Conjugate of Quantum Dot and Magnetic Nanoparticles. *Journal of the American Chemical Society* **2004**, *126* (18), 5664-5665.
190. Akbarzadeh, A.; Samiei, M.; Davaran, S. Magnetic nanoparticles: preparation, physical properties, and applications in biomedicine. *Nanoscale Research Letters* **2012**, *7* (1), 144-144.



## List of figures

<b>Figure 1</b> : NMR spectra and crystallographic structure of Co(COD)(COE). .....	14
<b>Figure 2</b> : Correlation between the observed AgNP size and the molecular volume IL anion .....	17
<b>Figure 3</b> : HRTEM image of metallic Co-NPs ( Table 3 run 1), reproduced. The fast Fourier transform image in the top-left corner shows hcp pattern.....	19
<b>Figure 4</b> : RDF of 5.0 nm Co-NPs (Table 3, run 11).....	19
<b>Figure 5</b> : TEM, HRTEM images of Co-NPs (1.5 nm) with a fcc structure (Table 3, run 4-6) .....	20
<b>Figure 6</b> : The unit cell of $\epsilon$ -cobalt: a) unit cell cube filled with eight atoms of Type I (dark) and twelve atoms of Type II (light); b) 111-projection of the same cube showing threefold symmetry along its main diagonal.....	20
<b>Figure 7</b> :HRTEM images for 1.6nm and 2.6nm Co-NPs (Table 3 run 8-9) .....	21
<b>Figure 8</b> : Experimental (solid line) and simulated (dashed line) reduced RDF for Co-NPs (Table 3 run 8-9).....	21
<b>Figure 9</b> : XRD pattern of Co-NPs in IL with a $\epsilon$ -Co structure (Table 4 run 7 ): a) experimental; b) calculated; c) the sample shown in a) after being heated to 500 °C, peaks corresponding to fcc are denoted by X, peaks corresponding to CoO are marked with a stick spectrum. ....	22
<b>Figure 10</b> : Experimental (solid line) and simulated polytetrahedral model (dashed line) reduced RDF for Co-NPs (Table 3 run 8-9).....	22
<b>Figure 11</b> : Mechanism of metal NPs formation through the H <sub>2</sub> decomposition of organometallic precursors dissolved in IL. ....	24
<b>Figure 12</b> : Comparison of the T <sub>d</sub> values of Co(COD)(COE) (5°C.min <sup>-1</sup> , N <sub>2</sub> atmosphere) according to the definitions T <sub>o</sub> , T <sub>start</sub> and T <sub>peak</sub> ; black line represents the sample mass and red line represents the first derivative. ....	29
<b>Figure 13</b> : Evolution of the IR spectra of solid Co(COD)(COE) with time upon exposure to 0.4 MPa of H <sub>2</sub> at 20°C. ....	30
<b>Figure 14</b> : (left) Chromatogram of the gas phase during the decomposition of solid Co(COD)(COE) under 0.4 MPa of H <sub>2</sub> , 20°C at different time intervals; (right) evolution of cyclooctane peak area with time. ..	31
<b>Figure 15</b> : Evolution with time of the chromatogram of the gas phase during the reaction of Co(COD)(COE) [5 x 10 <sup>-2</sup> mol.L <sup>-1</sup> ] in C <sub>1</sub> C <sub>4</sub> ImNTf <sub>2</sub> , with H <sub>2</sub> (0.4 MPa) at 100 °C. ....	32
<b>Figure 16</b> : Evolution of cyclooctane peak area with time (full line); % of Co(COD)(COE) decomposition (dashed line). ....	33
<b>Figure 17</b> : Proposed mechanism for the possible isomerization reactions catalyzed by Co(COD)(COE) in the presence of hydrogen .....	33
<b>Figure 18</b> : Evolution of the chromatograms of the evolved gas phase during the decomposition at 150°C of the solution of Co(COD)(COE) [ 5 x 10 <sup>-2</sup> mol.L <sup>-1</sup> ] in C <sub>1</sub> C <sub>4</sub> ImNTf <sub>2</sub> for 20 min under Ar (0.2 MPa), then 60 and 120 min under 0.4 MPa of H <sub>2</sub> .....	34



<b>Figure 19</b> : Evolution of Co-NP size with reaction temperature; Co-NP formed during the reaction of Co(COD)(COE) under 0.4 M Pa of H <sub>2</sub> for 4 hours.....	36
<b>Figure 20</b> : TEM images for Co-NPs generated at 100°C, 0.4 M Pa of H <sub>2</sub> in (a) C <sub>1</sub> C <sub>4</sub> ImNTf <sub>2</sub> , (b) C <sub>1</sub> C <sub>14</sub> ImNTf <sub>2</sub> . .....	37
<b>Figure 21</b> : GC spectra of condensed volatile compounds after the reaction of Et <sub>3</sub> SiH and Co(COD)(COE) in C <sub>1</sub> C <sub>4</sub> ImNTf <sub>2</sub> at 50 °C under Ar, A) during 2 h, and B) during 4 h. ....	38
<b>Figure 22</b> : TEM image of NPs generated by the reaction of Co(COD)(COE) with Et <sub>3</sub> SiH at 50°C under argon, A) during 2 h, and B) during 4 h.....	38
<b>Figure 23</b> : Size distribution of Co-NPs generated by reaction of Co(COD)(COE) with different R <sub>x</sub> SiH <sub>4-x</sub> compounds under argon, during 2 h at 50°C. ....	39
<b>Figure 24</b> : (a) Exemplary HRTEM image of CoNPs generated by the decomposition of Co(COD)(COE) in C <sub>1</sub> C <sub>4</sub> ImNTf <sub>2</sub> under 0.4MPa of H <sub>2</sub> for 4 h and (b) FFT of the particle in the white square indexed by a cubic structure along the (-321) zone axis with a lattice parameter of 6.1Å corresponding to ε-Co. .	41
<b>Figure 25</b> : X ray fluorescence spectra of a suspension of Co-NPs in C <sub>1</sub> C <sub>4</sub> ImNTf <sub>2</sub> measured at 2θ=110° for 10 minutes between 15 and 18keV. ....	42
<b>Figure 26</b> : WAXS curves of Co-NPs as-prepared, suspended in C <sub>1</sub> C <sub>4</sub> ImNTf <sub>2</sub> (red line) and of pure C <sub>1</sub> C <sub>4</sub> ImNTf <sub>2</sub> (green line). ....	42
<b>Figure 27</b> : (a) Scattering curves and (b) corresponding radial distribution functions (RDF) of Co-NPs as-prepared in C <sub>1</sub> C <sub>4</sub> ImNTf <sub>2</sub> and in C <sub>1</sub> C <sub>12</sub> ImNTf <sub>2</sub> , and after decantation over a magnet in C <sub>1</sub> C <sub>4</sub> ImNTf <sub>2</sub> .....	43
<b>Figure 28</b> : Magnetization versus temperature for pure C <sub>1</sub> C <sub>4</sub> ImNTf <sub>2</sub> sample. ....	44
<b>Figure 29</b> : Magnetization curves at 250K of Co-NPs synthesized in (a) C <sub>1</sub> C <sub>4</sub> ImNTf <sub>2</sub> and (b) C <sub>1</sub> C <sub>14</sub> ImNTf <sub>2</sub> . ....	45
<b>Figure 30</b> : Magnetization curves at 10K of Co-NPs synthesized in (a) C <sub>1</sub> C <sub>4</sub> ImNTf <sub>2</sub> and (b) C <sub>1</sub> C <sub>14</sub> ImNTf <sub>2</sub> . ....	46
<b>Figure 31</b> : FC-ZFC curves of Co-NPs synthesized in (a) C <sub>1</sub> C <sub>4</sub> ImNTf <sub>2</sub> and (b) C <sub>1</sub> C <sub>14</sub> ImNTf <sub>2</sub> recorded at 50 Oe. ....	46
<b>Figure 32</b> : Isothermal magnetic remanence and demagnetization DC measurements for Co-NPs synthesized in C <sub>1</sub> C <sub>14</sub> ImNTf <sub>2</sub> . ....	49
<b>Figure 33</b> : IRM/DCD response of Co-NPs synthesized in C <sub>1</sub> C <sub>4</sub> ImNTf <sub>2</sub> and C <sub>1</sub> C <sub>14</sub> ImNTf <sub>2</sub> . ....	50
<b>Figure 34</b> : FC/ZFC curve for Co-NPs suspended in C <sub>1</sub> C <sub>4</sub> ImNTf <sub>2</sub> (0.0025 mol.L <sup>-1</sup> ), recorded under 50 Oe magnetic field. ....	51
<b>Figure 35</b> : IRM/DcD measurements for Co-NPs suspended in C <sub>1</sub> C <sub>4</sub> ImNTf <sub>2</sub> (0.05 mol.L <sup>-1</sup> , blue, 0.0025 mol.L <sup>-1</sup> , red) showing the ΔM values plotted as a function of the applied magnetic field. ....	51
<b>Figure 36</b> : Magnetization curve for Co-NPs suspended in C <sub>1</sub> C <sub>14</sub> ImNTf <sub>2</sub> (0.0025 mol.L <sup>-1</sup> ) measured at 10 K. ....	52
<b>Figure 37</b> : Magnetization data for Co-NPs suspended in C <sub>1</sub> C <sub>14</sub> ImNTf <sub>2</sub> (0.0025 mol.L <sup>-1</sup> ) measured at 300 K (black) and the data fitting with Langevin model assuming 3.7 nm NPs (red). ....	52
<b>Figure 38</b> : IRM/DcD measurements for Co-NPs suspended in C <sub>1</sub> C <sub>14</sub> ImNTf <sub>2</sub> (0.05 mol.L <sup>-1</sup> , grey and 0.0025 mol.L <sup>-1</sup> , red) showing the ΔM values plotted as a function of the applied magnetic field. ....	53
<b>Figure 39</b> : The main types of alloying in nanoparticles; a) core-shell particles, b) subcluster-segregated alloys, c) mixed alloys (ordered or disordered), and d) multi-shell configuration. ....	58

<b>Figure 40</b> : Schematic illustration of Pt-Co bimetallic NPs: (a) disordered Pt <sub>3</sub> Co alloy, (b) disordered PtCo alloy, (c) ordered Pt <sub>3</sub> Co <i>L1</i> <sub>2</sub> intermetallics, (d) ordered PtCo <i>L1</i> <sub>0</sub> intermetallics, (e) Co@Pt core@shell structure, and (f) Pt <sub>3</sub> Co@Pt core@shell structure. Coloring denotes the type of atom: blue, Pt atom; bright green, Co atom .....	62
<b>Figure 41</b> : Local elemental mapping of Fe–Bi nanospheres giving evidence for an iron-rich shell and a concentration of Bi atoms in the core region. <sup>138</sup> .....	65
<b>Figure 42</b> : Kinetics control of the chemical ordering in FeRh NPS .....	66
<b>Figure 43</b> : Schematic representation of RuPt NPs synthesized from [Ru(COD)(COT)] and [Pt(CH <sub>3</sub> ) <sub>2</sub> (COD)]. .....	67
<b>Figure 44</b> : HAADF-STEM image of a set of Co/Pt nanoparticles and the particle size distribution histogram. ...	68
<b>Figure 45</b> : XRD analysis of the bimetallic CoPt-NPs prepared in C <sub>1</sub> C <sub>4</sub> Im PF <sub>6</sub> compared with bulk fcc Pt (gray lines). Inset: 220 reflections of bulk fcc Pt (gray line), CoPt <sub>3</sub> @Pt like and CoPt <sub>3</sub> (green line) structures .....	69
<b>Figure 46</b> : Diameter evolution of the RuCuNPs with Cu content as measured by TEM and ASAXS, and comparison with the model developed in the present work (with 147 atoms in the core). .....	70
<b>Figure 47</b> : Radial SAXS intensities as a function of the scattering vector, <i>q</i> , measured for the sample with $\chi_{Cu}$ = 0.9 (black curve) and pure IL (red dashed curve) (E = 22.1 keV). .....	70
<b>Figure 48</b> : (a) Change of the intrinsic scattering intensity of NPs, <i>INP</i> ( <i>q</i> ), with the Cu atomic fraction at 22.10 keV. (b) Variation of <i>INP</i> ( <i>q</i> ) with the photon energy ( $\chi_{Cu}$ = 0.1).....	71
<b>Figure 49</b> : Experimental (black solid line) and simulated (red dashed line) intensities obtained at 22.10 keV for (a) $\chi_{Cu}$ = 0.1, (b) $\chi_{Cu}$ = 0.75 and (c) $\chi_{Cu}$ = 0.9; the green points are the differential intensities, <i>INP</i> (21.6 keV) – <i>INP</i> (22.1 keV), after rescaling with respect to <i>INP</i> ( <i>q</i> ). (d) Comparison of the differential intensities obtained for the three compositions. ....	72
<b>Figure 50</b> : Proposed mechanism for Ru@Cu NPs formation. ....	74
<b>Figure 51</b> : Size and distribution of RuNi-NPs as a function of the molar fraction of Ni obtained at 100°C under 0.9 MPa of H <sub>2</sub> without stirring during 4 h in C <sub>1</sub> C <sub>6</sub> ImNTf <sub>2</sub> . ....	76
<b>Figure 52</b> : a) Radial SAXS intensities as a function of the scattering vector, <i>q</i> , measured at E=21.6 keV for pure IL, pure Ta and Ru NPs and two bimetallic NPs. b) For Ta <sub>8</sub> Ru <sub>2</sub> NPs, variation of the radial intensity with photon energy (K-Ru edge). ....	78
<b>Figure 53</b> : Size and distribution of NiCu-NPs as a function of the molar fraction of Cu, obtained at 100 °C under 0.9 MPa of H <sub>2</sub> without stirring during 4 h. ....	80
<b>Figure 54</b> : Catalytic cycle of isomerisation and hydrogenation of 1,5-COD. <sup>146</sup> Conversion and selectivity in function of molar fraction of Cu in bimetallic Ni-CuNPs. ....	80
<b>Figure 55</b> : TEM picture of Mn-CuNPs with 1:1 ratio of MnNp <sub>2</sub> and Mes-Cu.....	81
<b>Figure 56</b> : Comparative size distribution histograms fitted by log-normal law of Mn-NPs, MnCu-NPs ( $\chi_{Cu}$ = 0.5) and Cu-NPs obtained at 100 °C with 5x10 <sup>-2</sup> mol/L total concentration of precursors under 0.9 MPa of H <sub>2</sub> without stirring during 4 hour in C <sub>1</sub> C <sub>4</sub> ImNTf <sub>2</sub> . ....	82
<b>Figure 57</b> : XPS spectra of MnCu-NPs (ratio 1:1), top: Cu 2p <sub>3/2</sub> area, bottom: Mn2p area. ....	83

<b>Figure 58</b> : STEM images for Co-NPs cluster after reaction with tetramethyltin (left), STEM elemental mapping image reproduced by EDX considering Co Ka1 intensities (middle), STEM elemental mapping image reproduced by EDX considering Sn La1 intensities (right). .....	88
<b>Figure 59</b> : Size distribution for Co-NPs obtained through the decomposition of Co(COD)(COE) under 0.4 MPa H <sub>2</sub> , 100 °C, 4 h, in C <sub>1</sub> C <sub>4</sub> ImNTf <sub>2</sub> , before (left) and after (right) exposure to an equimolar solution of Ru(COD)(COT) for 24 h, at room temperature under Ar.....	91
<b>Figure 60</b> : Size distribution for Ru-NPs obtained through the decomposition of Ru(COD)(COT) under 0.4 MPa H <sub>2</sub> , 100 °C, 4 h, in C <sub>1</sub> C <sub>4</sub> ImNTf <sub>2</sub> , before (left) and after (right) exposure to an equimolar solution of Co(COD)(COE) for 24 h at room temperature under Ar.....	92
<b>Figure 61</b> : Size of Co <sub>1-x</sub> Ru <sub>x</sub> NPs plotted as a function of the mole fraction of Ru ( $X_{Ru}$ ) in the initial solution mixture.....	93
<b>Figure 62</b> : Scattered intensity as a function of the scattering vector q measured at E = 21.6 keV for the reference sample containing Ru-NPs. In red, the best fit obtained with a spherical particle model. .	94
<b>Figure 63</b> : Scattered intensity as a function of the scattering vector q measured at E = 21.6 keV for the reference sample containing Co-NPs. In red the best fit obtained with a model of sticky hard spheres. In blue and green, the contributions of the form factor and structure factor, respectively. ....	96
<b>Figure 64</b> : Potential energy landscape V(r) for the (left) hard sphere and (right) sticky hard sphere models. ...	96
<b>Figure 65</b> : TEM image and size distribution of Co-NPs obtained through the decomposition of Co(COD)(COE) under 0.4 MPa H <sub>2</sub> , 100 °C, 4 h, in C <sub>1</sub> C <sub>4</sub> ImNTf <sub>2</sub> , after exposure to equimolar solution of (COD)Pt(Me) <sub>2</sub> for 24 h, at room temperature under Ar.....	98
<b>Figure 66</b> : TEM image of a suspension of Co-NPs in C <sub>1</sub> C <sub>4</sub> ImNTf <sub>2</sub> after exposure to equimolar solution of Pt(dba) <sub>2</sub> for 24 h at room temperature under Ar.....	99
<b>Figure 67</b> : STEM image of the same spot as in Figure 66 showing the existence of distinct tiny NPs of a heavier metal, probably Pt.....	100
<b>Figure 68</b> : Co content as measured by EDX, plotted as a function of $X_{Pt}$ in the initial mixture. ....	101
<b>Figure 69</b> : TEM images of Co <sub>1-x</sub> Pt <sub>x</sub> NPs prepared by simultaneous decomposition of Co(COD)(COE) and Pt(dba) <sub>2</sub> in IL ( $X_{Pt}$ =0.25, 0.9) under 0.9 MPa H <sub>2</sub> , 150 °C, 24 h.....	102
<b>Figure 70</b> : Size of Co <sub>1-x</sub> Pt <sub>x</sub> NPs plotted as a function of the mole fraction of Pt ( $X_{Pt}$ ) in the initial solution mixture.....	102
<b>Figure 71</b> : Scattered intensity as a function of the scattering vector q measured at various energies close to the Pt-L <sub>III</sub> edge for the sample containing CoPt-NPs prepared in one step from an equimolar mixture of Co(COD)(COE) and Pt(dba) <sub>2</sub> . In red, the difference between the two extreme curves scaled to the initial response.....	103
<b>Figure 72</b> : Conversion of cyclohexadiene after 30 min under H <sub>2</sub> (0.12 MPa), at room temperature plotted as a function of $X_{Pt}$ .....	105
<b>Figure 73</b> : cyclohexene/cyclohexane ratio as a function of $X_{Pt}$ .....	105
<b>Figure 74</b> : crystal structure of Fe(COT) <sub>2</sub> .....	117
<b>Figure 75</b> : crystal structure of {Fe <sup>II</sup> [N(SiMe <sub>3</sub> ) <sub>2</sub> ] <sub>2</sub> } <sub>2</sub> .....	117

<b>Figure 76</b> : Integrated GC-MS peak areas of different H <sub>2</sub> decomposition byproducts of (a) solid Fe(COT) <sub>2</sub> , (0.4 MPa H <sub>2</sub> , 25°C) and (b) solution of Fe(COT) <sub>2</sub> (2.5x10 <sup>-3</sup> mol.L <sup>-1</sup> ) in C <sub>1</sub> C <sub>4</sub> ImNTf <sub>2</sub> , (0.4 MPa H <sub>2</sub> , 150°C), plotted versus time. ....	119
<b>Figure 77</b> : 2.5 x 10 <sup>-2</sup> mol.L <sup>-1</sup> solution of Fe(COT) <sub>2</sub> in C <sub>1</sub> C <sub>4</sub> ImNTf <sub>2</sub> , before (left) and after (right) the reaction with 0.4 MPa H <sub>2</sub> for 48 h at 150°C. ....	119
<b>Figure 78</b> : TEM images of Fe-NPs (4.4±0.5nm) prepared through the decomposition of 5x 10 <sup>-3</sup> mol.L <sup>-1</sup> solution of Fe(COT) <sub>2</sub> in C <sub>1</sub> C <sub>4</sub> ImNTf <sub>2</sub> under 0.4MPa H <sub>2</sub> for 48 h at 150°C. ....	120
<b>Figure 79</b> : HRTEM image of Fe-NP generated by the decomposition of Fe(COT) <sub>2</sub> in C <sub>1</sub> C <sub>4</sub> ImNTf <sub>2</sub> and the FFT of the particle indexed by a tetragonal structure along the (-110) zone axis with lattice parameters of a=6.8Å, c=6.1Å. ....	121
<b>Figure 80</b> : TEM images for Fe-NPs prepared from the decomposition of Fe(COT) <sub>2</sub> in (a) C <sub>1</sub> C <sub>2</sub> ImB(CN) <sub>4</sub> , (b) C <sub>1</sub> C <sub>2</sub> ImFAP and (c) C <sub>1</sub> C <sub>2</sub> ImNTf <sub>2</sub> . ....	122
<b>Figure 81</b> : HRTEM image of Fe <sub>2</sub> O <sub>3</sub> -NP generated by the decomposition of Fe(COT) <sub>2</sub> in C <sub>1</sub> C <sub>2</sub> ImB(CN) <sub>4</sub> and the FFT of the particle indexed by a cubic Fe <sub>2</sub> O <sub>3</sub> structure along the (1-11) zone axis with a lattice parameter of 8.3Å. ....	122
<b>Figure 82</b> : Sum of integrated GC-MS peak areas of different H <sub>2</sub> decomposition byproducts during the reaction of H <sub>2</sub> (0.4MPa) with {Fe <sup>II</sup> [N(SiMe <sub>3</sub> ) <sub>2</sub> ] <sub>2</sub> } <sub>2</sub> (a) in pure form starting at 25°C while raising T 1°C/min to 100°C and then keeping it constant for 5h, (b) in C <sub>1</sub> C <sub>4</sub> ImNTf <sub>2</sub> solution (2.5 x 10 <sup>-2</sup> mol.L <sup>-1</sup> , 100°C), plotted versus time. ....	124
<b>Figure 83</b> : GC-MS chromatograph recorded during the reaction with H <sub>2</sub> (0.4MPa) of (a) solid {Fe[N(SiMe <sub>3</sub> ) <sub>2</sub> ] <sub>2</sub> } <sub>2</sub> (corresponding to 70°C reaction temperature) and (b) {Fe[N(SiMe <sub>3</sub> ) <sub>2</sub> ] <sub>2</sub> } <sub>2</sub> solution in C <sub>1</sub> C <sub>4</sub> ImNTf <sub>2</sub> (2.5 x 10 <sup>-2</sup> mole.L <sup>-1</sup> , 100°C, after 1h of reaction). ....	125
<b>Figure 84</b> : 2.5 x 10 <sup>-2</sup> mol.L <sup>-1</sup> solution of {Fe[N(SiMe <sub>3</sub> ) <sub>2</sub> ] <sub>2</sub> } <sub>2</sub> in C <sub>1</sub> C <sub>4</sub> ImNTf <sub>2</sub> , left: before and right: after, the reaction with 0.4MPa H <sub>2</sub> for 4 h at 100°C. ....	125
<b>Figure 85</b> : GC chromatogram of the volatile byproducts resulting from the reaction of 2.5 x 10 <sup>-2</sup> mol.L <sup>-1</sup> solution of {Fe[N(SiMe <sub>3</sub> ) <sub>2</sub> ] <sub>2</sub> } <sub>2</sub> in C <sub>1</sub> C <sub>4</sub> ImNTf <sub>2</sub> with 0.4MPa H <sub>2</sub> for 4h at 100°C. ....	126
<b>Figure 86</b> : TEM image of NPs prepared through the decomposition of 2.5 x 10 <sup>-2</sup> mol.L <sup>-1</sup> solution of {Fe[N(SiMe <sub>3</sub> ) <sub>2</sub> ] <sub>2</sub> } <sub>2</sub> in C <sub>1</sub> C <sub>4</sub> ImNTf <sub>2</sub> under 0.4MPa of H <sub>2</sub> at 100°C for 4 h. ....	126
<b>Figure 87</b> : (a) Exemplary HRTEM image of Fe-NPs generated by the decomposition of {Fe[N(SiMe <sub>3</sub> ) <sub>2</sub> ] <sub>2</sub> } <sub>2</sub> in C <sub>1</sub> C <sub>4</sub> ImNTf <sub>2</sub> under 0.4MPa of H <sub>2</sub> for 4h, 100°C and (b) FFT of the particle in the white square indexed by a fcc structure along the (001) zone axis with a lattice parameter of 3.52Å corresponding to fcc Fe. ....	127
<b>Figure 88</b> : (a) HRTEM image of Fe <sub>2</sub> O <sub>3</sub> -NPs coexisting with the Fe-NPs from Figure 87 and (b) FFT of the particle in the white square indexed by a tetragonal Fe <sub>2</sub> O <sub>3</sub> structure along the (10 14 -3) zone axis. ....	128
<b>Figure 89</b> : Schematic illustration of the diffraction of X-rays on a lattice plane of a crystalline material (left), and illustration of the scattering vector in the reciprocal space (right). ....	139
<b>Figure 90</b> : Sealed capillaries in a multiple sample holder for SAXS experiment. ....	142
<b>Figure 91</b> : Graphical illustration for SQUID measurements. ....	144



## List of tables

<b>Table 1</b> : Main properties of metallic Cobalt .....	9
<b>Table 2</b> : 94.5 MHz $^{59}\text{Co}$ NMR shifts and line widths of $[\text{Co}(\eta^3\text{-C}_8\text{H}_{13})(\eta^4\text{-C}_8\text{H}_{12})]$ <sup>63, 65</sup> .....	13
<b>Table 3</b> : Size and shape of Co-NPs prepared through the $\text{H}_2$ decomposition of Co ( $\eta^3\text{-C}_8\text{H}_{13}$ ) ( $\eta^4\text{-C}_8\text{H}_{12}$ ) in different experimental conditions. ....	15
<b>Table 4</b> : Size and shape of Co-NPs prepared from $\text{Co}_2(\text{CO})_8$ in several ILs under different experimental conditions.....	18
<b>Table 5</b> : Size evolution of M- NPs (M = Co, Ru and Ni) generated from $\text{Co}(\text{COD})(\text{COE})$ , $\text{Ni}(\text{COD})_2$ and $\text{Ru}(\text{COD})\text{COT}$ , respectively, at $100^\circ\text{C}$ ( $75^\circ\text{C}$ in case of Ni-NPs) under 0.4 MPa of $\text{H}_2$ , 4 h, in $\text{C}_1\text{C}_n\text{ImNTf}_2$ where $n = 4; 8; 12; 14$ within 4 h (30 min in case of Ni-NPs). ....	36
<b>Table 6</b> : Anisotropy constants of Co .....	47
<b>Table 7</b> : Geometrical parameters of the RuCu nanoparticles deduced from the SAXS and TEM measurements for the three compositions. $\Phi_{core}$ is the Ru core diameter, $t_{shell}$ the Cu shell thickness, $\Phi$ the resulting total diameter of NPs and their concentration in the IL deduced from both SAXS and TEM. ....	73
<b>Table 8</b> : Size, shape, crystal structure and magnetic moment of Fe-NPs prepared through the decomposition of various Fe precursors under different experimental conditions. ....	113
<b>Table 9</b> : Size and oxidation state of Fe-NPs prepared through the decomposition of various Fe precursors in several ILs. ....	115
<b>Table 10</b> : Variation of Fe NPs size with the reaction temperature .....	128



# Appendix 1

---





## Magnetic behavior of NPs

Materials are classified by their response to an externally applied magnetic field. Five basic behaviors can be observed: diamagnetism, paramagnetism, ferromagnetism, antiferromagnetism, and ferrimagnetism. In the presence of an externally applied magnetic field, the atomic current loops created by the orbital motion of electrons respond to oppose the applied field. All materials display this type of weak repulsion to a magnetic field known as diamagnetism. Diamagnetism is observed in materials with filled electronic subshells where the magnetic moments are paired and overall cancel each other. Diamagnetic materials have a negative susceptibility ( $\chi < 0$ ) and weakly repel an applied magnetic field (e.g., quartz, SiO<sub>2</sub>). The effects of these atomic current loops are overcome if the material displays a net magnetic moment or has a long-range ordering of its magnetic moments.<sup>184</sup> Indeed, diamagnetism is very weak, and therefore, any other form of magnetic behavior that a material may possess usually overpowers the effects of the current loops. All other types of magnetic behaviors are observed in materials that are at least partially attributed to unpaired electrons in their atomic shells, often in the 3d or 4f shells of each atom.

Materials whose atomic magnetic moments are uncoupled display paramagnetism; thus, paramagnetic materials have moments with no long-range order, and there is a small positive magnetic susceptibility ( $\chi \approx 0$ ), e.g., pyrite.<sup>185, 186</sup>

Ferromagnetic materials have aligned atomic magnetic moments of equal magnitude, and their crystalline structures allow for direct coupling interactions between them, which may strongly enhance the flux density (e.g., Fe, Ni, and Co). Furthermore, the aligned moments in ferromagnetic materials can confer a spontaneous magnetization in the absence of an applied magnetic field. Materials that retain permanent magnetization in the absence of an applied field are known as hard magnets.

Materials having atomic magnetic moments of equal magnitude that are arranged in an antiparallel fashion display antiferromagnetism (e.g., troilite FeS). The exchange interaction couples moments in such a way that they are antiparallel, leaving a zero net magnetization.<sup>187</sup> Above the so-called Néel temperature, thermal energy is sufficient to cause the oppositely aligned atomic moments to randomly fluctuate, leading to a disappearance of their long-range order. In this state, the materials exhibit paramagnetic behavior.

Ferrimagnetism is a property exhibited by materials whose atoms or ions tend to assume an ordered but nonparallel arrangement in a zero applied field below a characteristic Néel

temperature (e.g.,  $\text{Fe}_3\text{O}_4$  and  $\text{Fe}_3\text{S}_4$ ). In the usual case, within a magnetic domain, a substantial net magnetization results from the antiparallel alignment of neighboring non-equivalent sublattices. The macroscopic behavior is similar to ferromagnetism. Above Néel temperature, the substance becomes paramagnetic (Figure 107).<sup>188, 189</sup>

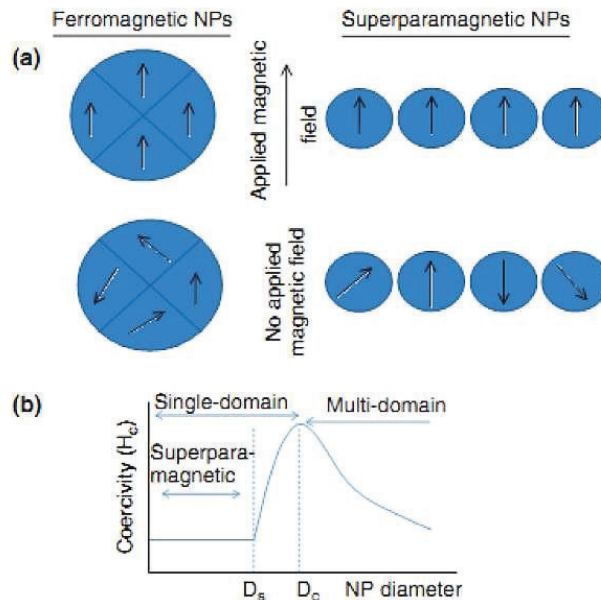


Figure 107 : Magnetization behavior of ferromagnetic and superparamagnetic NPs under an external magnetic field.<sup>190</sup>

### Size-dependent magnetic behavior

Magnetic effects are caused by movements of particles having both mass and electric charges. These particles are electrons, holes, protons, and positive and negative ions. A spinning electric-charged particle creates a magnetic dipole, so-called magneton. In ferromagnetic materials, magnetons are associated in groups. A magnetic domain (also called a Weiss domain) refers to a volume of ferromagnetic material in which all magnetons are aligned in the same direction by the exchange forces. This concept of domains distinguishes ferromagnetism from paramagnetism.

The domain structure of a ferromagnetic material determines the size dependence of its magnetic behavior. When the size of a ferromagnetic material is reduced below a critical value, it becomes a single domain (Figure 107).

The single domain nanoparticles, due to their magnetic configuration, possess unique properties. For example, a single domain nanoparticle, having a single easy axis of magnetization, is then considered as a uniaxial nanoparticle. Its magnetization can then be seen as a macro-spin which can have two positions of equilibrium, "up" or "down" around its

easy axis of magnetization. In the absence of an external magnetic field, the magnetization may, under certain conditions, turn spontaneously under the effect of thermal agitation. This reversal of the magnetization depends on the energy barrier ( $E_a$ ) between the two equilibrium positions (Figure 108). This energy barrier is expressed by:

$$E_a = K_a V \sin^2 \theta$$

Where  $K_a$  is the effective anisotropy constant including magneto-crystalline anisotropy, shape anisotropy and surface anisotropy,  $V$  is the volume of the particle and  $\theta$  is the angle between the particle's magnetic moment and the easy axis of magnetization.

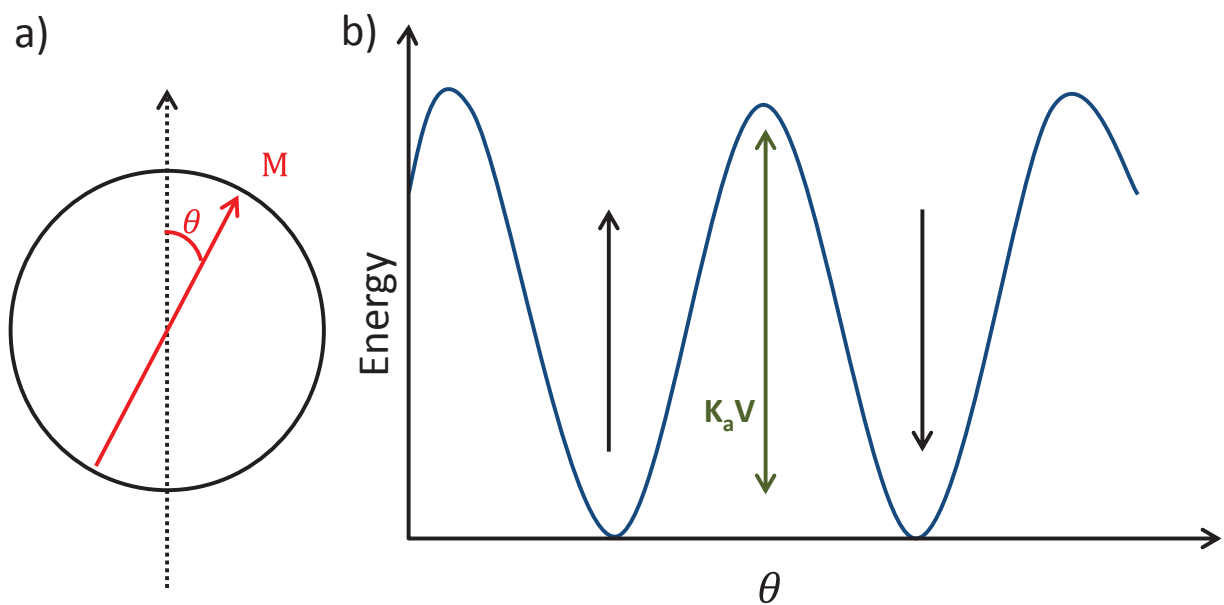


Figure 108 : a) Schematic representation of a uniaxial single domain nanoparticle with the angle  $\theta$  between the easy axis of magnetization and the magnetic moment. b) energy diagram of the nanoparticle as a function of  $\theta$ .

When the thermal energy is higher than the energy barrier, the magnetization reverses spontaneously. This phenomenon is called superparamagnetism. Louis Néel has determined the average time of reversal of the magnetization, relaxation time  $\tau$ :

$$\tau = \tau_0 e^{\frac{E_a}{k_B T}}$$

Where  $\tau_0$  is the limited relaxation time ( $\approx 10^{-9}$  s) and  $k_B$  is the Boltzman constant. This relaxation phenomenon therefore depends on three parameters: the volume of the nanoparticle, its effective anisotropy and temperature.

When the magnetization of such nanoparticles is measured, the observed result depends on the time of measurement ( $\tau_m$ ) with respect to the relaxation time of the magnetization.

- If  $\tau_m < \tau$ , the magnetization doesn't have the time to return and hence appears as being blocked in its position
- If  $\tau_m > \tau$ , the magnetization has the time to return back and appears to be statistically zero in value.

It is therefore possible to define a blocking temperature for a given measurement time. This temperature represents the transition between the blocked state and the superparamagnetic state. It is defined by:

$$T_B = \frac{E_a}{k_B \ln\left(\frac{\tau_m}{\tau_0}\right)}$$

Below this temperature, the nanoparticles will be in a blocked state whereas above, they will be superparamagnetic. Introduced in the living systems, particles are magnetic only in the presence of an external field, which gives them unique advantages in working in biological environments.

# Appendix 2

---



### Further attempts for the synthesis of Fe-NPs

Bis(tri-*t*Butyl mesityl)iron, Fe(Mes\*)<sub>2</sub>, was also considered for the synthesis of Fe-NPs. This compound seems to be very stable and not decomposing under H<sub>2</sub>. It is not very soluble in IL as well. In a first attempt, 2.5x10<sup>-2</sup> mol.L<sup>-1</sup> solution in IL was prepared. After 20 min of stirring, the yellow/orange compound was still not dissolved (just a very little coloring for the solution). Pentane was then added to dissolve but again, it was not very soluble. After, vacuum was applied to evaporate pentane and 0.4 MPa of H<sub>2</sub> were applied at room temperature for 21 hours. No color change was observed. The temperature was then increased to 100°C and kept for 3 hours. Again, there was no change in color. Temperature was further increased to 150°C and kept for 3 further hours. That time, color was slightly changed into a little bit more black, less yellow.

Based on these results, and since the compound seems to be very difficult to reduce, the synthesis of Fe-NPs was tested using a 5x10<sup>-3</sup> mol.L<sup>-1</sup> solution of the precursor in C<sub>1</sub>C<sub>4</sub>ImNTf<sub>2</sub> IL which is pale yellow in color. It was allowed to decompose under aggressive conditions (0.9MPa of H<sub>2</sub>, 150°C for 24 hours). The resulting solution was again, pale yellow in color with no indication of NPs formation.

The last trial was to mix 1mL solution of 5x10<sup>-3</sup> mol.L<sup>-1</sup> of Fe(Mes\*)<sub>2</sub> with 1mL of 5x10<sup>-3</sup> mol.L<sup>-1</sup> Pt(dba)<sub>2</sub> solution and to decompose them simultaneously (0.9MPa H<sub>2</sub>, 150°C, 24 hours). The idea was to check if initially formed Pt nuclei could assist and catalyze the decomposition of Fe(Mes\*)<sub>2</sub>. From TEM, this gave monodispersed NPs of size 2.6±0.2nm (Figure 109). Further experiments need to be considered in order to identify either the monometallic or the bimetallic nature of such NPs and to identify its exact structure.



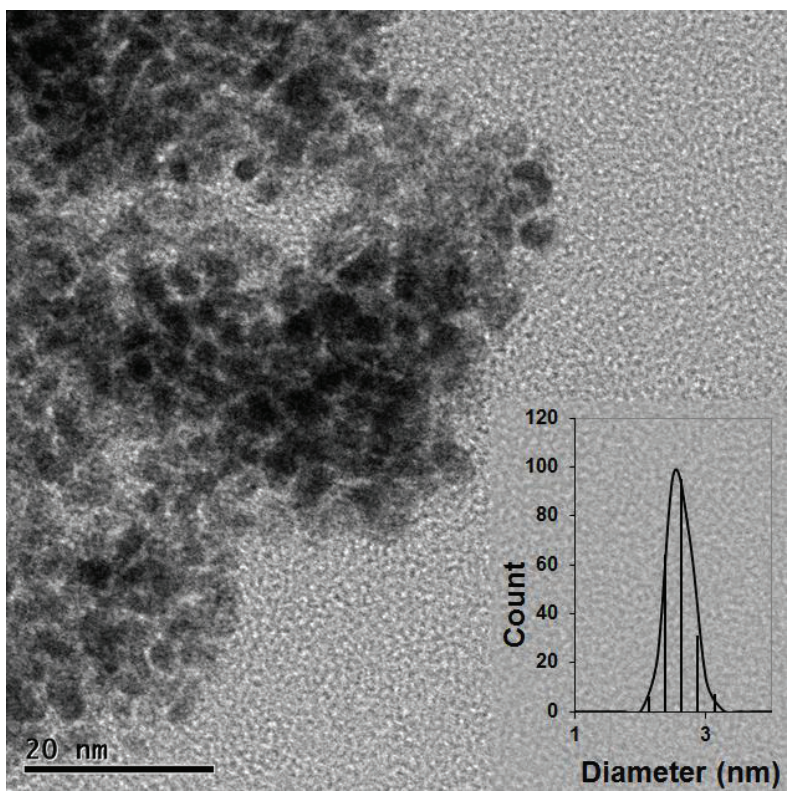


Figure 109 : TEM images for 2.6 nm Fe-Pt NPs prepared through the simultaneous decomposition of equimolar solution of 1 mL solution of  $\text{Fe}(\text{Mes}^*)_2$  and  $\text{Pt}(\text{dba})_2$  ( $5 \times 10^{-3}$  mol.L<sup>-1</sup> total concentration) under 0.9 MPa  $\text{H}_2$ , 150°C, 24 h.

# Appendix 3

---



### Phase diagram of CoRu systems:

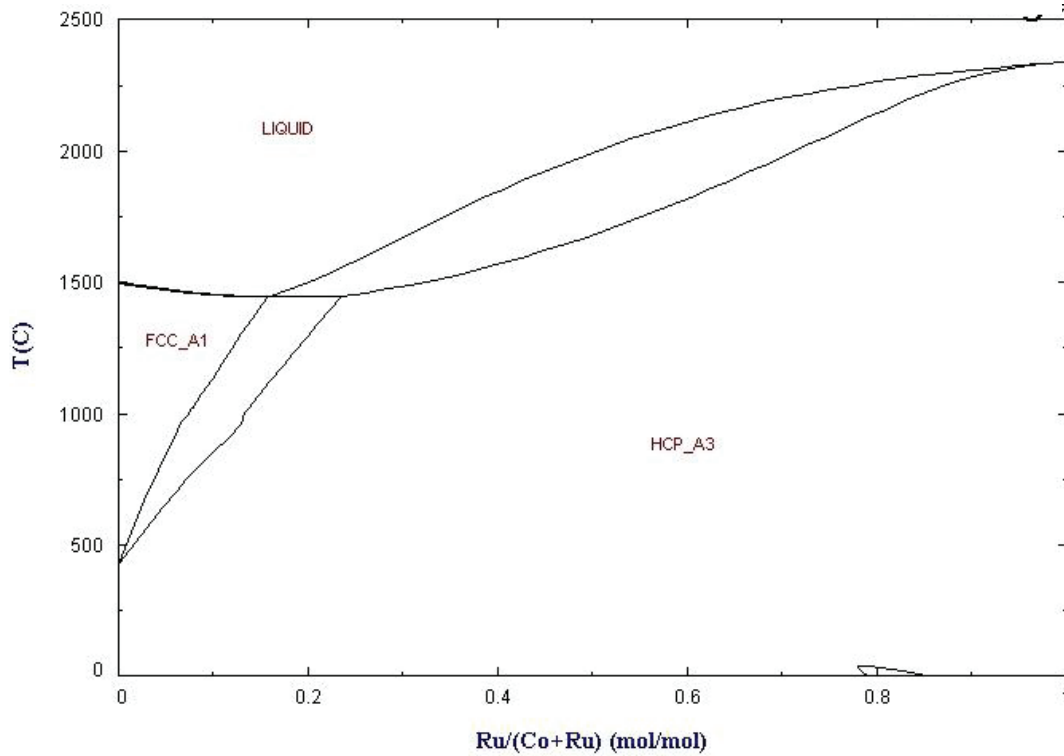


Figure 110 : Phase diagram of CoRu systems recorded at atmospheric pressure as reported in the SGTE noble metal alloy database. [http://www.crct.polymtl.ca/fact/documentation/SGnobl/SGnobl\\_Figs.htm](http://www.crct.polymtl.ca/fact/documentation/SGnobl/SGnobl_Figs.htm)

### Phase diagram of CoPt systems:

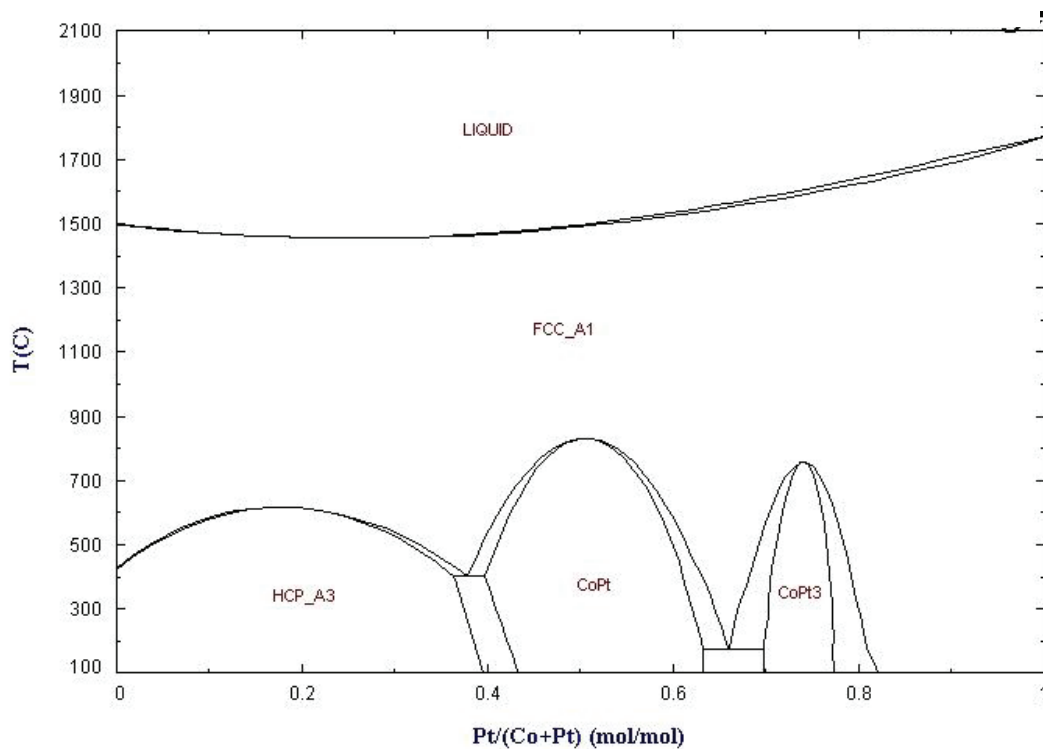


Figure 111 : Phase diagram of CoPt systems recorded at atmospheric pressure as reported in the SGTE noble metal alloy database. [http://www.crct.polymtl.ca/fact/documentation/SGnobl/SGnobl\\_Figs.htm](http://www.crct.polymtl.ca/fact/documentation/SGnobl/SGnobl_Figs.htm)

### Phase diagram of CoSn systems:

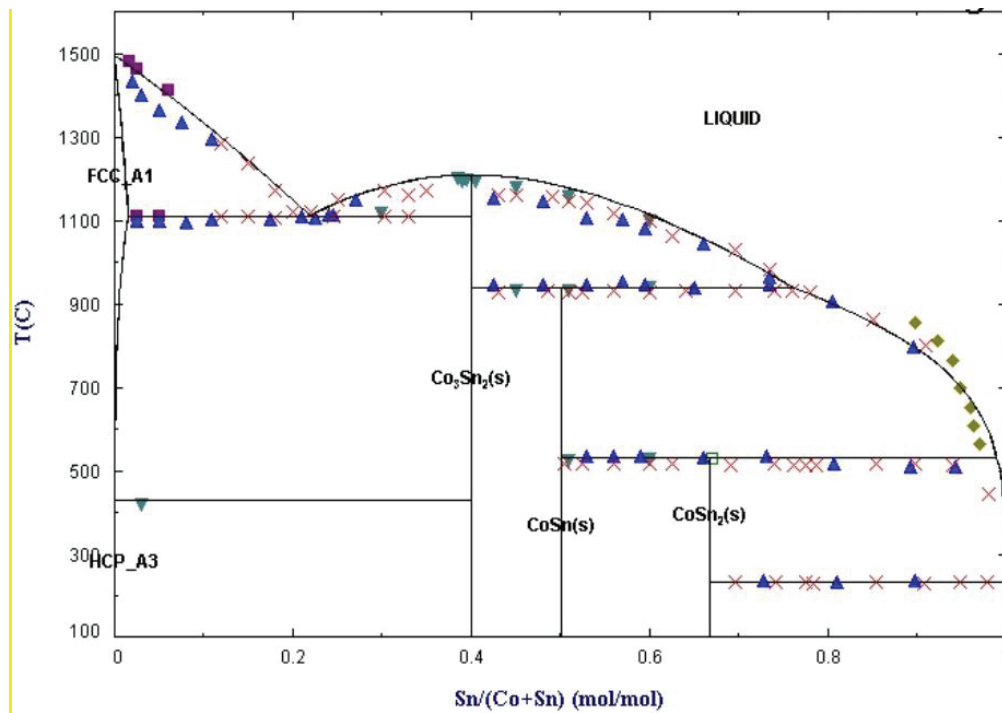


Figure 112 : Phase diagram of CoSn systems recorded at atmospheric pressure as reported in the SGTE noble metal alloy database. [http://www.crct.polymtl.ca/fact/documentation/SGnobl/SGnobl\\_Figs.htm](http://www.crct.polymtl.ca/fact/documentation/SGnobl/SGnobl_Figs.htm)

### Phase diagram of CoSi systems:

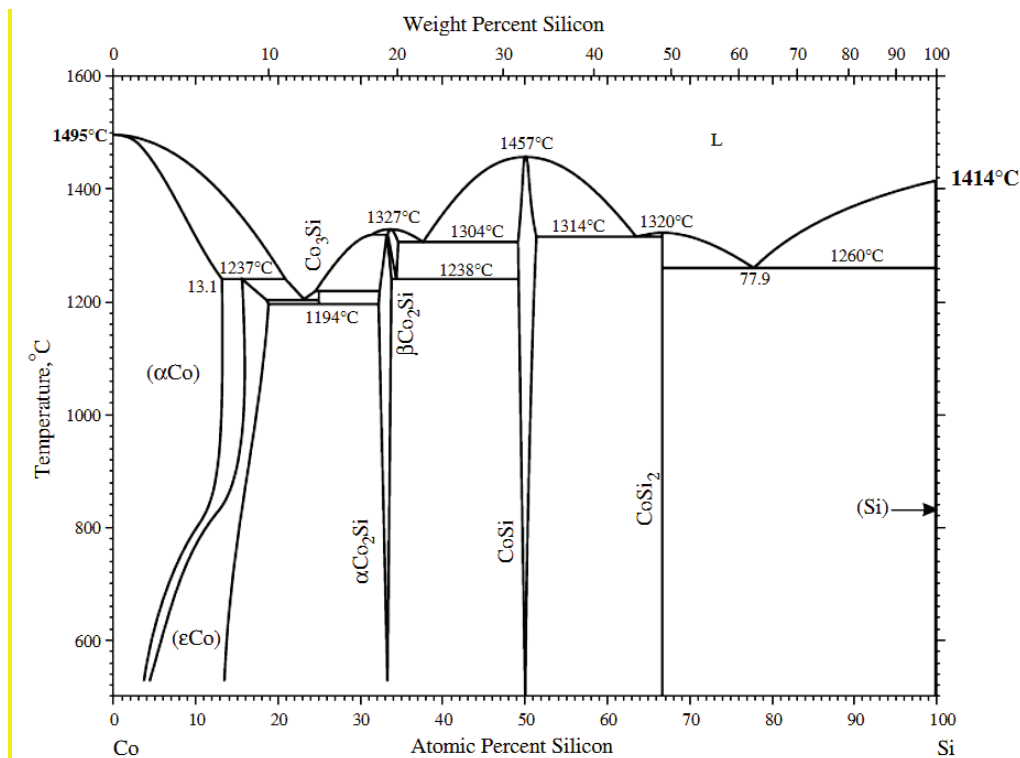


Figure 113 : Phase diagram of CoSi systems recorded at atmospheric pressure. (J. Phase equilibrium and diffusion, Vol. 29 No.3 2008)

# Appendix 4

---



## Application for beam time at ESRF – Experimental Method

### In-situ SAXS/WAXS study of bimetallic Co-Ru nanoparticles

#### **Proposal Summary (should state the aims and scientific basis of the proposal) :**

Bimetallic nanoparticles (bMNPs) have received considerable attention because they can be used in a variety of applications in catalysis and advanced magnetic or optical devices. In most cases, an accurate control of the size and structure of these bMNPs is mandatory. The structural arrangement of the two metals deeply modifies their physico-chemical properties. Depending on the application, either core-shell or Janus structures, or nanoalloys are needed. Also, a narrow size distribution generally ensures homogeneous properties of the NPs.

Co-Ru bMNPs are interesting for magnetic and catalytic applications. Their magnetic properties strongly depend on their internal structure [i]. They could also advantageously replace Ru NPs as a catalytic agent for hydrogenation reactions. In this case, a thin shell of Ru is desired around a Co core. Such a core-shell structure may also be needed to prevent oxidation of the bMNPs.

Our group is developing a new and versatile synthesis of size-controlled bMNPs (<10 nm) using various organometallic precursors in ionic liquid (IL) [ii]. We have shown that upon mixing ruthenium and copper precursors, smaller bMNPs are formed as compared to single metals with enhanced size control in a large range of copper molar fraction [iii]. Our recent ASAXS experiments on Ru-Cu NPs have been successful in demonstrating their core-shell structure with an accurate determination of the size of Ru core and the thickness of Cu shell [iv]. These experiments have validated the reaction mechanisms of formation of these objects. More recently, similar experiments have been conducted on Ru-Ta with more mitigated results (mostly because Ru and Ta form alloys). A core-shell structure was observed for NPs synthesised in two steps (i.e. addition of Ta precursor on pre-formed Ru NPs) [v].

We propose to perform another series of ASAXS experiments focused on Co-Ru bimetallic NPs synthesised in two steps (addition of Ru (resp. Co) precursor on pre-formed Co (resp. Ru) NPs). The goal is to demonstrate the validity of our approach to form both Co@Ru and Ru@Co (*core@shell*) bimetallic NPs. Indeed, ASAXS measurements have already proven successful at determining the internal structure of Co-Pt NPs prepared by condensation in an UHV chamber [vi].

#### **Scientific background:**

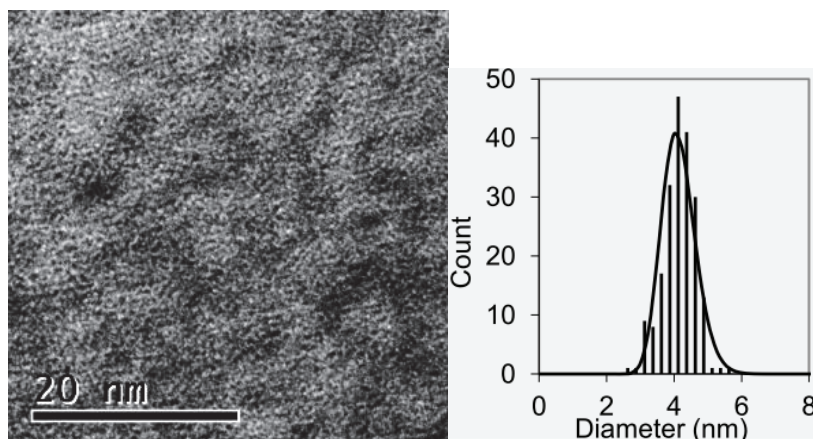
In a previous work, we have depicted the synthesis of bimetallic Ru-Cu nanoparticles from the decomposition of organometallic (OM) Ru and Cu precursors under H<sub>2</sub>. [iii] Interestingly enough, upon mixing the two OMs, smaller NPs are generally formed as compared to the pure metals. As mentioned above, owing to the ASAXS technique, the Ru(core)/Cu(shell) structure of the bMNPs [iv] unambiguously validates the mechanism of formation of these bMNPs: the fast reacting Ru(COD)(COT) precursor is first decomposed into Ru NPs, and the slowly reacting precursor CuMes then reacts at the Ru surface. This second reaction, which involves surface hydrides present on the RuNPs, is responsible for the size reduction of the final bMNPs.

Such size reduction by alloying two metals is also observed in other bimetallic systems. For instance, by decomposition of (Me<sub>3</sub>CH<sub>2</sub>)<sub>3</sub>Ta=CHCMe<sub>3</sub> under H<sub>2</sub> in IL, agglomerated TaNPs with large size distribution are obtained. When mixed to



Ru(COD)(COT), smaller Ru(core)-Ta(shell) bMNPs with much narrower size distribution, are formed. However, a core-shell structure could only be assessed for bMNPs synthesised by reaction of the Ta precursor on pre-formed Ru NPs [v].

In the past months, this synthetic technique has been extended to Co by decomposition of (1,5-cyclooctadiene)(cycloocta-dienyl)Cobalt(I), Co(COD)(COE) in 1-butyl-3-methylimidazolium bis-(trifluoromethane)sulfonimide  $C_1C_4ImNTf_2$  under 0.4 MPa  $H_2$  at 100°C for 4 h. These conditions afford Co NPs with a diameter of  $4.1 \pm 0.5$  nm (figure). Interestingly enough, these Co NPs also bear surface hydrides that react with Ru(COD)(COT). When a suspension of freshly prepared CoNPs is mixed with an IL solution of Ru(COD)(COT) and kept during 24 h under Ar at room temperature, the size of the NPs increases from 4.1 to 5.6 nm. Moreover, no isolated RuNPs are observed by STEM/TEM analysis.



*Left – TEM image and right – corresponding size distribution of CoNPs formed by decomposition of Co(COD)(COE) under  $H_2$  at 100°C in  $C_1C_4ImNTf_2$*

**Experimental technique(s), required set-up(s), measurement strategy, sample details (quantity, ...):**

In this project, we want to study the size and morphology of these Co-Ru NPs for both Co@Ru and Ru@Co configurations. For both configurations, the amount of the shell metal relative to the core will be varied between 0.5 and 3.

For it, we plan to perform ASAXS measurements at both Ru K-edge (22.117 keV) and Co K-edge (7.7 keV). In contrary to TEM, this technique brings a statistical information about the size and morphology of NPS. Taking advantage of the anomalous contrast, the core-shell structure can be revealed leading to the determination of the core diameter and shell thickness. Due to the high reactivity of Co and in order to prevent ageing, oxidation or sedimentation, the samples will be prepared in real time in sealed capillaries ( $\phi=1$ mm (resp 1.5mm) for Co (resp Ru) -edge measurements, wall thickness=10  $\mu$ m) during the beam time allocation. They will be filled with the IL containing the bMNPs. The different capillaries (including one filled with pure  $C_1C_4ImNTf_2$  liquid for correcting the strong liquid contribution) will be mounted perpendicularly on a multiple sample holder. At each edge, to overcome eventual sedimentation the measurements for one sample will be performed at the five selected energies before sample change.

**Beamline(s) and beam time requested with justification :**

To achieve these ASAXS measurements, including energy adjustments, sample alignment and transmission measurements, we need 12 shifts of beam time on the BM02 beamline. The SAXS images will be recorded using a XPAD detector.

### **Results expected and their significance in the respective field of research :**

In case of core-shell nanoparticles the variation of the differential SAXS intensities with the scattering vector is expected to be different from that of the total intensities. Moreover an inverse behaviour between the Co and Ru edge measurements has to be observed. Such findings are very important for a better understanding of the synthesis of cobalt-ruthenium nanoparticles (Co-Ru NPs) in ILs.

### **References**

- 
- 1 D. Zitoun, C. Amiens, B. Chaudret, M.C. Fromen, P. Lecante, M.J. Casanove and M. Respaud, *J. Phys. Chem. B*, **2003**, *107*, 6997-7005
  - 2 P. Campbell, M. HG Prechtl, C. C Santini, and P.-H. Haumesser, *Curr. Org. Chem.* **2013**, *17*, 414–429.
  - 3 I.S. Helgadottir, P. P. Arquillière, P. Bréa, C. C. Santini, P. -H. Haumesser, K. Richter, A. -V. Mudring, and M. Aouine, *Microelectronic Engin.* *107*, 2013, 229 – 232; Arquillière, P. P.; Helgadottir, I. S.; Santini, C. C.; Haumesser, P.-H.; Aouine, M.; Massin, L. & Rousset, J.-L., *Topics in Catal.*, **2013**, *56*, 1192-1198
  - 4 Helgadottir, I.; Freychet, G.; Arquillière, P.; Maret, M.; Gergaud, P.; Haumesser, P. & Santini, C, *Nanoscale*, **2014**, *6*, 14856-14862
  - 5 ESRF report 02-01-835
  - 6 ESRF report MA2231